

# Cooling for Microsystems: Miniaturization Prospects for Pulse Tube Cryocooler

Zur Erlangung des akademischen Grades eines

**DOKTORS DER INGENIEURWISSENSCHAFTEN (Dr.-Ing.)**

von der KIT-Fakultät für Maschinenbau des

Karlsruher Instituts für Technologie (KIT)

angenommene

**Dissertation**

von

**M.Sc. Natheer Almtireen**

Tag der mündlichen Prüfung: 25.07.2022

Hauptreferent: Prof. Dr. Jan G. Korvink

Korreferentin: Prof. Dr.-Ing. Bettina Frohnappel

Karlsruher Institut für Technologie  
Institut für Mikrostrukturtechnik  
H.-v.-Helmholtz Platz 1  
76344 Eggenstein-Leopoldshafen

This work is licensed under a Creative Commons “Attribution-NonCommercial-ShareAlike 4.0 International” license.



# Acknowledgement

I would like to thank my family, including my parents, wife, brothers and sisters. Without their encouragement and support, none of this would be possible. My cherished parents, thank you for everything you did to raise and shape me into the man I am today. Heartfelt thanks go to my wife, without whom my Ph.D journey would be impossible. My dear wife, I consider myself extremely fortunate to have you. Thank you for your love, care, and support. Every little thing you do for me is simply amazing.

I would like to thank my advisor, Prof. Dr. Jan G. Korvink, and my co-advisor, Prof. Dr. Jürgen J. Brandner, who have both given me support, time, and motivation throughout my Ph.D. studies. I am grateful for all of the discussions and knowledge-sharing that took place during our monthly meetings. I remember well my first meeting with Prof. Korvink at the German Jordanian University (GJU) in Amman, Jordan, when I realized that he had a brilliant mind. I am very grateful for Prof. Brandner's incredibly valuable guidance and support, which helped me overcome many academic and non-academic issues throughout my doctoral research. My sincere appreciation goes to Prof. Dr.-Ing. Bettina Frohnapfel for her effort in reviewing and examining my thesis as co-referent.

I would like to express my gratitude to the German Jordanian University (GJU) for its financial support throughout my studies. I would also like to thank the Karlsruhe Institute of Technology (KIT), Institute of Microstructure Technology (IMT), for permitting me to use their software tools, for providing financial support for my conference travel, and for their effort to ease the burden of the coronavirus pandemic.

Finally, I humbly express my gratitude to everyone who has helped me out in getting this far.

# Abstract

Regenerative cryocoolers such as Stirling, Gifford–McMahon, and pulse tube cryocoolers possess great merits such as small size, low cost, high reliability, and good cooling capacity. These merits led them to meet many IR and superconducting-based application requirements. Among these cryocoolers, a machine called *pulse tube cryocooler (PTC)* that exhibits excellent merits and has the potential to be miniaturized for on-chip and microsystems applications. This thesis investigates the miniaturization aspects of this machine using various numerical analyses and computational fluid dynamic (CFD) simulation models.

In this thesis, an analysis of the complex operation for the tube element is proposed for an orifice pulse tube cryocooler. This is achieved through phasor analysis using fundamental thermodynamic relations to estimate the approximated cooling power associated with this machine. Moreover, the phase shift angle effect is illustrated by forming an analogy between the phase shift mechanism and a series RLC circuit model. Following that, a one-dimensional model based on mass and energy conservation equations is presented; the reduced model is numerically solved for the temperature and velocity of the gas along the tube to determine the mass flow and time-averaged enthalpy flows at the cold and hot ends of the tube. The findings from the one-dimensional analysis are compared with the previous phasor analysis results.

The regenerator is a critical component in these closed-cycle cryocoolers. The thesis presents a one-dimensional numerical analysis of the idealized thermal equations of the matrix and working gas within the regenerator. The algorithm predicts the temperature profiles of the gas during heating and cooling and the matrix nodal temperatures. It investigates how the length and diameter of the regenerator, the geometric parameters of the matrix, the number of heat transfer units, and the volumetric flow rate affect the performance of an ideal regenerator. It also proposes a 2D axisymmetric CFD model to evaluate and validate the ideal regenerator model. Moreover, an analytic procedure is developed to estimate the losses that exist in the regenerator. The results are compared to that of another software, so-called REGEN, developed by NIST.

After that, an axisymmetrical CFD numerical simulation is reported that reveals the oscillating flow and heat transfer processes found in an inertance-type pulse tube cryocooler. The operating

frequency effects are investigated, and the impacts of the system's reduced size operating at high-frequency on the system's cooling performance are studied. Furthermore, a special-purpose software called Sage and CFD modeling is utilized to develop ultra-miniature PTC models. Their performance parameters are studied, and their eligibility for on-chip and micro-system applications is determined.

# Zusammenfassung

Regenerative Kryokühler wie Stirling-, Gifford-McMahon- und Pulsrohr-Kryokühler besitzen große Vorzüge wie geringe Größe, niedrige Kosten, hohe Zuverlässigkeit und gute Kühlleistung. Diese Vorzüge führten dazu, dass sie viele Anforderungen von IR- und supraleitenden Anwendungen erfüllen. Unter diesen Kryokühlern gibt es eine Maschine, die als Pulsröhren-Kryokühler (PTC) bezeichnet wird, die ausgezeichnete Vorzüge aufweist und das Potenzial hat, für On-Chip- und Mikrosystem-Anwendungen miniaturisiert zu werden. In dieser Arbeit werden die Miniaturisierungsaspekte dieser Maschine anhand verschiedener numerischer Analysen und computergestützter fluiddynamischer (CFD) Simulationsmodelle untersucht.

In dieser Arbeit wird eine Analyse des komplexen Betriebs für das Röhrenelement für einen Orifice Pulse Tube Cryocooler (OPTC) vorgeschlagen. Dies wird durch eine Phasenanalyse unter Verwendung fundamentaler thermodynamischer Beziehungen erreicht, um die mit dieser Maschine verbundene Kühlleistung näherungsweise abzuschätzen. Darüber hinaus wird der Effekt des Phasenverschiebungswinkels veranschaulicht, indem eine Analogie zwischen dem Phasenverschiebungsmechanismus und einem Serien-RLC-Schaltungsmodell gebildet wird. Anschließend wird ein eindimensionales Modell vorgestellt, das auf Massen- und Energieerhaltungsgleichungen basiert; das reduzierte Modell wird numerisch für die Temperatur und Geschwindigkeit des Gases entlang des Rohrs gelöst, um den Massenstrom und die zeitlich gemittelten Enthalpieströme am kalten und heißen Ende des Rohrs zu bestimmen. Die Erkenntnisse aus der eindimensionalen Analyse werden mit den bisherigen Ergebnissen der Phasoranalyse verglichen.

Der Regenerator ist eine kritische Komponente in diesen Kryokühlern mit geschlossenem Kreislauf. Die Arbeit präsentiert eine eindimensionale numerische Analyse der idealisierten thermischen Gleichungen der Matrix und des Arbeitsgases innerhalb des Regenerators. Der Algorithmus prognostiziert die Temperaturprofile des Gases während des Aufheizens und Abkühlens sowie die Matrix-Knotentemperaturen. Es wird untersucht, wie die Länge und der Durchmesser des Regenerators, die geometrischen Parameter der Matrix, die Anzahl der Wärmeübertragungseinheiten und der Volumenstrom die Leistung eines idealen Regenerators beeinflussen. Es wird auch ein achsensymmetrisches 2D-CFD-Modell vorgeschlagen, um das Modell des idealen Regenerators zu bewerten und zu validieren. Darüber hinaus wird ein analytisches Verfahren entwickelt, um

die im Regenerator vorhandenen Verluste abzuschätzen. Die Ergebnisse werden mit denen einer anderen Software, genannt REGEN, die vom NIST entwickelt wurde, verglichen.

Danach wird über eine achsensymmetrische numerische CFD-Simulation berichtet, die die oszillierenden Strömungs- und Wärmeübertragungsprozesse in einem Inertanz-Pulsrohr-Kryokühler aufzeigt. Die Auswirkungen der Betriebsfrequenz werden untersucht, und die Auswirkungen der reduzierten Größe des Systems bei Betrieb mit hoher Frequenz auf die Kühlleistung des Systems werden untersucht. Darüber hinaus wird eine spezielle Software namens Sage und CFD-Modellierung verwendet, um Ultra-Miniatur-PTC-Modelle zu entwickeln. Ihre Leistungsparameter werden untersucht und ihre Eignung für On-Chip- und Mikrosystemanwendungen wird bestimmt.

# Nomenclature

## *Symbols*

$\bar{m}$	Average mass flow rate	$kg.s^{-1}$
$\mathbf{w}$	Velocity vector	$m.s^{-1}$
$\Delta M_f$	Fluid mass element	$kg$
$\Delta p$	The pressure loss	$Pa$
$\Delta V_f$	Fluid control volume	$m^3$
$\Delta V_m$	Matrix control volume	$m^3$
$\dot{Q}_{c,loss}$	Axial heat conduction loss	$W$
$\dot{Q}_{net}$	Net cooling power	$W$
$\dot{Q}_{Th,loss}$	The regenerator's Thermal loss	$W$
$\dot{H}$	Enthalpy flow rate	$J.s^{-1}$
$\dot{m}$	Mass flow rate	$kg.s^{-1}$
$\dot{Q}$	Heat flow rate	$J.s^{-1}$
$\dot{V}$	System average pressure	$m^3.s^{-1}$
$\dot{W}_{ac,loss}$	Loss in acoustic power due to void volume	$W$
$\dot{W}_{ac}$	Input acoustic power	$W$
$u$	Specific internal energy	$J.kg^{-1}$
$v$	Specific volume	$m^3.kg^{-1}$
$A_m$	Matrix thermal conduction heat transfer area	$m^2$
$A_s$	Matrix total heat transfer area	$m^2$
$A_w$	Tube wall cross-sectional area	$m^2$
$A_{\perp}$	The surface area perpendicular to flow	$m^2$
$A_{ff}$	Free flow cross-sectional area	$m^2$
$A_{reg}$	Cross-sectional area of the regenerator	$m^2$
$C_2$	The inertial resistance factor	$m^{-1}$
$C_c$	Cold stream heat capacity rate	$J.K^{-1}$
$C_h$	Hot stream heat capacity rate	$J.K^{-1}$
$c_p$	Specific heat at constant pressure	$J.kg^{-1}.K^{-1}$
$c_v$	Specific heat at constant volume	$J.kg^{-1}.K^{-1}$
$D_h$	Hydraulic diameter	$m$
$d_w$	Matrix wire diameter	$m$
$D_{reg}$	Regenerator diameter	$m$

$E$	Energy	$J$
$f$	Frequency	$Hz$
$f_r$	The Fanning fluid coefficient of friction	
$G$	Mass flow rate per unit free flow area	$kg.s^{-1}.m^{-2}$
$h$	Heat transfer coefficient	$W.(m^{-2}.K^{-1})$
$K_f$	fluid thermal conductivity	$W.(m^{-1}.K^{-1})$
$K_m$	matrix thermal conductivity	$W.(m^{-1}.K^{-1})$
$K_t$	Tube wall thermal conductivity	$W.(m^{-1}.K^{-1})$
$L_{reg}$	The regenerator's length	$m$
$M_f$	Mass of the fluid	$kg$
$M_m$	Mass of the matrix	$kg$
$n$	Mesh number	
$N_t$	Number of time nodes	
$N_x$	Number of space nodes	
$P_0$	System average pressure	$Pa$
$P_1$	System pressure amplitude	$Pa$
$P_s$	System pressure	$Pa$
$Q_c$	Heat conduction	$J$
$Q_g$	Heat transported by the gas	$J$
$R$	The gas constant	$J.K^{-1}.mol^{-1}$
$r$	Radial coordinate	
$r_h$	Hydraulic radius	$m$
$S_i$	Pressure loss in porous medium	$Pa.m^{-1}$
$T$	Temperature	$K$
$T_f$	Fluid temperature	$K$
$T_g$	Gas temperature	$K$
$T_m$	Matrix temperature	$K$
$t_{reg}$	Regenerator tube thickness	$m$
$v$	Velocity	$m.s^{-1}$
$V_m$	Total volume of the matrix	$m^3$
$V_{r,v}$	The gas void volume in the regenerator	$m^3$
$V_{reg}$	The volume of the regenerator	$m^3$
$V_r$	Reservoir volume	$m^3$
$V_{void}$	Total volume of void spaces	$m^3$
$W_m$	Total weight of the matrix	$kg$
$x_t$	Screen transverse pitch	$m$
$z$	Axial coordinate	

### ***Unitless parameters***

$C_f$	Fluid capacity ratio
$C_m$	Matrix capacity ratio
$I$	Unit tensor
$j$	The imaginary number
$NTU$	The number of heat transfer units
$Re$	Reynolds number
$COP$	The coefficient of performance
$I_e$	The inefficiency of the regenerator
$NPH$	The Number of pressure heads
$Nu$	Nusselt number
$St$	Stanton number
$Pr$	Prandtl number

### ***Greek Letters***

$\alpha$	Permeability	$m^2$
$\beta_m$	Area density	$m^{-1}$
$\delta_{th}$	Thermal penetration depth	$m$
$\delta_v$	Viscous penetration depth	$m$
$\epsilon$	Thermal effectiveness	
$\gamma$	Heat capacity ratio	
$\lambda_p$	Flow period	$s$
$\mu$	Fluid dynamic viscosity	$J.kg^{-1}.K^{-1}$
$\phi_c$	Phase angle at the cold end	$rad$
$\phi_h$	Phase angle at the hot end	$rad$
$\phi_m$	Porosity of the matrix	
$\psi$	Mesh opening ratio	
$\rho$	Density	$kg.m^{-3}$
$\tau$	Viscous stress	$N.m^{-2}$
$\theta$	Angular cylindrical coordinate	
$\theta_{ph}$	Phase angle	$rad$

### ***Subscripts***

$ad$	Adiabatic
$c$	Cold
$g$	Gas
$h$	Hot

<i>m</i>	Matrix
<i>po</i>	Primary orifice
<i>pt</i>	Pulse tube
<i>reg</i>	Regenerator
<i>r</i>	Radial
<i>so</i>	Secondary orifice
<i>s</i>	Solid
<i>x</i>	axial

# Contents

<b>Acknowledgement</b>	<b>vi</b>
<b>Abstract</b>	<b>vii</b>
<b>Zusammenfassung</b>	<b>ix</b>
<b>Nomenclature</b>	<b>xi</b>
<b>1 Introduction</b>	<b>2</b>
1.1 Cryocoolers . . . . .	2
1.2 Overview of the research . . . . .	6
1.3 Research objectives . . . . .	7
1.4 Research motivations . . . . .	7
1.5 Outline of the thesis . . . . .	8
<b>2 Review</b>	<b>12</b>
2.1 Developments from the 19 <sup>th</sup> Century . . . . .	13
2.2 Recent developments since 1945 . . . . .	15
2.3 Review of Alternate Cooling Techniques . . . . .	17
2.3.1 Thermoelectric . . . . .	18
2.3.2 Magnetic Cooling . . . . .	18
2.3.3 Optical Cooling . . . . .	19
2.3.4 Other Technologies . . . . .	20
2.4 Types of Cryocoolers . . . . .	20
2.4.1 Stirling Cryocoolers . . . . .	21
2.4.2 G-M Cryocoolers . . . . .	24
2.4.3 PTC Cryocoolers . . . . .	26
2.4.4 Joule-Thomson Cryocoolers . . . . .	26

2.4.5	Brayton Cryocoolers . . . . .	27
2.5	Applications of Cryocoolers . . . . .	27
2.5.1	Magnetic Resonance Imaging (MRI) Systems . . . . .	28
2.5.2	Nuclear Magnetic Resonance (NMR) Systems . . . . .	29
2.5.3	Infrared Sensors (IR) & Detectors . . . . .	30
2.5.4	Other applications . . . . .	30
2.6	Review of Miniaturization Effort . . . . .	31
<b>3</b>	<b>Regenerative heat exchangers</b>	<b>36</b>
3.1	Introduction . . . . .	37
3.2	Design parameters . . . . .	38
3.2.1	Nusselt number . . . . .	38
3.2.2	Fluid and matrix capacity ratios . . . . .	39
3.2.3	Boundary layer thicknesses . . . . .	39
3.2.4	Reynolds number . . . . .	40
3.2.5	Porosity and area density . . . . .	40
3.2.6	Hydraulic diameter . . . . .	40
3.2.7	Pressure loss . . . . .	41
3.2.8	Number of heat transfer units (NTU) . . . . .	41
3.2.9	Effectiveness of heat exchanger . . . . .	41
3.2.10	Acoustic power & coefficient of performance . . . . .	42
3.3	Regenerator matrix selection . . . . .	43
3.3.1	Packing geometries . . . . .	44
3.3.1.1	Wire mesh screens . . . . .	44
3.3.1.2	Spheres . . . . .	46
3.3.2	Packing materials . . . . .	47
3.4	Theory of regenerative heat exchangers . . . . .	48
3.4.1	Mass flow rate and flow velocity . . . . .	48

3.4.2	Energy of flow . . . . .	49
3.4.3	Regenerator's principle of operation . . . . .	50
3.4.4	Governing equations . . . . .	50
3.4.4.1	Conservation of mass . . . . .	50
3.4.4.2	Conservation of energy . . . . .	53
3.4.4.3	Conservation of momentum . . . . .	55
3.5	Ideal regenerator . . . . .	57
3.5.1	Application of the model . . . . .	60
3.5.2	2D Axisymmetric Regenerator Validation Model . . . . .	61
3.6	Quantification of losses in the regenerator . . . . .	62
3.6.1	Phasor diagram of the regenerator . . . . .	64
3.6.2	Pressure loss . . . . .	69
3.6.3	Void volume pressure loss . . . . .	69
3.6.4	Axial heat conduction loss . . . . .	70
3.6.5	Regenerator thermal loss . . . . .	71
3.7	Losses and regenerator's optimisation . . . . .	72
3.7.1	Optimization of regenerator for 1 watt cooling power . . . . .	74
3.7.2	Sizing of the regenerator . . . . .	77
3.7.3	Numerical optimisation of the regenerator using REGEN3.3 . . . . .	78
<b>4</b>	<b>Pulse Tube Cryocooler System</b>	<b>86</b>
4.1	Introduction . . . . .	86
4.2	Theory . . . . .	87
4.2.1	Principle of operation . . . . .	88
4.2.2	Classification . . . . .	89
4.2.2.1	Classification based on operation . . . . .	89
4.2.2.2	Classification based on geometry . . . . .	90
4.2.2.3	Classification based on phase-shift mechanism . . . . .	91

4.3	Analytic modelling . . . . .	92
4.3.1	Phasor analysis for orifice-PTC . . . . .	93
4.3.2	Phasor representation for different phase shift mechanisms . . . . .	97
4.3.3	RLC Analogy & the transmission line model . . . . .	98
4.4	Numerical modelling . . . . .	104
4.4.1	1-D nodal numerical modelling . . . . .	105
4.4.1.1	Initial and boundary conditions for the pulse tube . . . . .	106
4.4.1.2	Numerical solution . . . . .	107
4.4.2	CFD analysis for inertance PTC . . . . .	110
4.4.2.1	Geometry, initial and boundary conditions . . . . .	110
4.4.2.2	Mathematical model and governing equations . . . . .	112
4.4.2.3	Numerical scheme and nodalization . . . . .	113
4.5	Common technical issues related to miniaturization . . . . .	114
4.5.1	Regenerator losses . . . . .	115
4.5.2	Thermal and viscous losses . . . . .	115
4.5.3	Axial heat flow . . . . .	116
4.5.4	Dead volume . . . . .	116
4.5.5	Issues with phase shift mechanisms . . . . .	116
4.5.6	Pressure wave generator . . . . .	117
4.6	Miniature PTCs models . . . . .	117
4.6.1	Sage <sup>®</sup> modelling . . . . .	119
4.6.1.1	PTC optimisation in Sage <sup>®</sup> . . . . .	120
4.6.2	CFD numerical modelling . . . . .	125
<b>5</b>	<b>Results and Discussion</b>	<b>128</b>
5.1	Ideal regenerator . . . . .	128
5.1.1	Ideal regenerator numerical model . . . . .	128
5.1.2	Ideal regenerator CFD evaluation Model . . . . .	131

5.2	1-D numerical pulse tube element model . . . . .	134
5.2.1	Application of the model . . . . .	134
5.2.2	Temperature profiles . . . . .	134
5.2.3	Enthalpy and cooling power . . . . .	137
5.3	2-D CFD axis-symmetric for inertance PTC . . . . .	138
5.3.1	Temperature-time profile & validation . . . . .	138
5.3.2	Spatial temperature distribution . . . . .	140
5.3.3	Pressure & velocity profiles . . . . .	140
5.3.4	Enthalpy distribution and cooling power . . . . .	144
5.4	Results of the miniature PTCs models . . . . .	145
5.4.1	Miniature Core model . . . . .	145
5.4.2	Ultra-Miniature models . . . . .	147
5.5	Inertance PTC design and optimisation tool . . . . .	152
5.6	Experimental setup . . . . .	154
5.6.1	Instrumentation equipment . . . . .	155
5.6.1.1	Temperature measurement . . . . .	155
5.6.1.2	Pressure measurement . . . . .	156
5.6.2	Pressure wave generator . . . . .	156
5.6.3	Planned experiments and test routines . . . . .	157
5.6.4	Difficulties and complications . . . . .	158

**6 Conclusions and Recommendations 160**

6.1	Conclusions . . . . .	160
6.1.1	Contribution statement . . . . .	161
6.1.2	Findings summary . . . . .	162
6.1.3	Implications of the study . . . . .	165
6.1.4	Limitations and challenges . . . . .	166
6.2	Suggestions for future work . . . . .	167

<b>References</b>	<b>168</b>
<b>Publications</b>	<b>186</b>
<b>Appendix</b>	<b>188</b>
Appendix A: Ideal regenerator model MATLAB code . . . . .	188
Appendix B: One-dimensional model for the pulse tube element . . . . .	191
Appendix C: User-defined function for the CFD modeling . . . . .	194
Appendix D: Post-processing MATLAB codes for the CFD models . . . . .	195
Appendix E: Experimental setup sectioned layout . . . . .	196
Appendix F: Hardware and transducers equipment . . . . .	197



*Generally, the size of the coolers for today's applications is quite large compared to the size of the device to be cooled.*

---

# Chapter 1

## Introduction

Up until the middle of the 20th century, the conventional vapor-compression cycle, as described by the fundamental laws of classical thermodynamics, met most of the world's refrigeration demands, producing cold temperatures down to about 230 K [1]. As technology advances and new applications emerge, there is an increased demand for thermal management at extremely low temperatures in a variety of applications, including food, electronics and detectors, military, medicine, and the superconducting industry. This emerging demand is being met through the development of compact, high-performance cryogenic refrigerators, also known as cryocoolers.

### 1.1 Cryocoolers

Cryocoolers or cryo-refrigerators are machines used to produce refrigeration at cryogenic temperatures. Cryogenics is the science that studies the behavior of materials or systems at low temperatures. Hence, a cryocooler is a device or group of equipment that produces refrigeration at temperatures typically lower than 120 K [2]. The significance of cryogenics stems from the

fact that certain materials, like superconducting materials, exhibit exceptional properties in this particular temperature range, enabling them to provide better performance and response times [3].

The general working principle for cryocoolers is based on thermodynamic cycles of expansion and compression of gases. Efficiency and output cooling power are factors of great importance in cryocoolers. In principle, the output refrigeration power is highly dependent on the produced temperature. Ideally, input powers of approximately 150 W, 15 W, and 1 W are required to generate 0.5 W of cooling power at 1 K, 10 K, and 100 K, respectively. based on the Carnot maximum theoretical efficiency ( $\frac{T_{cold}}{T_{hot}-T_{cold}}$ ), and assuming  $T_{hot} = 300\text{ K}$ . Cryocoolers can be classified into five levels, from 0 K to 120 K, depending on their temperature range. Figure 1.1 illustrates the ideal output cooling power based on Carnot efficiency for four different input powers for five cryogenic temperature levels. Four distinguished temperature benchmark levels are essential for classification purposes. These are 4 K, 20 K, 80 K, and 120 K, which approximately correspond to liquefaction temperatures of helium, hydrogen, nitrogen, and methane, respectively.

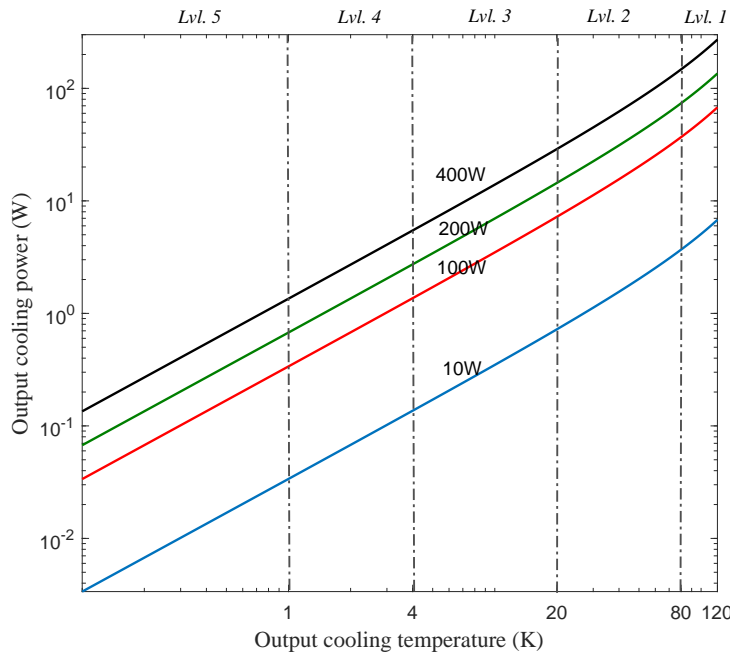


**Figure 1.1:** The ideal output cooling power, based on Carnot maximum theoretical efficiency, for four different input power for five cryogenic temperatures levels.

The cooling capacity is an important parameter that defines the cooling power with the associated effective temperature range. Typically, each cryogenic cooling system or cryocooler is only efficient for a particular temperature range. Hence, in terms of cooling capacity, cryocoolers

can be classified into five categories: micro-miniature, miniature, small, medium, and large size systems [2]. Table 1.1 summarizes different cryogenic cooling systems sizes in terms of cooling capacity for the five predefined temperature levels.

**Table 1.1:** Categories of cooling systems based on cooling capacity and the associated temperature range, as proposed by [2].

Category	Applications	Cooling Capacity				
		1 K	4 K	20 K	80 K	120 K
Micro-miniature	Electronic	—	—	<0.25 W	<1 W	<1.5 W
Miniature	Electronic & Instrument	—	<0.5 W	<2 W	<8 W	<12 W
Small	Laboratory & commercial	<1 W	<10 W	<100 W	<800 W	<1.2 kW
Medium	Small scale liquefaction & super-conductivity	<25 W	<100 W	<1 kW	<15 kW	<25 kW
Large	Large scale liquefaction, LNG production & helium recovery	>25 W	>100 W	>1 kW	>15 kW	>25 kW

Cryo-refrigerators, or cryocoolers, mainly produce cooling by alternating expansion and compression actions of the gas. The literature reports two main categories for these machines [2, 4]:

- *Reciprocating*: they are efficient for small-sized machines as well as large sizes and a wide operating range even when the operating conditions drift away from the design conditions. Life expectancy decreases due to the presence of parts and various rubbing seals and sliding bearings. However, reliability and life expectancy are drastically enhanced when using improved materials for the rubbing contact. For some engines, a non-rubbing operation is achieved with piston-based devices using flexure, gas, or magnetic bearings, or even with diaphragm devices in which a flexing diaphragm causes compression and expansion of the working fluid.
- *Rotary*: they include turbines, rotary expanders/compressors, which have the features of small size, low weight, high fluid flows with low-pressure ratios. Commonly, they are inefficient for the small size, but as the size and speed increase, the efficiency increases. Usually, they are optimized for certain design conditions and fail to perform well away from these conditions. Reliability is ensured by employing few bearings and minimal rubbing action, which also can extend their life expectancy.

Heat exchangers are core components for any cryocooler and are vital elements in identifying the machine's family. Hence, cryocoolers can be further categorized based on the heat exchanger utilized in the machine [2, 4, 5], As depicted in Figure 1.2:

- *Recuperative*: the flow could be continuous or periodic, with a direct solid separator be-

tween the hot and cold fluid streams, hence the heat transfers via conduction. Examples of these machines are Linde, Hampson, Claude, and Joule-Thomson (J-T) cryocoolers.

- *Regenerative*: the cold and hot streams are not separated, where they flow simultaneously and periodically through the regenerative matrix. The regenerative matrix, in which the heat exchange happens between both streams, is a porous medium, commonly constructed from fine metal meshes and spheres. Examples of these machines are Gifford-McMahon (G-M), Vuilleumier, Stirling, and pulse tube cryocoolers.

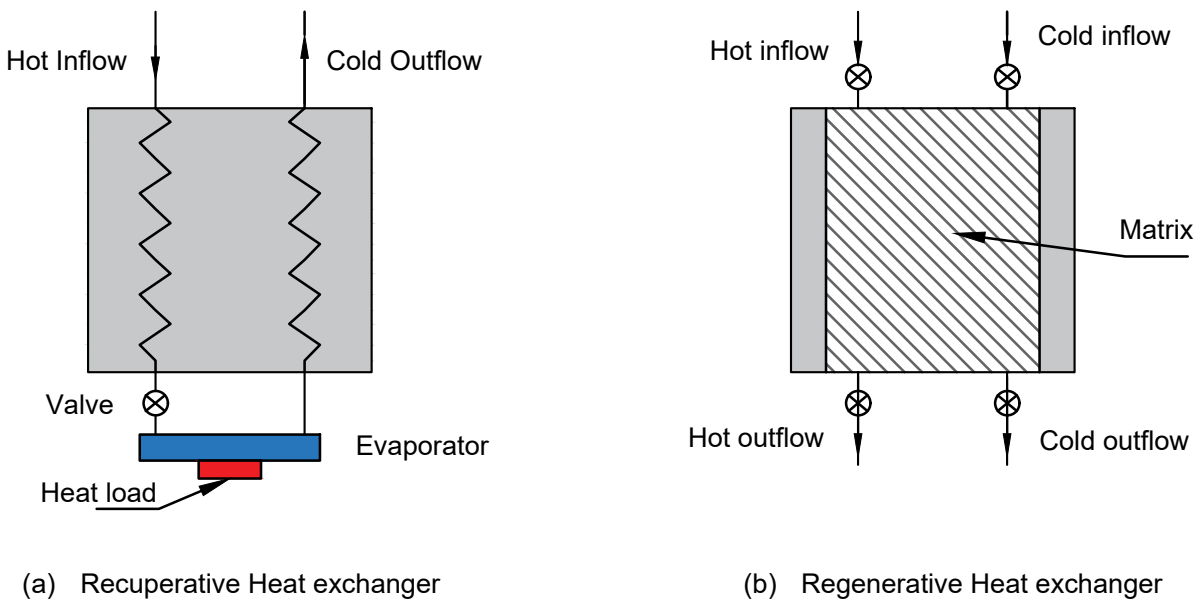


*Figure 1.2: Schematic diagrams for the recuperative and regenerative heat exchangers.*

Typically, using valves or volume variations are the standard two methods that regulate or control the flow. These can be used to identify the cryocooler categories further, whereas all recuperative cryocoolers have valves. Regenerative cryocoolers could be further classified into valved, like Gifford-McMahon cryocooler, and no-valved, such as Stirling cryocoolers.

The literature classifies cryocoolers as static when they have no moving components [5]. Examples include radiative cryocoolers that utilize high reflectivity surfaces to provide thermal shielding for the cooled target [6]. A sorption compressor-based J-T cryocooler [7] is another example. The adiabatic demagnetization refrigerator (ADR) is a third example, which provides cooling depending on a strong magnetocaloric effect in some material. A fourth example is laser beam cooling, where the force of a beam subjected to an object nearly stops the motion of its

atoms, reducing their stored energy and decreasing their temperature. Static cryocoolers are not cost-effective for certain applications. However, they are mainly desired for applications where high reliability and vibration-free behaviour are required and, in general, represent less than 2% of the cryocoolers used worldwide.

## 1.2 Overview of the research

Cryocoolers are involved in a variety of application areas. The impact of cryocoolers' development is not only limited to helping many applications to flourish and be more practical but also resulting in opening up new emerging application areas. For example, reliable and efficient space instruments could not be possible without the development of compact, reliable, and durable space cryocoolers [8]. Generally, space applications were limited by the constraints enforced by the size, durability, and lifetime of their associated refrigeration system. In the same sense, developing miniature and micro-scale cryocoolers vows to promote a vast range of improved miniature sensors/detectors with faster response time and enhanced efficiency.

The miniaturization of cryocoolers is a topic that has begun to gain attention from many researchers. However, scant evidence exists on the level of miniaturization that could be reached while maintaining efficient operation. Therefore, the main aim of this PhD thesis is to, in some part, close the gap in the literature by examining the use of software tools and computational models to predict the performance of cryocoolers. Essentially, developing miniature cryocoolers requires useful methods and tools, mainly for their design and performance analysis. The lack of software tools for optimizing cryocoolers at the miniature level may be behind the current vagueness of how much miniaturization could be attained with a pulse tube cryocooler.

For the last three decades, the literature has addressed miniature pulse tube cryocoolers [9–17], in which various miniature PTC systems have been built and their performance evaluated [14, 15, 18–20]. There have been arguments about how small the size could be reduced while maintaining efficient cooling operation since thermodynamic operations put limits and confinements on the system dimensions. Additionally, losses, primarily in the regenerator, would increase when the size is drastically reduced, imposing a minimum size limit below which PTCs are practically infeasible. On the other hand, other factors that are important to be considered for any efficient miniature machines are being discussed, these include, but are not limited to, high-frequency operation, small pressure wave generator, and efficient phase shift mechanisms and their implication on the size, cost and power density are being addressed. A significant portion of the

research is devoted to improving the regenerator performance since its performance, and porous media properties primarily determine the efficient cooling operation.

### 1.3 Research objectives

This research investigates miniaturization prospects of a regenerative pulse tube cryocooler, although a great deal of the discussion, results, and conclusions of this research could still be valid to other regenerative cryocoolers. This research pushes steps towards designing a micro pulse-tube refrigerator for on-chip cryogenic applications. This Ph.D. study has six main objectives:

1. present a better understanding of the theory and the physics of a pulse tube system (PTC), both generally and in relation to particular types of PTC systems.
2. examine how some analogous models, like the RLC circuit and the transmission line models, are used to describe, predict and optimize the performance of the system.
3. investigate the factors influencing the efficient operation for a PTC system, especially in the regenerator component.
4. improve the design methods and software tools to be used for miniature cryocoolers.
5. employ software tools and computational models to quantify or estimate various thermodynamic phenomena expected to limit their performance, in particular, to estimate the losses associated with the regenerator in a regenerative cryocooler.
6. employ the implications and the results from the analytical and numerical investigations to generate models of hypothetical PTCs that are more miniature than the current forms which can be implemented and used in on-chip applications in the future. Implementing an effective micro-cryocooler would necessitate the use of a micro-compressor. Hence, these models would contemplate smaller compressors with very short piston strokes.

### 1.4 Research motivations

For various applications, the present cryocoolers are very large compared to the size of the device to be cooled. Several cryocooler development requirements must be met to keep up with contemporary advancements in a variety of emerging applications. Research efforts seeking miniature or micro-scale cryocoolers are numerous. One example is the effort undertaken by DARPA [21] for micro cryogenic cooling (MCC) for cooling a wide range of sensors, amplifiers, and other electronic-based devices. This effort's target was to scale down the cryocooler to the same scale as the device being cooled and removing hindrances like size, weight, cost, and

complexity of the cooling system. Of course, successful micro-cryocooler implementation would also necessitate the use of a micro pressure wave generator as well.

Practical applications based on compact NMR using small magnets and micro-coils, and miniature spectrometers [22, 23] are expected to develop rapidly in the near future. Cryoprobe technology can be used to increase the sensitivity of conventional electronics. The thermal noise in the probe circuitry is reduced dramatically via cryocooling, where the signal-to-noise ratio ( $S/N$ ) may be enhanced 3-5 times [24]. Although current setups incorporate both either liquid nitrogen and cold gaseous helium cooling systems into the probe and preamplifier assembly, stand-alone miniature cryocoolers are expected to supplant them in the near future.

Another motivation for miniaturization is the possibility of embedding cryocoolers in space applications for portable and wearable devices. It requires the incorporated cooling system to be as small and light as possible. Miniaturization entails shrinking the final stage in a multi-stage configuration. Hence, the miniature final stage carries out an even smaller heat load at a lower temperature, thereby increasing the overall efficiency of the multi-stage cooling system.

The utilization of cryocoolers for higher temperature levels is another motivation for cryocoolers miniaturization. For instance, cooling of microchips and microprocessors would result in faster response time, higher reliability, longer lifetimes for these devices; moreover, much-improved signal-to-noise ratios ( $S/N$ ) are obtained when thermally managing localized hot spots in electronic detectors. Although the literature recommends miniature vapor-compression refrigerators for this application area [25, 26], it also suggests that cryocoolers would eventually compete very well in this particular application area [27–29].

Among all cryocoolers, Stirling and pulse tube cryocoolers are excellent candidates for miniaturization due to their simple design and higher efficiency compared to other types of cryocoolers. Even more intriguingly, the absence of the mechanical displacer and the low-vibration operation in pulse tube cryocoolers made them even more suitable for miniaturization, generating a research momentum toward their miniaturization over the last decade. Indeed, an effective micro-cryocooler development would necessarily require the miniaturization of all associated parts, including the development of a micro-compressor.

## 1.5 Outline of the thesis

This work is subsequently organised as follows:

- Chapter 2 starts by reviewing the development of cryogenics in the last century after

presenting a brief historical background. It proceeds by reviews of the literature on the developments in cooling techniques, with a focus on cryocoolers. The literature is then reviewed for alternative cooling techniques. Following that, a summary of cryocooler types and classifications is provided. One purpose of this chapter is to construct a workable definition of the cryocoolers classification scheme. After that, it summarizes potential application areas of cryogenics that could be further enhanced due to breakthroughs in cryogenics and cryocoolers miniaturization. Finally, a thorough review of the miniaturization effort on a pulse tube system is provided in order to appreciate the availability of PTC miniaturization existing attempts.

- Chapter 3 mainly focuses on regenerative heat exchangers. The regenerator and the heat exchangers play a vital, if not the most important, role in ensuring an optimum operation for any cryocooler. The chapter studies their design parameters. It introduces standard geometry and materials that are used as filler materials and their defining parameters. It then discusses the regenerator's theory and working principles, which form the regenerative cryocooler design and optimization foundation. After that, the regenerator key principles are then explained using numerical aids and tools used in modeling, designing, and optimizing their operation. In particular, it proposes a numerical ideal regenerator model that rules the essential heat exchange operation in the regenerator. It evaluates and quantifies the effects of various types of losses and connects them to the system dimensional and operating parameters. The above provides a simple analytical procedure to estimate different types of losses found in the regenerator. The chapter concludes by presenting a numerical optimization process using special-purpose software called REGEN to further optimize the regenerator over various geometry and operating parameters.
- Chapter 4 discusses the theory and working principles of the pulse tube cryocooler (PTC) system. It starts by describing the various classes of PTCs based on their geometry, operation, and phase shift mechanism. After that, It conducts an in-depth analysis of various types of PTC cryocoolers, their strengths, and limitations, related to their phase shift mechanisms using phasor diagram studies and RLC circuit analogy. Additionally, it performs a one-dimensional numerical study of the tube element in an orifice-PTC system to determine the implications of high-frequency operation on the system's size. Numerical methods, including Computational Fluid Dynamics (CFD), are developed and applied to the entire PTC system and its sub-components to describe physical phenomena in the system and evaluate the feasibility of CFD modeling for predicting PTC performance while minimizing modeling assumptions and simplifications. The chapter concludes by

using CFD modeling and special-purpose software called Sage to design and optimize a miniature inertance-PTC system for maximum cooling power and higher coefficient of performance.

- Chapter 5 presents and discusses the qualitative and descriptive results of the previous hypotheses. The results are presented and discussed on the:
  - The ideal regenerator model.
  - One-dimensional model of the pulse tube element in a PTC system.
  - Axis-symmetric CFD model of an inertance-PTC system.
  - CFD model for the base miniature PTC system.
  - performance results of three ultra-miniature PTC models. These systems are derived from previous analytical and numerical investigations.

Based on the results of various analytic and numerical studies, the chapter presents a stand-alone tool that could be used in designing and optimising inertance-type pulse tube cryocoolers.

- Chapter 6 provides the summary and conclusions of the thesis. Further, it outlines the contributions made by this Ph.D. investigation to the research literature, implications of the results, limitations of the study, and recommendations for future work.



*Recently, cryocooler's miniaturization has become a buzz phrase. It is obvious now that not only the production of low temperatures is essential, but also the size of the equipment*

---

## Chapter 2

### Review

Historically, man needed to cool food using natural primitive means, such as positioning it near water sources such as streams, rivers, or runoff from melting snow and ice, or even blowing cold air into it on occasion. Refrigeration has become gradually necessary thanks to pioneering scientists such as William Cullen, Oliver Evans, Michael Faraday, and last but not least, Jacob Perkins, who built the first operational closed-cycle continuous working vapor-compression refrigeration system. Nowadays, refrigeration is required in a wide variety of applications, not just household appliances and food preservation. The rapid expansion of low-temperature applications in research and high-technology applications spawned cryogenics, a science that examines the behavior of materials or systems at low temperatures. Cryogenics has considerably assisted the evolution of numerous low-temperature applications, such as superconductivity-based applications and infrared-detecting systems, and has created new avenues in both research and industry. In the future, cryogenic coolers, or cryocoolers, are expected to be utilized in many everyday applications, facilitating supercomputers and small-scale detectors. This thesis investigates the miniaturization aspects of a specific type of cryocooler, the so-called pulse tube

cryocooler. In this chapter, a general introduction of cryocoolers, a short description of pulse tube cryocoolers, and the working principle are summarized.

## 2.1 Developments from the 19<sup>th</sup> Century

The 19<sup>th</sup> century was a period of many scientific findings and inventions, with substantial developments in various scientific fields such as mathematics, physics, chemistry, electricity, metallurgy, and engineering, which laid the groundwork for many modern-day technological advances. The invention of the reciprocating steam engine, the development of improved metals, materials, and manufacturing processes, and many other vital advances led to serious developments in mechanical refrigeration. The very first machines were mainly used for making ice and processing refrigeration. Significant propulsion for large-scale refrigeration followed the Suez Canal opening and the development of the meat trade between Australia, New Zealand, and Great Britain [2].

In 1815, Robert Stirling, a minister in the Church of Scotland, invented the regenerative heat exchanger and the first engine, now known as the Stirling engine, to generate electricity from furnace heat. Although John Herschel first suggested that the Stirling Engine could be used to make ice in 1834, it was not until 1874 that Alexander Kirk succeeded in putting the concept into practice [30].

Collins and Cannaday [31] presented a historical viewpoint to the growth of low-temperature work. Collins suggested that refrigeration expansion engines were not developed as independent machinery but rather as components of integrated systems, including compressors and the associated heat exchange equipment [2]. The majority of the early machines used air as the working fluid. They reported that the first air refrigerator was built by Dr. John Gorrie of Apalachicola, Florida, in 1849, followed by the development of an incredibly good air-refrigerator by Kirk [30, 31]. Kirks's machine produced temperatures nearly twenty degrees below the freezing point of mercury ( $\sim -89^\circ \text{C}$ ) [31]. The exception for Collins and Cannaday's viewpoint was Davy Postle, in 1873, who conceived the earliest version of a hydrogen free-piston engine machine, regarded as the forerunner of the class of cryocooler now referred to as "Gifford-McMahon" machines. Collins [31] suggested that expansion engines are unsuitable for ice production due to the heat being absorbed at a constant temperature. They did, however, mention its utility in gas liquefaction applications.

The original air-liquefaction system was a hydrogen engine described by E. Solvay in an 1887 patent [32]. Cailletet and Pictet liquefied air for the first time in 1877, simultaneously but independently, by expanding high-pressure precooled air and oxygen in a nozzle to produce

liquefied gas [2]. Even though Solvay's engine failed to produce a sufficient temperature drop to achieve air liquefaction, Collins credits Solvay with "a real understanding of the problems of gas liquefaction in general" and refers to him as the first to specify broadly the apparatus needed.

Walker reports [2] that a professor at the Munich Polytechnical Institute, Karl von Linde, was the first to attain the liquefaction of air in quantity in 1895. Linde's machine consisted of a compressor, counterflow heat exchanger, and Joule-Thomson expansion valve. Linde's work laid the foundation for the German Linde Company. In England, Hampson carried out similar work that was adopted by Brin's Oxygen Company, London, England (known now as the "British Oxygen Company" well-known in innovative work in cryogenic field [2]).

Walker [2] reported several accomplishments that occurred in the 19<sup>th</sup> century. In 1896, despite failing in his early attempts and giving up on hydrogen liquefaction after he had outlined schemes for this using a heat exchange system employing liquid oxygen in the first stage and a hydrogen expansion engine for the final stage [2, 31], Kamerlingh Onnes of the Leiden Laboratory was the first to introduce the first liquefaction of helium and the initial observation of the phenomenon of superconductivity [2, 31].

In 1899, the Frenchman Claude achieved successful operation for his first expansion engine, although it was similar in design to Solvay's machine [2, 31]. Claude's engine represented the first reasonably efficient combined expansion engine and heat exchanger with compressed air free of water and carbon monoxide [2]. Combining Claude's machine in conjunction with an auxiliary liquefaction and separation element, a continuous stream of liquid air was finally achieved in May 1902 [2]. Claude's work in liquid air production and separation led to the foundation of the French industrial company Air Liquide [2].

In 1912, Heylandt presented a crowned-piston expansion engine. A low-conductivity cap was mounted on the piston to separate the cold gas from the piston rings used to seal the high-pressure gas in the cylinder [2]. His design isolates the thermal energy resulting from frictional degradation of the seals, thus preventing dissipation of the low-temperature refrigeration resulting from the expansion of gas in the cylinder [2], which is the leading property of nowadays liquefaction machines. The first expansion engine for hydrogen, which was similar in design to the earlier air engines, was constructed by Claude in 1920 to separate hydrogen from coke oven gas [2].

In 1934, Peter Kapitza, professor at the University of Cambridge, described an apparatus consisting of a helium expansion engine used in helium's liquefaction. The Kapitza engine expanded helium at 30 bar to 2.2 bar [2]. In 1938, Collins presented a diaphragm expansion engine that operated very well. Temperatures of 10 K were achieved in late 1939, but no liquid helium

was produced on compressed air to demonstrate incorporating the unit in a helium liquefaction system [31]. WWII redirected the effort to oxygen generation, and the work on the diaphragm engine was never resumed.

### 2.2 Recent developments since 1945

Two key events for low temperature technology started in 1945 and finally resulted in significant impacts on cryogenics development and, in particular, cryocoolers. The first was developing a helium liquefier in 1946 by Samuel Collins at the Massachusetts Institute of Technology (MIT). The apparatus consisted of two expansion cylinders and a compact counterflow heat exchanger and could liquefy any gas without the need for additional refrigeration. The Collins helium liquefier was commercially developed by the A. D. Little Co. of Cambridge, Massachusetts, and was commercially sold by an associated company, Cryogenic Technology, Inc., of Waltham, Massachusetts [2]. This development allowed any well-equipped university or laboratory that could acquire moderate capital funds to hold helium research capability. In the 1950s, the need to develop long-range rockets led to the development of cryogenic engineering, where funds were generously available for military, research, and space-related activities in the United States at that time and all through the 1960s. One impact is the emerging interest in some fields at extremely low temperatures, such as superconductivity applications. One example is the use of SQUIDS (superconducting quantum interference devices) as sensitive magnetometers for all manner of dynamic measurements, varying from magneto-cardiograms of the heart to the detection of nuclear submarines [2]. Other applications include the use of superconducting magnets in fusion and magneto-hydrodynamic power systems, in magnetic levitation rapid-transit systems, high-speed propulsion, and electric motors with high power-to-weight ratios [2].

According to [2], the second significant development was the production of Stirling engines. In the late 1930s, the engines were used as refrigerators by the Philips Company in Holland. The initial purpose of these Stirling engines was to generate power for radios in rural areas where there is no electricity. However, the invention of transistors and storage batteries shifted them to application areas ranging from artificial hearts to installed engines in vehicles and boats with advantages like good efficiency, low noise, and reduced environmental pollution [33]. Although using Stirling engines as a refrigerator was noted since 1834 by John Herschel, as confirmed by Alexander Kirk [30] in 1874, who has reported that Stirling engines were used as refrigerators for at least ten years. Little progress had been made since then till 1946. The significant development occurred in 1946 when one of the Philips units was used by researchers to attain a temperature

low enough to liquefy air [2]. After that, the research on Stirling engine refrigerators was held by a team led by Jan Köhler [34], in 1954. That yielded to the first commercial Stirling engine air liquefier in 1956, which was later expanded by introducing a separation column to produce nitrogen. Various developments followed that leading to the invention of multiple expansion machines to attain temperatures as low as 7 K, which are incorporated in hydrogen and helium liquefiers [2]. Most of these applications in this era were basically for the liquefaction of air and natural gas. Therefore, huge plants with large capacity cooling machines were developed for industrial gas liquefaction, where power inputs of many megawatts are typical for such systems.

On the other hand, smaller capacity refrigerators were produced for military and electronic applications. Near the end of WWII, Infrared night vision equipment and missiles were at an early stage of development in Germany. The early momentum for infrared-based applications in the 1950s and 1960s was driven by the need to develop military applications such as infrared night vision equipment and heat-seeking infrared missile guidance systems in the United States. Numerous sensitive infrared detectors have been developed to operate optimally at liquid nitrogen ( $\sim 80$  K) and liquid hydrogen ( $\sim 20$  K) temperatures.

The development in cryocoolers was motivated by the substantial funding by the U.S. government in the early 1960s like the Air force program from the Flight Dynamics Laboratories of the Wright-Patterson Air Force Base, the U.S. Army Night Vision and Electro-Optics Laboratory, other programs supported by the U.S. Navy interests in cryocooler development, and some small programs supported by the National Aeronautics and Space Administration (NASA) in IR systems and spacecraft cryocoolers [2]. An example of this progress was producing many advanced Stirling and Vuilleumier cryocoolers for missile infrared detectors and guidance systems by the Hughes Santa Barbara research center and the Hughes Aircraft Co. in California [2, 35]. Small capacity machines used in in-field applications were mainly free-liquid cryogens, which led to small refrigerator development capable of reaching low-temperature levels. Most of the research was centered in the USA due to the applications' military nature where these refrigerators were employed and the availability of financial resources that backed up these application areas.

William Gifford co-invented the Gifford-McMahon cryocooler, a relatively large, heavy machine with separate compressor and expander units characterized by durability and long life [36]. Gifford-McMahon cryocoolers consist of valves, two or four in number, with two connecting lines, one supply, and one return between the expander and compressor units. Because of the sensitivity of the infrared detectors and superconducting devices, the requirement of complete isolation of mechanical shock and vibration were fulfilled by condensing liquid nitrogen and then transferring the droplets along using a tube to the cold region by the evaporative- boiling process known

as "Leidenfrost boiling" [2]. Later on, this technique was abandoned with the development of cooling engines having separate or "split" compressor/expander units. Many miniature split-Stirling cryocoolers have the arrangement whereby a displacer operates in a separate cylinder with the advantage of having no valves and only one connecting tube. An example of this is the reinvention of free displacer cooling engines by Walter Higa of the Jet Propulsion Laboratory, Pasadena [37].

Reliability in small cryocoolers has been a struggle for many years. A straightforward solution is to reduce the size and weight by eliminating some moving parts in mechanical refrigerators. In 1963, Gifford and Longworth [38] managed to invent a new cooling method, a pulse tube cryocooler, by simply eliminating the mechanical displacer in a Stirling cryocooler. At that time, the pulse tube cryocooler achieved 124 K in single-stage and 79 K in two stages [39]. However, the work on pulse tube refrigeration was nearly stopped for 15 years due to the low efficiency comparing to other types. In 1984, Mikulin et al. [40] added an orifice at the end of the tube element, allowing gas to flow in no small compliance volume. They managed to achieve a temperature as low as 105 K with a single-stage cryocooler. Radebaugh et al. [41] modified the geometry for the orifice pulse tube cryocooler by using a needle valve and changing the original orifice position, which resulted in 60 K temperature. Furthermore, improved efficiency pulse tube cryocoolers were constructed by adding a long tube [42], and the refrigerator is commonly called the inertance pulse tube cryocooler.

### 2.3 Review of Alternate Cooling Techniques

Various thermal control technologies exist in the literature. Researchers utilized these technologies to create modules that operate as heat pumps, more specifically for cooling objects or systems. Thermal control has gained significant success in many applications, including mini-refrigeration, solar cells, circuit packaging, infrared detectors, micro-fuel cells, and cooling of micro-systems in biomedical and communication applications. There is also a strong need to integrate cooling technologies into microelectronic circuits since increasing microprocessors' performance is usually associated with increased power consumption and on-chip power density [43].

One great motivation to use these technologies is that localized spots of high heat flux on microelectronics can produce hot spots, which affect their reliability and performance. Also, cooling down a sensor would enhance its associated signal-to-noise ratio (S/N). As a result, these technologies' development reflects positively on micro-systems' performance, allowing them to reach considerably smaller sizes and open up new research areas and commercial applications.

This section introduces several cooling principles found in the literature. The sections that follow provide an overview of several gas cycle cooling systems, which are discussed in greater detail since they are essential to the scope of this thesis.

### **2.3.1 Thermoelectric**

The thermoelectricity phenomenon was first observed between 1821 and 1851 [44]. The Peltier effect primarily influences thermometric cooling [2], where a temperature difference is developed across two junctions of different types of materials, i.e., P-type and N-type thermo-elements, that are connected electrically in series and thermally in parallel whenever an electrical voltage is applied [45]. Riffat and Ma [45] limited thermoelectric (TE) devices to niche applications, i.e., under 25 W, because of their relatively low conversion efficiency and low figure-of-merit (ZT) when compared to other technologies. Some excellent features include the absence of moving parts and associated noise, lightweight, easy controllability, operation-orientation flexibility, and reliability. These features make TE devices more suitable for various applications like mini-refrigerators and microsystems, microprocessors & microelectronics applications, and some medical applications [46]. To some extent and for specific applications, they can replace other conventional refrigerators, i.e., greenhouse-based cooling, which has a high negative environmental impact. The maximum temperature lift achieved with a multi-stage thermoelectric cooler is less than 160 K [47], thus making them acquire a small coefficient of performance (COP) at these temperatures. Generally, they can not compete with vapor-compression technologies other than specific niche applications with low cooling requirements [46, 48].

### **2.3.2 Magnetic Cooling**

The main principle for magnetic cooling is based on the magnetocaloric effect (MCE). For most magnetocaloric materials, magnetization causes the material to heat up, while demagnetization causes the material to cool down. The discovery of magnetic materials that show a remarkable change in their temperature when they are adiabatically magnetized close to room temperature has enormously increased the number of publications on MCE in the last two decades [49, 50]. The magnetocaloric effect is most prominent near the Curie temperature, where increasing the magnetic field intensifies the effect. The Curie temperature is where ferromagnetic material shifts from permanent magnetism to paramagnetic [48]. Typically, for cooling and refrigeration, the most suitable materials have Curie points near room temperature. An example is the rare earth metal gadolinium.

Magnetic prototypes are based on either the movement of magnetocaloric materials across a static magnetic field or the movement of a magnet mechanism relative to a static magnetocaloric material medium. The magnetocaloric material is coupled to the external heat transfer fluid to establish a heat pumping effect [51]. The merits of magnetic refrigeration include environmental friendliness, energy efficiency, and excluding the need for greenhouse gases [49].

This technology development requires advances in MCE materials and system engineering to maximize the temperature lifts. Several problems are associated with this technology that need addressing, like irreversibility and hysteresis, coupling to an external heat transfer fluid, internal conduction, and considerable pressure loss through the regenerator bed, as well as relatively high cost and the limited capabilities of magnetic materials to achieve large temperature changes. As a result, significant breakthroughs in magnetocaloric materials and design concepts are required to make magnetic cooling competitive with vapor-compression technology [48].

### 2.3.3 Optical Cooling

Optical, or laser, cooling of ions and atoms is based either on Doppler [52] or Sisyphus [53] cooling effects. Optical cooling was based on anti-Stokes fluorescence before observing these two effects, which were predicted by Peter Pringsheim in 1929 [54].

It has been demonstrated that some materials emit light at shorter wavelengths with higher energy than those with which the material is illuminated due to thermal interactions associated with phonon absorption with the excited atoms [55]. In anti-Stokes fluorescence, when triggering a laser on rare-earth (RE) material, the atoms emit higher energy photons than those absorbed. The extra energy must be extracted from the adjacent material. The advantages include free mechanical vibration operation, the absence of moving parts and liquids, and the compactness and long-life of diode pump lasers. They may be beneficial for applications like satellite instrumentation and small sensors.

The literature proposes several developments to improve the cooling process, like the multi-passing of the pump beam with an extra-cavity and the intra-cavity [56]. An example of this technique is the LASSOR—the Los Alamos Solid-State Optical Refrigerator, capable of achieving a temperature lift of 65 K [57]. Hehlen et al. [58] demonstrated an optical refrigerator to cool a HgCdTe sensor that is part of a working Fourier Transform Infrared (FTIR) spectrometer to 135 K.

### 2.3.4 Other Technologies

Examples of other cooling technologies are thermionic, thermoacoustic, and thermotunneling cooling. Edison discovered thermionic emission during early experiments with the light bulb. The principle of thermionic cooling is the following: when voltage is applied across two materials with a gap barrier that has a thickness less than an electron mean free path, high-energy electrons will leave one surface for the other while being replaced by average energy electrons, resulting in lowering the temperature of the first surface and heating the second [59]. The prospects for this concept in space cooling or food refrigeration applications are meager due to its low efficiency compared with vapor compression. No multi-layer device has been developed that could eliminate the backward conduction of heat.

On the other hand, thermoacoustic engines (TE) use a resonator to produce high-amplitude acoustic waves to pump heat out. They acquire some merits like low cost, reliability, the absence of moving parts that eliminate the need for dynamic sealing or lubrication, environmental friendliness, being well suited for proportional control, and the ability to efficiently generate cooling using waste heat as a power source [59]. An application example is a thermoacoustic engine introduced by Zink et al. [60] for automotive applications, which can be powered by engine exhaust and be used to drive a thermoacoustic air conditioner. It has promising prospects for this technology in cryogenic applications due to the combination of high-performance potential, significant prototype development, and industry interest in this field.

Finally, thermotunneling describes a process where the transfer of relatively warm electrons from one surface to another is made possible by nano-scale gaps, resulting in cooling of the surface and losing the warm, energetic electrons [59]. The efficiency can be enhanced by using a vacuum for the gap to eliminate the backward thermal conduction problem that is also associated with thermionic and thermoelectric principles. However, creating and maintaining this is considered a daunting hindrance and limits the prospects for this technology [59].

## 2.4 Types of Cryocoolers

This section covers the most common dynamic cryocoolers used in industry by discussing their working principles and mentioning their advantages and limits. As illustrated in Figure 2.1, cryocoolers may be classified into regenerative and recuperative. Common regenerative cryocoolers include Stirling, Gifford–McMahon (GM), and pulse tube cryocoolers (PTC's), while common

recuperative cryocoolers include Joule-Thomson (J-T) and Brayton cryocoolers. The schematics for these five common cryocoolers are shown in Figure 2.2.

### 2.4.1 Stirling Cryocoolers

Stirling cryocoolers were the first cryocoolers to be developed in the 1950s, and all other regenerative cryocoolers may be looked at as modified versions of this type. They are also considered the most efficient of all types since their principle is based on the ideal Stirling cycle, which is internally and externally reversible and therefore has a thermal efficiency close to the Carnot cycle [61].

Stirling cryocoolers mainly consist of a compressor, a regenerative heat exchanger, i.e., the regenerator, and a mechanical displacer in an expansion chamber. The valve-less compressor consists of an oscillating piston that provides the system with an oscillating pressure signal, causing the system temperature to oscillate. The mechanical displacer is coupled to the compressor piston and operates at the same frequency as the compressor piston but with a fixed phase shift. This phase shift is a vital parameter designed to separate the heating and cooling effects efficiently. For most miniature Stirling cryocoolers, the displacer is hollow and contains the regenerator matrix.

The operation principle can be thoroughly explained by explaining the ideal Stirling cycle [2, 33, 62]. For a Stirling cryocooler pressurized with helium gas, this cycle is composed of four reversible processes, as depicted in Figure 2.3a:

- *Isothermal compression (1–2)*: At the start, the piston is initially away from the regenerator. After that, the gas is isothermally compressed as the compressor piston starts to move forward towards the regenerator while the expansion displacer is still stationary. The generated heat is rejected into the room-temperature surroundings via the warm heat exchanger. At the end of this phase, the pressure is at its maximum level.
- *Isochoric or constant volume heat rejection (2–3)*: The displacer starts moving towards the warm end, maintaining constant volume operation, forcing the gas to flow through the regenerator to the cold end, where the hot gas is cooled down by heating the regenerator matrix, and thus the pressure of the gas decreases due to cooling.
- *Isothermal expansion (3–4)*: Both the displacer and the compressor pistons move to the left, expanding the gas near the cold heat exchanger and absorbing heat from the cold heat exchanger, i.e., producing refrigeration. The cyclic system pressure is reduced to its minimum level after this stage.

- *Isochoric heat absorption (4-1)*: The displacer moves to the right towards the cold end, forcing the gas from the cold end through the regenerator to the warm end. During this process, the heat stored in the regenerator during process (2-3) is given back to the gas, thus cooling the matrix and raising the gas's pressure to its initial value. Both the displacer and the compressor piston are at their original positions at the end of this process.

Figure 2.3b depicts the pressure-volume and temperature-entropy diagrams. The two diagrams define the two prominent isothermal heat exchange processes and constant-volume regenerative processes in the Stirling cycle. Thus, the regenerator pressure and thermal losses are key parameters in determining the refrigeration power and the cryocooler's cooling performance.

For practical applications, the motion of both the piston and the displacer is sinusoidal. The relative motion between the displacer and the piston decides the net cooling effect. In a sense, the optimum refrigeration occurs when the phase difference ensures that the regenerator's mass flow is always in phase with the pressure. This condition is satisfied when the change in volume in the expansion space leads the change in volume in the compression space by about  $90^\circ$ .

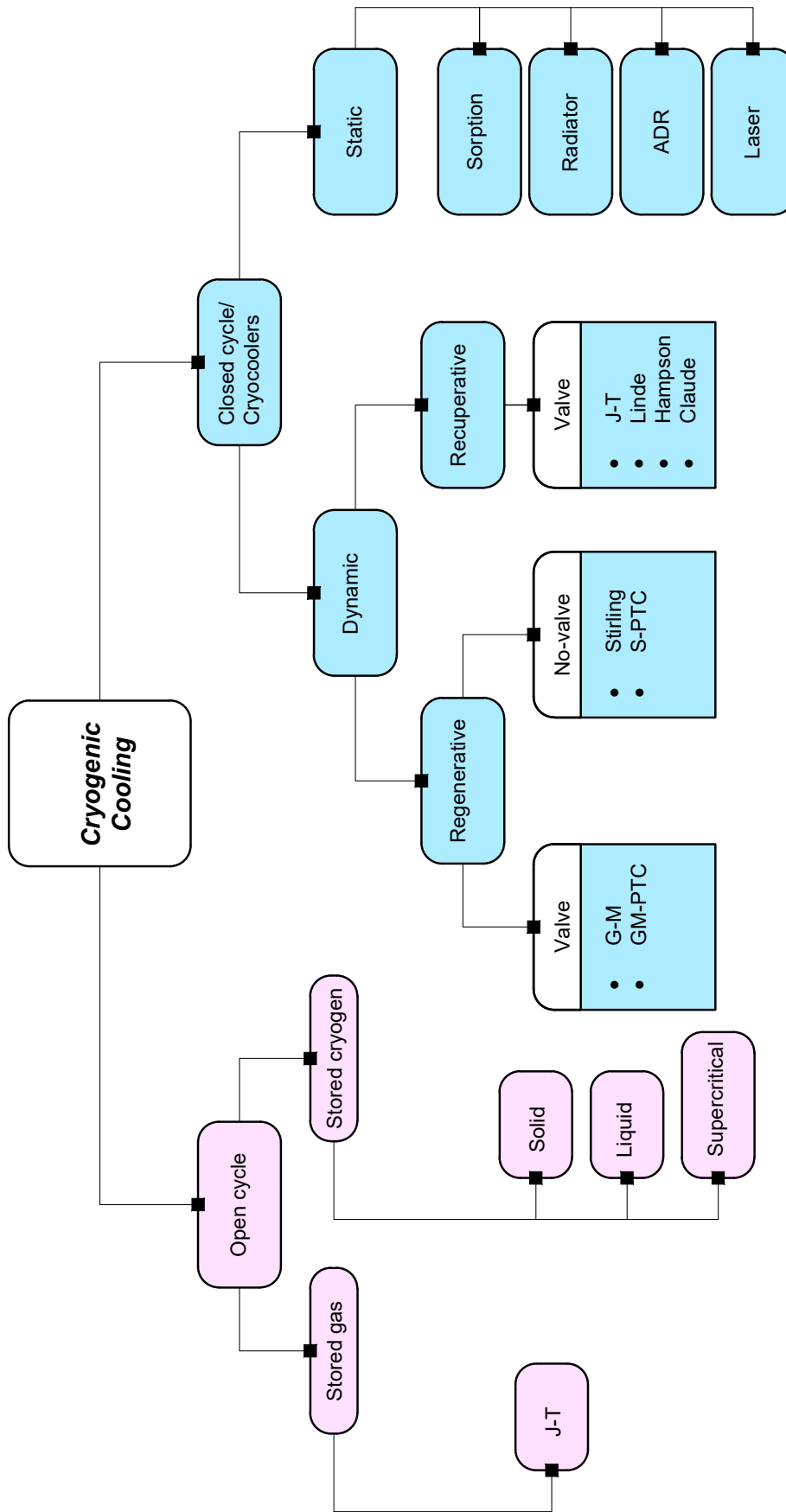
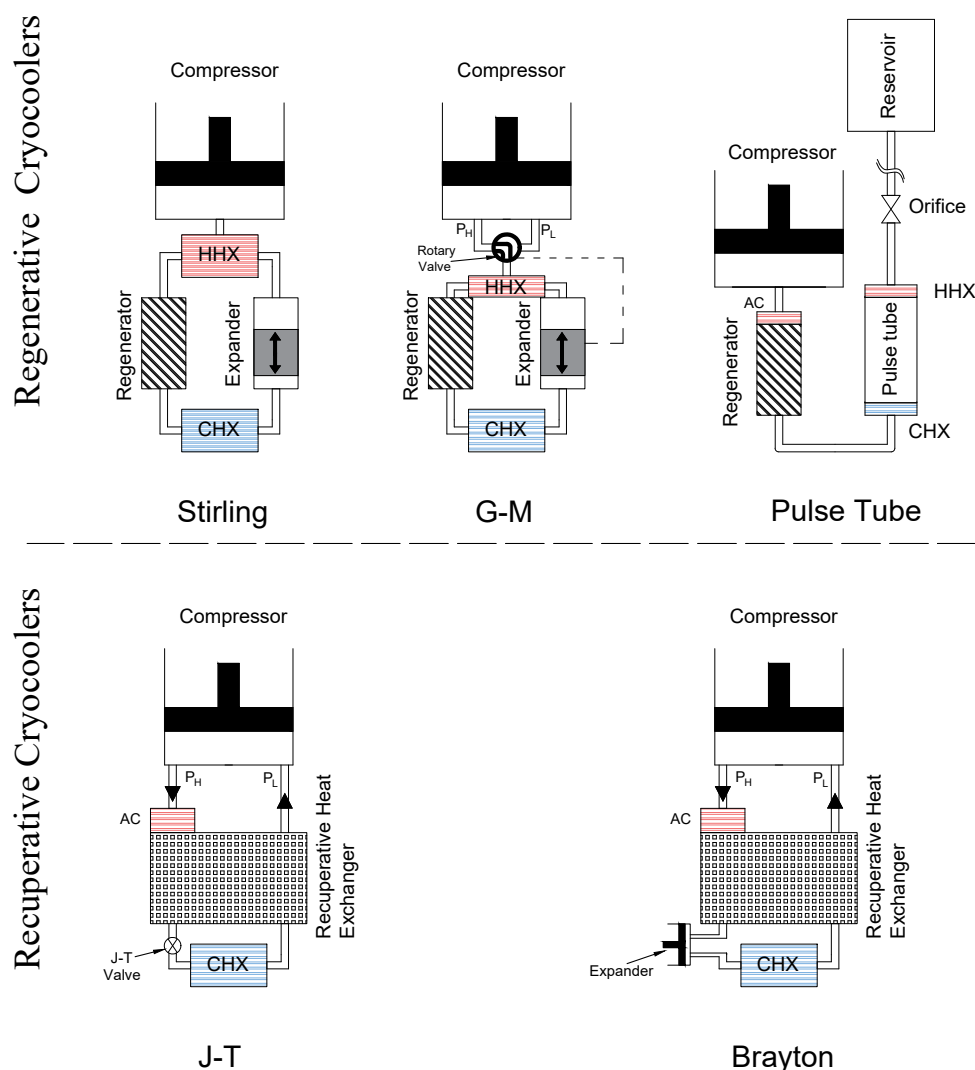


Figure 2.1: Classification of cryogenic cooling.



*Figure 2.2: Schematics of five common types of dynamic cryocoolers.*

Since the 1960s, Stirling cryocoolers have been used as cooling devices for infrared (IR) sensors in communication applications and night vision surveillance equipment. The required cooling power is around 1–2 W at 80 K [5]. Stirling cryocoolers' efficiency and reliability have been improved due to the adaptation of flexure bearings, gas-bearing support systems in the compressor, and non-contacting clearance seals, making them fulfill the strict requirements of space-based applications [8]. Miniature Stirling cryocoolers generally used in space applications deliver a cooling effect of 1–5 W at around 80 K with a power input of around 20–50 W [5].

#### 2.4.2 G-M Cryocoolers

G-M cryocoolers are considered modified versions of Stirling cryocoolers, sharing the same cold head. The significant differences are the presence of a valve connected between the compressor

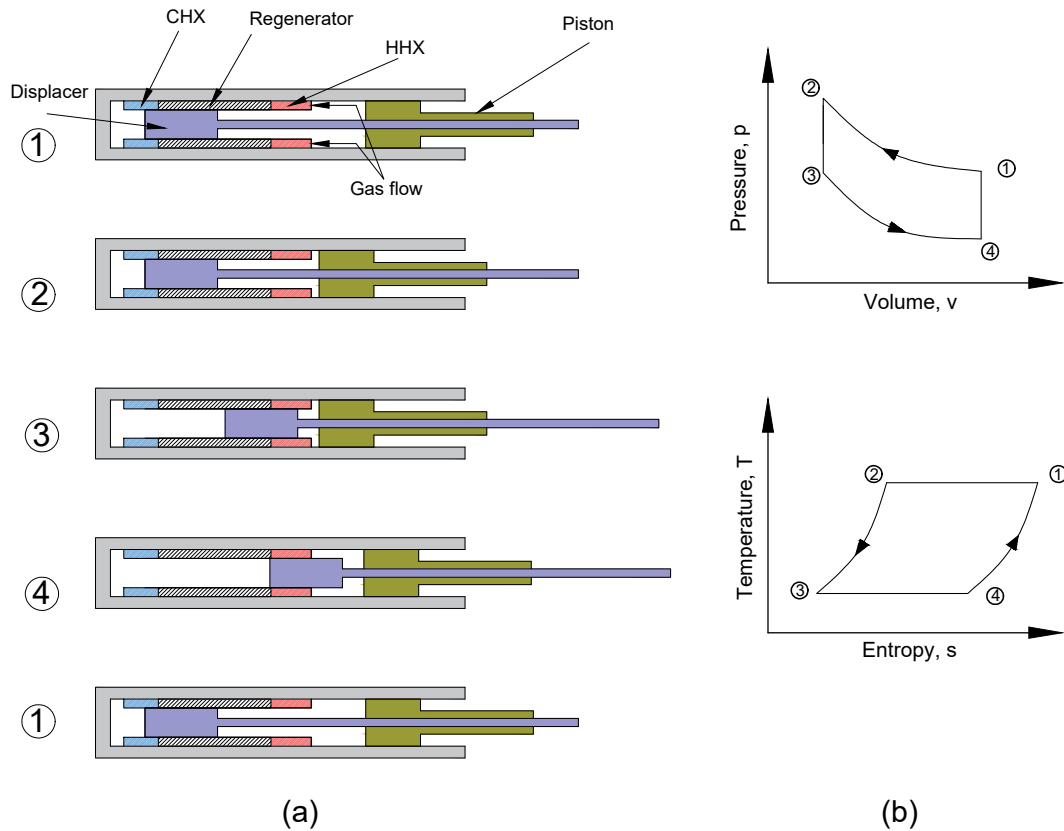


**Figure 2.3:** (a) Ideal Stirling cycle processes (b) Pressure-volume and temperature-entropy diagrams for an ideal Stirling cycle cryocooler.

and the expander units in the G-M cryocooler, the existence of a low-temperature seal at the cold end, and the low frequency of operation.

In 1960, Gifford and McMahon [63] showed that variable pressure oscillation could be produced by using a rotary valve to switch between high and low pressure for the oscillating piston, as illustrated in Figure 2.2. The advantages of this modification include:

- It allows the utilization of more common oil-lubricated compressors, which have historically reduced the cost and improved the reliability of G-M cryocoolers.
- It enables the placement of the cold spot relatively far away from the compressor, thereby reducing the noise and vibration levels.

The disadvantages of the rotary valve include its low-frequency operation, typically 1–2 Hz, and the requirement for a displacer seal capable of withstanding low temperatures. Additionally, they have the disadvantage of requiring an oil removal apparatus between the compressor and the cold head due to their large size compared to other cryocoolers. Generally, G-M cryocoolers are used for applications where portability is not a fundamental requirement. Due to the oil removal device and low-frequency operation, they are also difficult to miniaturize. They are commonly

used in MRI and NMR for shield cooling to increase the liquid helium hold time. The modern zero boil-off (ZBO) MRI systems use 4 K G-M-type cryocoolers [5].

### 2.4.3 PTC Cryocoolers

Pulse tube cryocoolers (PTC's) own the great advantage of not having a mechanical displacer near the cold end. Instead, the oscillating gas in a thin tube associated with a phase shift mechanism provides the cooling effect in the PTC system; this may be perceived by assuming a gas displacer within the tube element. The lack of moving parts in the cold end gives PTCs many potential advantages, including reliability, lower cost, lower vibration, and less electromagnetic interference. Since Gifford and Longsworth [38] discovered the basic pulse tube refrigeration technique, the efficiency of pulse tube cryocoolers has been greatly enhanced in the last few years due to the better understanding of its working principle and the introduction of passive elements to enhance their phase shift mechanisms.

This study looks into the miniaturization prospects of the pulse tube cryocooler; thus, Chapter 4 provides a more comprehensive study of the machine history, types, and operation principles for the various types, as well as analytical and numerical studies.

### 2.4.4 Joule-Thomson Cryocoolers

Joule-Thomson (J-T) cryocoolers are among the recuperative types, depicted in Figure 2.2. They operate with a steady high-pressure gas flow that gets expanded through a valve; typically, nitrogen or argon is the working fluid at 20 MPa pressure. Since the expansion happens at constant enthalpy, the working fluid should exhibit real gas behavior, where enthalpy is a function of both pressure and temperature. The expansion results in lowering the temperature only if the gas's initial temperature is below its inversion temperature. The efficiency is mainly enhanced by using a mixture of gases that significantly improves J-T cryocooler performance [41]. The J-T machine's efficiency depends mainly on the recuperative heat exchanger's efficiency; therefore, the heat exchangers are mostly counter-flow types for maximum effectiveness.

The main operation can be summarized as follows: the high-pressure gas from the compressor passes through the aftercooler to be cooled down. It enters the counter-flow recuperative heat exchanger to be further pre-cooled by the returning gas before flowing to the J-T expansion valve. The J-T valve undergoes a constant-enthalpy expansion that absorbs the evaporator's heat load and lowers its temperature, then returns to the compressor through the recuperative

heat exchanger to complete the cycle. The Joule-Thomson valve could be an expansion valve, orifice, capillary, or porous plug.

The downsides include the requirement for pre-cooling via other stages or cryocoolers, the expansion valve's susceptibility to clogging, and low efficiency compared to other cryocoolers. The advantages of the J-T cryocooler include the absence of moving parts near the cold parts and the rapid cooling process, which makes them straightforward to miniaturize.

### 2.4.5 Brayton Cryocoolers

A Brayton cryocooler is a modified version of a J-T. It replaces the J-T valve with an expansion engine to utilize the work produced by expanding the high-pressure working fluid and, thus, enhance the system's efficiency. The advantages include using an ideal gas as a working fluid and the possible employment of rotary compressors and turbo-expanders with reduced associated vibration. However, the efficiency is still less than that of a Stirling machine, and pulse tube cryocoolers. A notable example of a Brayton cooler is the NICMOS cooler on the Hubble Space Telescope [64].

Enhanced designs that utilize gas bearings eliminate rubbing contact and thus provide the extended lifetimes required for space applications. Brayton cryocoolers have cold moving parts, i.e., turbine expanders, and hence are difficult to miniaturize. The miniaturization effort involves fabricating miniature turbo-expanders that maintain moderate expansion efficiency. Also, because of the low-pressure ratio involved in turbo-Brayton cryocoolers and its implications for reducing the refrigeration power per unit flow, the heat exchanger must attain high efficiency, reflecting on increasing the system's size. However, research efforts on producing micromachined silicon high-effective heat exchangers pledge to reduce the size of the heat exchanger [65].

## 2.5 Applications of Cryocoolers

Cryocoolers have improved immensely since the 1960s, which qualified them to be utilized in many application areas ranging from spacecraft technology, gas liquefaction, MRI, NMR spectroscopy, IR sensors and detectors, and other miniature applications. The thriving of all these applications is dependent on developing more reliable, durable, and high-efficiency cryocoolers. This section highlights cryocoolers' applications as stated in Figure 2.4.

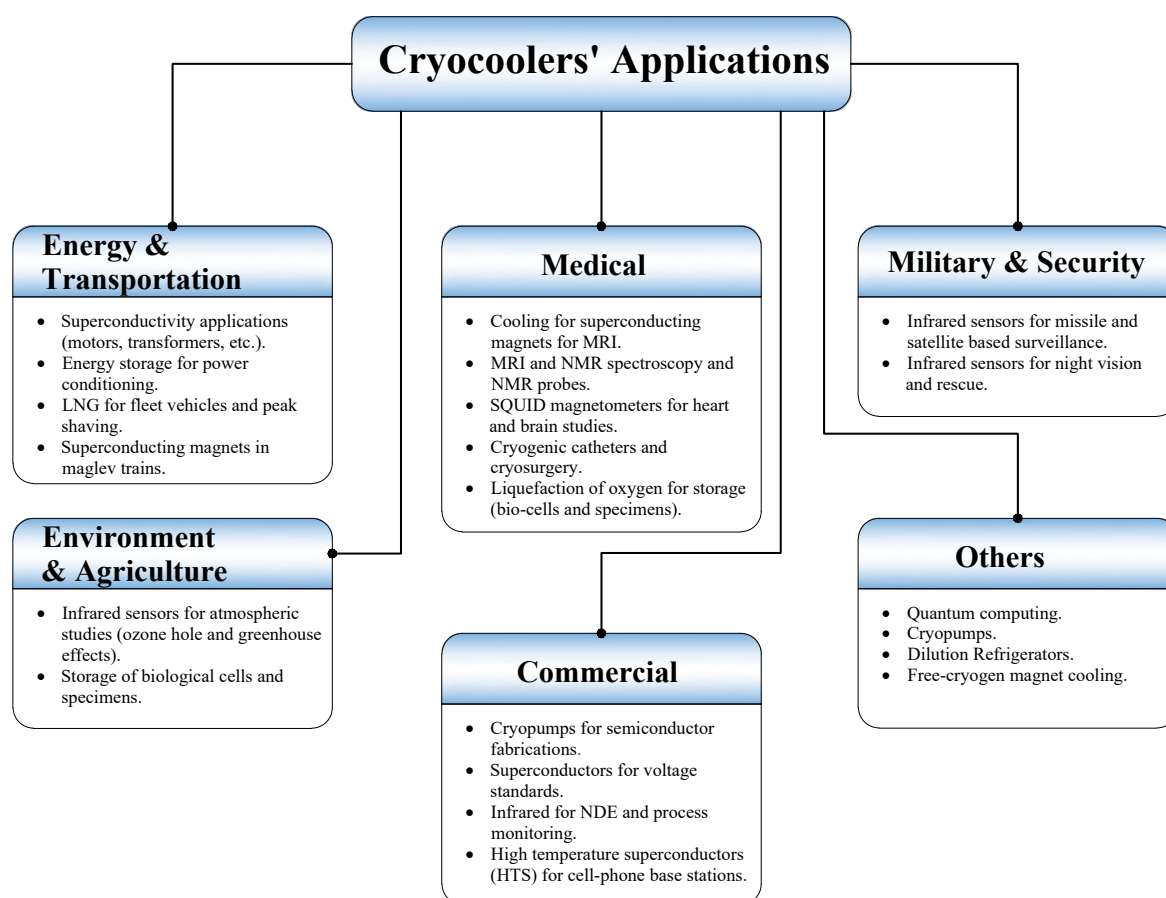


*Figure 2.4: Common applications of cryocoolers.*

### 2.5.1 Magnetic Resonance Imaging (MRI) Systems

Among the most extensive applications for superconductivity is magnetic resonance imaging (MRI). Over 22,000 MRI magnets have now been used since their first introduction in 1980, and more than one thousand systems per year are being produced [66]. The majority of the MRI systems available in hospitals and clinics all around the world use low-temperature superconducting (LTS) magnets, with magnetic fields of 1.5–3 T and where liquid helium is generally used in cooling these NbTi coils to a temperature level of 4 K [66, 67]. For the last few years, 10 K G-M cryocoolers have been used for shield cooling and to reduce liquid helium boil-off for most MRI scanners [5, 67].

Zero boil-off systems are now applicable owing to the development of 4 K G-M cryocoolers and integrating them with the MRI magnets starting in 1995 [66]. The advantages include reducing the costs associated with liquid helium refills, increasing the affordability of MRI systems for hospitals and clinics, and minimizing downtime required for maintenance and refill processes. Also, in low-field MRI systems with permanent magnets (0.1–0.5 T), the use of HTS radio

frequency sensor coils can significantly increase the signal-to-noise ratio, making them more competitive than superconducting magnet systems [67].

In most cases, G-M cryocoolers meet the requirements of the MRI systems. However, for smaller MRI systems that feature semiconductors with improved spatial resolution, the vibration resulting from the mechanical displacer in the G-M cryocooler becomes a problem, along with seal maintenance and electromagnetic interference. Some efforts have been made to replace G-M with pulse tube cryocoolers (PTC), but the main struggle here is the orientation dependence of the pulse tube cryocooler. An example is using a pulse tube for MRI head scanners, where low vibration is needed to prevent distortion of the MRI signal [67].

More compact MRI systems dictate the elimination of the liquid helium tank, where the direct conduction by the cryocooler cools the magnets, which results in minimizing the size and reducing maintenance. The research in this area is pushing towards invisible cryogenics, where the end-user interaction with the cooling system is eliminated [68].

### 2.5.2 Nuclear Magnetic Resonance (NMR) Systems

Nuclear magnetic resonance (NMR) spectroscopy studies the interaction of electromagnetic radiation with matter. It is employed in many sciences where precise structural determination, solution interactions, and reaction studies are required. NMR spectrometers conventionally use high-field superconducting magnets (10–25 T) to investigate the structure and the physical, chemical, and biological properties of macromolecules, such as proteins, in solutions. Because of special requirements like the high magnetic fields and homogeneity compared to MRI scanners, cryocoolers have not been incorporated, even for helium re-liquefaction, in these systems because the vibration can reduce the signal-to-noise ratio (SNR) [67]. However, an improved pulse tube cryocooler with the merit of low vibration is an excellent candidate to be used in this field.

Cryocooler-based NMRs are desired to reduce the operating, replenishment, and maintenance costs. Examples of HTS and LTS magnet-based NMRs can be found in the literature [69–72]. Moreover, several cryogenically cooled probes have been developed that have improved SNR. They typically employ a G-M or PTC to cool the electronics of the NMR probe [73–76]. Despite the commercially available cryogenic NMR probes and several demonstration systems, cryostat NMRs with zero boil-off and direct conductively cooled HTS systems are still in the emerging research phase.

### 2.5.3 Infrared Sensors (IR) & Detectors

Cooling infrared sensors to about 80 K was introduced in the 1960s to enhance the military's night vision capability. Early applications like missile guidance were incorporated with open-cycle J-T coolers due to special requirements like fast cool down.

By the mid-1960s, Stirling cryocoolers were developed for cooling infrared sensors for military night vision equipment. Since then, hundreds of thousands of Stirling cryocoolers have been produced to serve this purpose [77]. The cooling power rating for IR sensors using Stirling cryocoolers ranges from 0.15–1.75 W. Stirling cryocoolers have a massive market in space IR applications due to their higher COPs than other types of cryocoolers. Stirling and J-T cryocoolers are ideal for IR surveillance detectors because they can be easily miniaturized and have a notable cooling effect. However, the SNR signal can be deteriorated by the Stirling cooler's vibrations due to the displacer movement.

Critical requirements for IR applications like low cost, low noise, small size, and low vibration drove much of the research work to attempt to replace Stirling cryocoolers with PTCs [78–81]. One notable area is the use of cryocoolers for IR detectors in space applications like astronomy and earth-observing applications, where the first cryocooler used in space was in 1991 [82]. The requirements include high reliability, low weight, and a long lifespan, making pulse tube cryocoolers a good contender in this area. However, the orientation dependency of pulse tube cryocoolers may limit the utilization of PTCs in spacecraft IR detectors.

### 2.5.4 Other applications

Superconductor-based electronic applications require miniature cryocoolers to dispose of the concentrated heat spots transferred via electrical leads. An application example is high-temperature superconducting (HTS) microwave filters for cellular phone stations, which have cooling power requirements of about 6 W at 77 K [66]. Although low-temperature superconducting (LTS) electronics provide better performance advantages over HTS electronics, their input powers are in the range of kilowatts to obtain 0.1 W of cooling power.

Cryocoolers have been used in surgical applications. The literature mentions a few significant applications; the first is developing a mixed-refrigerant J-T cryocooler to treat abnormal menstrual bleeding in women's uterine lining [83]. Another application is developing cryogenic catheters using the J-T cryocoolers for cryoablation of particular locations in the heart that cause

heart arrhythmia [84]. Furthermore, cryocoolers are employed in cancer cryotherapy to freeze many cancer tumors [85].

## 2.6 Review of Miniaturization Effort

Many miniature pulse tube cryocoolers have been reported in the literature over the last three decades, along with their performance and experimental findings. In 1996, Xu et al. [86] reported reaching 160 K with a coaxial Double-Inlet Pulse Tube refrigerator (DIPTR) with a tube diameter of 5 mm, an operating frequency of 11 Hz, and an average pressure of 1.19 MPa. In 1997, Curlier [87, 88] proposed a technical description for an ultra-reliable linear compressor with flexure bearing for pulse tube with dynamic vibration control to deliver 1 watt of cooling at 80K, which matches the requirement for most of the Integrated Dewar Assembly (IDA) for Infrared Focal Plane Array (IFPA) based applications. They managed to reach 90K with a DIPTR having a total diameter of 10 mm and reached below 70K with a DIPTR with a U-tube arrangement having a diameter of 5 mm for both the pulse tube and the regenerator elements [89].

In 2000, Liang et al. [90] reported a cooling power of 200 mW at 81 K with a coaxial pulse tube refrigerator (PTR) of 9 mm total outside diameter and a 50 Hz operating frequency. In 2002, Lockheed Martin's Advanced Technology Center (LM-ATC) developed a miniature, lightweight pulse tube cryocooler system for space applications under funding from NASA/GSFC; the device was a U-tube configuration and was driven by a dual-opposed piston flexure bearing compressor. The machine delivered 0.3 W of cooling power at 65 K with a 310 K rejection temperature, 15 W of compressor power, and a total system mass of less than 1.25 kg [16]. In 2002, another remarkable effort was reported, the Integrated Multispectral Atmospheric Sounder (IMAS) cryocooler, which was developed to provide 0.5-watt cooling at 55K in a lightweight, compact configuration [91]. Chen et al. [92] reached a no-load temperature of 50 K and 0.9 W of cooling power at 80 K with an air-cooled compressor of 40 W of input power.

In 2004, Trollier et al. [93] designed and manufactured a U-shaped miniature pulse tube cryocooler that weighs 2.85 kg, works at an operating frequency of 50 Hz, and has a charging pressure of 40 bars, which delivers cooling power of 1.3 watts at 80 K. Tward et al. [94] developed a coaxial cryocooler reaching 65 K with an operating frequency of 80 Hz and delivering cooling power of 5 W at 95 K. Other examples include an in-line pulse tube cryocooler (PTC) developed by Fuji Electric with a cooling capacity of 3 W at 70 K and requiring 100 W of electrical input power, and with a U-shaped PTC, the cooling performance was 2 W at 70 K while requiring 51 W of input power [95].

Although the previous examples are small-scale, the operating conditions are still similar to those on a conventional scale. These examples did not comprehensively address the previously listed considerations affecting miniaturization and the associated high-frequency operation. One example of an unconventional approach is Nika et al. [11], who used electrical analogy and semiconductor fabrication techniques to design and fabricate a prototype of a micro DIPTR device weighing a few grams and made entirely of glass and silicon with a 1 mm x 5 mm rectangular cross-section. However, the device's cooling performance was modest. The reason behind that was most likely the 50 Hz frequency limitation on its compressor and the losses related to the high thermal conductivity of the silicon.

Any reliable effort for miniature pulse tube cryocooler should address associated parameters like high-frequency operation and optimized phase shift mechanism. In 2006, Radebaugh et al. [13] used the NIST numerical model REGEN3.2 to outline a measure for the very high-frequency operation of regenerators for micro-coolers; they deduced that regenerators could be operated at frequencies up to about 1 kHz without large increases in the losses, given that the average pressure is increased by 7 MPa. This effort was carried on, producing an experimental demonstration of a small pulse tube device operating at an average pressure of 3.5 MPa and a 120 Hz frequency [15, 96], as illustrated in Figure 2.5a. The regenerator and the pulse tube elements were both 30 mm in length and approximately 10 mm and 5 mm in diameter, respectively. However, the compressor employed in this work was quite large, and a no-load temperature of 50 K was reached.

Due to the importance of the high-frequency operation, Garaway et al. [97] presented a numerical study on high-frequency oscillating compressible flow applied to miniature cryocoolers in which they deduced that compressibility and temperature-dependent oscillating flow phenomena affect the friction factor dependence on frequency. They continued their work and established guidelines for the proper design of a miniature pulse tube cryocooler, eventually developing a miniature in-line PTC with a diameter of 3.5 mm and a length of 12 mm for both the regenerator and pulse tube elements. The total system volume was  $2.3 \text{ cm}^3$ , excluding the compressor, and reached 146 K with a charging pressure of 3.85 MPa and an operating frequency of 128 Hz [98]. Moreover, the pulse tube and the regenerator walls were constructed of low thermal conductivity materials to minimize conductive losses; the consequences were complicated system assembly. Later, the same authors reported a subsequent miniature system with more conventional materials for the pulse tube and the regenerator components. The system excluded the reservoir and introduced only an inertance tube as its phase-shifting device. However, this idea was soon abandoned in favor of an inertance tube with a reservoir configuration.

Associated miniaturization issues are the size of the compressor and the implications of high-frequency operation, which are crucial to the minimization of the PTC system. Garaway and Grossman attempted to develop non-conventional compressors or pressure wave generators. In 2008, Garaway et al. [99] developed a piezo-hydraulic membrane oscillator that was successful in producing cooling in a miniature pulse tube in Split Stirling.

In 2009 Garaway [14] modified the miniature system previously built by NIST [15, 96] that was driven by a relatively large compressor and thus did not reach higher frequencies, which are theoretically possible for such a miniature system. Garaway's adapted system, illustrated in Figure 2.5c, included a whole new commercial linear compressor from RICOR. The system's regenerator and pulse tube, both shown in Figure 2.5b, were 27 and 40.4 mm in length and 4.5 mm and 2.1 mm in diameter, respectively, with an operating frequency of 150 Hz and a charging pressure of 5 MPa. A low pressure ratio of only 1.17 was obtained with such a small compressor, and the pulse tube system achieved a low temperature of 97.5 K. However, the cool-down was relatively quick, with the cryocooler dropping below 100K in under 100 seconds. In later work, the cooler was optimized for such a low-pressure ratio, and the fair treatment of the unstable flow phenomena in its pulse tube element resulted in enhanced performance [100].

Sobol et al. [101] reported in-line miniature PTC, which is an adaptation of the previous cooler constructed by Garaway and Grossman [98], the system managed to reach 99 K and provided 400 mW of cooling at 110 K after 75 seconds of the cooldown, with a reduced operating frequency of 100 Hz and a fill pressure of 4 MPa. Although they maintained the original system dimensions, alterations incorporated stainless steel pulse tube and regenerator walls and a stepped inertance tube with a reservoir. Petach et al. [18] continued the work of Tward et al. [94], wherein they altered the cryocooler's coaxial pulse tube cold-head to utilize the small swept volume and high resonant frequency. The system was capable of delivering 1.3 W at 77 K, and while they succeeded in extending the operation of the system to frequencies up to 144 Hz, the cold head maintained its performance up to 124 Hz, where modifications were advised to achieve proper operation at 144 Hz with the same efficiency as at 100 Hz.

Several miniaturization attempts were reported in the last decade. Zhang et al. [102] manufactured and tested an inline PTC with a regenerator and pulse tube, measuring 60 and 71 mm in length and 20 and 14.9 mm in diameter, respectively. The cryocooler obtained a cooling power of more than 10 W at 90 K cold head temperature and a no-load temperature of 46 K with a cooldown time of 22 minutes and input electric power of 160 W. In 2012, Trolhier et al. [103] optimized their existing 80 K Miniature PTC to serve as a 150 K PTC for Micro-Satellite applications. It delivered a specific power at 150 K as low as 4.6 W/W with a cold finger weight

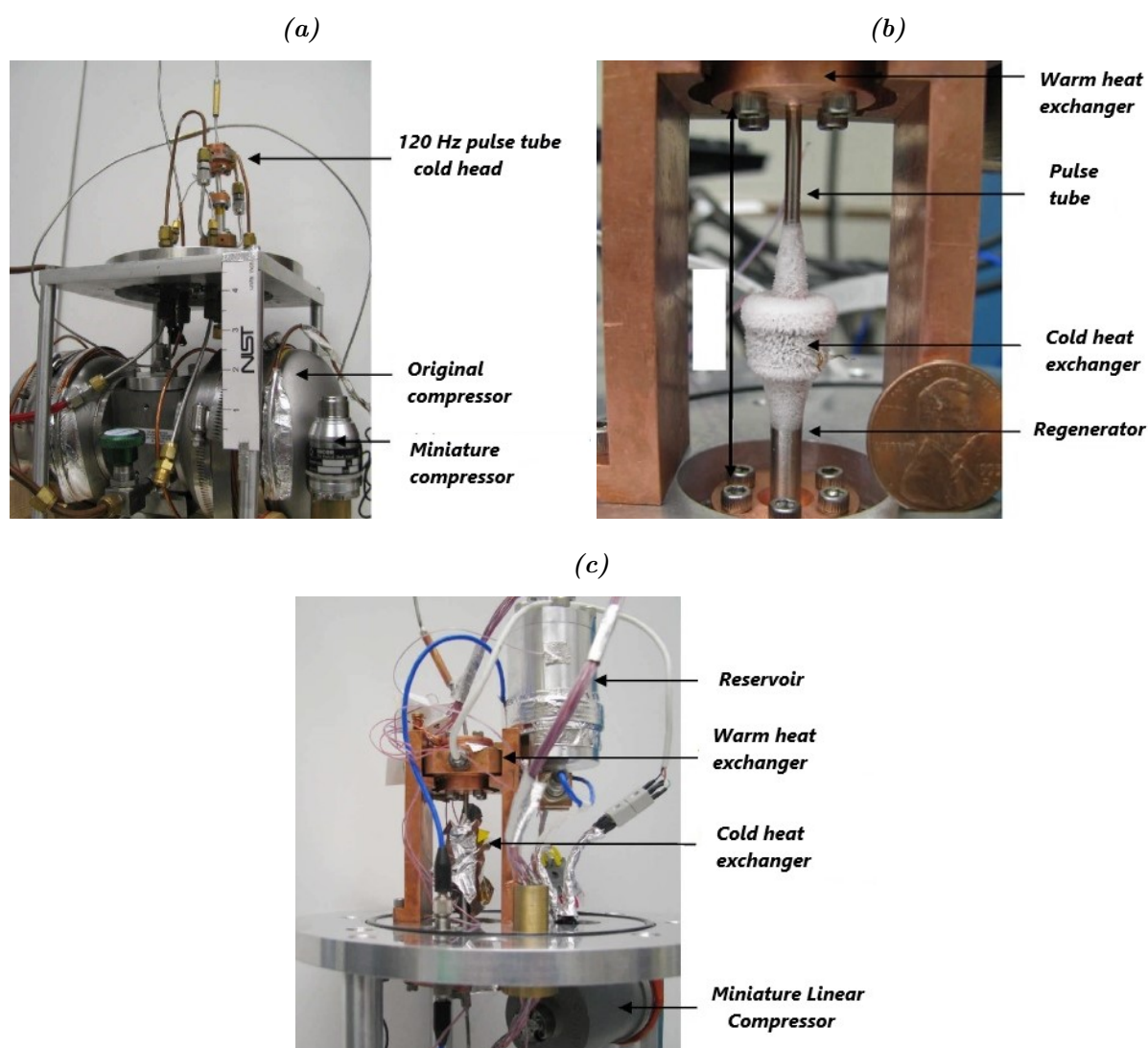


**Figure 2.5:** (a) NIST 120 Hz PTC cryocooler. (b) The cold head assembly. (c) 150 Hz Pulse Tube assembly with attached sensors [14].

of 420 g. Conard et al. [104] presented design details and experimentally measured performance of Raytheon Advanced Miniature (RAM-100), a high frequency, single-stage PTC, which was capable of achieving a no-load temperature of 42 K. The device is shown in Figure 2.6.

In 2017, Dang et al. [105] reported a coaxial Stirling pulse tube cryocooler (STPC) operating at 90–400 Hz that weighs 800 g. The following year, the total mass of the cryocooler, including the linear compressor, had been further reduced to 700 g, as illustrated in Figure 2.7a, maintaining the exact cooling effect, for which 1.2 W of power at 80 K can be achieved with an electric input power of 60 W and a cool-down time of about 6.2 minutes. Jiang et al. [106] reported developing a 120 Hz miniature coaxial PTC for super-spectral imagers; the cold finger diameter was 13 mm, and the total length was 124 mm, including the buffer volume. The system achieved a no-load temperature of 53.5 K and a cooling power of 1 W at 80K was achieved, with an input power of 34 W.

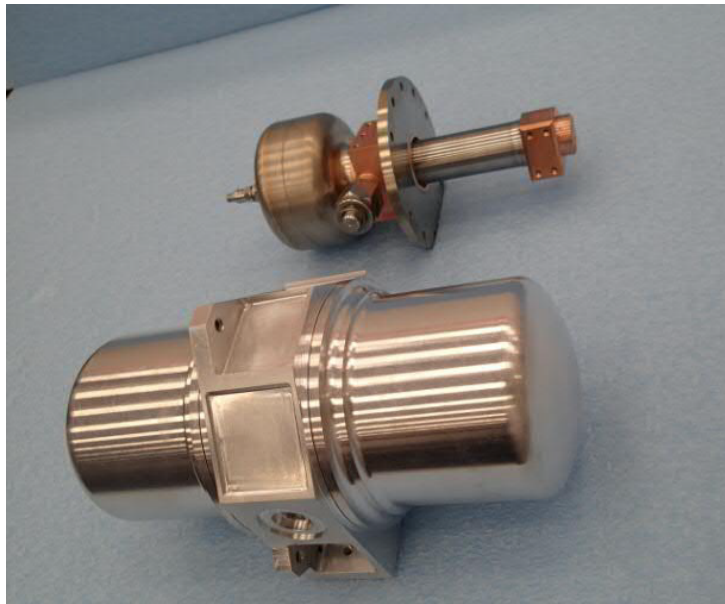


*Figure 2.6: RAM-100 Compressor and Expander [104].*

(a)



(b)



*Figure 2.7: (a) 700 g micro SPTC (b) Micro and mid-size compressors [105, 107].*

*“The lack of a compelling interest in the achievement of low-temperature seems to have caused the many competent scientists and engineers of that day to neglect the subject.”*

---

*Collins, 1958*

## Chapter 3

### Regenerative heat exchangers

This chapter provides a thorough discussion of the theory and design of regenerative heat exchangers used for cryogenic applications, particularly in pulse tube cryocoolers (PTCs). Regenerators are a vital class of heat exchangers in which heat is transferred through a matrix with a high heat capacity. In place of the continuous heat exchange process found in counter-flow heat exchangers, the regenerator produces a periodic heat exchange. The successful commercialization of any cryogenic application depends on two factors: the extent to which high-performance and compact heat exchangers can be developed and the ability to solve the difficult mathematical models associated with the regenerator’s periodic flow and time-dependent temperature and heat transfer parameters, which involve complex programming and software packages. The regenerator’s primary function is to transfer power to the cold end with as few losses as possible. Taking into account required qualities such as high efficiency, small size, low pressure loss, and low thermal losses. The theory, physics, and numerical analysis of the regenerator are described in the following sections for effective PTC design. This chapter details a study of regenerative heat exchangers in a pulse tube cryocooler system. It includes a parametric analysis to recommend geometrical attributes for the regenerator component, then moves on to numerical analyses to optimize this component for optimal performance in a miniature cryocooler.

### 3.1 Introduction

Heat exchangers can be divided into recuperative and regenerative types. In contrast to regenerative heat exchangers, heat exchange in the recuperative type occurs due to an indirect interaction between two fluids via a barrier or wall that prevents fluid mixing. Regenerative heat exchangers utilize high heat capacity materials with a large surface area and low heat conductivity in the direction of the periodic gas flow [2, 62]. Regenerators are vital components in closed-cycle regenerative cryocoolers, such as the Stirling, Gifford–McMahon (G-M), or pulse tube machines. In pulse tube cryocoolers, a regenerator works as a thermal storage component, transmitting the pressure signal from the compressor to the pulse tube element and other cryocooler components. The working principle involves thermal energy exchange between the working gas and the matrix material. Periodically, the matrix takes away the heat from the incoming gas during the heating phase due to compression and delivers it back to the returning gas during the cooling phase to maintain considerable refrigeration.

In 1816, Stirling was the first to employ a regenerative heat exchanger in a hot air engine [108]. In 1927, Nusselt published a mathematical analysis of a particular case regenerator with infinite matrix heat capacity [109]. In 1948, Iliffe used the ideal analyses of several German scholars to perform a first-order graphical numerical analysis that accounted for time variations in the matrix temperature [110]. One of the most significant advancements occurred in 1960, when Gifford and McMahon developed a small regenerative cryogenic refrigerator for cooling infrared detectors and maser amplifiers, bringing cryogenics out of the laboratory and into the industry [63]. Kuriyama et al. [111] used rare-earth regenerative materials in combination with a G-M multi-stage cryocooler to reach ultra-low temperatures.

In principle, a regenerator is very similar to a lossy spring in that it accepts energy in one direction and releases it in the opposite direction when the excitation is removed. Another comparable model is a thermal flywheel, which absorbs energy on the downstroke and returns it on the upstroke [112]. The regenerator matrix is contained within a tube housing that can withstand the oscillating high-pressure stream formed in the regenerator element. The matrix should have a high thermal storage capacity, a large heat transfer area, and impose the least amount of pressure loss on the flow. Unfortunately, the last two qualities are rather contradictory, because increasing heat transfer area requires decreasing free flow area, which reduces gas volume and increases pressure loss. According to Walker [112], the following are some of the advantages of regenerative heat exchangers:

- A large area for heat transfer can be obtained using finely stacked material.

- The construction is relatively simple, and considerable savings can be made on the same heat exchanger duty.
- The regenerator tends to be self-cleaning due to the nature of the periodic flow reversals, and this is advantageous if contaminated gas is being processed.
- If proper optimization processes are followed, well-designed regenerators can be produced.

Despite these advantages, the primary downside of static regenerative exchangers is the mixing of hot and cold streams, which is unavoidable due to flow switching carryover [112]. Stream mixing has the potential to disrupt the heat exchange process, thereby compromising cooling. To ensure optimal operation, significant caution should be exercised when designing or producing the regenerator element.

## 3.2 Design parameters

The performance of a regenerative heat exchanger is defined by a number of parameters. This section studies the different thermal and flow parameters that characterize the operation of the regenerative heat exchangers. These include, but are not limited to, the number of heat exchanger units (NTU), the fluid capacity ratio, the matrix capacity ratio, the Nusselt number, Reynolds number, and hydraulic diameter.

### 3.2.1 Nusselt number

The Nusselt number,  $Nu$ , is a non-dimensional number that defines the ratio of convective to conductive heat transfer by relating the convective heat transfer coefficient,  $h$ , the fluid thermal conductivity coefficient,  $K_f$ , and the characteristic flow dimension,  $D_h$ . This is defined as [62]:

$$h = Nu \frac{K_f}{D_h}. \quad (3.1)$$

$Nu$  denotes that convection heat transfer occurs between the solid and the fluid in a thin layer of fluid near the solid's surface. When the fluid's velocity is low and the flow is nearly laminar, heat is transferred primarily via conduction rather than microscopic mixing of flow streams. This scenario occurs when the value of  $Nu$  is in the range of 1 – 10, i.e., the value of 1 refers to pure conduction. Larger values of  $Nu$  indicate a high flow velocity and a transient or turbulent flow; as a result, mixing between the hot and cold fluids is more pronounced, and heat transfer occurs via convection rather than conduction. Assuming this scenario, heat transfer takes place across a narrow boundary region and is essentially determined by the temperature difference between

the solid matrix and the working fluid [62]:

$$\dot{Q} = hA_s(T_m - T_f) \quad (3.2)$$

### 3.2.2 Fluid and matrix capacity ratios

The fluid and matrix capacity ratios define the variation between the cold fluid heat capacity rate,  $C_c$ , and the hot fluid heat capacity rate,  $C_h$ . While the matrix capacity ratio defines the variation of the matrix thermal capacity relative to the minimum flow capacity. A large matrix capacity ratio indicates a small temperature swing and thus more efficient regenerator operation. These equations are expressed as [62]:

$$\text{Fluid capacity ratio } (C_f) = \frac{\min\{C_h, C_c\}}{\max\{C_h, C_c\}}. \quad (3.3)$$

$$\text{Matrix capacity ratio } (C_m) = \frac{(M_m c_p)_m}{\lambda_p (\dot{m} c_p)_{\min}}. \quad (3.4)$$

### 3.2.3 Boundary layer thicknesses

The thermal penetration depth,  $\delta_{th}$ , is an essential parameter for cryocooler applications with oscillating flows and pressures at high frequencies. Oscillating heat flow at a particular frequency can only reach a limited depth within a solid, referred to as  $\delta_{th}$ , defined by:

$$\delta_{th} = \sqrt{\frac{K_f}{\pi f \rho_f c_p}} \quad (3.5)$$

$K_f$  is the thermal conductivity,  $f$  is the flow frequency,  $\rho_f$  is the fluid density, and  $c_p$  is the specific heat. The higher the frequency, the smaller the thermal penetration depth; thus, for efficient operation in regenerative heat exchangers, the lateral characteristic lengths of the solid should be less than  $\delta_{th}$ . For instance, if the packing material in a helium regenerator is a mesh screen, the hydraulic diameter,  $D_h$ , of the screen should be significantly less than  $\delta_{th}$ .

The viscous penetration depth,  $\delta_v$ , is another decisive parameter for streaming losses between the working fluid and the pulse tube walls.  $\delta_v$  is the thickness of the layer near the boundaries where the viscosity is effective, and it is defined as:

$$\delta_v = \sqrt{\frac{\mu}{\pi f \rho_f}} \quad (3.6)$$

### 3.2.4 Reynolds number

The Reynolds number relates the mass flow rate to the heat transfer and the pressure loss due to friction for different operating conditions. In regenerative heat exchangers,  $Re$  is defined as [62]:

$$Re = \frac{D_h \dot{m}}{\mu \phi_m A_{reg}}. \quad (3.7)$$

$D_h$  is the hydraulic diameter,  $\dot{m}$  is the mass flow rate,  $\phi_m$  is the porosity of the matrix,  $\mu$  is the dynamic viscosity, and  $A_{reg}$  is the regenerator's cross-sectional area.

### 3.2.5 Porosity and area density

The porosity of the matrix,  $\phi_m$ , and area density,  $\beta_m$ , are two geometrical parameters that describe the regenerator. These are [62]:

$$\phi_m = \frac{V_{void}}{V_m} \quad (3.8a)$$

$$\beta_m = \frac{A_{s,void}}{V_m} \quad (3.8b)$$

$V_{void}$  represents the total volume of void spaces,  $A_{s,void}$  represents the total surface area of voids, and  $V_m$  represents the total volume of the matrix.  $\phi_m$  can be determined experimentally by evaluating the dimension of the matrix geometry element and the filling matrix's overall weight, which is expressed as [62]:

$$\phi_m = 1 - \frac{W_m}{\rho_m V_{reg}} \quad (3.9)$$

where  $W_m$  is the weight of the matrix,  $\rho_m$  is the density of the matrix, and  $V_{reg}$  is the volume of the regenerator housing tube.

### 3.2.6 Hydraulic diameter

The hydraulic diameter,  $D_h$ , is a parameter that defines the critical flow dimension. For the regenerator's mesh matrix, the hydraulic diameter  $D_h$  is the ratio of the cross-sectional area that is free for flow to the heat transfer area per unit length. This is expressed as follows [62]:

$$D_h = \frac{4L_{reg}A_{ff}}{A_s} = 4r_h. \quad (3.10)$$

$A_{ff}$  is the free flow cross-sectional area,  $r_h$  is the hydraulic radius, and  $L_{reg}$  is the regenerator's length.  $r_h$  can also be found from the porosity and area density, as follows:

$$r_h = \frac{\phi_m}{\beta_m} \quad (3.11)$$

### 3.2.7 Pressure loss

Pressure loss is an important factor in cryogenic applications and in evaluating refrigeration efficiency. The pressure loss in the regenerator can be found by applying the Navier-Stokes equations to the regenerator flow model. Section 3.4.4.3 presents detailed analysis for deriving the pressure loss formula, where equation 3.58 illustrates a commonly used expression for calculating the pressure loss in a regenerative heat exchanger.

### 3.2.8 Number of heat transfer units (NTU)

The number of heat transfer units ( $NTU$ ) is a dimensionless parameter that indicates the size of the heat transfer [113]. It is directly related to the size, flow, and thermodynamics of the regenerator. The larger the  $NTU$ , the more thermally effective the heat exchanger, provided that effectiveness is confined by flow and thermodynamic constraints [62].  $NTU$  is defined as follows:

$$NTU = \frac{A_s \bar{U}}{\min\{C_h, C_c\}} \quad (3.12)$$

where:

$$A_s \bar{U} = \left[ \left( \frac{1}{\bar{h} A_s} \right)_c + \left( \frac{1}{\bar{h} A_s} \right)_h \right]$$

$\bar{U}$ ,  $\bar{h}_c$  and  $\bar{h}_h$  are the overall heat transfer coefficient, the cooling, and heating heat transfer coefficient, respectively.

### 3.2.9 Effectiveness of heat exchanger

The effectiveness of a heat exchanger is a quantitative measure of how well it operates compared to an ideal heat exchanger operating at the same temperature conditions. "Effectiveness" and "efficiency" are used interchangeably [62] and are defined as the ratio of actual heat exchanged between the fluids and media,  $Q$  to the ideal heat exchanged,  $Q_{ideal}$ , when no temperature difference exists between the two fluids at any position. This can be defined as [62]:

$$\epsilon = \frac{Q}{Q_{ideal}} \quad (3.13)$$

where

$$Q = \lambda_h(\dot{m}c_p)_h(T_{in} - \bar{T}_{out})_h = \lambda_c(\dot{m}c_p)_c(\bar{T}_{out} - T_{in})_c$$

$$Q_{ideal} = \lambda(\dot{m}c_p)_{min}(T_{in} - \bar{T}_{out})$$

$T_{h,in}$  is the temperature of the inlet heating fluid,  $T_{c,in}$  is the temperature of the inlet cooling fluid, and  $T_{c,out}$  is the temperature of outlet cooling fluid.  $\lambda_h$  and  $\lambda_c$  are the flow time periods during heating and cooling phases, respectively. The effectiveness of a heat exchanger when the inlet and outlet flows are balanced, i.e.,  $C_h = C_c$ , is as follows:

$$\epsilon = \frac{T_{h,in} - \bar{T}_{h,out}}{T_{h,in} - T_{c,in}} = \frac{\bar{T}_{c,out} - T_{c,in}}{T_{h,in} - T_{c,in}} \quad (3.14)$$

Generally, the effectiveness or performance of a cryogenic regenerator is given in terms of an inefficiency (Ie), [62]:

$$(Ie) = 1 - \epsilon = 1 - \frac{C_c(\bar{T}_{out} - T_{in})_c}{C_{min}(T_{h,in} - T_{c,in})} = 1 - \frac{C_h(T_{in} - \bar{T}_{out})_h}{C_{min}(T_{h,in} - T_{c,in})} \quad (3.15)$$

### 3.2.10 Acoustic power & coefficient of performance

In a pulse tube cryocooler, the input pressure and produced volume flow are typically sinusoidal and can be written as:

$$P_s[t] = P_0 + P_1 \cos[2\pi ft] \quad (3.16a)$$

$$\dot{V}_s[t] = \dot{V}_1 \cos[2\pi ft + \theta_{ph}] \quad (3.16b)$$

$P_0$  is the average pressure,  $P_1$  is the pressure amplitude,  $f$  is the operating frequency,  $\dot{V}_1$  is the amplitude of the sinusoidal volume flow, and  $\theta_{ph}$  is the phase between the volume flow and the pressure. The acoustic power is the power delivered by the compressor or the pulse wave generator and can be expressed as follows:

$$\dot{W}_{ac} = \frac{1}{\lambda_p} \int_0^{\lambda_p} (P_s - P_0)\dot{V} \cdot dt = \frac{1}{2}P_1\dot{V}_1 \cos(\theta_{ph}) \quad (3.17)$$

where  $\lambda_p$  is the time period of the oscillation. The result in equation 3.17 is obtained using the trigonometric identities. The acoustic power can be described by rewriting the volume flow in terms of mass flow rate,  $\dot{m}$ , using the ideal gas law  $V = mRT/P$ .

$$\dot{W}_{ac} = \frac{1}{2}P_1 \frac{\dot{m}RT}{P_0} \cos(\theta_{ph}) \quad (3.18)$$

$R$  and  $T$  denote the specific gas constant and the local mean gas temperature, respectively. In

ideal Stirling cryocooler, the gross refrigeration power,  $\dot{Q}_c$  is equal to the acoustic power at the cold end,  $\dot{W}_{ac,c}$ :

$$\dot{Q}_c = \dot{W}_{ac,c} = \frac{1}{2} P_1 \frac{\dot{m} R T_c}{P_0} \cos(\theta_{ph}) \quad (3.19)$$

If the working fluid is assumed to be an ideal gas and the heat regeneration is perfect, with no pressure loss, the refrigerator's coefficient of performance (COP) relative to the regenerator warm end is given by [114]:

$$COP_{ideal} = \frac{\dot{Q}_{net}}{\dot{W}_{ac,h}} = \frac{T_c}{T_h} \quad (3.20)$$

$T_h$  and  $T_c$  are the hot and cold end temperatures of the regenerator, respectively. In an ideal system, isothermal compression and expansion and ideal regenerator conditions are assumed; hence, a reversible process occurs. As a result, the COP is maximum and defined by the Carnot COP, which is given by [114]:

$$COP_{Carnot} = \frac{\dot{Q}_{net}}{\dot{W}_{ac,in}} = \frac{T_c}{T_h - T_c} \quad (3.21)$$

The presence of  $T_c$  in the denominator of equation 3.21 results from the acoustic power, which is proportional to  $T_c$ , being recovered and used to aid in compression [114]. Typically, the cryocooler's ideal second-law efficiency is expressed as:

$$\eta_{ideal} = \frac{COP_{ideal}}{COP_{Carnot}} = \frac{T_h - T_c}{T_h} \quad (3.22)$$

For a cryocooler with  $T_h = 300$  K and  $T_c = 80$  K,  $\eta_{ideal} = 70\%$ . However, for practical Stirling and pulse tube refrigerators with the same  $T_h$  and  $T_c$  and  $Q_c < 200$  W efficiencies are less than 20% [115].

### 3.3 Regenerator matrix selection

A great deal of the design of regenerative heat exchangers involves selecting different materials and geometries that are highly demanded to optimize their operation over a specific temperature range. This is a critical factor that requires further investigation because material properties and performance vary depending on the active temperature range. More precisely, materials that perform excellently and are considered good candidates for temperatures above 50 K lose their decent characteristics and become less appropriate for the lower temperature band. Similarly, geometries that exhibit good characteristics, such as low-pressure loss, for relatively high-temperature ranges will be incompetent and perform poorly over a lower temperature range. For instance,

bronze and stainless steel mesh screens are typically used in the first stage of all commercial regenerative cryogenic refrigerators operating at temperatures down to 30 K [62]. However, below that point, the loss of specific heat reduces the effectiveness of screen packing significantly [62]. Consequently, to design an effective regenerator, it is essential to understand critical properties such as fluid viscosity, porosity, and specific heat.

### 3.3.1 Packing geometries

The regenerator is typically constructed of a thin hollow tube filled with mesh screens, metallic spheres, or other fillers subjected to periodic gas flow. Figure 3.1 depicts four commonly used packing geometries in cryogenic applications. The following are the primary characteristics that a filling/packing material should possess in order to achieve optimal regenerator performance and, as a result, efficient cryocooler operation [62]:

- Maximum heat transfer area.
- Minimum pressure loss.
- Minimum axial conduction.
- High heat capacity.
- Minimum dead (void) volume.

The overall efficiency of any cryocooler is significantly affected by the effectiveness of the regenerator and heat exchangers. Mainly, the regenerator's effectiveness is determined by the first two items in the above list. As a result, an efficient design for any regenerator would either make trade-offs or consider maximizing the heat transfer area while minimizing pressure loss. The following sections discuss two distinct types of geometries and their associated design parameters.

#### 3.3.1.1 Wire mesh screens

Wire mesh screens are the most frequently used regenerator packing material due to their relatively high heat transfer area and low-pressure loss. Wire mesh screens are available in various pore sizes (from  $20 \times 20$  to  $635 \times 635$  pore/in<sup>2</sup>) and different materials. The merits of this type include low cost, small wire diameter, and high thermal conductivity, which optimizes the utilization of its thermal capacity [62]. They are widely used in a variety of heat exchange configurations in both research and industry, including air vents, cryogenics equipment, cryocoolers, cold heads, and heat pipes. *The notation  $n \times n$  indicates the mesh size, i.e.  $20 \times 20$  refers to 20 openings per inch.*

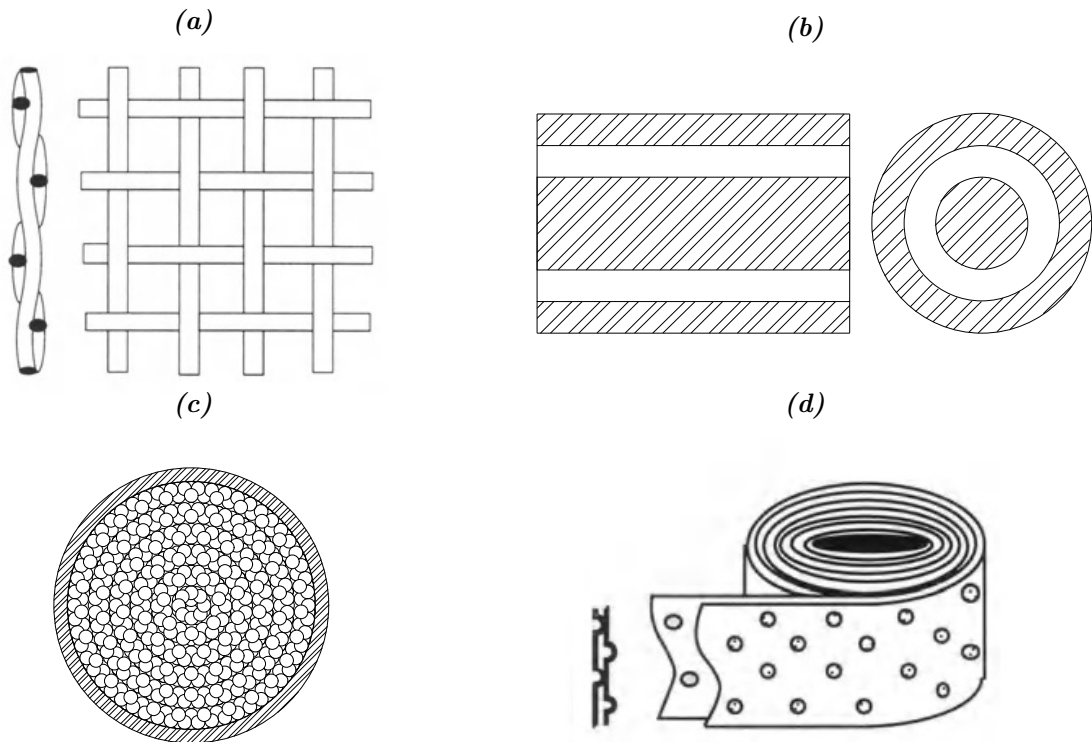


**Figure 3.1:** Typical regenerator filling geometries: (a) Wire mesh screens, (b) Annular gap regenerator, (c) cylinder packed with spheres and (d) dimpled ribbon. Pictures (a) and (d) are reproduced from [62].

The hydraulic radius for screens is the ratio of the porosity to the area density shown in equations 3.8a and 3.8b. The area density is calculated from the circumferential heat transfer area ratio to the volume occupied by one segment of screen mesh. Figure 3.2 depicts the geometrical parameters for woven mesh screens, where  $1/n$  is the opening length,  $d_w$  is the screen wire diameter and,  $t_{screen}$  is the screen thickness.

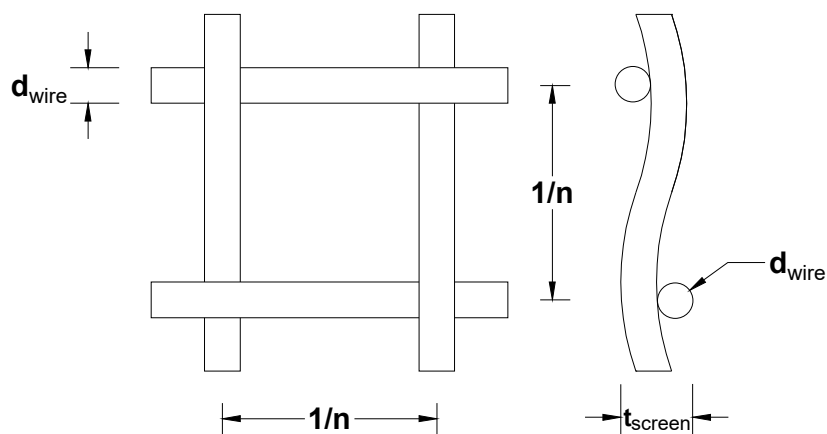


**Figure 3.2:** Geometrical parameter for woven screen.

The area density can be computed from equation 3.8b, where [62]:

$$\beta_m = \frac{(\text{wire circumference area subject to flow})(\text{No. of sides})}{\text{Volume enclosing the wires}} \quad (3.23a)$$

$$\beta_m = \frac{0.5(\pi d_{\text{wire}})(1/n)(4)}{(1/n)^2(t_{\text{screen}})} = \frac{2\pi d_w n}{t_{\text{screen}}} \quad (3.23b)$$

If perfect stacking is assumed such that  $t_{\text{screen}} = 2d_w$ ; this means that no inclination or misalignment occurred during the weaving of the wire and no separation occurred during the packing of the screens, i.e., (Overall filling depth) =  $2(d_w)(\text{No. of screens})$ , as such:

$$\phi_m = 1 - \frac{V_m}{V_{\text{reg}}} = 1 - \frac{\pi n d_w}{4} \quad (3.24a)$$

$$\beta_m = \pi n \quad (3.24b)$$

$$D_h = \frac{\phi_m d_w}{(1 - \phi_m)} \quad (3.24c)$$

### 3.3.1.2 Spheres

Metallic spheres, such as lead spheres, are primarily used in extremely low-temperature refrigerators, where mesh screens' specific heat properties deteriorate and make them unsuitable for such temperature ranges due to a significant decrease in efficiency. Spherical fillers are typically composed of randomly sized spheres with a diameter tolerance of  $\pm 0.04 \text{ mm}$ . In general, the porosity of the matrix can be found using equation 3.9. However, if a perfectly stacked uniform sphere matrix with very small sphere diameters is assumed, i.e.  $d_{\text{sphere}}$  approaching zero, then the porosity  $\phi_m$  becomes independent of sphere size and can reach a value of 30% where the area density,  $\left(\beta_m = \frac{4\pi}{3d_{\text{sphere}}}\right)$  [62]. The main characteristics of spherical matrix include [62]:

- They are efficient for temperature ranges below 30 K due to the low porosity,  $\phi_m$ , resulting in significant pressure loss. At this temperature range, the viscosity of the working fluid is very low.
- The low porosity also increases the total heat transfer surface area substantially compared to the screen matrix.
- Materials like lead and lead-antimony are usually used as packing materials since they have high heat capacity, making them perform very well at low temperatures, i.e., below 25 K. However, materials that contain magnetic intermetallic compounds are used to achieve cooling below 4.2 K.

### 3.3.2 Packing materials

In general, the geometry and materials of regenerative heat exchangers are classified into three groups based on the temperature ranges in which they are most efficient [62]:

- [300 → 30 K]: Copper, bronze and stainless steel woven screens.
- [30 → 10 K]: Lead and lead antimony spheres.
- [10 → 3 K]: Magnetic intermetallic compounds.

Over the first temperature range, copper, bronze, and stainless steel are typically used in screen fillers due to their outstanding properties, such as low-pressure loss and axial conduction, high heat capacity, and large total heat transfer area. However, they lose these advantages, and their efficiency is significantly reduced below 30 K.

Due to their higher heat capacity than materials in the first category, lead and lead-antimony spheres perform exceptionally well in the 10 – 30 K range. Additional advantages include low void/dead volume, lower porosity, and lower pressure loss due to the fluid's viscosity decreasing over this temperature range.

Below 10 K, lead tends to lose a great deal of its heat capacity, i.e., lead loses 89% of its room temperature specific heat, causing more significant temperature swings of the matrix material and decreasing the regenerative heat exchanger efficiency. However, developing a new class of materials with phase transitions from ferromagnetic to paramagnetic or even nonmagnetic states resulted in an increase in the material's heat storage capacity. As a result, regenerative cycle refrigerators can reach cooling temperatures less than 3 K [62].

At extremely low temperatures, the specific heat of solids decreases dramatically with temperature because it is a function of lattice vibrations and conduction electrons, both of which are inversely proportional to temperature. The advantage of heavy rare earth intermetallic compounds is that they have a higher heat capacity below 10 K. Their exhibited magnetic phase transition effect and its associated significant entropy effects result in higher specific heat, one to two orders larger than the lattice specific heat. Figure 3.3 depicts the specific heat capacity for three common regenerator materials; it can be seen that the values for both copper and stainless steel largely drop for temperatures below 40 K.

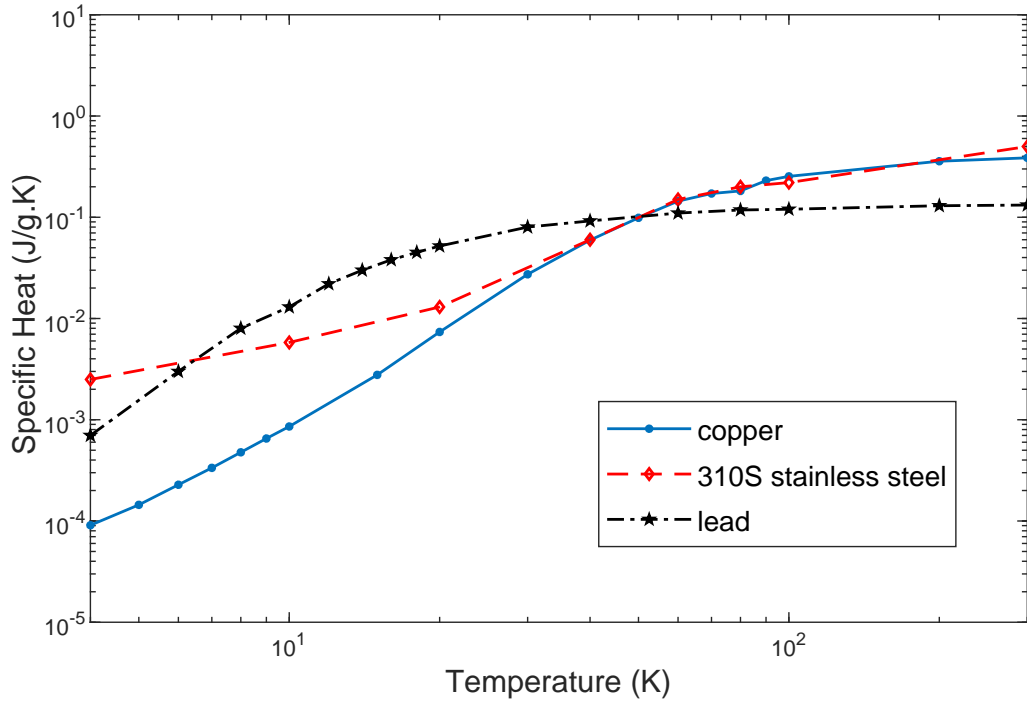


*Figure 3.3: Specific heat for three commonly used packing materials. Source of Data [116].*

### 3.4 Theory of regenerative heat exchangers

This section explains the theory of regenerative heat exchangers, which defines the physics behind the thermal and flow interactions. Generally, the regenerator's model is composed of differential equations that define the temperature profiles in the matrix and fluid over time and space. This section describes the fluid and thermal dynamics that govern the operation of the regenerator in a cryocooler system.

#### 3.4.1 Mass flow rate and flow velocity

Transportation of energy depends on the mass flow of the fluid across the control volume in the regenerator. In three-dimensional system, the flow velocity vector,  $\mathbf{w}$ , is described by:

$$\mathbf{w} = w_x \mathbf{x} + w_y \mathbf{y} + w_z \mathbf{z}, \quad \text{for Cartesian coordinate system.} \quad (3.25a)$$

$$\mathbf{w} = w_r \mathbf{r} + w_\theta \boldsymbol{\theta} + w_z \mathbf{z}, \quad \text{for cylindrical coordinate system.} \quad (3.25b)$$

and the mass flow rate is calculated as follows:

$$\dot{m} = \rho_f \mathbf{w} A_\perp \quad (3.26)$$

$A_{\perp}$  is the surface area perpendicular to the direction of the flow, and  $w$  is the flow velocity.

### 3.4.2 Energy of flow

Assuming a fluid particle with a mass element,  $\Delta M_f$ , is traveling from coordinate point  $r_1$  to coordinate point  $r_2$ , as illustrated in Figure 3.4. This flow's energy is a combination of four terms: internal, kinetic, and potential energy, as well as the work done by the force acting on the face of the fluid mass element to push it from  $r_1$  to  $r_2$ . Thus, the energy difference between these two location points can be expressed as the sum of these four terms, as follows:

$$\Delta E = \Delta M_f \left[ (u_2 - u_1) + \frac{1}{2}(w_2^2 - w_1^2) + g(z_2 - z_1) + (p_2 v_2 - p_1 v_1) \right] \quad (3.27)$$

$u$ ,  $w$ ,  $z$ ,  $p$ , and  $v$  are the specific internal energy, velocity of the flow, vertical position coordinate, fluid pressure, and specific volume, respectively. Further simplification results in the term:

$$e = u + pv \quad (3.28)$$

This is known as the specific enthalpy, and sometimes the term  $pv$  is called the *flow work*. Constant pressure specific heat capacity of fluid can be then written as [62]:

$$c_p = \left[ \left( \frac{\partial u}{\partial T} \right)_p + p \left( \frac{\partial v}{\partial T} \right)_p \right] = \left( \frac{\partial e}{\partial T} \right)_p \quad (3.29)$$

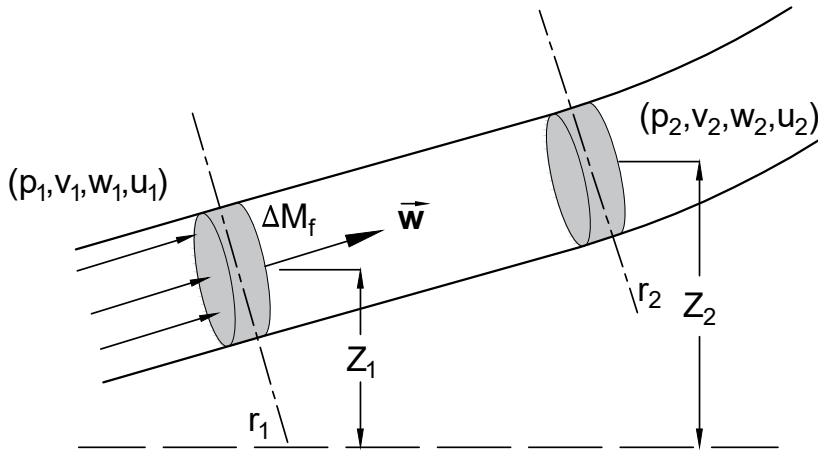


**Figure 3.4:** Energy flow for a differential element relative to a position coordinate,  $r$ .

### 3.4.3 Regenerator's principle of operation

In a regenerative cryocooler, regenerators are utilized to transfer heat between two balanced, similar gas flows operating at the same pressure. The matrix temperature profile reaches its maximum value as the gas flows from the hot to the cold end of the regenerator during the heating period, leaving the regenerator with a variable lower temperature. The flow reverses direction, and the gas at cold temperature  $T_c$  is heated by the matrix's higher temperature as it enters the regenerator, causing the matrix temperature profile to reach its minimum value and leaving the regenerator with a variable warmer temperature. The flow is reversed again at the end of this cooling period, and the gas enters the regenerator at a hot temperature  $T_h$ . The matrix cools it down to the cold temperature  $T_c$ , causing the matrix distribution to climb back to its maximum level. The gas temperature distribution is at its highest point at this moment. Figure 3.5 illustrates the expected temperature distributions for the gas and matrix over a single cycle.

The temperature of the gas and the matrix solid elements varies with location and time. However, a periodic steady state is achieved after several cycles of heating and cooling. As a result, the temperature at any point in the regenerator is equal to the temperature at that point before and after one complete cycle. It is worth mentioning that the cryocooler system is a closed system, which means that no mass can be transported out of or into it, just energy. As a result, any mention of gas inflow or outflow refers to flow inside the system, particularly from one component to the regenerator.

### 3.4.4 Governing equations

The thermal interaction and energy exchange between the matrix and the fluid are described by the conservation of mass equation (the continuity equation), momentum (Navier-Stokes equations), and energy equations in the fluid domain. Figure 3.6 depicts the control volume,  $\Delta V$ , in both Cartesian and cylindrical coordinate systems, which incorporates both the fluid and the matrix and establishes a relationship between the inflow mass, outflow mass, and energy transferred into and out of the control volume via fluid dynamics.

#### 3.4.4.1 Conservation of mass

The continuity equation describes the mass balance between the inflow and the outflow entering and leaving the control volume,  $\Delta V$ , per unit time, as illustrated in Figure 3.6. Assuming  $\Delta V$

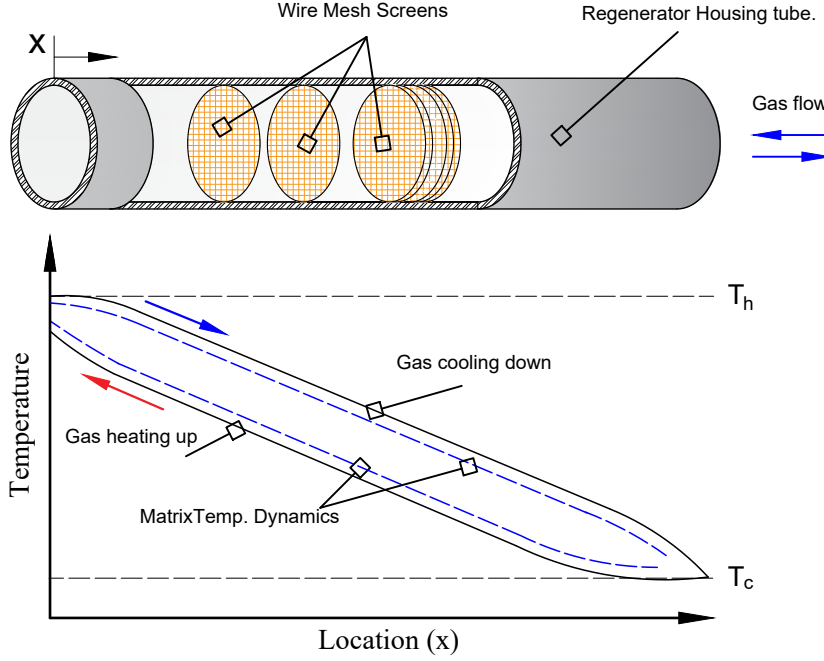


**Figure 3.5:** Expected matrix and gas temperature dynamics, where  $T_h$  and  $T_c$  are the respective hot and cold temperature levels [117].

in Figure 3.6 has a mass,  $\Delta M$ , that is composed of the fluid and matrix mass components:

$$\Delta M = \Delta M_m + \Delta M_f = \rho_m \Delta V_m + \rho_f \Delta V_f \quad (3.30)$$

$\rho_f$ ,  $\rho_m$ ,  $\Delta V_m$  and  $\Delta V_f$  are the density of the fluid, density of the matrix, the matrix volume element, and the fluid volume element, respectively. where  $\Delta V = \Delta x \Delta y \Delta z$  is the control volume in the Cartesian coordinate system, and  $\Delta V = \Delta r (r \Delta \theta) \Delta z$  is the control volume in the cylindrical coordinate system, as illustrated in Figure 3.6. Then the mass flow balance through the control volume is:

$$\frac{\partial(\rho \Delta V)}{\partial t} = \sum \dot{m}_{in} - \sum \dot{m}_{out} \quad (3.31)$$

$\dot{m}_{in}$  and  $\dot{m}_{out}$  are the mass inflow and outflow, respectively. Figure 3.6a illustrates the mass inflow and the mass outflow in the three main directions of  $x$ ,  $y$ , and  $z$ . The mass balance equations are:

$$\begin{aligned} \sum \dot{m}_{in} &= \dot{m}(x) + \dot{m}(y) + \dot{m}(z) \\ &= \rho w_x \Delta y \Delta z + \rho w_y \Delta x \Delta z + \rho w_z \Delta x \Delta y \end{aligned} \quad (3.32a)$$

$$\sum \dot{m}_{out} = \dot{m}(x + \Delta x) + \dot{m}(y + \Delta y) + \dot{m}(z + \Delta z) \quad (3.32b)$$

Expanding equation 3.32b using Taylor series and ignoring higher order terms, by assuming the control volume,  $\Delta V$  approaches zero. The outflow terms can be related to the inflow terms, as

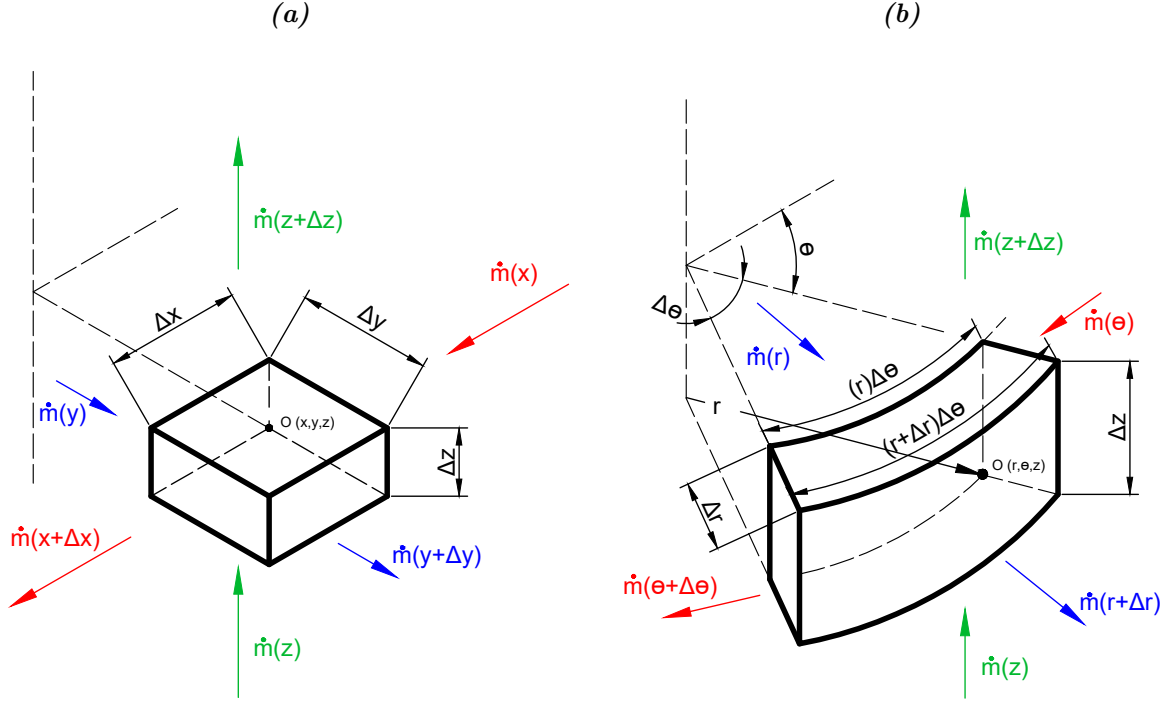


**Figure 3.6:** Control volume element for the regenerator: (a) in Cartesian coordinate system, (b) in Cylindrical coordinate system, where  $\dot{m}$  is the fluid mass flow rate.

follows:

$$\begin{aligned} \sum \dot{m}_{out} &= \rho w_x \Delta y \Delta z + \frac{\partial \rho w_x}{\partial x} \Delta x \Delta y \Delta z \\ &+ \rho w_y \Delta x \Delta z + \frac{\partial \rho w_y}{\partial y} \Delta x \Delta y \Delta z \\ &+ \rho w_z \Delta x \Delta y + \frac{\partial \rho w_z}{\partial z} \Delta x \Delta y \Delta z \end{aligned} \quad (3.33)$$

By substituting equation 3.33 in equation 3.31, the general form of the continuity equation is obtained:

$$\frac{\partial \rho \Delta V}{\partial t} + \left( \frac{\partial \rho w_x}{\partial x} + \frac{\partial \rho w_y}{\partial y} + \frac{\partial \rho w_z}{\partial z} \right) \Delta V = 0 \quad (3.34)$$

Due to the regenerator's typical geometry being a cylinder, it is more common to represent the continuity equation in cylindrical rather than rectangular form. The same analysis can be performed on the control volume depicted in Figure 3.6b, yielding the following equation:

$$\frac{\partial (\rho \Delta V)}{\partial t} + \left( \frac{\partial \rho w_r}{\partial r} + \frac{\rho w_r}{r} + \frac{1}{r} \frac{\partial \rho w_\theta}{\partial \theta} + \frac{\partial \rho w_z}{\partial z} \right) \Delta V = 0 \quad (3.35)$$

$r$ ,  $\theta$  and  $z$  are the cylindrical coordinate components as shown in Figure 3.6b. A simplified versions of equations 3.34 and 3.35 can be deduced if assuming that the fluid is incompressible, and  $\Delta V$  is assumed constant due to small pressure change across the regenerator. For these

conditions, equation 3.35 becomes:

$$\frac{\partial \rho w_r}{\partial r} + \frac{\rho w_r}{r} + \frac{1}{r} \frac{\partial \rho w_\theta}{\partial \theta} + \frac{\partial \rho w_z}{\partial z} = 0 \quad (3.36)$$

#### 3.4.4.2 Conservation of energy

The conservation of energy equation describes the heat balance between the inflow and the outflow that enters and leaves the control volume,  $\Delta V$ , per unit time. The general form of energy balance equation can be summarized as:

$$dQ_{in} + dQ_{int} = dQ_{out} + dU \quad (3.37)$$

$dQ_{in}$ ,  $dQ_{int}$ ,  $dQ_{out}$  and  $dU$  are the heat inflow, internal generated heat, heat outflow, and the change in internal energy, respectively. If this is applied to the control volume in Figure 3.6b, the energy balance for the matrix, assuming only slight changes in flow pressure, is:

$$\begin{aligned} \frac{dQ_c}{dt} \Big|_{(r,\theta,z)} + \frac{dQ_g}{dt} \Big|_{(r+\frac{\Delta r}{2},\theta+\frac{\Delta \theta}{2},z+\frac{\Delta z}{2})} &= \frac{dQ_c}{dt} \Big|_{(r+\Delta r,\theta+\Delta \theta,z+\Delta z)} \\ &+ [(\rho c_p \Delta V)_m \frac{dT_m}{dt}] \Big|_{(r+\frac{\Delta r}{2},\theta+\frac{\Delta \theta}{2},z+\frac{\Delta z}{2})} \end{aligned} \quad (3.38)$$

$dQ_c$ ,  $dQ_g$ ,  $T_m$ ,  $\rho_m$ , and  $c_{pm}$  are the heat conducted, heat transported by the gas, temperature, the density, and the specific heat of the matrix at the center of the volume element. For the matrix,  $dQ_g = dQ_h$ , where  $dQ_h$  is the heat convection across the interface area between the matrix and fluid. The conductive heat transfer can be expressed with Fourier's law [62]:

$$\frac{dQ_c}{dt} = -(K_m \Delta A_m) \frac{\partial T_m}{\partial s} \quad (3.39)$$

$K_m$ ,  $\Delta A_m$  and  $s$  are the thermal conductivity, the matrix element surface area through which the heat flows, and the space notation perpendicular to the heat flow direction. The minus sign indicates that the heat flow direction is opposite to the temperature gradient direction,  $dT_m/ds$ . Adding up  $dQ_c$  for the three faces shown in Figure 3.6 and then using the Taylor series to expand  $dQ_{c,out}$ , the conductive three-dimensional heat transfer equation through the matrix is:

$$\dot{Q}_{c,in} - \dot{Q}_{c,out} = \left[ \frac{\partial}{\partial r} \left( K_m \frac{\partial T_m}{\partial r} \right) + \frac{K_m}{r} \frac{\partial T_m}{\partial r} + \frac{\partial}{\partial \theta} \left( \frac{K_m}{r^2} \frac{\partial T_m}{\partial \theta} \right) + \frac{\partial}{\partial z} \left( K_m \frac{\partial T_m}{\partial z} \right) \right] \Delta V_m \quad (3.40)$$

Convective heat transfer within the volume element, between the fluid and the matrix and the fluid, is summarized as:

$$\frac{dQ_h}{dt} = \dot{Q}_h = (h \Delta A_s) (T_f - T_m) \quad (3.41)$$

$\Delta A_s$  is the matrix heat transfer area within the element. The generalized thermal energy equation for the matrix material is [62]:

$$\left[ \frac{\partial}{\partial r} \left( K_m \frac{\partial T_m}{\partial r} \right) + \frac{K_m}{r} \frac{\partial T_m}{\partial r} + \frac{\partial}{\partial \theta} \left( \frac{K_m}{r^2} \frac{\partial T_m}{\partial \theta} \right) + \frac{\partial}{\partial z} \left( K_m \frac{\partial T_m}{\partial z} \right) \right] \Delta V_m + (h \Delta A_s)(T_f - T_m) = (\rho c_p \Delta V)_m \frac{\partial T_m}{\partial t} \quad (3.42)$$

Similarly, and assuming that heat conduction occurs solely through the matrix material, the energy balance equation for the fluid can be written as follows:

$$\frac{dQ_g}{dt} \Big|_{\theta}^r + \frac{dQ_{fr} - dQ_h}{dt} \Big|_{z + \Delta z/2}^{r + \Delta r/2} = \frac{dQ_g}{dt} \Big|_{\theta + \Delta \theta}^{r + \Delta r} + (\rho c_p \Delta V)_f \frac{dT_f}{dt} \Big|_{z + \Delta z/2}^{r + \Delta r/2} \quad (3.43)$$

$dQ_{fr}$  and  $dQ_h$  is the frictional heating and the heat convection between the fluid and the matrix, respectively, the heat transferred to the faces of the volume element is:

$$\frac{dQ_f}{dt} = (\rho w c_p \Delta A_{\perp})_f T_f \quad (3.44)$$

$\Delta A_{\perp f}$  is the surface area perpendicular to the direction of the flow and through which the fluid transfers heat. Summing  $dQ_c$  for the three faces shown in Figure 3.6b and then using Taylor series to expand  $dQ_{g,out}$  terms, the general equation for the heat transferred into the control volume:

$$\frac{dQ_g}{dt} \Big|_{\theta}^r - \frac{dQ_g}{dt} \Big|_{\theta + \Delta \theta}^{r + \Delta r} = -(\rho_f \Delta V_f) \left[ w_r \left( \frac{\partial (c_p T)_f}{\partial r} \right) + \frac{w_{\theta}}{r} \frac{\partial (c_p T)_f}{\partial \theta} + w_z \left( \frac{\partial (c_p T)_f}{\partial z} \right) \right] \quad (3.45)$$

Ackermann [62] conducted tests on a regenerator used in a small helium Stirling cryocooler with a swept volume of  $0.5 \text{ cm}^3$ , operating at 60 Hz, and a temperature range of 300 to 80 K. In this case, the total heat transfer was ten orders of magnitude larger than the frictional heating. As a result, neglecting the frictional heating and substituting equation 3.45 in equation 3.43 gives the thermal energy equation for the fluid [62]:

$$(\rho_f \Delta V_f) \left[ w_r \left( \frac{\partial (c_p T)_f}{\partial r} \right) + \frac{w_{\theta}}{r} \frac{\partial (c_p T)_f}{\partial \theta} + w_z \left( \frac{\partial (c_p T)_f}{\partial z} \right) \right] \quad (3.46)$$

$$+ (h \Delta A_s)(T_f - T_m) + (\rho c_p \Delta V)_f \frac{\partial T_f}{\partial t} = 0 \quad (3.47)$$

### 3.4.4.3 Conservation of momentum

A thorough analysis of a regenerator should include not only its thermal behavior and the equations that define it, but also its pressure loss characteristics. The momentum equation defines the pressure loss, which is derived from Newton's second law, which asserts that mass times acceleration equals the sum of the external forces acting on the fluid. Assuming a control volume  $\Delta V$  with a fluid mass  $\Delta M_f$  and external forces acting on it, including the surface forces (i.e., pressure and friction forces acting on the faces of the control volume)  $\mathbf{F}$  and the gravitational force  $\mathbf{P}$ , the momentum equation reads as follows in vector notation:

$$\Delta M_f \frac{D\mathbf{w}}{Dt} = \mathbf{F} + \mathbf{P} \quad (3.48)$$

Generally, the velocity vector for a particle of fluid within the control volume is a function both of time,  $t$ , and location. Hence [118]:

$$\frac{D\mathbf{w}}{Dt} = \frac{\partial \mathbf{w}}{\partial t} + \frac{d\mathbf{w}}{dt} \quad (3.49)$$

$D\mathbf{w}/Dt$  is the substantial acceleration made up of the local acceleration,  $\partial \mathbf{w}/\partial t$  and the convective acceleration, ( $d\mathbf{w}/dt = (\mathbf{w} \cdot \nabla)\mathbf{w}$ ) due to the change in position [118]. For cylindrical coordinate system:

$$\frac{Dw_r}{Dt} = \frac{\partial w_r}{\partial t} + \left( w_r \frac{\partial w_r}{\partial r} + \frac{w_\theta}{r} \frac{\partial w_r}{\partial \theta} - \frac{w_\theta^2}{r} + w_z \frac{\partial w_r}{\partial z} \right) \quad (3.50a)$$

$$\frac{Dw_\theta}{Dt} = \frac{\partial w_\theta}{\partial t} + \left( w_r \frac{\partial w_\theta}{\partial r} + \frac{w_\theta}{r} \frac{\partial w_\theta}{\partial \theta} + \frac{w_r w_\theta}{r} + w_z \frac{\partial w_\theta}{\partial z} \right) \quad (3.50b)$$

$$\frac{Dw_z}{Dt} = \frac{\partial w_z}{\partial t} + \left( w_r \frac{\partial w_z}{\partial r} + \frac{w_\theta}{r} \frac{\partial w_z}{\partial \theta} + w_z \frac{\partial w_z}{\partial z} \right) \quad (3.50c)$$

Schlichting [118] demonstrated that the resultant surface force applied to each facet of the control volume comprises perpendicular components defined by the normal stress,  $\sigma$ , and parallel components defined by the shear stress,  $\tau$ . The vector components of equation 3.48 for  $\mathbf{F}$  can be rewritten as:

$$F_r = (\sigma_r + \tau_{r\theta} + \tau_{rz}) \Delta A_r \quad (3.51a)$$

$$F_\theta = (\sigma_\theta + \tau_{\theta r} + \tau_{\theta z}) \Delta A_\theta \quad (3.51b)$$

$$F_z = (\sigma_z + \tau_{zr} + \tau_{z\theta}) \Delta A_z \quad (3.51c)$$

Schlichting derived the stress components in terms of the pressure and friction stresses by applying Hooke's law to relate the stresses to strains in a solid elastic body. Substituting these

expressions into the generalized equation of motion, equation 3.48, leads to the Navier-Stokes equations for an incompressible fluid ( $\rho = \text{constant}$ ) [62]:

$$\rho \frac{Dw_r}{Dt} = \rho g_r - \frac{\partial p}{\partial r} + \mu \left( \frac{\partial^2 w_r}{\partial r^2} + \frac{1}{r} \frac{\partial w_r}{\partial r} - \frac{w_r}{r^2} + \frac{1}{r^2} \frac{\partial^2 w_r}{\partial \theta^2} - \frac{2}{r^2} \frac{\partial w_\theta}{\partial \theta} + \frac{\partial^2 w_r}{\partial z^2} \right) \quad (3.52a)$$

$$\rho \frac{Dw_\theta}{Dt} = \rho g_\theta - \frac{1}{r} \frac{\partial p}{\partial \theta} + \mu \left( \frac{\partial^2 w_\theta}{\partial r^2} + \frac{1}{r} \frac{\partial w_\theta}{\partial r} - \frac{w_\theta}{r^2} + \frac{1}{r^2} \frac{\partial^2 w_\theta}{\partial \theta^2} + \frac{2}{r^2} \frac{\partial w_r}{\partial \theta} + \frac{\partial^2 w_\theta}{\partial z^2} \right) \quad (3.52b)$$

$$\rho \frac{Dw_z}{Dt} = \rho g_z - \frac{\partial p}{\partial z} + \mu \left( \frac{\partial^2 w_z}{\partial r^2} + \frac{1}{r} \frac{\partial w_z}{\partial r} + \frac{1}{r^2} \frac{\partial^2 w_z}{\partial \theta^2} + \frac{\partial^2 w_z}{\partial z^2} \right) \quad (3.52c)$$

The Navier-Stokes equations are applied to a regenerator model with flow moving in the z-direction to determine the regenerator's pressure loss. Numerous assumptions are made:

- Because the flow is along the z-direction, the velocity in the z-direction is much larger than the velocity components in other directions ( $w_z \gg w_r, w_\theta$ ).
- The rate of change of velocity components in other directions is much lower than that along the z-direction.
- The gravitational force and the force component in the z-direction.

Applying these assumptions to equations 3.50c and 3.52c result in:

$$\rho \left( \frac{\partial w_z}{\partial t} + \frac{1}{2} \frac{\partial (w_z)^2}{\partial z} \right) = -\rho g_z - \frac{\partial p}{\partial z} + \mu \frac{\partial^2 w_z}{\partial z^2} \quad (3.53)$$

By rearranging the terms into time-dependent velocity differential and position-dependent differential terms and integrating along the length of the regenerator between points  $z_1$  and  $z_2$ . Assuming very small stream tubes where the velocity in any cross section is constant, The unsteady energy equation for the flow through the regenerator is obtained [62]:

$$\left( \frac{w_z^2}{2g} + \frac{p}{\rho g} + z \right)_1 = \left( \frac{w_z^2}{2g} + \frac{p}{\rho g} + z \right)_2 + h_{vf} + \frac{1}{g} \int_{z_1}^{z_2} \frac{\partial w_z}{\partial t} dz \quad (3.54)$$

$h_{vf} = (\mu/\rho g)(\partial w_z/\partial z)$  is the energy loss in the flow caused by viscous friction. Generally, evaluation of pressure loss is done experimentally using flow and fluid property values averaged over both the cross-sectional flow area and the time to find flow resistance coefficient  $f_r$ . To obtain a generalized steady-state formula for the loss in the pressure head between points 1 and 2 in terms of the changes in velocity head and viscous losses, assuming:

- Velocity is expressed as time-averaged velocity where  $\bar{W}_z = \frac{1}{\lambda} \int_0^\lambda w_z dt$ , and  $\partial(\bar{W}_z)/\partial(t) = 0$ . where  $\bar{W}_z$  is the average flow velocity over the free flow area and flow period.

- The velocity is a function of mass flow rate per unit area and given by

$$(\rho\bar{W}_z)_1 = (\rho\bar{W}_z)_2 = \frac{\bar{m}}{A_{ff}} \quad (3.55)$$

- The viscous friction loss,  $h_{vf}$  is defined experimentally by the flow resistance coefficient  $f$  as follows [62]:

$$h_{vf} = f_r \frac{L\bar{W}_z}{2gr_h} \quad (3.56)$$

$L$ ,  $r_h$  are the length and the hydraulic radius of the regenerator, respectively.

Substituting these terms in equation 3.54 lead to the generalized steady-state formula for the loss in the pressure:

$$\left(\frac{p}{\rho g}\right)_1 - \left(\frac{p}{\rho g}\right)_2 = \frac{1}{2g\rho_1^2} \left(\frac{\bar{m}}{A_{ff}}\right)^2 \left[ \frac{(\rho_1)^2}{(\rho_2)^2} - 1 + f_r \frac{L\rho_1^2}{r_h(\bar{\rho}_f)^2} \right] \quad (3.57)$$

where  $\bar{\rho}_f$  is the mean fluid density between points 1 and 2. The Fanning pressure loss equation is deduced by assuming constant density,  $\rho_1 = \rho_2$ , and this gives the Fanning pressure loss as [62]:

$$\Delta p = f_r \frac{L}{2r_h\bar{\rho}_f} \left(\frac{\bar{m}}{A_{ff}}\right)^2 \quad (3.58)$$

$\Delta p$  is the pressure loss,  $f_r$  is the Fanning friction coefficient,  $\bar{\rho}_f$  is the fluid's average density, and  $\bar{m}$  is the fluid's average mass flow rate. Equation 3.58 represents the steady flow pressure drop. Regenerative cryocoolers machines are operating under periodically reversing flow, hence the mass flow in the regenerator periodically oscillates and, thus, has a zero average value. The previous steady-state formula can be used for regenerator optimization by employing the root-mean-square value (RMS) of the mass flow rate or simply,  $A_{\bar{m}}/\sqrt{2}$ ; where  $A_{\bar{m}}$  is the amplitude of the mass flow rate signal. Another approach is to use the half-wave average, because the cooling effect occurs during half of the pressure cycle, and so  $\bar{m}$  is set to  $\frac{2}{\pi}A_{\bar{m}}$ .

### 3.5 Ideal regenerator<sup>1</sup>

Due to the complexity of the regenerator equations derived in the preceding sections, no closed-form solutions can be obtained. Typically, finite element analysis and high-performance digital computers are required to solve these equations. This section considers the case of an ideal regenerator to provide a more concrete understanding of how a regenerator works. The ideal regenerator model is based on several assumptions that simplify the regenerator model.

During the cooling phase, the ideal regenerator can be thought of as a thermodynamic object that receives the gas at a low-temperature  $T_c$  and discharges it at a high-temperature  $T_h$ . When

the flow direction is reversed during the heating period, the gas enters at  $T_h$  and exits at  $T_c$ . The ideal regenerator case is hard to achieve in practice since maintaining a constant inlet and outlet temperature would require an infinitely slow operation, an infinite heat transfer coefficient, and a large heat transfer area. Furthermore, the heat capacity of the fluid and the matrix should be zero and infinity, respectively. Moreover, the absence of a pressure loss would require frictionless flow. The lack of void volume, on the other hand, would prevent fluid flow passages across the matrix [112].

The mathematical model used here is based on a simplified model of the governing equations that were discussed previously. The assumptions for an ideal regenerator should satisfy the following terms [62]:

- The heat stored in the fluid is small compared to the heat stored in the matrix. Therefore, the fluid's stored thermal energy is zero.
- The pressure loss along the length of the regenerator is negligible.
- The thermal conductivity of the matrix is zero in the longitudinal direction and infinite everywhere else. Thus, there should be no conduction loss between the warm and cold ends of the regenerator and no heat transferred to the cold end of the regenerator as a result of imperfect heat transfer between the gas and the solid.
- The working gas is ideal, and the flow is one-dimensional.
- The fluid and matrix properties are temperature-dependent and do not change over the length of the regenerator. The mass flow and the working gas pressure through the regenerator are constant, and their magnitudes are equal during the heating and cooling periods.
- No gas flow mixing occurs during the cooling and heating phases (i.e., during the reversal from hot to cold flows). In other words, hot gas enters the regenerator at a constant temperature and uniform velocity across the cross-sectional area. It stops when the flow is reversed, while cold gas enters at a constant temperature and flow rate.
- The boundary temperature conditions for the working gas are constant for heating and cooling periods.

Based on the previous assumptions, the matrix and fluid thermal equations can be summarized as [62]:

$$\text{Matrix balance equation: } h\Delta A_s (T_g - T_m) = (\rho c_p \Delta V)_m \frac{\partial T_m}{\partial t}, \quad (3.59a)$$

$$\text{Fluid balance equation: } h\Delta A_s (T_g - T_m) = -(\rho c_p \Delta V)_g w_x \frac{\partial T_g}{\partial x}. \quad (3.59b)$$

Here,  $h$ ,  $A_s$ ,  $T_m$ ,  $T_g$ ,  $\rho$ ,  $w_x$ ,  $\Delta V$ , and  $c_p$  are the convection heat transfer coefficient, matrix heat transfer area, matrix temperature, gas temperature, the density of the gas, the velocity of the gas, the control volume, and constant pressure specific heat capacity, respectively. Both equations' left-hand sides describe convection heat transfer between the matrix material and the working fluid, while the right-hand sides of equations 3.59a and 3.59b represent the varying built-up heat in the matrix and the working fluid. Equations 3.59a and 3.59b are then represented in finite-element difference form as proposed by Ackermann [62], which divides the regenerator into spatial elements and divides the heating and cooling periods into sufficiently small time steps. The one-dimensional computational mesh for the regenerator during heating and cooling periods is shown in Figure 3.7.

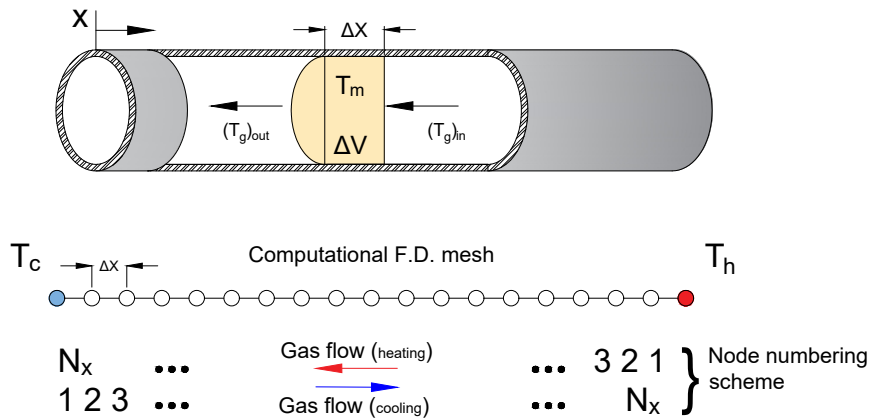


**Figure 3.7:** Numerical schematic for the regenerator during heating and cooling periods, where  $N_x$  and  $N_t$  are the total number of spatial and time elements and  $T_h$  and  $T_c$  are the hot and cold temperature levels [117].

The model is then transformed into two linear algebraic equations that are used to compute the nodal temperatures of the matrix and gas, thereby predicting regenerator performance and finally yielding:

$$\text{Matrix time marching scheme: } (T_g)_{i+1}^j = (T_g)_i^j - K_1((T_g)_i^j + (T_m)_i^j), \quad (3.60a)$$

$$\text{Fluid time marching scheme: } (T_m)_i^{j+1} = (T_g)_i^j + K_2((T_g)_i^j + (T_m)_i^j). \quad (3.60b)$$

The indexes  $i$  and  $j$  are the number of spatial and time nodes, and  $K_1$  and  $K_2$  are constants [62]:

$$K_1 = \left( \frac{\left( \frac{hA_s}{(\dot{m}c_p)_f} \right)_{\Delta x}}{1 + \frac{1}{2} \left( \frac{hA_s}{(Mc_p)_m} \Delta t \right)_{\Delta x} + \frac{1}{2} \left( \frac{hA_s}{(\dot{m}c_p)_f} \right)_{\Delta x}} \right)$$

$$K_2 = \left( \frac{\left( \frac{hA_s}{(Mc_p)_m} \Delta t \right)_{\Delta x}}{1 + \frac{1}{2} \left( \frac{hA_s}{(Mc_p)_m} \Delta t \right)_{\Delta x} + \frac{1}{2} \left( \frac{hA_s}{(\dot{m}c_p)_f} \right)_{\Delta x}} \right)$$

Here,  $\dot{m}$ ,  $M$ ,  $\Delta t$ , and  $\Delta x$  are the gas mass flow rate, the mass of the matrix material, and the time and the space differential elements, respectively. During both the heating and cooling periods, the equations are solved sequentially for each spatial and time node. The numerical scheme assumes a linear temperature distribution from  $T_h$  to  $T_c$  across the matrix. Additionally, it is assumed that the fluid enters the regenerator at  $T_h$  during the heating period and at  $T_c$  during the cooling period. The MATLAB<sup>®</sup> code computes the nodal temperatures of the matrix and gas during the heating period, see appendix A. The matrix's output spatial nodal temperatures at the end of the heating period are then used to set the matrix's input spatial nodal temperatures at the start of the cooling period, and this can be expressed mathematically as:

$$(T_m)_{1:N_x/Cooling}^1 = (T_m)_{N_x:1/Heating}^{N_t}$$

An increased number of time steps is required for the algorithm to converge to a solution. Generally, the number of spatial nodes should exceed the number of heat transfer units (NTU) [62]. The regenerator's effectiveness and inefficiency are expressed in equations 3.14 and 3.15, for balanced inlet and outlet flows, respectively.

### 3.5.1 Application of the model

The model is used to investigate the effect of changing the regenerator's dimensions (length and diameter) on its inefficiency (Ie). Secondly, it examines the effect of matrix mesh screen parameters (wire diameter and mesh size) on the regenerator's performance and efficiency. A particular case is highlighted, with the following parameters: a regenerator of 7.5 mm and 30 mm in diameter and length. The regenerator matrix mesh size is a 150 × 150 phosphorous-bronze screen; the wire diameter of the screen is 63 μm; and the screens have the same diameter as the regenerator. The mesh size and wire diameter were used in the numerical model to calculate the hydraulic diameter for the screen, the porosity, the heat transfer coefficient, and the total heat

transfer area  $A_s$ . Furthermore, if perfect stacking is assumed, the number of screens is set to 238, and the cold and hot end temperatures are assumed to be 80 K and 300 K, respectively.

### 3.5.2 2D Axisymmetric Regenerator Validation Model

This section presents a two-dimensional axisymmetric transient regenerator model to test the ideal regenerator model's validity. The CFD model was simulated using ANSYS Fluent software, which is widely used for modeling and simulating fluid flows and heat transfer in a wide variety of engineering problems. While the momentum, continuity, and energy governing equations in Fluent are not modifiable, Fluent allows users to program their own user-defined functions (UDF) and connect them to the primary model in order to modify boundary conditions, alter domain properties, or introduce variable sources or signals.

The proposed system consists of three zones: hot temperature gas zone, cold temperature gas zone, and solid porous zone. The model assumes that the hot temperature zone contracts constantly, forcing the hot gas into the regenerator. The cold temperature zone expands simultaneously to maintain a constant overall volume throughout the cooling period. Following that, the hot zone expands, and the cold zone contracts to maintain their original volumes as cold gas enters the regenerator zone from the opposite side during the heating period. The hot and cold temperature zones were created to ensure that gas entered at  $T_h$  and  $T_c$  during the cooling and heating periods.

Figure 3.8 depicts the schematic diagram for the 2D model. The dynamic mesh feature in Fluent, with C-language UDF, which defines the wall's motion, was employed to enable the simultaneous motion of the left and right walls at constant speeds. The dynamic mesh feature allows the user to create moving walls and deforming zones, making any applications involving volume contraction and expansion easily modeled. In the dynamic mesh model, the layering option was used to enable the addition or elimination of cells adjacent to a moving boundary based on the layer's height adjacent to the moving surface in rectangular mesh zones [119].

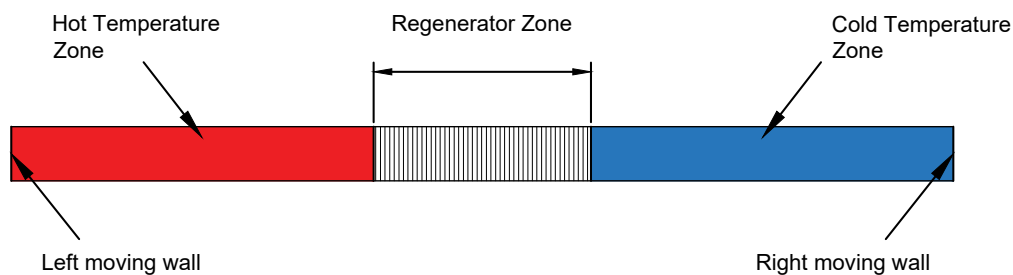


*Figure 3.8: 2-D axisymmetric regenerator Validation model schematic [117].*

The regenerator had identical dimensions to the highlighted case in section 3.5.1. The porous medium was modeled by adding a momentum source term to the standard fluid flow equations. This source term creates a pressure loss proportional to the fluid velocity, and it is composed of two terms: a viscous loss and an inertial loss term. The loss source is defined as [119]:

$$(S_i) = \frac{\Delta p}{L} = - \left( \frac{\mu v_i}{\alpha} + C_2 \frac{\rho |v| v_i}{2} \right) \quad (3.61)$$

$L$ ,  $\alpha$ ,  $C_2$ ,  $\mu$ , and  $v_i$  are the length of the regenerator, the permeability, the inertial resistance factor, the fluid viscosity, and the fluid velocity, respectively. The porous medium for this model was constructed of perfectly stacked #635 stainless steel screens with a wire diameter of 20.3  $\mu\text{m}$ . The viscous and inertial resistance factors were applied to the porous zone, and their values were utilized from [120]. Landrum et al. [120] calculated the hydrodynamic parameters of two fine-mesh screens (#325 and #635 mesh screens) by conducting experiments on steady and oscillatory flows with pressure variations across these mesh screens. They then simulated these experiments using CFD models, iteratively adjusting the viscous and inertial resistances until an agreement between the experimental results and the simulated predictions was achieved.

The calculations described here were performed using four cores Intel<sup>®</sup> Core™ i7-5500U processor at 2.4 GHz clock speed. The model's settings were axisymmetric and laminar, with helium as the working fluid. The numerical discretization schemes were second-order for the pressure, second-order upwind for both the momentum and energy, and with implicit first-order transient time formulation. The simulated flow time was 80 seconds, with a 2 ms time step size and ten iterations per time step. The space element size in the dynamic mesh zones was set carefully to avoid negative volume calculation errors.

### 3.6 Quantification of losses in the regenerator

Many of the assumptions made in the previous sections do not hold true in practical or non-ideal regenerator systems. For instance, irreversible heat transfer effects and time-dependent boundary conditions negatively affect the regenerator's thermal efficiency [62]. Additionally, various losses occur in the regenerator in practice, causing it to deviate from previous idealized assumptions and deteriorating its operation if not appropriately quantified. Ackermann [62] summarized the non-ideal effects that may occur:

- During both the heating and the cooling periods, the flow through the regenerator is not constant but rather depends on the cyclic pressure changes.
- The fluid's inlet temperature will be constant in one case only: if compression and expan-

sion occurs slowly enough to allow for reversible isothermal formation, which is not the case in a practical regenerator.

- At extremely low temperatures, the matrix material properties will not remain constant. Specifically, the specific heat of metals decreases dramatically below 40 K.
- Axial heat conduction is not negligible, which results in longitudinal heat conduction through the regenerator matrix and housing tube.

Any cryocooler's design procedure aims to maximize available refrigeration, i.e., cooling power, for a given cold end temperature,  $T_c$ . Equations 3.17, 3.18 and 3.19 demonstrate that after some losses are eliminated, the cooling power available to refrigerate a thermal load is equal to the acoustic power delivered to the cold end. The losses in a regenerator system can be classified into two types: *flow losses*, which result in a decrease in the pressure across the regenerator, thereby reducing the cooling power, and *thermal losses*, which directly result in a decrease in its thermal efficiency, thereby reducing the cooling power. The flow and thermal losses in a regenerator can be summarized as:

1. Flow losses:
  - Pressure loss through the regenerator.
  - Void volume pressure loss.
2. Thermal losses:
  - Heat loss due to conduction across the regenerator.
  - Axial thermal conduction loss along the regenerator's length.
  - Thermal loss due to a decrease in the heat capacity of the filling matrix, which is significant only at extremely low temperatures.

Before discussing each of these losses in detail, it is convenient to analyze the oscillating pressure variations along the regenerator's length using a phasor analysis. The phasor analysis, presented by Radebaugh [121] to analyze orifice pulse tube refrigerators, is not the only type of analysis developed, nor necessarily the most efficient. However, simplicity in structure, and the excellent work that has been done in this area, has delivered useful features without the complexities that come with other higher-degree analyses. Additionally, it enables developing an intuitive understanding of the types of losses that occur in a regenerator. This section conceptualizes these various losses in a practical regenerator system.

### 3.6.1 Phasor diagram of the regenerator

The fundamentals of phasor analysis must be briefly explained before presenting the phasor analysis to the regenerator. In most sinusoidal-driven engineering systems, the sinusoidal signal is represented as a phasor, drawn as an arrow in the complex plane. A sinusoidal pressure function  $P(t) = P_1 \cos(\omega t + \theta)$  is normally defined by magnitude, phase and angular frequency. In phasor form, the previous pressure signal is represented by an arrow with a length of  $P_1$  and an orientation of  $\theta$  degrees measured in the counterclockwise direction. Normally, the phasor is displayed when  $t = 0$ . Although complex arithmetic can then be applied to the phasor, it should be highlighted that phasors are not to be confused with vectors. Oscillating pressure, for example, can be represented by a phasor, yet pressure is essentially a scalar quantity. The phasor for the previous pressure sinusoid can be represented as follows:

$$\mathbf{P} = P_1 e^{j(\omega t + \theta)} \quad (3.62)$$

The time derivative of the previous phasor is:

$$\dot{\mathbf{P}} = \frac{d}{dt} P_1 e^{j(\omega t + \theta)} = j\omega P_1 e^{j(\omega t + \theta)} \quad (3.63)$$

Using Euler's formula,  $j = e^{j\pi/2}$ , the above derivative can be reduced to:

$$\dot{\mathbf{P}} = \omega P_1 e^{j(\omega t + \theta + \pi/2)} \quad (3.64)$$

Equation 3.64 shows that the phase shift between the time derivative of a sinusoidal signal and the original signal is  $90^\circ$ . Figure 3.9 illustrates the phasor representation of an oscillating sinusoidal pressure function and its derivative.

Now the phasor analysis for the regenerator element begins by applying the law of conservation of mass to the regenerator element in Figure 3.10. Assuming that the regenerator is an isothermal element, which means that while the temperature varies along its length, the regenerator spatial temperature at any cross-section is assumed to be constant, implying that the mass flow at the regenerator's hot end is proportional to the mass flow at the regenerator's cold end, and is given by:

$$\dot{m}_h = \dot{m}_c + \frac{d(\rho V_{reg})}{dt} \quad (3.65)$$

$V_{reg}$ , is the regenerator volume. Assuming a mean temperature,  $T_{mean}$  to account for the temperature gradient across the regenerator, the density,  $\rho$  can be defined as  $\rho = P/(RT_{mean})$ , where

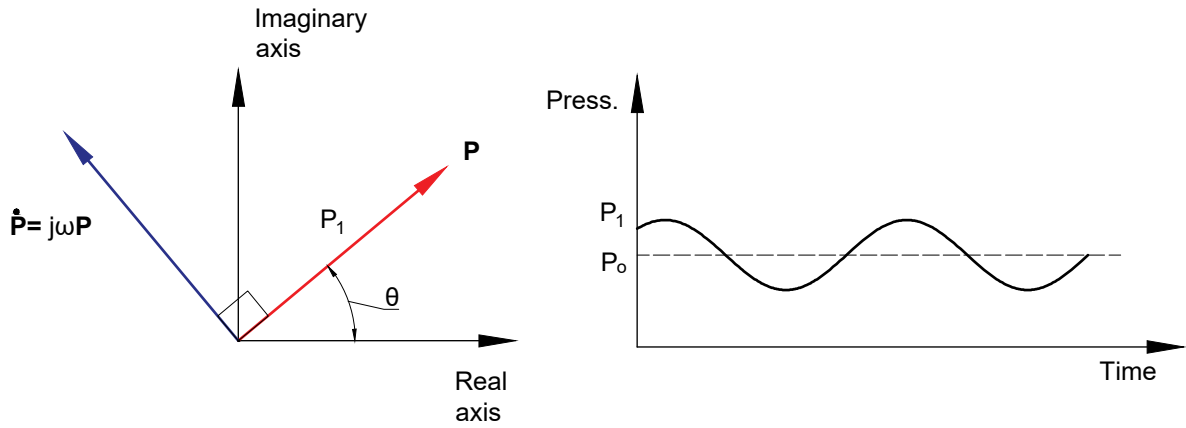


**Figure 3.9:** Phasor representation of an oscillating sinusoidal pressure signal, having an average pressure  $P_0$  and an amplitude of  $P_1$ .

R is the gas constant and P is the pressure. Equation 3.65 becomes:

$$\dot{m}_h = \dot{m}_c + \frac{V_{reg}}{RT_{mean}} \frac{dP}{dt} \quad (3.66)$$

or simply, after differentiating the sinusoidal pressure signal and using the phasor principle:

$$\dot{m}_h = \dot{m}_c + j(\omega) \frac{V_{reg}}{RT_{mean}} P = \dot{m}_c + \frac{V_{reg}}{RT_{mean}} \dot{P} \quad (3.67)$$

Equation 3.66 can be generalized for any isothermal component, assuming no pressure loss in the other pulse tube cryocooler's components, including the aftercooler, the cold heat exchanger, and the hot heat exchanger. The equation can be further expanded to cover the case of the

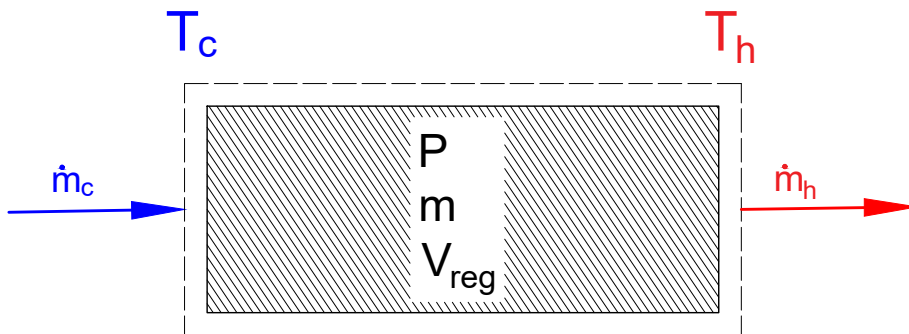


**Figure 3.10:** Schematic of the regenerator.

adiabatic element, i.e., the pulse tube, assuming:

$$P \cdot V_{ad}^\gamma = \text{constant} \quad (3.68)$$

$\gamma$  and  $V_{ad}$  is the ratio of the specific heats and the volume of adiabatic element, respectively. Differentiating equation 3.68 and taking  $V_{ad}^{\gamma-1}$  as common factor gives:

$$V_{ad}^{\gamma-1}(V_{ad} \cdot dP + \gamma P \cdot dV_{ad}) = 0 \quad (3.69)$$

since  $V_{ad}^{\gamma-1}$  is non-zero term, then [121]:

$$V_{ad} \cdot dP + \gamma P \cdot dV_{ad} = 0 \quad (3.70)$$

Assuming the gas enters the adiabatic element at  $T_c$  and exits at  $T_h$ , the following result is obtained:

$$P \cdot dV_{ad} = RT_h dm_h - RT_c dm_c \quad (3.71)$$

By substituting equation 3.71 in equation 3.70, the phasor representation of an adiabatic element is obtained:

$$\dot{m}_c = \frac{T_h}{T_c} \dot{m}_h + \frac{V_{ad}}{\gamma RT_c} \dot{P} \quad (3.72)$$

A generalized form can be deduced from equations 3.72 and 3.66, which can be rewritten to illustrate the phasor mass relation for any isothermal or adiabatic element as follows:

$$\dot{m}_{in} = \frac{T_{out}}{T_{in}} \dot{m}_{out} + \frac{V_e}{kRT_{in}} \dot{P} \quad (3.73)$$

$$\text{where, } \left\{ \begin{array}{l} (m_{in} = m_h), (m_{out} = m_c), \\ (T_{in} = T_{out} = T_{mean}), \quad \text{if element} \in \text{Isothermal} \\ (k = 1) \\ (m_{in} = m_c), (m_{out} = m_h), \\ (T_{in} = T_c), (T_{out} = T_h), \quad \text{if element} \in \text{Adiabatic} \\ (k = \gamma) \end{array} \right.$$

$V_e$ ,  $\dot{m}_{in}$  and  $\dot{m}_{out}$  are the volume of the element, the mass flow entering the element at temper-

ature  $T_{in}$ , and the mass flow leaving the element at  $T_{out}$ , respectively. Figure 3.11a shows the general phasor representation for any thermodynamic element.

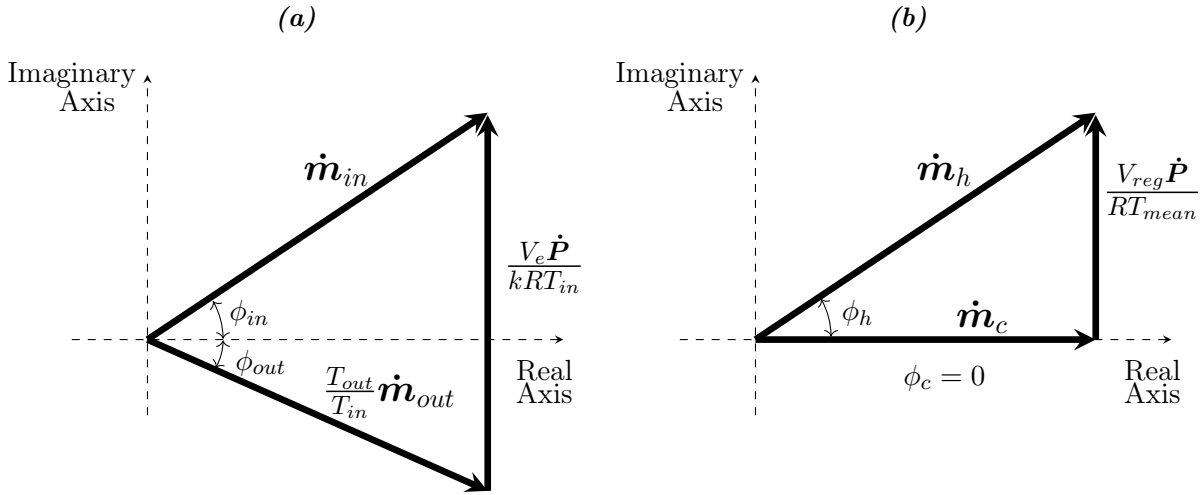


**Figure 3.11:** (a) General phasor representation of the mass flow rates in thermodynamic components of the pulse tube system as illustrated in equation 3.73. (b) Phasor representation of the mass flow rates in a regenerator for maximum cooling power.

There should be good heat exchange between the gas and the matrix for an efficient regenerator operation. According to equation 3.65, when the pressure in the regenerator is sinusoidal, and the cold end's mass flow rate is constant,  $\dot{m}_c$ , the hot end's mass flow rate increases when either the gas volume in the regenerator,  $V_{reg}$ , or the operating frequency,  $f$ , is increased. However, increasing the regenerator's volume requires a significantly larger swept volume and a larger compressor to drive the system. The second drawback is the need for a larger heat transfer area to compensate for increased mass flow to maintain efficient heat exchange, increasing the pressure loss. These two results would, eventually, deteriorate the overall efficiency of the whole system. The desired scenario is to have a small gas volume associated with a high heat exchange efficiency while still accounting for minimal pressure loss. This occurs when the pressure is in phase with the mass flow just at the regenerator's center. Hence, the mass flow magnitude is minimised. For this optimal phase relationship case, the flow at the cold end should lag the pressure by about  $30^\circ$ , and the flow at the hot end should lead the pressure by about  $30^\circ$ , according to [122]. Figure 3.11b shows the phasor notation for the mass flow rates in the regenerator for maximum cooling power. Typically, orifice pulse tube cryocoolers have positive values of  $\phi_c$  [123].

In contrast to Stirling cryocoolers, where this condition is easily satisfied by selecting the appropriate swept volume and phase for the displacer. Pulse tube cryocoolers satisfy this condition solely by adding an orifice or other phase-shifting components. In general, an orifice results in a phase shift of approximately  $30^\circ$  at the cold end,  $50^\circ$  or more at the regenerator's midpoint,

and up to  $70^\circ$  at the regenerator's hot end [122]. As a result of this scenario, the mass flow and swept volume will increase, leading to more input acoustic power and lowering the system efficiency. Instead, introducing a proper inertance tube at the hot end of the pulse-tube would satisfy the condition for pulse tube cryocoolers [122]. The inertance tube utilizes the inertia of the oscillating flow to bring about a phase shift between the flow and the pressure [4]. A detailed discussion of various phase shift mechanisms is presented in section 4.3.2.

Figure 3.12 illustrates the regenerator losses as a function of the phase angle between the flow and the pressure for several cryocooler types. The results were calculated using the NIST numerical regenerator model tool, REGEN3.2 [124].  $\dot{S}_{reg}$ ,  $\dot{S}_{\Delta P}$  and  $\dot{S}_{total}$  are the entropy flow for the regenerator ineffectiveness loss, the pressure loss and the total loss, respectively. Radebaugh et al. [122] suggested that for small pulse tube cryocoolers with small inertance mass flow, the phase shift may be only a few degrees. Hence, to achieve the optimum phase angle of flow lagging pressure by about  $30^\circ$  at the cold end means that the *inertance tube flow will need to lag the pressure at its inlet by nearly  $60^\circ$  to compensate for the change in phase across the pulse tube.*

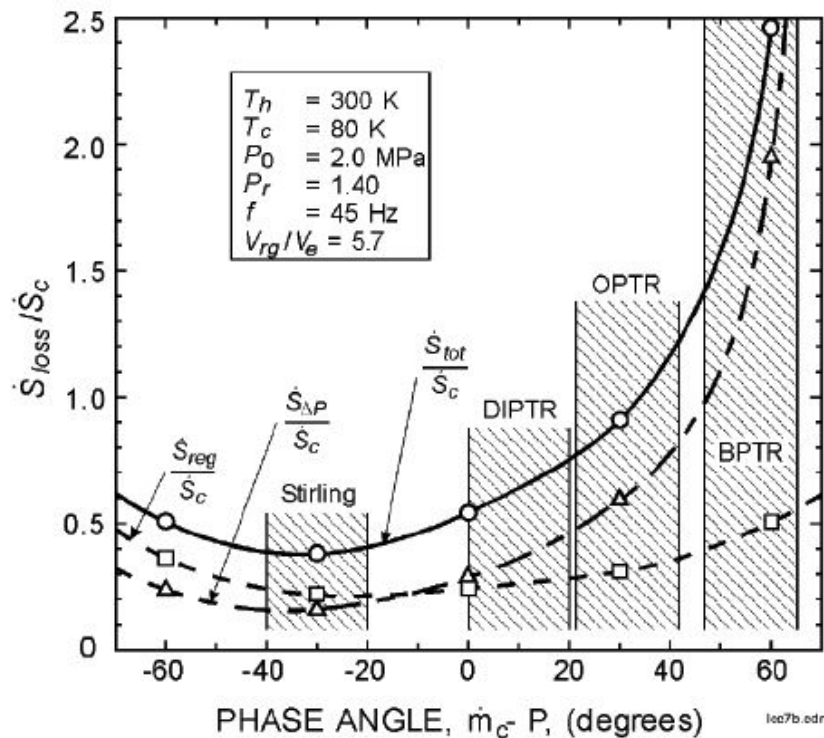


**Figure 3.12:** Regenerator losses associated with ineffectiveness and pressure loss for various phase angles and for several cryocooler types. DIPTR, OPTR, BPTR refers to double inlet, orifice and basic pulse-tube refrigerator respectively. Reproduced from [122], with the permission of AIP Publishing.

### 3.6.2 Pressure loss

Pressure loss was discussed in section 3.4.4.3, where equation 3.58 illustrates the pressure loss,  $\Delta p$ , for a gas flowing through a channel or screen matrix. The pressure loss represents the cooling power wasted as a result of the pressure difference between compression and expansion. One significant study is to examine the correlations between friction factors for various regenerator filling materials and geometry. Radebaugh et al. [125] studied and compared several different geometries in terms of the ratio between heat transfer and pressure loss. Rühlich et al. [126] investigated the shapes and arrangements of matrix elements and calculated the pressure loss to heat transfer ratio for a variety of filling matrix geometries. They came up with the concept "number of pressure heads" (NPH) to refer to the pressure loss along a given length of the regenerator. NPH is defined as follows [126]:

$$\text{NPH} = \frac{\Delta p}{\frac{1}{2\rho} \left( \frac{\bar{m}}{A_{ff}} \right)^2} = \frac{fL}{D_h} \quad (3.74)$$

The pressure loss in equation 3.58 does not associate the pressure loss to the heat transfer, which is beneficial for optimizing the regenerator. Kays and London [113] came up with a geometric correlation factor ( $\Gamma$ ) that relates the dimensionless Stanton and Prandtl numbers to the friction factor.

$$\Gamma = \frac{\text{St} \text{Pr}^{(2/3)}}{fr} = \frac{2(\text{NTU}) \text{Pr}^{(2/3)}}{fr} \left( \frac{r_h}{L} \right) \quad (3.75)$$

where NTU relates to St by:

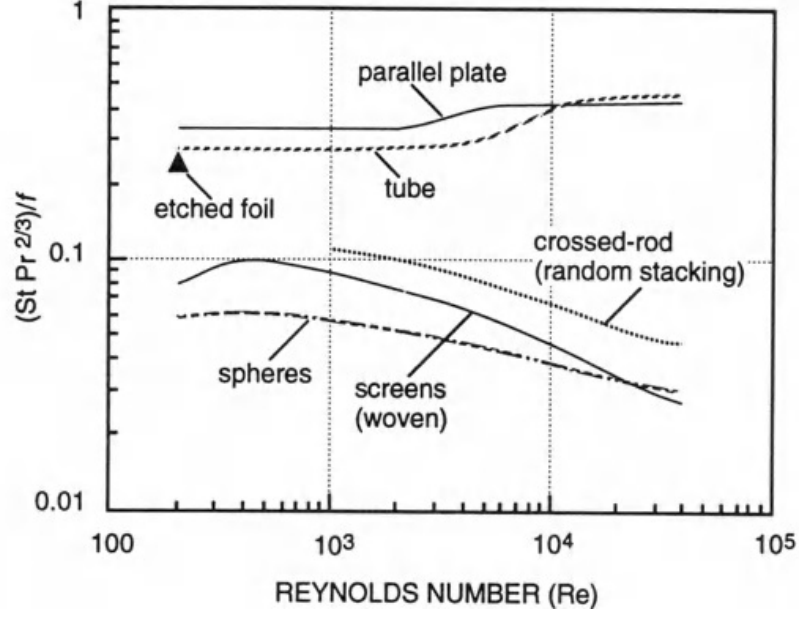
$$\text{NTU} = \frac{\text{St} L}{2r_h} \quad (3.76)$$

Figure 3.13 shows the relation between this correlation factor ( $\Gamma$ ) and the Reynolds number for different filling geometries. Substituting,  $\Gamma$ , in the pressure loss in equation 3.58 results in the modified frictional pressure loss equation in terms of the NTU and the geometric factor:

$$\Delta p = \frac{(\text{NTU}) \text{Pr}^{(2/3)}}{(\Gamma) \bar{\rho}_f} \left( \frac{\bar{m}}{A_{ff}} \right)^2 \quad (3.77)$$

### 3.6.3 Void volume pressure loss

The void volume pressure loss is defined as the difference between the pressure without the void volume and the pressure with the void volume. Assuming no gas volume at the cold end, the phase between pressure and mass flow at the cold end,  $\phi_c$  would be zero. This scenario corresponds to the maximum cooling power condition in Figure 3.11b. However, the presence of



**Figure 3.13:** Relation between the geometric correlation factor ( $\Gamma$ ) and Reynolds number for several filling geometries [62].

the gas volume,  $V_{r,g}$  in the regenerator would make the flow lag the pressure by  $\phi_c$ . Thus, the ratio of the loss in the acoustic power due to void volume pressure loss:

$$\frac{\dot{W}_{ac,loss}}{\dot{W}_{ac}} = 1 - \frac{\dot{W}_{ac,c}}{\dot{W}_{ac}} = \frac{\dot{W}_{ac} - \dot{W}_{ac} \cos(\phi_c)}{\dot{W}_{ac}} = 1 - \cos(\phi_c) \quad (3.78)$$

Assuming the regenerator is isothermal and applying trigonometry to Figure 3.11a and by assuming balanced flows and the pressure is in-phase with the mass flow rate at the middle of the regenerator, the sine and cosine of the angle,  $\phi_c$ , can be found, and hence the void volume loss can be expressed as:

$$\frac{\dot{W}_{ac,loss}}{\dot{W}_{ac}} = 1 - \sqrt{1 - \left( \frac{\omega V_{r,v} P_1}{2R\dot{m}_c T_{mean}} \right)^2} = 1 - \sqrt{1 - \left( \frac{\pi f P_1}{RT_{mean}} \right)^2 \left( \frac{A_{ff} L_{reg}}{\dot{m}_c} \right)^2} \quad (3.79)$$

### 3.6.4 Axial heat conduction loss

In practice, the matrix and the regenerator's tube conduct heat, resulting in axial heat conduction loss. This occurs as a result of the solid conduction path formed by the physical contact of the matrix's layers. Axial conduction loss is quantified in terms of the matrix cross-sectional area  $A_m$ , the regenerator length  $L_{reg}$ , the matrix thermal conductivity  $K_m$ , and the temperature gradient across the regenerator. The axial heat conduction loss is expressed as:

$$\dot{Q}_{c,loss} = \frac{A_m}{L} \int_{T_c}^{T_h} K_m dT = \frac{(1 - \phi_m) A_{reg}}{L_{reg}} \int_{T_c}^{T_h} K_m dT \quad (3.80)$$

where  $\phi_m$  is the matrix porosity. For wire screens, the axial conduction for many commonly used matrix materials is governed primarily by the interfacial resistance between screens [62]. Generally, the thermal conductivity should be corrected to include the interfacial contact between the regenerator material [127]. Ackermann [128] carried out thermal conductivity tests, which were carried out to evaluate the thermal conductance through the matrix material as a function of packing density, and suggested that the thermal conductivity, for bronze screens, can be represented as:

$$\bar{K}_m = 0.7 \frac{T_m}{300} \quad (3.81)$$

Thus, the thermal conduction can be expressed in terms of the average thermal conductivity,  $\bar{K}_m$  for the temperature range from 80 to 300 K as follows:

$$\dot{Q}_{c,loss} = \bar{K}_m \frac{(1 - \phi_m) A_{reg}}{L} (T_h - T_c) = \bar{K}_m \frac{(1 - \phi_m) A_{ff}}{\phi_m L} (T_h - T_c) \quad (3.82)$$

Equation 3.82 shows that the conduction losses increase with the cross-sectional area and decrease with the regenerator's length.

### 3.6.5 Regenerator thermal loss

The effectiveness and inefficiency of a regenerator were previously defined in section 3.2.9. Kays and London [113] provided the expression for inefficiency ( $I_e$ ), in which they related the NTU to inefficiency ( $I_e$ ). They used Lambertson's [129], and Bahnke and Howard's [130] data to determine the relationship between inefficiency and NTU for periodic-flow type heat exchangers. They found that efficiency can be expressed as a function of both NTU and the heat capacity ratio of the matrix and the flowing gas through the regenerator:

$$\epsilon = f \left( \text{NTU}, \frac{C_{min}}{C_{max}}, \frac{C_s}{C_{min}} \right) \quad (3.83)$$

NTU and heat capacity ratios definitions can be found in section 3.2. Bahnke [130] concluded that at temperatures higher than 80 K, the regenerator's performance is almost identical to that of a recuperative heat exchanger, and the inefficiency can be reduced to a function of NTU. Figure 3.14 illustrates these relation results for different heat capacity ratios. The thermal loss of a regenerator can be defined by the regenerator's effectiveness ( $I_e$ ) and the enthalpy flow caused by the temperature difference across the regenerator. Hence, the thermal loss of a regenerator can be summarized as [62]:

$$\dot{Q}_{Th,loss} = (I_e) \bar{m} c_p (T_h - T_c) \quad (3.84)$$

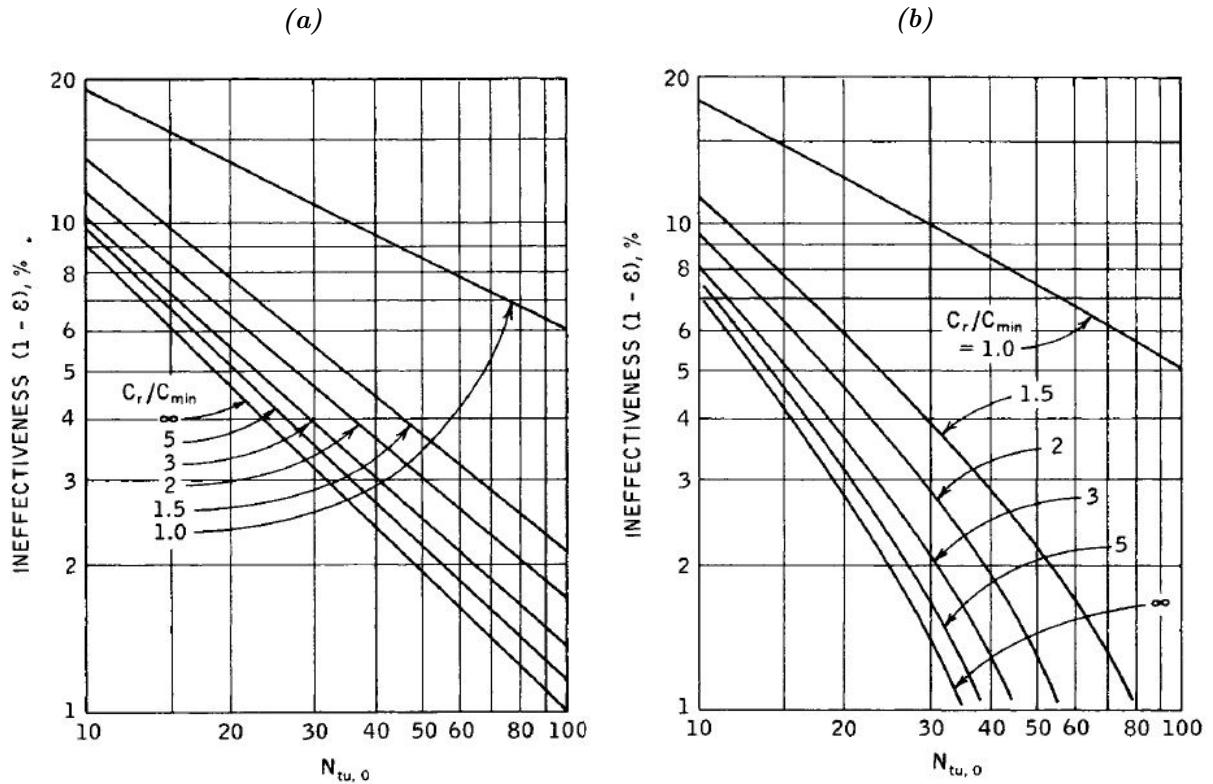


**Figure 3.14:** (a) Thermal conduction Inefficiency ( $I_e$ ) relative to the number of transfer units and matrix capacity-rate ratio of  $\left(\frac{C_{min}}{C_{max}} = 1\right)$ . (b) Thermal conduction Inefficiency ( $I_e$ ) relative to the number of transfer units and matrix capacity-rate ratio of  $\left(\frac{C_{min}}{C_{max}} = 0.95\right)$  [113].

### 3.7 Losses and regenerator's optimisation

In the previous sections, the regenerator's losses were summarized in equations 3.77, 3.79, 3.82, and 3.84. Minimizing these losses is necessary for optimizing the operation of the regenerator, and consequently the cryocooler as a whole. Unfortunately, reducing one form of loss leads to an increase in another. For instance, equation 3.77 suggests that in order to minimize pressure loss for a given regenerator's geometry, the number of heat exchangers (NTU) should be reduced, but this would increase the regenerator's thermal loss in equation 3.84 due to the resulting increased inefficiency ( $I_e$ ), as illustrated in Figure 3.14. Similarly, reducing the regenerator's length reduces the void volume loss in equation 3.79 but increases the heat conduction loss in equation 3.82.

For the matrix material, decreasing the hydraulic diameter increases the pressure loss in equation 3.58. However, increasing the hydraulic diameter increases the regenerator's void volume loss, and decreasing the total heat transfer area, which results in increasing the regenerator's

inefficiency and, thus, increased thermal loss as well. Moreover, increasing the ratio between the cross-sectional area and the mass flow rate, i.e. the specific area, would increase the conduction losses in equation 3.82 and the void volume loss in equation 3.79. In contrast, reducing the specific area, i.e. increasing  $\bar{m}$  and reducing  $A_{ff}$  would increase the pressure loss in equation 3.77, and the thermal loss in equation 3.84.

The optimization procedure begins by determining the regenerator's parameters, such as length, cross-sectional area, matrix geometry, matrix material, and porosity, that are necessary for optimizing cooling power and other operating parameters. Following that, the total losses are minimized iteratively. These losses include those caused by axial heat conduction, pressure, void volume, and the regenerator's thermal loss. Then, a trade-off between these losses should be made by adjusting the regenerator's parameters to minimize significant dominant losses.

To mitigate these contradictory optimization requirements for a cryogenic regenerator, a procedure is proposed for optimizing the regenerator's operation over the temperature range of 300 K to 80 K for a given operating frequency. The optimization's objective is to maximize cooling power for a given set of regenerator parameters, such as length, area, and matrix properties. The net cooling power of a cryocooler system can be expressed as the sum of the gross cooling power and all other losses in the system; this can be expressed as:

$$Q_{Net} = W_{PV} - (W_{\Delta p} + W_{ac,loss} + Q_{c,loss} + Q_{Th,loss} + \Sigma Q_{Others}) \quad (3.85)$$

$\Sigma Q_{Others}$  are the other losses associated with the other cryocooler's components. It is more convenient to represent the losses in fractional form relative to the acoustic power,  $W_{PV}$ , to obtain the unitless equation that defines the fractions of losses, as follows:

$$\frac{Q_{Net}}{W_{PV}} + \frac{W_{\Delta p}}{W_{PV}} + \frac{W_{ac,loss}}{W_{PV}} + \frac{Q_{c,loss}}{W_{PV}} + \frac{Q_{Th,loss}}{W_{PV}} + \frac{\Sigma Q_{Others}}{W_{PV}} = 1 \quad (3.86)$$

$W_{PV}$  is the acoustic expansion power and is equal to:

$$W_{PV} = \bar{m}q_f\lambda_c \quad (3.87)$$

$\lambda_c$ , is the cooling period, and  $q_f$  is the heat transferred to the ideal working gas during the isothermal compression and expansion processes and can be expressed as:

$$q_f = RT_c \ln \left( \frac{P_0 + P_1}{P_0 - P_1} \right)$$

### 3.7.1 Optimization of regenerator for 1 watt cooling power

This section provides an analytic approach that aims to optimize the regenerator operation for a net cooling power of 1 watt. This value is suggested to size the system for other desired cooling powers. The procedure represents the best case scenario as it does not include other losses in the other components. The constraints for this optimization procedure that is imposed on the cryocooler design are as follows:

1. The regenerator has a temperature gradient of 300 to 80 K.
2. The operating frequency of the cryocooler is 20 Hz.
3. A sinusoidal pressure wave with a mean operating pressure of 3 MPa and a peak pressure of 3.5 MPa is supplied by the compressor.

Table 3.1 lists the optimization process's operating parameters and properties. The optimization procedure begins by assuming initial rough estimates for the various regenerator losses. Table 3.2 contains the estimated values for the regenerator losses fractions. The procedure carry on with calculating the ratio between the void,  $V_{r,v}$  volume and the expansion volume amplitude,  $V_1$  using equation 3.79. The mass flow rate through the regenerator can be calculated by equation 3.87. Hence, the ratio between the void volume and the swept volume,  $V_{r,v}/V_1$ , can be found by equation 3.79:

$$\frac{V_{r,v}}{V_1} = \frac{\sqrt{1 - \left(1 - \frac{W_{ac,loss}}{\dot{W}_{ac}}\right)^2 (T_{mean})}}{T_c \ln\left(\frac{P_0 + P_1}{P_0 - P_1}\right)} = 4.668$$

By substituting the value  $(W_{PV} = \frac{W_{Net}}{0.15})$  from Table 3.2 into equation 3.87, and since the refrigeration in a regenerative cycle cryocooler only occurs during one-half of the cycle, the average mass flow rate through the regenerator during each period is as follows:

$$\bar{m} = \frac{W_{Net}}{(0.15)RT_c \ln\left(\frac{P_0 + P_1}{P_0 - P_1}\right)} = 0.238 \text{ g/s}$$

The expansion volume amplitude can be found using equation 3.17

$$V_1 = \frac{W_{Net}}{(0.15)(\pi f)P_1 \cos(\theta_{ph})} = 0.245 \text{ cm}^3 \quad (\text{Assuming } \theta_{ph} = 30^\circ)$$

Thus, the regenerator's void volume can be determined from the previous ratio, and thus the regenerator's volume:

$$V_{reg} = \frac{V_{r,v}}{\phi_m} = \frac{(4.668)(V_1)}{\phi_m} = 1.76 \text{ cm}^3$$

**Table 3.1:** Regenerator Design parameters

Parameter	Value
<b>Operating Parameters</b>	
Working fluid	Helium
Hot temperature, $T_h$	300 K
Cold temperature, $T_c$	80 K
Net cooling, $W_{net}$	1 W
Operating frequency, $f$	20 Hz
Filling material	Bronze wire screen
screen wire diameter, $d_w$	0.05 mm
Average pressure, $P_0$	3 MPa
Pressure Amplitude, $P_0$	0.5 MPa
<b>Fluid and matrix properties</b>	
Gas constant, $R$	2080 J/kg.K
Matrix porosity, $\phi_m$	0.65
Matrix density, $\rho_m$	8700 kg/m <sup>3</sup>
Matrix specific heat, $c_{pm}$	300 J/kg.K
Matrix mean thermal conductivity, $\bar{k}_m$	0.76 W/m.K
Mean helium density, $\rho_f$	10.8 kg/m <sup>3</sup>
Helium specific heat, $c_{pf}$	5200 J/kg.K
Helium mean thermal conductivity, $\bar{k}_f$	0.1 W/m.K
Helium mean viscosity, $\bar{\mu}_f$	$14.4 \times 10^{-6}$ kg/m.s

**Table 3.2:** Assumption for the fractional losses in PTC cryocooler.

Unitless fractional losses	Value
Pressure loss $\left(\frac{W_{\Delta p}}{W_{PV}}\right)$	0.1
Void volume pressure loss $\left(\frac{W_{ac,loss}}{W_{PV}}\right)$	0.25
Axial heat conduction loss $\left(\frac{Q_{c,loss}}{W_{PV}}\right)$	0.05
Thermal loss $\left(\frac{Q_{Th,loss}}{W_{PV}}\right)$	0.2
Other losses $\left(\frac{\Sigma Q_{Others}}{W_{PV}}\right)$	0.25
Total losses	0.85
Net cooling $\left(\frac{W_{Net}}{W_{PV}}\right)$	0.15

If the ratio of the regenerator's diameter to its length  $\frac{L_{reg}}{D_{reg}}$  is set to three, then the regenerator's geometric parameters are as follows:

$$D_{reg} = 0.907 \text{ cm}$$

$$L_{reg} = 2.7 \text{ cm}$$

$$A_{reg} = 0.65 \text{ cm}^2$$

$D_{reg}$ ,  $L_{reg}$ , and  $A_{reg}$  are the diameter, length and area for the regenerator housing, respectively. The volume and mass of the matrix can be calculated as follows:

$$V_m = (1 - \phi_m)V_{reg} = 0.617 \text{ cm}^3$$

$$M_m = (\rho_{mat})V_{mat} = 5.4 \text{ g} \quad (\text{Bronze mesh screen, } \rho_m = 8.7\text{g/cm}^3)$$

The mass flow rate per unit area  $G$  is:

$$G = \frac{\bar{m}}{A_{ff}} = \frac{\bar{m}}{\phi_m A_{reg}} = 0.56 \text{ g/(cm}^2 \cdot \text{s)}$$

Based on the assumption of perfect stacking, the hydraulic diameter of the matrix wire can be calculated using the following formula:

$$D_h = \frac{\phi_m d_w}{(1 - \phi_m)} = 0.092 \text{ mm} \quad (\text{Assuming, } d_w = 0.05 \text{ mm})$$

$d_w$  is the diameter of the wire. The Reynolds and Prandtl numbers are as follows:

$$Re = \frac{GD_h}{\mu} = 37$$

$$Pr = \frac{c_p \mu}{K_f} = 0.75$$

$\mu$ ,  $c_p$ , and  $K_f$  are the viscosity of the working fluid, the gas-specific heat, and the mean thermal conductivity for the working fluid, respectively. Stanton number is derived from Kays and London's experimental data [113]:

$$StPr^{2/3} = 0.68Re^{-0.4}; \quad St = 0.195$$

The number of heat transfer units (NTU) is then evaluated from equation 3.76 to be 114. Additionally, the matrix capacity ratio can be determined using equation 3.4:

$$\text{Solid capacity ratio } (C_s) = \frac{(Mc_p)_s}{\lambda(\dot{m}c_p)_{min}} = 51.7$$

The inefficiency (Ie) of the system can be determined using the ideal regenerator analysis presented in the preceding section. The thermal loss of the regenerator can be calculated using equation 3.84:

$$\dot{Q}_{Th,loss} = (Ie)\bar{m}c_p(T_h - T_c) = 1.97 \text{ W}$$

From equation 3.82, the axial conduction loss is calculated:

$$\dot{Q}_{c,loss} = \bar{k}_m \frac{(1 - \phi_m) A_{reg}}{L} (T_h - T_c) = 0.14 \text{ W} \quad (3.90)$$

After estimating the friction factor  $\Gamma$  from Figure 3.13, the pressure loss is calculated by equation 3.77 as follows:

$$\frac{W_{\Delta p}}{W_{PV}} = \frac{\Delta p}{P_1} = 0.029$$

Table 3.3 shows a comparison between the calculated and initially assumed losses. The dominant loss is the regenerator's thermal loss caused by the regenerator's low NTU number and short length. By increasing the tube length to 3.5 cm, the NTU increases to 148, the matrix capacity ratio increases to 67, and the void volume ratio increases to 6. The significant change in net losses, primarily due to doubling the void volume losses, demonstrates that the regenerator is nearly designed with optimal geometrical parameters for the previously mentioned operating conditions.

### 3.7.2 Sizing of the regenerator

After optimizing the regenerator, the system can be sized proportionally with the new cooling power,  $\dot{Q}_{net}^\dagger$ , with respect to the reference net cooling power,  $\dot{Q}_{net}^*$ , to find the operating and geometrical parameters for the new regenerator element. These new parameters can be summarized as:

$$\dot{W}_{PV}^\dagger = \frac{\dot{Q}_{net}^\dagger}{\dot{Q}_{net}^*} \dot{W}_{PV}^* \quad (3.91)$$

$$\dot{m}^\dagger = \frac{\dot{Q}_{net}^\dagger}{\dot{Q}_{net}^*} \dot{m}^* \quad (3.92)$$

$$V_1^\dagger = \frac{\dot{Q}_{net}^\dagger}{\dot{Q}_{net}^*} V_1^* \quad (3.93)$$

**Table 3.3:** Calculated and initial assumed regenerator's losses

Fractional loss	Calculated Value (W)	Calculated Value (W) ( $L = 3.5 \text{ cm}$ )	Assumed Value (W)
Pressure loss	0.19 W	0.24 W	0.667 W
Void volume pressure loss	1.667 W	3.16 W	1.667 W
Axial heat conduction loss	0.14 W	0.11 W	0.33 W
Thermal loss	1.97 W	1.55 W	1.33 W
Total losses	3.97 W	5.06 W	4 W
Net cooling	1 W	1 W	1 W

$\dot{W}_{PV}^\dagger$ ,  $\dot{m}^\dagger$  and  $V_1^\dagger$  are the scaled acoustic power, mass flow and the volume amplitude for the new regenerator. The discussion concludes by presenting the axial conduction loss along the regenerator tube wall's cross-sectional area,  $A_w$ , is equal to:

$$\dot{Q}_{c,wall} = \frac{A_w}{L_{reg}} \int_{T_c}^{T_h} k_t dT = k_t \frac{A_w}{L_{reg}} (T_h - T_c) \quad (3.94)$$

$k_t$  is the thermal conductivity for the regenerator's tube. The area of the tube wall,  $A_w$  can be simplified to  $A_w = \pi(D_{reg}t_{reg})$ , assuming the diameter of the regenerator tube,  $D_{reg}$  is much larger than the tube thickness,  $t_{reg}$ . For stainless steel with a yield strength of ( $\sigma_y = 250$  MPa), the thickness of the regenerator tube,  $t_{reg}$ , in terms of the maximum tensile strength of the material is:

$$t_{reg} = (SF) \frac{(P_0 + P_1)d_{reg}}{2\sigma_y} \quad (3.95)$$

$SF$  is the safety factor that usually introduced in the design to account for the oscillatory flow's dynamic behavior. However, the tube's thickness should be kept as small as possible to minimize heat conduction losses. Utilizing materials with a higher yield strength (such as titanium) will reduce the tube's thickness.

### 3.7.3 Numerical optimisation of the regenerator using REGEN3.3

Although phasor and losses analysis described in the previous sections provided good intuition into the effect of operating conditions and geometrical parameters on the performance of the regenerator. Numerical analyses of critical components, such as the regenerator, are required to develop more efficient pulse tube cryocoolers and replace potentially conventional concepts in existing or emerging application fields. These numerical analyses, in particular, are critical for providing a more accurate interpretation of the thermal interaction between the working gas and the regenerator matrix material.

Radebaugh [125] introduced an optimization procedure for designing regenerators. Many researchers used the REGEN software developed at the National Institute of Standards and Technologies (NIST) to study the regenerator performance for different matrix materials [131]. The REGEN tool was used extensively to design regenerative cryocoolers. It was employed to optimize the regenerative heat exchangers' geometry and operating parameters for a desired cooling power and cold end temperature [14, 132–134]. Among these studies, the predicted performance of a regenerative cryocooler was experimentally validated [133].

The model in REGEN3.2 assumes sinusoidal mass flow at both ends of the regenerator, where the incoming gas temperature for both ends and the gas pressure are initially stated. Moreover,

the initial temperature profile is generally considered a linear profile. Further, the model sets the amplitude, frequency, and phase of the mass flow at both ends as input parameters. However, the equation used to describe the flow is not the conservation equation but rather a predictive equation for pressure. Additionally, the gas velocity for all mesh cells is calculated simultaneously by solving a non-linear system; the remaining variables at each mesh cell are advanced in time explicitly. Hence, the model numerical approximation is considered semi-implicit [135]. REGEN3.3 is referred to as a fully implicit model; since the numerical approximation involves discretization of the conservation of mass, momentum, and energy differential equations, whereas the non-linear system of equations for temperature, pressure, and mass flow at all mesh points are solved simultaneously by Newton iteration [135].

Other available software packages, including Sage<sup>®</sup> and DELTAE<sup>®</sup>, which solve the conservation equations and hence describe the regenerator performance, are also often used. These numerical analyses have a range of complexity levels that depend on the assumptions employed and the degree of freedom used. For all complexity levels, the design parameters of the regenerator, such as its diameter-to-length ratio, physical dimensions, pore structure, and matrix material parameters, affect the overall performance of any regenerative cryocooler. Typically, these parameters have been designed or optimized empirically, using relatively crude lumped parameter considerations or the results of dimensional analysis. However, more complex numerical models should account for pressure loss, void volume, conduction losses, pressure variations, time-varying mass flow rates, time-varying inlet gas temperature, and temperature-dependent thermal properties.

REGEN3.3 is used to numerically optimize the regenerator. The software solves conservation equations that satisfy the input conditions, where the parameters for the input conditions are as follows:

1. The average pressure and the pressure ratio along with frequency of the oscillation.
2. Mass flow rate at the cold end, and the phase of the mass flow relative to the pressure at the cold end.
3. The geometrical parameters of the regenerator matrix, i.e. hydraulic diameter, material, porosity, and the type of the matrix (parallel plates, parallel tubes, spherical pellets). of the matrix).
4. The hot and cold end temperatures.

The software calculates the losses in the regenerator, including thermal loss due to ineffectiveness, axial conduction loss, and pressure loss. In this study, Stainless steel was chosen as the

filling material since Lewis and Radebaugh [127] compared the regenerator losses of various filling materials and determined that stainless steel is an excellent choice for a regenerator filler at this temperature range. Additionally, they examined the degradation of the thermal conductivity factor and proposed that it be corrected to account for the matrix type when calculating the matrix axial conduction loss. The contact affects the thermal conductivity of the filling material [127], and this new effective conductivity is typically less than that of the solid material.

Numerous studies have been identified in the literature [136–138] that conducted a comprehensive parametric study utilizing the most recent version of the regenerator design software tool, REGEN3.3. Pfothenauer et al. [138] surveyed over 10,000 cases of input combinations for the regenerator length, cross-sectional area, mass flux at the cold end, frequency, and cold end temperature. They processed the data to present equations, as a function of temperature and frequency, for the regenerator length, free-flow cross-sectional area to mass at cold end ratio  $A_g/\dot{m}_c$ , and phase angle. These parameters were used to obtain the optimum coefficient of performance (COP) that can be attained for regenerators operating with a typical average pressure of 2 MPa, and a dynamic pressure ratio of 1.2 [138].

Samples of the regenerator geometry optimization runs for various frequencies are shown in Table 3.5. The operating parameters for these runs are shown in Table 3.4. The first run is the same case scenario as discussed in section 3.7.1, where it can be seen that the net cooling power is close to 1 watt. However, the COP is low since the regenerator output power and associated losses were roughly estimated. By utilizing fine mesh screens with higher mesh numbers, the hydraulic diameter is reduced. It was observed that the COP is significantly increased when a smaller hydraulic diameter, i.e.,  $32\ \mu\text{m}$ , is used, that is associated with a 600-mesh screen matrix, which agrees with what was suggested by Wang et al. [139].

**Table 3.4:** *Operating Parameters for REGEN3.3 runs*

Parameter	Value
Average pressure	3 MPa
Pressure ratio	1.4
Matrix Porosity	0.6
Cold end temperature ( $T_c$ )	80 K
Hot end temperature ( $T_h$ )	300 K
Regenerator shell thickness	0.21 mm
Matrix conduction degradation factor	0.18

The study suggests that a regenerator length of 3 cm and a cross-sectional area of  $0.65\ \text{cm}^2$  would provide optimum COP. However, it reveals clearly that slight variation in these parameters would only reduce the COP by minor factors. The runs suggest that operating the regenerator at

higher frequencies for these operating parameters would increase the losses due to the increase in the mass flow caused by the larger buffered mass flow. As a result, the high-frequency operation is only preferred when the gas volume is small, requiring higher average pressure and finer mesh size.

Table 3.5: Sample of cooling power and performance Results from REGEN3.3 for different regenerator parameters.

#	$f$ (Hz)	$L_{reg}$ (cm)	$A_{reg}$ (cm <sup>2</sup> )	$\dot{m}_c$ (g/s)	$D_h$ ( $\mu$ m)	$W_{PV,h}$ (W)	$W_{PV,c}$ (W)	$\dot{Q}_{net}$ (W)	COP	Losses (W)			
										$\dot{Q}_{c,wall}$	$\dot{Q}_{c,loss}$	$\dot{Q}_{Th,loss}$	$W_{\Delta p}$
001	20	2.7	0.65	0.373	92	12.46	4.70	1.32	0.0847	0.548	0.538	2.08	0.21
002	20	2.7	0.65	0.373	92	16.64	4.70	2.16	0.1297	0.552	0.206	1.55	0.24
003	20	2.7	0.65	0.373	62	16.80	4.70	2.63	0.1565	0.555	0.206	1.11	0.21
004	20	2.7	0.65	0.373	32	17.46	4.70	2.99	0.1714	0.558	0.205	0.71	0.23
005	20	2.7	0.65	0.5	32	24.16	6.30	4.22	0.1749	0.557	0.218	0.95	0.35
006	20	2.0	0.65	0.5	32	23.64	6.30	3.69	0.1563	0.751	0.284	1.22	0.35
007	20	3.0	0.65	0.5	32	24.37	6.30	4.37	0.1797	0.502	0.196	0.89	0.34
008	20	4.0	0.65	0.5	32	25.13	6.30	4.70	0.1874	0.377	0.151	0.72	0.35
009	20	5.0	0.65	0.5	32	25.97	6.30	4.89	0.1886	0.302	0.123	0.65	0.33
010	20	6.0	0.65	0.5	32	27.03	6.30	5.01	0.1855	0.253	0.107	0.56	0.37
011	20	8.0	0.65	0.5	32	29.93	6.30	5.15	0.1722	0.191	0.087	0.47	0.40
012	20	6.7	0.65	0.312	32	17.04	3.94	3.04	0.1782	0.227	0.123	0.373	0.18
013	20	6.7	3.94	1.1	32	84.65	13.06	9.94	0.1175	0.514	0.307	1.199	1.09
014	20	6.7	2.21	0.643	32	42.3	6.63	4.96	0.1172	0.385	0.185	0.553	0.54
015	20	6.7	1.42	0.41	32	10.98	1.58	0.57	0.052	0.340	0.472	0.137	0.068
016	20	3.0	0.65	0.65	32	32.84	8.199	5.86	0.1784	0.506	0.138	1.25	0.441
017	20	3.0	0.65	0.45	32	21.72	5.67	3.86	0.1781	0.508	0.184	0.813	0.303
018	40	3.0	0.65	0.45	32	22.16	5.67	3.87	0.1750	0.510	0.241	0.804	0.243

Table 3.5: Continued...

#	$f$ (Hz)	$L_{reg}$ (cm)	$A_{reg}$ (cm <sup>2</sup> )	$\dot{m}_c$ (g/s)	$D_h$ ( $\mu$ m)	$W_{PV,h}$ (W)	$W_{PV,c}$ (W)	$\dot{Q}_{net}$ (W)	COP	Losses (W)			
										$\dot{Q}_{c,wall}$	$\dot{Q}_{c,loss}$	$\dot{Q}_{Th,loss}$	$\dot{W}_{\Delta p}$
019	40	3.0	0.65	0.55	32	27.41	6.937	4.91	0.1792	0.509	0.214	0.98	0.321
020	40	3.0	0.65	0.65	32	32.96	8.199	5.92	0.1799	0.509	0.194	1.164	0.403
021	40	2.7	0.65	0.373	92	17.27	4.70	2.01	0.1164	0.557	0.259	1.60	0.27
022	40	2.7	0.65	0.373	32	18.04	4.70	2.95	0.1638	0.561	0.303	0.683	0.20
023	40	2.7	0.65	0.5	32	24.41	6.30	4.26	0.1746	0.559	0.265	0.930	0.28
024	40	4.0	0.65	0.5	32	26.22	6.30	4.70	0.1793	0.379	0.189	0.765	0.27
025	40	5.0	0.65	0.5	32	28.35	6.30	4.85	0.1712	0.305	0.165	0.686	0.29
026	40	5.0	0.65	0.446	32	20.09	4.81	3.59	0.1720	0.305	0.166	0.534	0.21
027	40	6.0	0.65	0.5	32	31.37	6.30	4.93	0.1574	0.256	0.155	0.611	0.34
028	40	5.0	2.18	0.905	32	45.58	9.71	6.89	0.1512	0.562	0.769	1.071	0.42
029	40	5.0	1.228	0.51	32	25.42	5.46	3.69	0.1452	0.425	0.466	0.435	0.45
030	40	5.0	0.786	0.326	32	16.41	3.49	2.35	0.1430	0.337	0.277	0.386	0.15
031	40	5.0	0.545	0.226	32	11.29	2.42	1.55	0.1368	0.284	0.207	0.196	0.196
032	60	2.7	0.65	0.373	92	18.09	4.70	1.68	0.0933	0.561	0.323	1.83	0.30
033	60	2.7	0.65	0.373	92	18.09	4.70	1.68	0.0933	0.561	0.323	1.83	0.30
034	60	2.7	0.65	0.373	62	18.04	4.70	2.33	0.1291	0.564	0.325	1.17	0.31
035	60	2.7	0.65	0.373	32	18.85	4.70	2.87	0.1524	0.564	0.356	0.68	0.22

Table 3.5: Continued...

#	$f$ (Hz)	$L_{reg}$ (cm)	$A_{reg}$ (cm <sup>2</sup> )	$\dot{m}_c$ (g/s)	$D_h$ ( $\mu$ m)	$W_{PV,h}$ (W)	$W_{PV,c}$ (W)	$\dot{Q}_{net}$ (W)	COP	Losses (W)			
										$\dot{Q}_{c,wall}$	$\dot{Q}_{c,loss}$	$\dot{Q}_{Th,loss}$	$W_{\Delta p}$
036	60	4.2	0.65	0.55	32	24.97	5.65	4.14	0.1660	0.364	0.200	0.70	0.24
037	60	4.0	0.65	0.15	32	11.62	1.89	0.735	0.0632	0.387	0.440	0.247	0.081
038	60	4.0	0.65	0.25	32	16.08	3.15	1.87	0.1162	0.387	0.350	0.413	0.135
039	60	4.0	0.65	0.45	32	25.84	5.68	4.01	0.1552	0.386	0.264	0.603	0.410
040	60	4.0	0.65	0.65	32	37.12	8.20	6.20	0.1671	0.384	0.193	1.024	0.39
041	60	4.0	0.65	0.75	32	43.30	9.46	7.26	0.1676	0.384	0.177	1.17	0.475
042	60	4.0	0.283	0.65	32	47.01	8.20	6.26	0.1332	0.253	0.058	0.962	0.658
043	60	4.0	0.442	0.65	32	39.11	8.20	6.32	0.1616	0.316	0.1058	0.993	0.462
044	60	3.0	0.442	0.65	32	35.76	8.20	6.00	0.1678	0.419	0.1318	1.165	0.483
045	60	3.0	0.65	0.65	32	33.79	8.20	5.90	0.1745	0.510	0.23	1.18	0.382
046	60	3.0	0.866	0.65	32	33.45	8.20	5.63	0.1683	0.592	0.3898	1.06	0.530
047	60	2.0	0.442	0.65	32	33.27	8.20	5.327	0.1600	0.626	0.1838	1.56	0.499
048	80	2.7	0.65	0.373	32	20.06	4.70	2.79	0.1393	0.566	0.403	0.74	0.20
049	80	3.7	0.65	0.64	32	28.19	6.32	4.54	0.1611	0.413	0.228	0.86	0.276
050	80	3.0	0.55	0.65	32	35.26	8.199	5.75	0.1633	0.512	0.285	1.09	0.556
051	80	3.0	0.65	0.65	32	35.57	8.199	5.86	0.1649	0.47	0.216	1.1	0.544
052	80	3.0	0.65	0.45	32	24.7	5.67	3.66	0.1484	0.514	0.357	0.764	0.376
053	80	3.0	0.55	0.45	32	24.45	5.67	3.79	0.1553	0.472	0.271	0.764	0.371
054	80	3.0	0.85	0.65	32	35.4	8.199	5.53	0.1561	0.587	0.438	1.1	0.543

Table 3.5: Continued...

#	$f$ (Hz)	$L_{reg}$ (cm)	$A_{reg}$ (cm <sup>2</sup> )	$\dot{m}_c$ (g/s)	$D_h$ ( $\mu$ m)	$W_{PV,h}$ (W)	$W_{PV,c}$ (W)	$\dot{Q}_{net}$ (W)	COP	Losses (W)			
										$\dot{Q}_{c,wall}$	$\dot{Q}_{c,loss}$	$\dot{Q}_{Th,loss}$	$\dot{W}_{\Delta p}$
055	100	3.0	0.85	0.65	32	38.04	8.199	5.37	0.1413	0.588	0.507	1.14	0.580
056	100	3.4	0.65	0.72	32	30.94	6.83	4.82	0.1560	0.450	0.251	0.98	0.323
057	100	3.0	0.65	0.6	32	24.76	5.69	3.75	0.1515	0.509	0.300	0.885	0.246
058	100	3.0	0.822	0.5	32	30.48	6.30	3.87	0.1270	0.576	0.550	1.03	0.278
059	100	3.0	0.65	0.5	32	21.11	4.74	2.87	0.1367	0.514	0.352	0.668	0.323
060	100	3.0	0.57	0.5	32	28.96	6.307	4.24	0.1465	0.479	0.305	0.991	0.29
061	100	3.0	0.57	0.5	32	20.70	4.74	3.00	0.145	0.482	0.280	0.658	0.32
062	100	3.0	0.65	0.65	32	37.36	8.20	5.72	0.1531	0.509	0.316	1.28	0.373
063	100	3.0	0.866	0.65	32	38.27	8.19	5.42	0.1417	0.589	0.507	1.31	0.364
064	100	3.0	0.55	0.65	32	37.31	8.199	5.84	0.1567	0.467	0.24	1.25	0.392
065	100	3.0	0.45	0.65	32	37.76	8.199	5.94	0.1574	0.421	0.177	1.25	0.404
066	100	2.0	0.55	0.65	32	32.97	8.199	5.26	0.1597	0.703	0.29	1.57	0.353
067	100	1.5	0.55	0.65	32	31.58	8.199	4.614	0.1461	0.934	0.378	1.91	0.359
068	100	3.0	0.55	0.55	32	31.6	6.93	4.803	0.1519	0.468	0.267	1.08	0.3155
069	100	2.0	0.45	0.65	32	33.59	8.199	5.37	0.1599	0.634	0.222	1.59	0.38
070	120	3.1	0.65	0.55	32	32.80	7.24	5.00	0.1527	0.494	0.271	1.13	0.336
071	120	3.0	0.65	0.55	32	34.32	6.93	4.46	0.1301	0.515	0.417	0.957	0.582

*“The pressurization and depressurisation of any closed volume from a point on its periphery sets up temperature gradients in the volume”*

---

*Gifford and Longworth, 1963*

## Chapter 4

### Pulse Tube Cryocooler System

**P**ulse tube cryocooler’s root principle was first explained based on thermoacoustic oscillations. Thermoacoustic oscillation is a common phenomenon caused by the large temperature gradient in tubes and channels driven by an alternating pressure source. Lord Rayleigh, in 1877, established two critical principles for these oscillations: heating must occur in the high-pressure region, i.e., the closed-end, and poor thermal contact between the tube wall and the gas must be established to create a lag between gas flow and heat transfer.

#### 4.1 Introduction

Numerous advances in cryogenics, particularly for cryocoolers, have resulted in an expansion of their potential applications and even opened new application areas, such as in superconducting devices [140, 141], IR sensors [142–144], compact resonance magnets [72], and various medical and space applications [67, 145, 146]. This increasing demand for cryogenic cooling, particularly in satellite applications, has forced the development of more reliable cryocoolers with fewer moving components and improved materials for rubbing seals or even the replacing them with clearing seals. As a result, reducing rubbing friction and moving parts is essential for a reliable cryocooler [121].

Among the cryocoolers reported, pulse tube cryocoolers (PTCs), a variation of the Stirling cycle but without the moving mechanical displacer, are of special interest [147]. They are widely used due to their outstanding characteristics, including their relatively lightweight, high efficiency, high reliability, compact size, and relatively short response time. Unlike other regenerative devices, like Stirling and Gifford-McMahon (G-M) cryocoolers, PTCs lack mechanical moving components (i.e., mechanical displacers or rubbing seals). This results in a low vibration process, particularly at the cooler's cold end, making PTCs an excellent choice for miniaturized cooling systems. Although the Joule-Thomson cryocooler (JT), a recuperative machine, offers significant advantages, such as rapid cooling, the absence of moving components, and the potential for downsizing. The limitations, such as the possibility of valve clogging, inherent inefficiency, relatively high charge pressure, and short cooling duration, make them less desirable or even impossible to use for a wide range of critical applications [148].

Lowering the temperature at one end of a hollow tube with alternating pressure at the other end was first presented by Gifford and Longworth at Syracuse University [38]. They referred to it as the "basic pulse tube cryocooler" (BPTC) after observing that when a pressure oscillation is present inside the tube, the closed end's temperature increases, whereas the open end's temperature decreases. They achieved a 124 K cold end temperature by optimizing the geometry, with tube diameters ranging between 20 and 25 mm, and applying water-cooling to the hot end. In this type, the cooling effect is achieved through the partial thermal contact between the gas and the tube walls, rather than through an orifice or a separate reservoir. Unfortunately, the proposal was abandoned soon after due to inefficiency and a lack of a clear description of its working principle.

## 4.2 Theory

As with other regenerative cryocoolers, a pulse tube cryocooler (PTC) removes heat by compressing and expanding the working gas. To achieve the desired refrigeration, it relies on the theory of oscillatory compression and expansion of an ideal gas within a closed volume. The refrigeration effect in the system is caused by oscillating gas flow in a thin tube, accompanied by a phase shift mechanism [5]. As a result, for a PTC refrigeration process to be of any significance, reliable phase shift mechanisms are necessary. Figure 4.1 depicts the schematic diagram for a conventional pulse tube cryocooler.

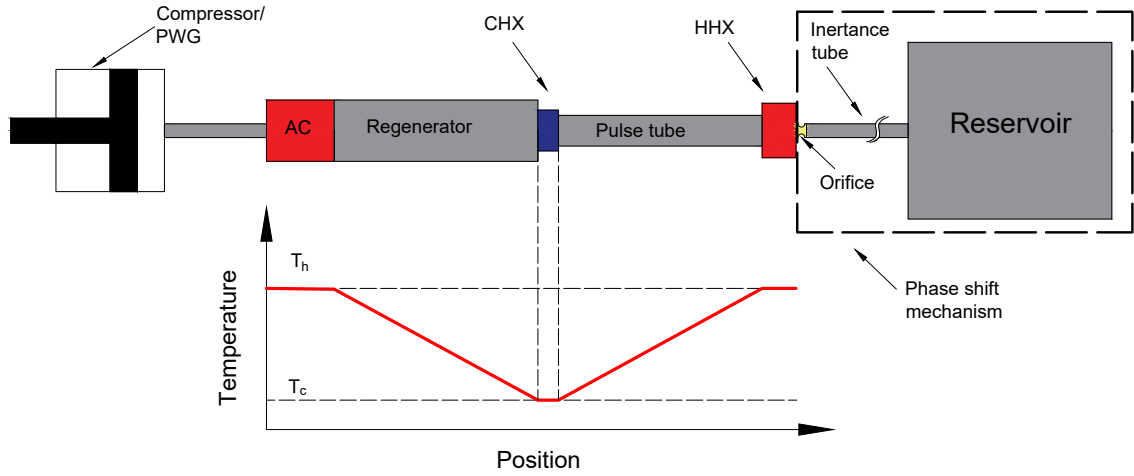


**Figure 4.1:** Schematic diagram for conventional PTC, the hot end heat exchanger (HHX), the cold end heat exchanger (CHX), the aftercooler (AC) the compressor or the pressure wave generator (PWG) are indicated. It shows also the phase shift mechanism, an orifice accompanied with a reservoir.

#### 4.2.1 Principle of operation

The complex phenomenon of gas compression and expansion in the pulse tube machine can be interpreted by plotting the temperature distribution along its length, as illustrated in Figure 4.1.

The thermodynamic processes behind the operation can be summed up as follows:

- *Adiabatic compression:* while the gas in the tube is initially at low pressure, the incoming high-pressure gas flows across the regenerator and into the pulse tube element, compressing the existing gas. This pressurization action compresses the gas in the tube adiabatically, resulting in an increase in temperature at the hot end. The ideal gas adiabatic temperature equation describes this phenomenon:

$$\left(\frac{T_1}{T_0}\right) = \left(\frac{P_1}{P_0}\right)^{\left(\frac{\gamma-1}{\gamma}\right)} \quad (4.1)$$

- *Adiabatic expansion:* because of the compressor's oscillation, the pressure drops, causing the gas to expand adiabatically, resulting in a temperature drop and movement of the expanded gas element down the tube toward the cold end. Gradually, the gas expansion creates a temperature gradient across the tube element, creating cold at the cold end of the pulse tube element while the tube's hot end is maintained at room temperature via ambient or water cooling.

- *Periodic steady-state*: as a result of the periodic pressurization and depressurization, the temperature decreases cycle after cycle. This forms a finite temperature gradient across the tube, which eventually settles into a periodic steady-state, making the pulse tube system a harmonically driven system. Typically, the system is accompanied by a phase shift mechanism (PSM) that assists in providing the cooling effect.

In conclusion, the cyclic process can be summarized as follows: the gas in the tube is compressed, shifted toward the hot end, expanded, and re-shifted toward the cold end, resulting in out-of-phase flows with distinct magnitudes at both the hot and cold ends [149].

### 4.2.2 Classification

In general, PTCs can be classified into subtypes based on their operation, phase shift mechanism, and geometry. Table 4.1 lists different PTC types based on these categories.

*Table 4.1: PTCs types and classifications.*

Operation	Geometry	Mechanism
Gifford-McMahon	Inline	Orifice (OPTC).
Stirling	U-type	Double-inlet (DIPTC).
	Coaxial/Annular	Inertance (IPTC).

#### 4.2.2.1 Classification based on operation

Pulse tube cryocoolers can be either of the Gifford-McMahon (G-M) type or of the Stirling type. The valved PTCs are referred to as G-M pulse tube cryocoolers (GM-PTCs), whereas the valveless PTCs are referred to as Stirling PTCs (S-PTCs) [5]. In Stirling types (S-PTCs), unlike Gifford-McMahon types, the gas flow is not controlled via motorized valves but rather by alternating the pressure signal itself. Usually, the Stirling type is more suitable for miniaturization for many reasons; these are the valveless operation and fewer mechanical moving parts that facilitate the high-frequency operation.

Due to the switching mechanism, Gifford-McMahon types are considered low-frequency machines. The system's efficiency is adversely affected by the pressure signal being rectified using motorized controlled valves, making them more suitable for low-temperature, bulky ground applications.

### 4.2.2.2 Classification based on geometry

PTCs are classified into three configurations based on the pulse tube element's connection to the regenerator element, as illustrated in Table 4.1. Figure 4.2 shows the different geometrical configurations of a PTC. The inline arrangement is the most straightforward and efficient type because it eliminates the need for a void space at the cold end and thus does not introduce turbulence into the pulse tube due to the flow reversal [143]. However, the drawbacks include low compactness and the possible inconvenience associated with having the cold end at the center between the two warm ends, making it not easily accessible for some applications.

U-type PTCs have the regenerator and the tube elements placed parallel to each other and connected by a U-shaped tube. This arrangement has advantages over the inline configuration, including an easy-to-access cold end and size compactness. Unfortunately, U-type configurations have a high pressure drop due to the void volume at the cold end of the tube element. This reduces the configuration's efficiency due to the 180° change in the flow direction, where pressure drop is typically proportional to the shape of the bend.

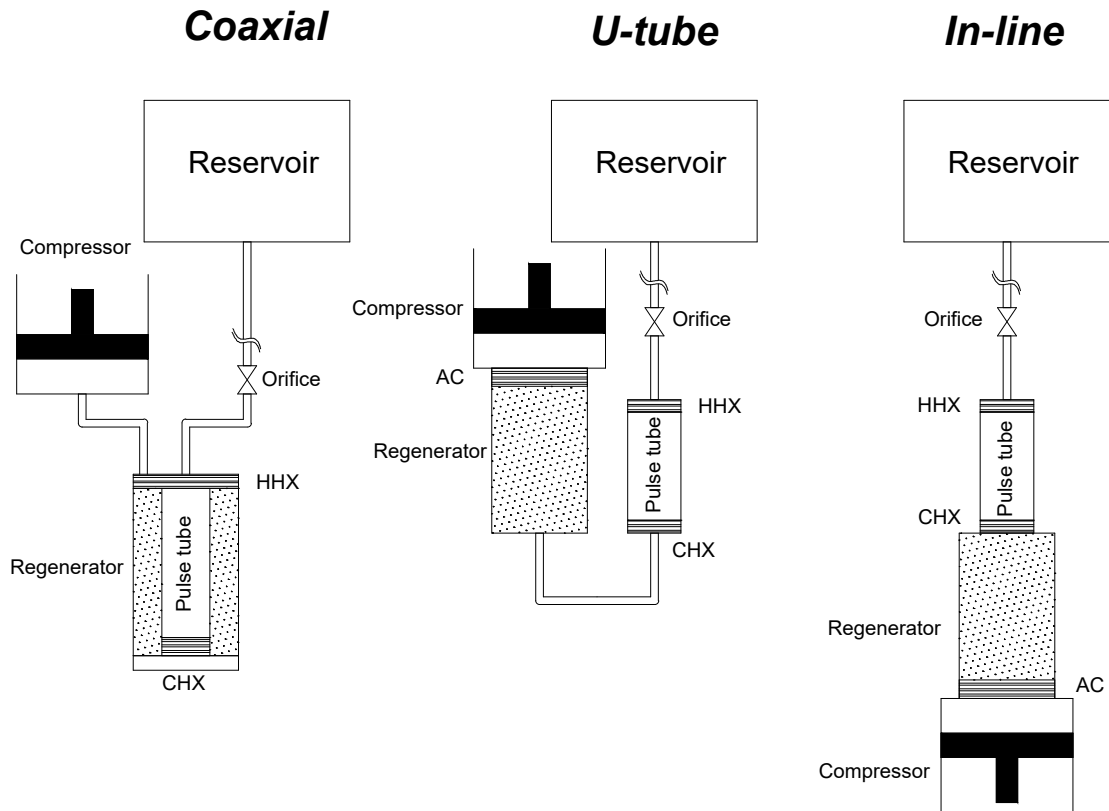


**Figure 4.2:** Schematic diagram for conventional PTCs based on geometrical configuration.

Coaxial and annular configurations are the most compact and resemble the Stirling cryocooler's geometry. The coaxial arrangement is similar to the annular arrangement with one exception:

in the annular configuration, the regenerator is housed inside the pulse tube, whereas in the coaxial configuration, the assembly is reversed. The disadvantages include a significant pressure drop caused by the abrupt change in direction at the cold end and the possibility of heat flow between the tube and the regenerator elements, caused by the mismatch in the temperature profiles of these two elements, which would reduce efficiency. However, the literature indicates that this configuration's disadvantages were minimized when the coaxial geometry was used to implement an oxygen liquefier for NASA with a 17% efficiency of Carnot [150]. Additionally, it is the most appropriate geometry for meeting the Standard Advanced Dewar Assembly (SADA) specifications for 2<sup>nd</sup>—generation thermal imaging systems [143, 151].

### 4.2.2.3 Classification based on phase-shift mechanism

In regenerative cryocoolers, the optimum cooling effect occurs when the mass flow leads the pressure at the regenerator's warm end, lags the cold end pressure, and is in-phase with the pressure near the regenerator's center, as discussed previously in section 3.6.1. In this case, the magnitude of the average mass flow rate through the regenerator can be minimized for a given input power, as shown in Figure 3.11a, thereby minimizing regenerator losses and increasing system efficiency, as discussed in the previous chapter.

Other types of regenerative cryocoolers, such as Stirling and G-M, can consistently achieve the optimal phase angle by designing the displacer motion phase shift with the compressor motion. To achieve this phase criterion, pulse tube cryocoolers require a phase shift mechanism. Pulse tube cryocoolers fall into four main categories, as illustrated in Figure 4.3: basic, orifice, inertance tube, and double inlet [152]. As previously stated, the basic was the first type to be developed, and it provided a slight cooling effect at a relatively high temperature, with a cold end temperature of 124 K achieved with a two-stage cryocooler [39]. Mikulin et al. [40] introduced the orifice type by modifying the primary type with an orifice connected to a gas reservoir. The mass flow rate and pressure are in phase at the orifice since it is typically a pure resistive flow element. In addition to an orifice, a needle valve, a capillary, or a porous plug were used [143].

In 1990, Zhu et al. [153] introduced the double inlet type by adding a second bypass valve that allows a small portion of the gas to flow directly between the hot end and the compressor. The result was a reduction in the amount of gas flowing through the regenerator, thereby decreasing regenerator loss. Basically, the flow through the secondary valve is in phase with the flow across the regenerator and thus leads the pressure; this results in the flow at the warm end of the pulse tube lagging behind the pressure, as the sum of flows must be in phase at the main orifice [143]. The disadvantages include the possibility of irreproducible performance and a temperature swing

of several degrees at the cold end temperature caused by the DC flow that can occur around the loop formed by the regenerator, pulse tube, and secondary orifice [143]. However, the issue can be resolved using a needle valve as the secondary orifice pointing toward the warm end, or by canceling the DC flow with a tapered pulse tube element [154].

Godshalk et al. [155] characterized the benefit of using an inertance tube within a pulse tube for the first time in 1996. The inertance effect is ensured by using a long, narrow tube between the pulse tube and the gas reservoir [4, 42, 156]. The inertia of the oscillating gas causes the pressure to lead the mass flow by up to  $90^\circ$ , reducing the regenerator's flow magnitude. In addition, the inertance type PTC has the benefit of preventing DC flow. The arrangement is analogous to the inductive effect in electrical circuits.

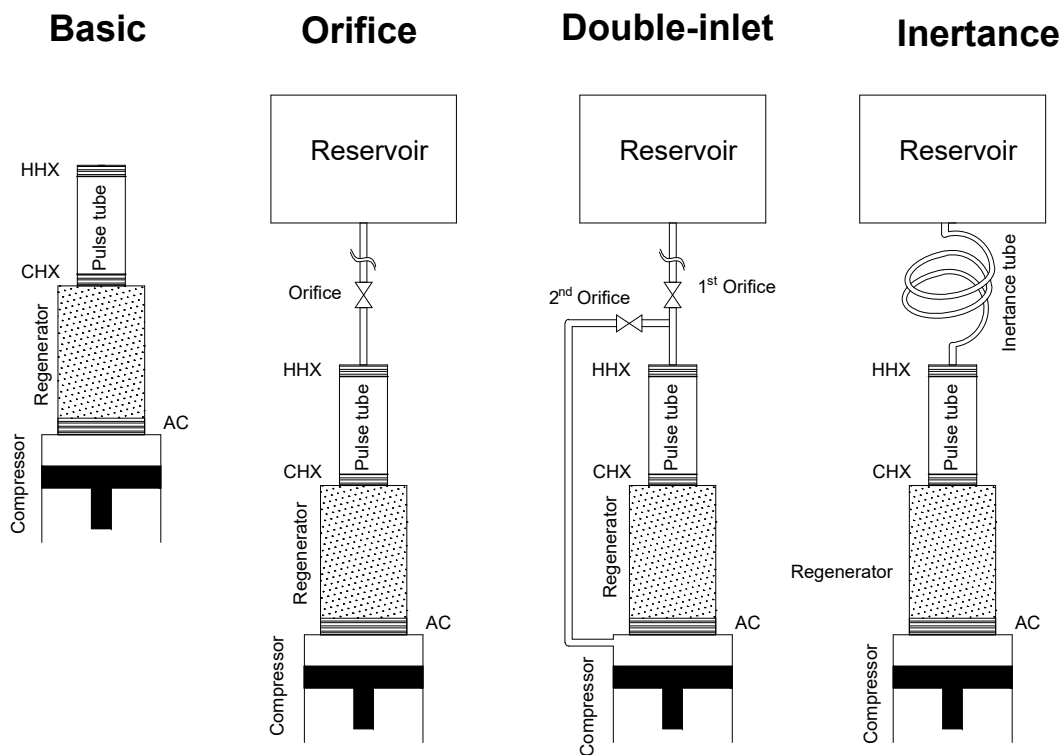


**Figure 4.3:** A schematic diagram for conventional PTCs based on various phase shifting mechanisms.

### 4.3 Analytic modelling

Effective prediction of pulse tube cryocooler operation, which is required before implementation, necessitates the conduct of theoretical, analytical, and numerical studies and the examination of these studies for inconsistency. Numerous analyses have been published in the literature to investigate the phenomena associated with various types of PTCs, including fundamental

analyses for PTC [38, 39, 157]. Thermodynamic models, like in [158, 159], are essential to understand the physics behind cooling action in PTCs. Multiple studies have been published in the literature describing the primary behavior of various PTC types [121, 149, 160, 161]. These theoretical studies are necessary to predict pulse tube cryocoolers' operation accurately and investigate the cyclic compression-expansion process and phase shift phenomena between pressure and mass flow. Several essential thermodynamic models, such as [162, 163], are available in the literature that are thought to be convenient and straightforward for the analysis of PTCs. They do not, however, address the system's detailed flow and heat transfer.

As explained previously, phasor analysis is a representation of the mass flow rates, pressures, and temperatures at the various components of the PTC system in the complex plane. It is critical for developing a thorough understanding of the operating principles of various types of PTCs and giving insights into the phase shift effect. Since Radebaugh et al. [121] exploited phasor analysis to explain pulse tube operation, numerous authors have applied it to various types of PTCs [149, 156, 160, 164–167] to estimate the net cooling power and the phase relationship between the pressure and the flow.

Kittel et al. [160] demonstrated the fundamental thermodynamic behavior of a PTC using phasor analysis. Hofmann and Pan [149] illustrated the operation of various types of PTCs using phasor diagrams. They asserted that it represents a straightforward method for determining the optimal phase shift angle. Chokhawala et al. [167] presented a phasor diagram for a DIPTC system. Gardner et al. [156] used phasor diagrams to introduce the inertance tube to modify the existing orifice type. Additionally, they investigated the system using an electrical analogy and complex geometry techniques. This section introduces phasor analysis to comprehend the operating principle and cooling capacity of standard Orifice-PTC (OPTC) and then generalizes the concept to other PTC types. Then, an analogy to an RLC circuit is presented to illustrate the concept of phase shift. After that, the phase shift induced by an inertance tube is then characterized using the transmission line model.

### 4.3.1 Phasor analysis for orifice-PTC<sup>2</sup>

In phasor analysis, sinusoidal mass flow rates, pressures, and temperatures are represented graphically in the complex plane by arrows and angles, refer to section 3.6.1. This section employs phasor analysis to determine the operating principle and cooling capacity of a standard Orifice-PTC machine. The analysis assumes that the working fluid is helium and that the pressure

signal is sinusoidal, as in equation 3.16a. Figure 4.4 shows the energy, enthalpy, and mass flows in the tube element of an orifice-PTC.

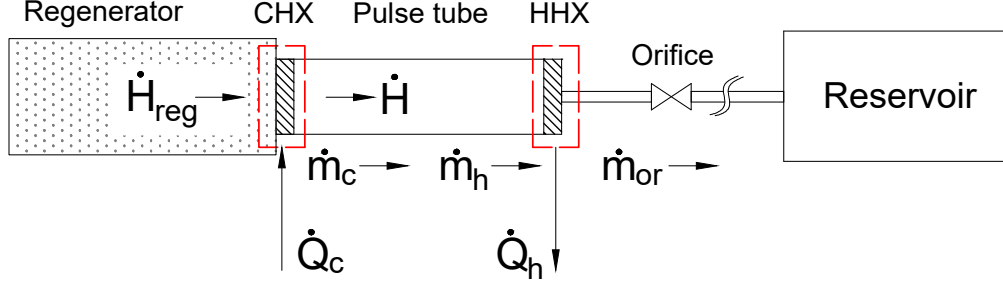


**Figure 4.4:** Energy balance diagram illustrating mass, heat and enthalpy flows in the tube segment in Orifice-PTC.

Since there are no moving elements, the work term is considered zero; where the first law of thermodynamics indicates that the average heat flow at the cold end,  $\dot{Q}_c$ , is given by:

$$\dot{Q}_c = \dot{H} - \dot{H}_{reg} \quad (4.2)$$

The enthalpy flow rates in the pulse tube and regenerator are denoted by  $\dot{H}$  and  $\dot{H}_{reg}$ , respectively. Assume an ideal gas and a perfect heat regeneration, in which the regenerator stores no energy between cycles. Then  $\dot{H}_{reg} = 0$ . The following result was obtained:

$$\dot{Q}_c = \dot{H} = \frac{c_p}{\lambda} \int_0^\lambda \dot{m}_c[t] T \cdot dt \quad (4.3)$$

where  $c_p$  and  $\lambda$  are the specific heat capacity and the pressure cycle period, respectively.  $T$  denotes the sinusoidal temperature variation provided by ( $T = T_0 + T_1 \cos[\omega t]$ ). In equation 4.3, only dynamic temperature contributes to,  $\dot{H}$ . Since the temperature is also sinusoidal, the equation 4.1 can be simplified, using Taylor series expansion and ignoring higher order terms, to [160]:

$$\left(\frac{T_1}{T_0}\right) = 0.4 \left(\frac{P_1}{P_0}\right) \quad (4.4)$$

Assuming the pulse tube element as a control volume, and applying the principle of conservation of mass. The change in mass in the tube element is then:

$$\dot{m}_{pt} = \dot{m}_h - \dot{m}_c \quad (4.5)$$

where  $\dot{m}_{pt}$ ,  $\dot{m}_h$  and  $\dot{m}_c$  are the changes in mass in the tube element, at the hot end and cold

ends, respectively. For an orifice-PTC, the mass flow rate near the hot end is given by [160]:

$$\dot{\mathbf{m}}_h = \dot{\mathbf{m}}_{or} = C_{or} \cdot \Delta \mathbf{p} = C_{or} P_1 \cos(\omega t) \quad (4.6)$$

Assuming an adiabatic process inside the tube element, and performing the same analysis in equations 3.68 through 3.72. The phasor representation for the pulse tube element is found:

$$\dot{\mathbf{m}}_c = \frac{T_h}{T_c} \dot{\mathbf{m}}_h + \frac{V_{pt}}{\gamma R T_c} \dot{\mathbf{P}} \quad (4.7)$$

This phasor relationship was previously demonstrated in equation 3.73, for an adiabatic element, and illustrated in Figure 3.11. Assuming sinusoidal behavior, the relationship can be represented using a phasor diagram. The pressure is in phase with the flow, as shown in equation 4.6, and thus at 90° with  $\dot{\mathbf{P}}$ . Substituting equations 4.7 and 4.4 in equation 4.3 and canceling out some periodic terms results in the following cooling power relation [121, 160]:

$$\dot{Q}_c \approx \frac{R T_c P_1}{2 P_0} |\dot{\mathbf{m}}_c| \cos \phi_c \quad (4.8)$$

Where  $|\dot{\mathbf{m}}_c|$ ,  $P_1$  and  $\phi_c$  are the magnitude of the mass flow at the cold end, the amplitude of pressure wave and the angle between  $\dot{\mathbf{m}}_c$  and the pressure, respectively. Equation 4.8 indicates that the cooling power is not only dependent on the pressure ratio but also on the phase shift. As a result, the presence of  $\phi_c$  in equation 4.8 implies that, theoretically, no significant cooling is done by a PTC unless there is some phase shift mechanism that ensures that  $\phi_c$  is as small as possible. For orifice PTC, it was found that  $\phi_c \approx 30^\circ$ . Radebaugh et al. [121] found that the cooling power defined in equation 4.8 as ratio of isothermal cooling power, resulted from expanding the gas from high pressure,  $P_h$  and low pressure,  $P_l$  is 0.34.

Figure 4.5 illustrates the relative magnitudes of the mass flow rates in the complete orifice-PTC system, which considers the gas volumes and the mean temperatures associated with each element in an orifice-PTC system. It can be shown clearly that the pulse tube element is assumed to be adiabatic while all other elements are considered to be isothermal elements. Refer to equation 3.73. It is shown here that the void volumes in the regenerator and the other heat exchangers result in larger compressor swept volumes due to the required higher mass flow rate to drive the entire system. With all the components considered, Radebaugh et al. [121] estimated the gross refrigeration power to be equal to:

$$\dot{Q}_c = \frac{\omega T_c P_0 (V_{co}/T_{co})^2}{16(V/T)_{Total}^2} \quad (4.9)$$

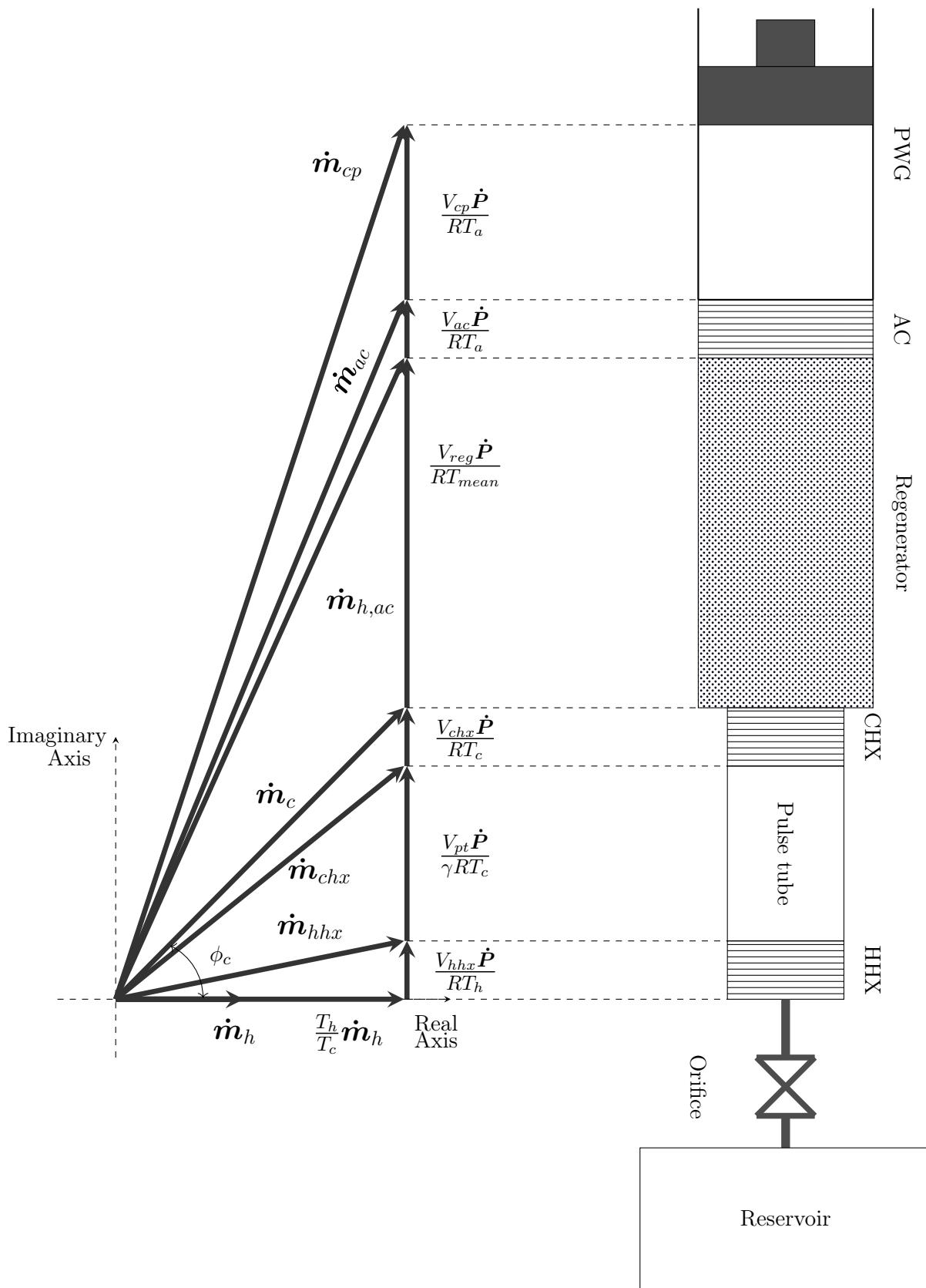
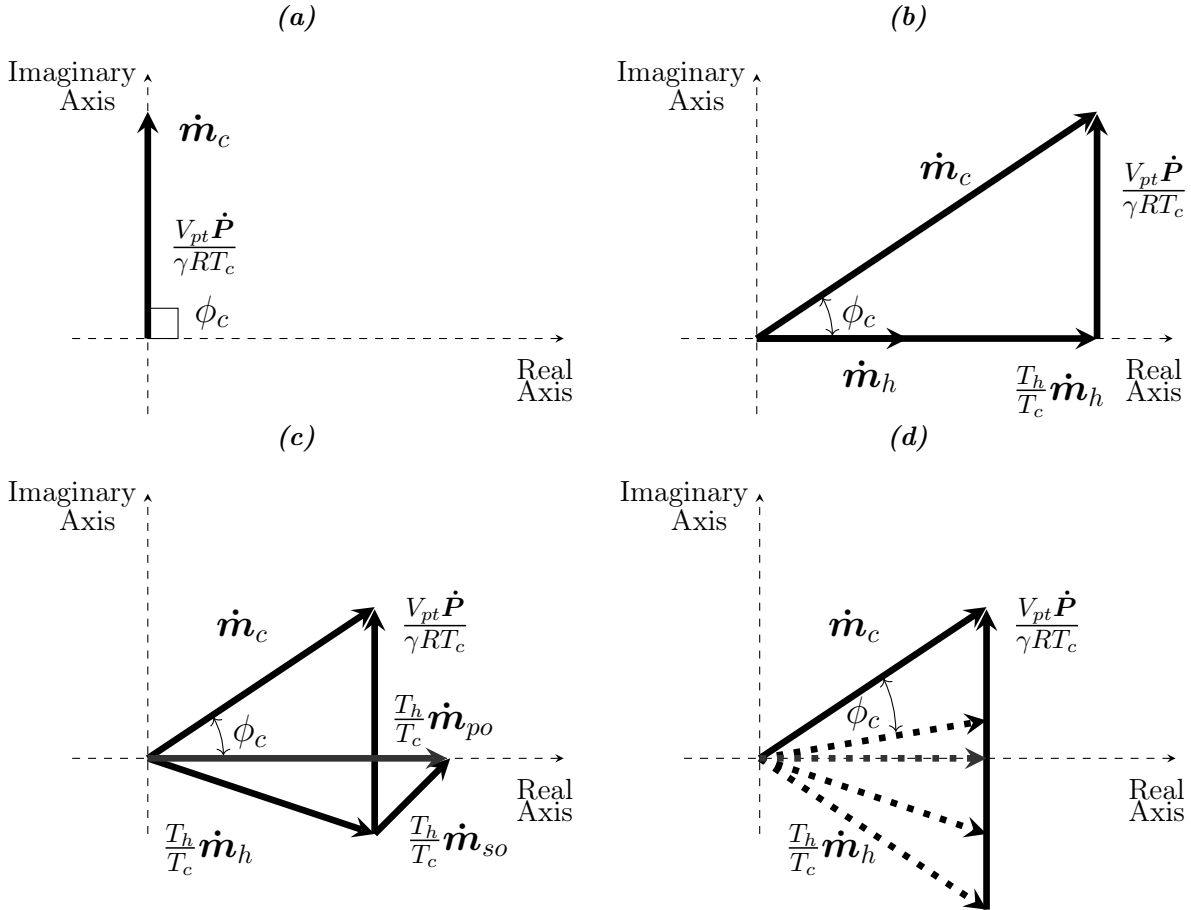


Figure 4.5: Full phasor diagram for the mass flows in the different elements for an orifice-PTC system.

where  $\omega$ ,  $V_{co}$ ,  $T_{co}$  and  $(V/T)_{Total}$  are the angular frequency, the compressor swept volume, the mean compressor temperature, and the sum for the volume to temperature ratio ( $V/T$ ) for each element, respectively.

### 4.3.2 Phasor representation for different phase shift mechanisms

The phasor diagrams for the Basic-PTC, Orifice-PTC, Double-Inlet-PTC, and Inertance-PTC are shown in Figure 4.6. In basic-PTC, the mass flow at the hot end is zero since the tube is closed at the hot end and equation 4.7 yields to the result depicted in Figure 4.6a. In this case, it is evident that the phase angle,  $\phi_c$ , between the mass flow and pressure vectors at the cold end is  $90^\circ$ , implying that the cooling effect, defined by equation 4.8, is zero. However, due to the viscous flow of the gas against the tube wall, considerable heat transfer occurs, causing  $\cos(\phi_c)$  to be close to zero, and thus some cooling effect was observed.



**Figure 4.6:** Phasor representation of the mass flow rates in different types the pulse tube system: (a) Basic-PTC, (b) Orifice-PTC, (c) Double-inlet-PTC, (d) Inertance-PTC (representative).

Figure 4.6b shows the phasor representation for orifice-PTC and demonstrates the phase shift angle between the mass flow at the cold end and the pressure phasor. The resultant cooling effect is summarized in equation 4.8. In this case, the phase will be zero at the orifice and may range

from approximately  $30^\circ$  at the cold end to  $50^\circ$  or more at the midpoint, and up to  $60^\circ$  or more at the regenerator's warm end. This implies that the magnitude of mass flow at the hot end is twice what it is when the phase shift is zero at the regenerator's midpoint, implying greater regenerator losses as discussed in the previous chapter. In principle, changing the orifice size or the type of flow resistance element would alter the resultant cooling power.

Earlier in this chapter, the principle of adding a second orifice, or the double-inlet-PTC was discussed, and a schematic for the double-inlet PTC was depicted in Figure 4.3. Figure 4.6c shows the phasor representation of this type, where the effect of adding a secondary, or bypass orifice, on the cooling power of the PTC system is graphically explained. The mass flow rate at the primary orifice end is defined as a phasor summation:

$$\dot{\mathbf{m}}_{po} = \dot{\mathbf{m}}_h + \dot{\mathbf{m}}_{so} \quad (4.10)$$

where  $\dot{\mathbf{m}}_{po}$  and  $\dot{\mathbf{m}}_{so}$  are the mass flow rates at the primary and secondary orifices, respectively. It is important to note that, unlike in the orifice-PTC, it is not the mass flow at the hot end that is in phase with the pressure, but rather the mass flow rate at the primary orifice. The mass flow at the hot end, in Figure 4.6c, is drawn down below the real axis to satisfy this in-phase relation. Assuming the magnitude of the phasor  $\dot{\mathbf{P}}$  remains constant, the configuration reduces the phase angle,  $\phi_c$ , and maximizes cooling power.

Finally, the influence of substituting an inertance tube for an orifice in the PTC system is illustrated in Figure 4.6d. The inertance tube's goal is to minimize the phase angle,  $\phi_c$ , and thus maximize cooling power by reducing the phasor of  $\dot{\mathbf{m}}_h$ . More details about the principle of adding the inertance tube are explored in light of the RLC analogy and the transmission line model in the next section.

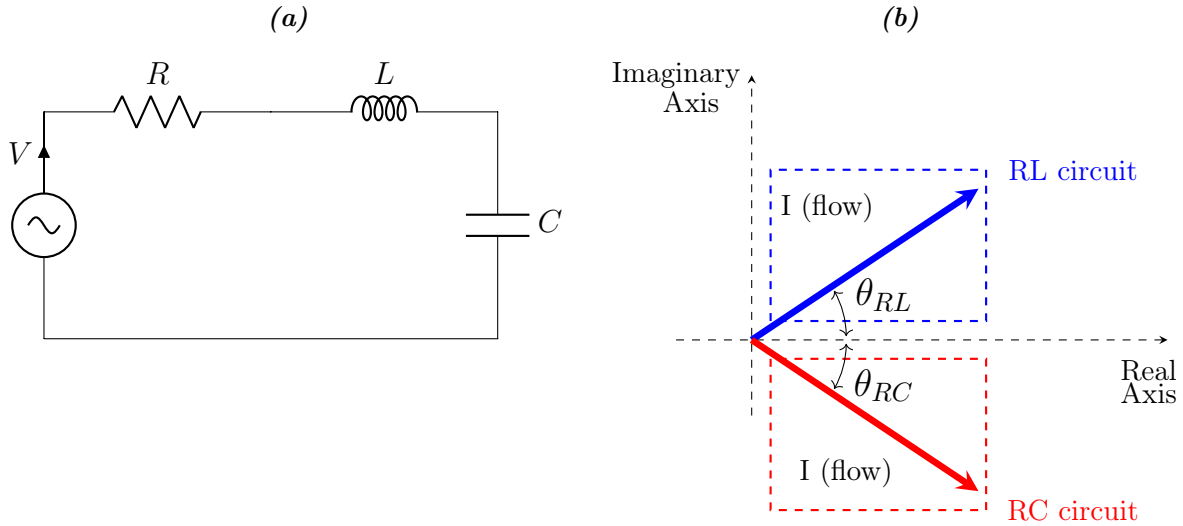
### 4.3.3 RLC Analogy & the transmission line model

Numerous publications have discussed electrical analogy methods for deriving meaning from pulse tube dynamics. See [156, 168]. Table 4.2 outlines the key mechanical phenomena and their electrical analogies.

Figure 4.7a illustrates a harmonically driven series RLC circuit model that can be efficiently used to study the effects of various phase shift mechanisms. An RLC model is described by a second-order ordinary differential equation that is able to resonate. The resultant mechanical impedance,  $Z$ , which is contributed to by all phase-shifting components, including the orifice, reservoir, and inertance tube, is proportional to the phase angle,  $\theta$ . Both can be summarized as

**Table 4.2:** RLC circuit analogy [165].

Quantity	Electrical Quantity	Flow Quantity
Pressure	Voltage (V)	$P_s$
Flow rate	Current (I)	$Q = \left( \frac{\pi r^4 \Delta P}{8h\mu} \right)$ [169]
Compliance	Capacitance (C)	$C = \left( \frac{V}{\gamma p} \right)$
Inertia of gas	Inductance (L)	$L = \left( \frac{\rho l}{A} \right)$
Orifice	Resistance (R)	$R = \frac{64f_r  m }{\pi^3 \rho D^5}$ [122]


**Figure 4.7:** (a) Series RLC circuit model, (b) Phasor diagram for RL and RC circuits.

follows:

$$Z = R + j(\omega L - (\omega C)^{-1}) \quad (4.11a)$$

$$\theta = \tan^{-1} \left( \frac{\omega L - (\omega C)^{-1}}{R} \right) \quad (4.11b)$$

Where  $Z$  denotes the impedance, and  $\omega$  denotes the angular frequency. In an RC circuit, the current (flow) leads the voltage (pressure) with  $\theta$  having a negative value, as illustrated in Figure 4.7b. Contrary to RC circuit, for RL circuit, the current lags the voltage with positive  $\theta$ . However, for the RLC circuit, the inductance and the capacitance have a collective influence on determining the sign for the angle  $\theta$ , which can be either positive or negative depending on the values of  $L$ ,  $C$ , and  $\omega$ .

According to equation 4.11b, the inductance term is significantly more dominant in the case of a high-frequency machine and less dominant in the case of a low-frequency machine. This implies that with Stirling type PTCs, an inertance tube, analogous to an RLC circuit, is recommended. On the other hand, orifice or double-inlet, analogous to the RC circuit, is recommended for Gifford-McMahon machines. Additionally, an orifice associated with a reservoir is the minimum condition to generate a substantial phase difference in the tube. This explains why the original basic pulse tube cooler (Basic-PTC), analogous to an electrical resistance circuit, failed to provide significant cooling; in this case, the only cooling effect is caused by heat transfer from the gas to the pulse tube's wall [164].

The inertance tube employs the inertia of the alternating flow to produce a phase shift between the flow and the pressure. The beneficial influence of introducing inertance effect within the pulse tube was first observed in 1996 by Godshalk et al. [155] for an orifice-PTC operating at 350 Hz. As discussed in section 3.6.1, the optimum phase relation is that the flow at the cold end is lagging the pressure by about  $30^\circ$ , this dictates that the phase shift at the inertance tube inlet is about  $60^\circ$ .

Radebaugh et al. [122] used the transmission-line model to find the diameter and length of the inertance tube corresponding to the maximum phase shift for a given acoustic power. In the transmission line analogy, electrical elements such as resistance, inductance, and capacitance are replaced by fluid elements such as resistance, inertance, and compliance. Hence, the complex impedance of a terminated transmission line of length  $L$  can be expressed as [170]:

$$Z_m(D, x) = Z_0(D) \left[ \frac{Z_r + Z_0(D) \tanh[k(D)(L - x)]}{Z_0(D) + Z_r \tanh[k(D)(L - x)]} \right] \quad (4.12)$$

Figure 4.8 depicts the schematic of an inertance tube with a length  $L$  and a reservoir.  $Z_r$  is the impedance of the reservoir of volume  $V_r$  at the end of the transmission line.  $Z_r$  is then given by:

$$Z_r = 1 / (j\omega C_r) \quad (4.13)$$

where  $C_r$  is the compliant load given by:

$$C_r = V_r / (\gamma R T_r) \quad (4.14)$$

$T_r$  is the mean temperature of the reservoir.  $Z_0$  is the complex characteristic impedance for

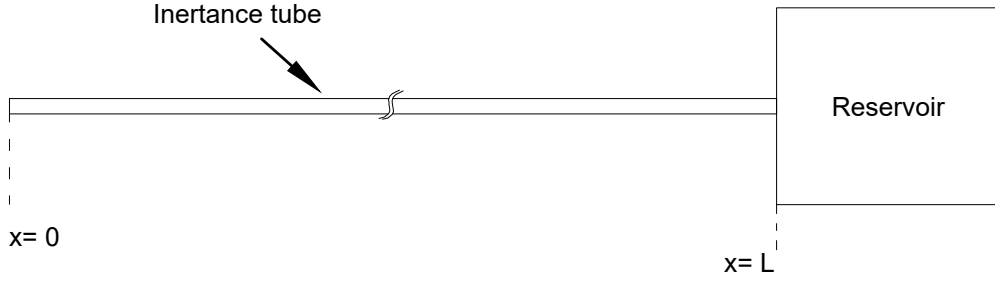


**Figure 4.8:** Schematic of inertance tube and reservoir.

the transmission line, i.e. the inertance tube, and can be expressed as:

$$Z_0(D) = \sqrt{\frac{r(D) + j\omega\ell(D)}{j\omega c(D)}} \quad (4.15)$$

where the fluid transmission line resistance, inertance, and compliance per unit length are:

$$\text{(Resistance/length)} \quad r(D) = (2/\pi) \left[ \frac{32f_r |\dot{m}|}{\pi^2 \rho_0 D^5} \right] \quad (4.16)$$

$$\text{(Inertance/length)} \quad \ell(D) = 4/(\pi D^2) \quad (4.17)$$

$$\text{(Compliance/length)} \quad c(D) = (\pi D^2) / (4\gamma RT_0) \quad (4.18)$$

and the complex propagation function or wave number is:

$$k(D) = \sqrt{[r(D) + j\omega\ell(D)]j\omega c(D)} \quad (4.19)$$

$D$  is the diameter of the inertance tube,  $f_r$  is the Fanning friction factor. This model can be used in both laminar and turbulent flow zones because the friction factor is incorporated in the above equations. The transmission line model predicts a  $90^\circ$  phase shift between pressure and flow at the inertance tube's end according to equation 4.12. To meet the criteria for minimal regenerator losses, the pressure must lead the flow at the warm end of the pulse tube by nearly  $60^\circ$ . This implies that the phase at the inertance tube inlet should be greater by a few degrees.

Figure 4.9a shows the phase difference between flows at the two ends of the optimised inertance tube for typical operating conditions. Figure 4.9b shows the corresponding length for the optimised inertance tube for a given acoustic power and the same operating conditions. The diameter of inertance tubes is found approaching the thermal penetration depth for small acoustic

power systems. The transmission line model results can be used to construct the inertance tube and produce initial estimates for the tube's length, diameter, and reservoir volume for a given cooling power.

Figure 4.10 shows the complete phasor diagram for Inertance-PTC. The case in the figure represents the optimum phase relationship where the pressure and the flow are in-phase at the regenerator midpoint and both the inertance tube and the reservoir are appropriately sized.

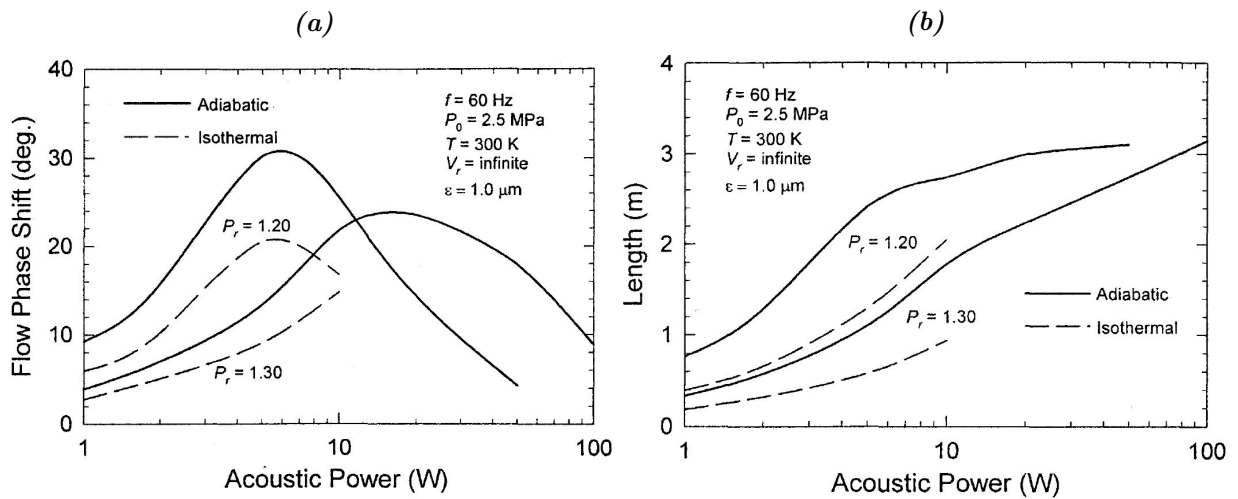


**Figure 4.9:** (a) Phase shift between flows at each end of optimized inertance tubes, (b) the optimised length for a give acoustic power. Reproduced from [122], with the permission of AIP Publishing.

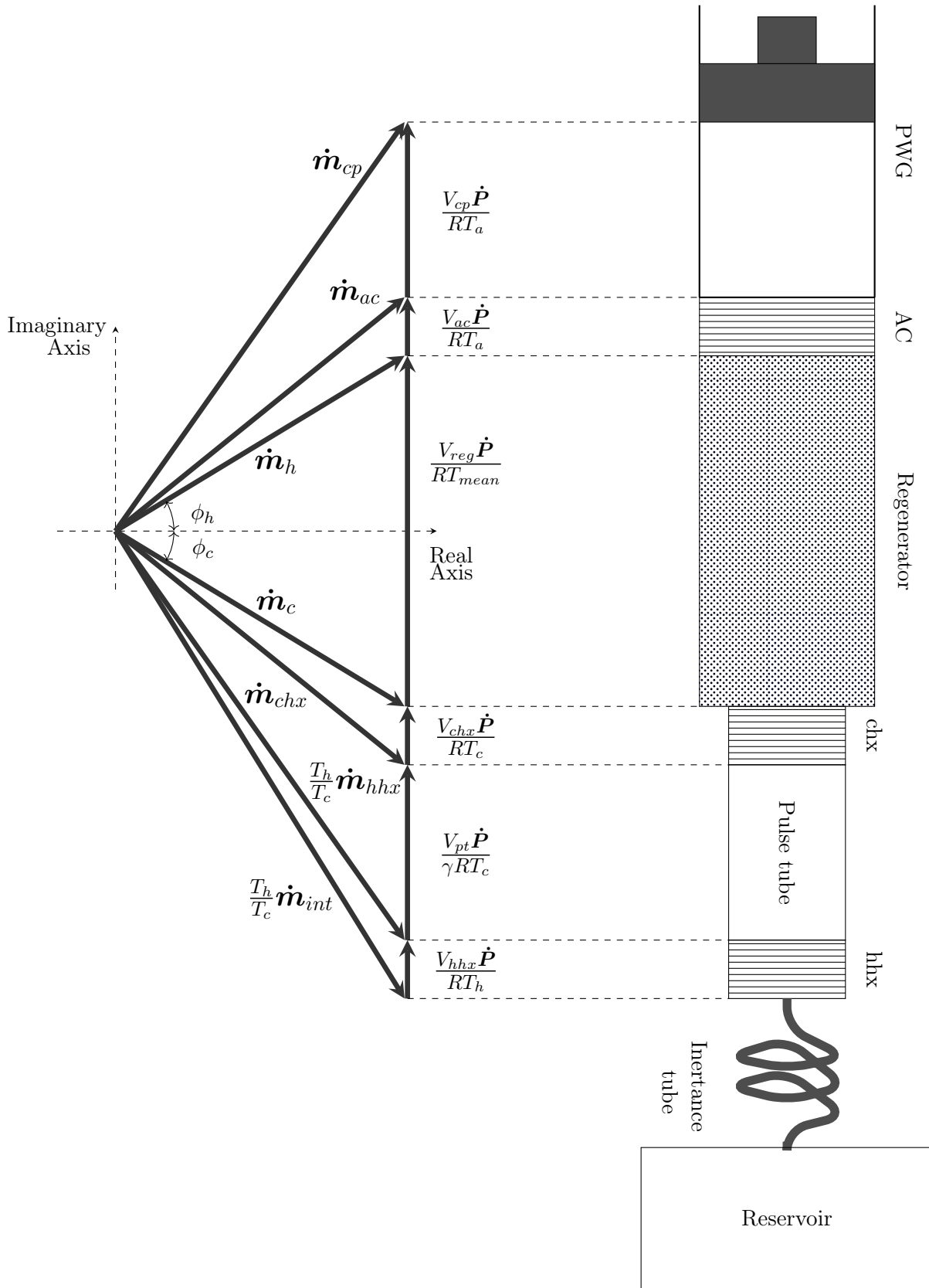


**Figure 4.10:** Full phasor diagram for the mass flows in the different elements in Inertance-PTC system.

## 4.4 Numerical modelling

Dimensional numerical models are required to gain a more precise understanding of the oscillating gas flow behavior, temperature dynamics, and mass flow inside the pulse tube. Various numerical models have been introduced, all of which produce good results [171–173]. Zhu and Chen [174] introduced the isothermal model, which is the most commonly used for analyzing PTCs, based on an intuitive and helpful methodology for analyzing Stirling-type cryocoolers. Atrey et al. [175] expanded the isothermal model to include cyclic analysis to study the performance and design of two-stage Stirling-type PTCs.

Generally, numerical dimensional models [165, 171–173, 176–181] use the continuity, momentum, and energy conservation equations to analyze space and time changes in thermodynamic phenomena by changing the boundary conditions corresponding to different PTC types. Despite their simplicity, one-dimensional computational models like those described in [171, 177, 178, 182, 183] provide reasonable predictions of different operating parameters. However, due to the assumptions given, it may oversimplify the problem by disregarding multidimensional flow and heat transfer effects. Other 1-D tools include Sage<sup>®</sup> software [184], a commercial tool for simulating a PTC or Stirling system, where the system parameters for a user-specified geometric parameter are tuned to provide the best performance achievable.

Basically, the governing equations for a PTC system have a nonlinear-transient response, making it nearly impossible to analytically solve two-dimensional models. Thus, two-dimensional numerical models are crucial to accurately describing PTC system. Lee et al. [185, 186] developed 2-D differential equations to describe the steady secondary flows caused by the periodic compression and expansion of an ideal gas, this provided intuitions about the physics of the pulse tube element in a basic and orifice PTC.

Many computational fluid dynamics (CFD) analyses have been performed on PTCs, like [181, 187–192]. Hozumi et al. [193] presented an axisymmetric model and a three-dimensional model and investigated the effects of gravity and orientation on the system’s performance. Flake and Razani [181] conducted a two-dimensional axisymmetric CFD analysis using ANSYS Fluent<sup>®</sup> software. They demonstrated the effects of cyclic flow patterns in a basic PTC and an orifice PTC. Cha et al. [187] carried out two-dimensional axisymmetric CFD analyses on two distinct inertance PTC systems with varying geometrical parameters. They discovered that when the system’s length-to-diameter ratio ( $L/D$ ) is small, significant multi-dimensional effects and swirling streams occur, reducing the system’s performance. Ashwin et al. [194] used a non-equilibrium model to simulate the heat exchangers and regenerator. They investigated the effect of tube wall thickness

on the performance of the PTC system. They noticed that the cold end temperature increased significantly due to the tube wall's heat conduction effect.

Antao et al. [195] presented an axisymmetric CFD model for an orifice-inertance pulse tube cryocooler system with similar geometric parameters to [187] but with a larger diameter and assuming thermal non-equilibrium in the porous zones. They discovered that the phase shift angle increases with frequency in porous zones. They observed steady counter-rotating streaming recirculation or swirling patterns, consistent with the predictions of [187]. At frequencies of 34 Hz and higher, two counter-rotating streaming patterns are formed at each of the pulse tube's two ends; these are advantageous at high frequencies because they act as a buffer zone to isolate the pulse tube's cold and hot ends. However, at a lower frequency, the recirculation pattern is reduced to one, resulting in the mixing of hot and cold regions and a reduction in system performance. This section starts by performing a 1-D numerical analysis on the tube element, and after that, it presents a 2-D CFD model for the whole PTC system.

#### 4.4.1 1-D nodal numerical modelling<sup>3</sup>

Multiple formulations of the governing equations for one-dimensional flow of compressed fluids are available in the literature [196, 197]. The conservation of mass, momentum, and energy, as well as the equation of state, can be written as [196]:

$$\frac{\partial \rho}{\partial t} + \frac{\partial (\rho u)}{\partial x} = 0 \quad (4.20)$$

$$\rho \left( \frac{\partial u}{\partial t} + u \frac{\partial u}{\partial x} \right) = -\frac{\partial p}{\partial x} + \frac{4}{3} \frac{\partial}{\partial x} \left( \mu \frac{\partial u}{\partial x} \right) \quad (4.21)$$

$$\rho c_p \left( \frac{\partial T}{\partial t} + u \frac{\partial T}{\partial x} \right) = \frac{\partial p}{\partial t} + u \frac{\partial p}{\partial x} + \frac{\partial}{\partial x} \left( K_f \frac{\partial T}{\partial x} \right) \quad (4.22)$$

$$p = \rho R T \quad (4.23)$$

where  $\rho$ ,  $u$ ,  $\mu$  and  $K_f$  are the fluid density, velocity, viscosity and thermal conductivity, respectively. These equations are based on the following assumptions:

- Helium, a Newtonian and ideal gas, is the working fluid.
- The flow is laminar.
- Quasi-steady wall friction is only significant in two or three-dimensional analysis.

- Viscous and inertial forces are insufficient to generate significant pressure changes along the tube; thus, the tube's pressure is uniform and only time-dependent (i.e.,  $\partial p/\partial x = 0$ ).

Thus, the momentum equation 4.21 can be omitted (see [177, 198]). The pressure signal in equation 4.22 is sinusoidal and can be expressed as  $p[t] = p_o + p_1\bar{p}[t]$ , where  $\bar{p}[t]$  denotes the varying component of the pressure signal. By substituting equation 4.20 and equation 4.22, equation 4.23 can be rearranged to obtain:

$$\frac{\partial u}{\partial x} = \Phi \frac{\partial^2 T}{\partial x^2} + f_1 \quad (4.24)$$

Similarly, equation 4.22 can be reshaped to obtain the temperature equation:

$$\frac{\partial T}{\partial t} = \Phi T \frac{\partial^2 T}{\partial x^2} - u \frac{\partial T}{\partial x} + f_2 T \quad (4.25)$$

Here,  $\Phi$ ,  $f_1$  and  $f_2$  are defined by:

$$\begin{aligned} f_1 &= \left( \frac{1}{A_o + A_1\bar{p}[t]} \right) \left( \frac{A_1}{c_p} - A_1 \right) \frac{\partial p}{\partial t} \\ f_2 &= \left( \frac{1}{A_o + A_1\bar{p}[t]} \right) \left( \frac{1}{c_p} \right) \frac{\partial p}{\partial t} \\ \Phi &= \left( \frac{1}{A_o + A_1\bar{p}[t]} \right) \left( \frac{K_f}{c_p} \right); \ni A_o = \left( \frac{p_o}{R} \right), A_1 = \left( \frac{p_1}{R} \right) \end{aligned}$$

Equation 4.25 is a non-linear convection-diffusion partial differential equation (PDE). The diffusion term is attenuated by the diffusion coefficient  $\Phi$ , which has a minimum value of about  $\sim 10^{-8}$ . This results in a more convective nature for the equation, which can be approximated as hyperbolic.

A MATLAB<sup>®</sup> finite difference code was generated to solve the one-dimensional model numerically. See Appendix B. First, the governing PDEs were discretized in both time and space after replacing all temperature and velocity derivatives with the finite difference equivalents. Finally, the numerical solution was computed using Algorithm 1, which is discussed in details in the next sections.

#### 4.4.1.1 Initial and boundary conditions for the pulse tube

To solve the system of equations, initial and boundary conditions are needed. The tube is assumed to be one-dimensional, with  $0 < x < l_t$ , where  $l_t$  is the tube's length. The velocity of the gas at the hot end (i.e.,  $x = 0$ ) needs to be defined as a boundary condition for equation 4.24 to be solved. This can be expressed as the volumetric flow of gas across the orifice divided by

the tube's cross-sectional area to obtain the velocity at the hot end:

$$u_h[t] = - \frac{C_{or}}{A_t} (\bar{p}[t] - \bar{p}_r[t]) \quad (4.27)$$

$\bar{p}[t]$  and  $\bar{p}_r[t]$  are the sinusoidal time pressure functions for the tube and the reservoir, respectively. According to the thermodynamic Poisson law, the pressure in the reservoir changes adiabatically over time due to volumetric flow across the orifice. This can be stated as follows:

$$\dot{V}_h[t] = \left( \frac{c_p V_r}{c_v p_r[t]} \right) \frac{dp_r[t]}{dt} \quad (4.28)$$

where  $V_r$  and  $c_v$  are the reservoir volume and the constant volume specific heat capacity, respectively. Equation 4.28 is solved to determine the change in pressure within the reservoir, and thus the velocity of the gas in equation 4.27. Finally, equation 4.25 requires two temperature boundary conditions at both the hot and cold ends, which are as follows:  $T_0^t = T_h$  and  $T_L^t = T_c$ . If the entire tube is assumed to be at ambient temperature, the temperature equation requires only one initial condition:  $T_x^0 = T_h$ .

#### 4.4.1.2 Numerical solution

After establishing the mathematical model, the differential equations 4.24 and 4.25 are solved numerically. To begin, we introduce two equally-spaced computational time and space grids:

$$\begin{aligned} x_i = i\lambda; \quad i=1, \dots, N_x; \quad \Rightarrow \quad \lambda &= \frac{l_t}{N_x}, \\ t^k = k\delta; \quad k=0, \dots, N_t; \quad \Rightarrow \quad \delta &= \frac{1}{N_t}. \end{aligned}$$

The formulas for velocity and temperature are determined by discretizing time and space using finite difference approximations. More specifically, a forward time centered space difference (FTCS) method, sometimes referred to as an explicit forward Euler method, was first adopted, as seen in equation 4.29 and equation 4.30, to find the first and second-order derivatives. These include the following:

$$u_i^k = u_{i-1}^k + \left( \frac{\Phi^k}{\lambda} \right) (T_{i-1}^k - 2T_i^k + T_{i+1}^k) + \lambda f_1^k \quad (4.29)$$

$$T_i^{k+1} = T_i^k + \delta \left( \frac{\Phi^k T_i^k}{\lambda^2} \right) (T_{i-1}^k - 2T_i^k + T_{i+1}^k) + \delta \Psi_i^k + \delta f_2^k T_i^k \quad (4.30)$$

where:

$$\Psi_{N_x}^k = \begin{cases} \left(\frac{-u_i^k}{\lambda}\right) (T_i^k - T_{i-1}^k); & u_i^k > 0 \\ \left(\frac{-u_i^k}{\lambda}\right) (T_{i+1}^k - T_i^k); & u_i^k < 0 \end{cases};$$

$$\Psi_i^k = \begin{cases} \left(\frac{-u_i^k}{2\lambda}\right) (3T_i^k - 2T_{i-1}^k + T_{i-2}^k); & u_i^k > 0 \\ \left(\frac{-u_i^k}{2\lambda}\right) (3T_{i+1}^k - 2T_i^k + T_{i-1}^k); & u_i^k < 0 \end{cases};$$

$$u_{N_x}^k = u_{N_x-1}^k + \left(\frac{\Phi^k}{\lambda}\right) (T_{N_x}^k - 2T_{N_x-1}^k + T_{N_x-2}^k) + \lambda f_1^k.$$

The solution for the approximated temperature equation depends on the direction of the flow velocity. Hence, the function  $\Psi$  determines which differencing scheme is used to solve this equation. Moreover, a first-order upwind/downwind model was used to avoid numerical noise and prevent nonphysical oscillation. Thus, a second order upwind scheme was used for all inner elements. The generated code calculates the predicted temperature,  $T_i^k$ , and velocity,  $u_i^k$ , profiles for each time and space node.

---

**Algorithm 1:** Algorithm for the finite difference computation [165].

---

**Data:** Input pressure signal  $p[t]$  **and** physical parameters for the tube, reservoir and orifice.

**Result:**  $T_i^k$  and  $u_i^k$  with  $i=1, \dots, N_x$  and  $k=0, \dots, N_t$   
initialization;

**while** *Periodic temperature steady state is not satisfied* ( $Err.\% \geq Tolerance$ ) **do**

**for**  $k = 0$  **to**  $N_t$  **do**

        Data  $\leftarrow f_1^k, f_2^k, A_o, A_1, \Phi, \bar{p}_r[t]$

$\bar{p}_r[t] \leftarrow u_h^k$  ▷ Calculate the velocity near the hot end.

**for**  $i = 2$  **to**  $N_x$  **do**

$\Psi_i^k \leftarrow u_{i-1}^k$

$T_i^{k+1} \leftarrow T_i^k, \Psi_i^k, f_2^k, \Phi^k$  ▷ Using equation (4.30)

**end**

$u_i^k \leftarrow u_{i-1}^k, f_1^k, \Phi^k$  ▷ Using equation (4.29)

**end**

**end**

---

The code can be outlined as follows:

- The code starts by calculating the pressure signals in the tube  $\bar{p}[t]$  and the reservoir  $\bar{p}_r[t]$ . It uses the previous values to evaluate the boundary condition for the velocity  $u_h$ .
- Then, it computes the temperature  $T_i^{k+1}$  depending on the  $T_i^k$  and  $u_{i-1}^k$  taking into consideration the direction of the flow (as illustrated by function  $\Psi$ ) and the boundary conditions for the temperature at the hot and cold ends.
- It evaluates the velocity  $u_i^k$  using the temperature value for the same time element.

FTCS was first chosen due to its explicit approach. The interior points' values are given by known data (i.e., boundary data or previously computed interior points). Unfortunately, the convergence of this algorithm is strongly sensitive to the value of  $(\delta/\lambda^2)$ , the ratio between time and space grids, which can noticeably affect its convergence if ill-chosen. Moreover, since increasing the operating frequency requires increasing the time grid points, this regime will fail when considering higher frequencies or even studying reduced tube lengths. However, it showed good results for low operating frequency systems if a fine space grid is not vital. Thus, another algorithm was employed for higher operating frequency systems. The implicit BTCS (Backward Time, Centred Space), sometimes referred to as the implicit Backward Euler method. This algorithm involves solving a system of instantaneous linear PDEs, which is expected to converge regardless of the size of time and space grids because of its unconditional stability due to the linear equation's tridiagonal structure, and the system matrix  $A$ 's diagonal dominance [199]. As a result, equation (4.30) is modified to:

$$T_i^{k+1} = T_i^k + \delta \left( \frac{\Phi^k T_i^k}{\lambda^2} \right) \left( T_{i-1}^{k+1} - 2T_i^{k+1} + T_{i+1}^{k+1} \right) + \delta \Psi + \delta f_2^{k+1} T_i^{k+1} \quad (4.31)$$

Equation 4.31 is then transformed into a system of linear equations with the general form  $(AT_i^{k+1} = T_i^k + F)$  with  $A$  and  $F$  are matrices containing constant elements at a given time instant. This can be stated more explicitly as follows:

$$\begin{bmatrix} \Omega_d & -\Omega_2 & 0 & 0 \\ -\Omega_1 & \ddots & \ddots & 0 \\ 0 & \ddots & \ddots & -\Omega_2 \\ 0 & 0 & -\Omega_1 & \Omega_d \end{bmatrix} \cdot \begin{bmatrix} T_1^{k+1} \\ T_2^{k+1} \\ \vdots \\ T_{N_x-1}^{k+1} \end{bmatrix} = \begin{bmatrix} T_1^k + \Omega_1 T_0^k \\ T_2^k \\ \vdots \\ T_{N_x-1}^k + \Omega_2 T_{N_x}^{k+1} \end{bmatrix}$$

Here  $\Omega_1, \Omega_d$ , and  $\Omega_2$  are the elements in the  $A$  and  $F$  matrices whose values depend on the direction of the gas nodal velocity, and are represented as:

*if*  $u_i^k < 0$ ;

$$\implies \Omega_d = 1 + \delta \left( \frac{2\Phi^k T_i^k}{\lambda^2} \right) + \delta (f_2)^k - \left( \frac{\delta u_i^k}{\lambda} \right), \quad \Omega_2 = \left( \frac{\Phi^k T_i^k}{\lambda^2} \right), \quad \Omega_1 = \left( \frac{\Phi^k T_i^k}{\lambda^2} \right) - \left( \frac{\delta u_i^k}{\lambda} \right).$$

*if*,  $u_i^k > 0$ ;

$$\implies \Omega_d = 1 + \delta \left( \frac{2\Phi^k T_i^k}{\lambda^2} \right) + \delta (f_2)^k + \left( \frac{\delta u_i^k}{\lambda} \right), \quad \Omega_2 = \left( \frac{\Phi^k T_i^k}{\lambda^2} \right) + \left( \frac{\delta u_i^k}{\lambda} \right), \quad \Omega_1 = \left( \frac{\Phi^k T_i^k}{\lambda^2} \right).$$

Unlike the previous algorithm, BTCS begins by computing the velocity of the current space/-

time element and then solves a system of linearized equations to determine the corresponding space temperatures for each time step. The algorithm has the advantage of converging to a solution unconditionally. The quality of the computed solution, to some extent, depends on the size of the space element, as is expected from the finite difference method. The algorithm now allows investigating the effect of different operating frequencies on the tube lengths.

#### 4.4.2 CFD analysis for inertance PTC<sup>4</sup>

In this section, ANSYS<sup>®</sup> Fluent software [119] is used to report a 2-D CFD transient model designed to investigate the process that occurs in an in-line inertance pulse tube system. This is accomplished by solving the mass (continuity), momentum (Navier–Stokes equations), and energy equations in the gas and porous medium domains. The purpose of this study is to investigate the effects of operational and geometric parameters on the flow and heat transfer processes and the machine’s overall performance. The objectives include proving the validity of the design software tool as a digital twin and determining its applicability for miniature cryocoolers. Fluent will be used to quantify or estimate various thermodynamic processes that are likely to limit the performance of the cryocooler.

##### 4.4.2.1 Geometry, initial and boundary conditions

The heat transfer for the inertance PTC is simulated using a 2-D axisymmetric CFD model. The inertance PTC’s flow characteristics and cooling performance are then investigated at different operating frequencies. Figure 4.11 illustrates the schematic for the simulated inertance PTC system. The system is composed of the following components: (1) the pressure wave generator that supplies an alternating pressure signal for the system, (2) the transfer line, (3) the aftercooler, (4) the regenerator, (5) the cold heat exchanger (CHX), (6) the pulse tube component, (7) the hot heat exchanger (HHX), (8) the first inertance tube, (9) the second inertance tube, and (10) the compliance volume or reservoir.

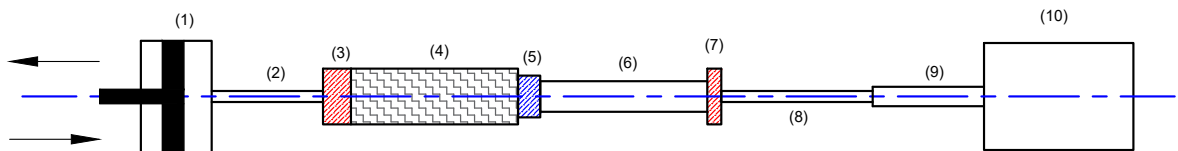


**Figure 4.11:** Schematic diagram for the simulated system [200].

The dimensions and boundary conditions for the inertance PTC system are summarized in Table 4.3. The system described here is identical to the experimental apparatus described by Vanapalli et al. [96, 201], except that the simulation employs a smaller compressor and a different

<sup>4</sup> This Section is reproduced from previous work by the author, see [200].

porous media characteristic. The downsized compressor is used to investigate the feasibility of a miniature compressor with a small piston stroke on an inertance PTC machine's cooling performance.

**Table 4.3:** *Dimensions and boundary conditions for the Inertance PTC system [200].*

No.	Component	Radius (mm)	Length (mm)	Walls boundary conditions
1	Compressor	9.5	7.5	Adiabatic
2	Transfer-line	1	100	Adiabatic
3	Aftercooler	4.5	3.4	$T = 293K$
4	Regenerator	4.5	30	Adiabatic
5	Cold heat exchanger	2.38	4.4	Adiabatic
6	Pulse tube element	2.2	30	Adiabatic
7	Hot heat exchanger	2.38	3.4	$T = 293K$
8	Inertance tube 1	0.7	864	Adiabatic
9	Inertance tube 2	0.8	746	Adiabatic
10	Reservoir	15	70	Adiabatic

The piston's motion can be modeled by assuming that it oscillates at a certain frequency to generate the required input harmonic pressure wave. The velocity of the piston is then defined as:

$$u_p(t) = X_0 2\pi f \cos(2\pi ft) \quad (4.32)$$

Where  $X_0$  denotes the piston motion's displacement amplitude, and  $f$  denotes the operating frequency. To simulate the input piston velocity signal to the inertance PTC system, user-defined functions (UDFs) are written in the C-language and compiled into Fluent; the UDF is presented in Appendix C. CFD simulations do have several advantages, however, complex problems require a significant amount of time to solve due to the numerous cycles required to reach a steady state. Because of this prohibitively high cost, i.e., almost 45 days of simulation time, only three distinct operational frequencies were simulated. Thus, the experiment was replicated at a high frequency of 120 Hz, identical to the frequency used in the original report [96, 201], a medium frequency of 50 Hz (a typical frequency for conventional Stirling or PTC cryocoolers), and a low frequency of 20 Hz.

The outer wall boundary conditions are listed in Table 4.3. The system temperature is initially set to a value of 300 K, with a pressure of 3.5 MPa. The flow is assumed to be laminar, with helium as ideal gas and assuming temperature-dependent thermal conductivity. Fluent was then employed to solve the governing equations and associated boundary conditions. Transient simulations were then run until a periodic-steady state was reached.

#### 4.4.2.2 Mathematical model and governing equations

Fluent simulates PTC by incorporating mass conservation (the continuity equation), momentum conservation (Navier–Stokes equations), and energy conservation equations. The regenerator and heat exchangers are modeled as porous media, whereas the rest of the regions is assumed to be a fluid zone. In the fluid (helium) zones, the governing equations are as follows [119, 187]:

$$\frac{\partial \rho_f}{\partial t} + \frac{1}{r} \frac{\partial}{\partial r} (r \rho_f v_r) + \frac{\partial}{\partial x} (\rho_f v_x) = 0 \quad (4.33)$$

$$\frac{\partial (\rho_f \bar{v})}{\partial t} + \nabla \cdot (\rho_f \bar{v} \bar{v}) = -\nabla p + \nabla \cdot \tau \quad (4.34)$$

$$\frac{\partial \rho_f E}{\partial t} + \nabla \cdot (\bar{v} (\rho_f E + p)) = \nabla \cdot (k_f \nabla T + (\tau \cdot \bar{v})) \quad (4.35)$$

where:

$$\tau = \left( \mu (\nabla \bar{v} + \nabla \bar{v}^T) - \frac{2}{3} \nabla \cdot \bar{v} I \right) \quad (4.36)$$

$$E = h - \frac{p}{\rho} + \frac{v^2}{2} \quad (4.37)$$

The fluent model pre-supposes that the fluid and solid are in local thermodynamic equilibrium in the porous zones. In fluent, the governing equations for porous zones are as follows [119, 187]:

$$\frac{\partial \phi_m \rho_f}{\partial t} + \frac{1}{r} \frac{\partial}{\partial r} (\phi_m r \rho_f v_r) + \frac{\partial}{\partial x} (\phi_m \rho_f v_x) = 0 \quad (4.38)$$

$$\frac{\partial \phi_m \rho_f \bar{v}}{\partial t} + \nabla \cdot (\phi_m \rho_f \bar{v} \bar{v}) = -\phi_m \nabla p + \nabla \cdot (\phi_m \tau) + S_i \quad (4.39)$$

$$\begin{aligned} & \frac{\partial (\phi_m \rho_f E_f + (1 - \phi_m) \rho_s E_s)}{\partial t} + \nabla \cdot (\bar{v} (\rho_f E_f + P)) \\ & = \nabla \cdot [(\phi_m k_f + (1 - \phi_m) k_s) \nabla T + (\tau \cdot \bar{v})] \end{aligned} \quad (4.40)$$

where  $\phi_m$ ,  $k_f$  and  $k_s$  are the porosity and the thermal conductivity of both the fluid and the solid structures, respectively. According to the literature, the contact resistance between the mesh layers reduces thermal conductivity, hence a degradation factor of 0.1 was assumed [181]. Thermal conductivity is also assumed temperature dependent and anisotropic.

$S_i$  is the additional term introduced by Fluent to model the gas flow resistance through the porous zones as described in equation 3.61. Using the pressure gradient in porous media and assuming steady flow, the permeability and inertial resistance factor for the particular screen-filling are determined using the relationships described in [192, 202]; these are represented by:

$$\frac{1}{\alpha} = \frac{33.6n\phi_m}{2l\psi}; \quad C_2 = \frac{0.337n\phi_m^2}{\psi^2}$$

Assuming that all screen layers are perfectly stacked inside the regenerator and that there are no gaps in the heat exchangers, it is possible to calculate the screen's porosity and opening ratio [62]:

$$x_t = \frac{1}{d_w n}; \quad \phi_m = 1 - \frac{\pi}{4x_t}; \quad \psi = (x_t - 1)^2 / x_t^2$$

Although these calculated hydrodynamic parameters are considered a good approximation, they show some inconsistency with previous results when applied to periodic flow regimes [120, 203–205]. The parameters for various mesh porous materials suitable for miniature regenerative cryocoolers are shown in Table 4.4. The regenerator and heat exchangers are made of 635# stainless steel and 325# copper. Furthermore, in both the regenerator and the heat exchangers, the solid structure's thermal conductivity is considered anisotropic and temperature-dependent. In the regenerator, the solid structure material is considered stainless steel with a constant density of  $7800 \text{ kg m}^{-3}$ , and specific heat assumed constant at  $460 \text{ J kg}^{-1} \text{ K}^{-1}$ . For the heat exchangers, the solid structure material is copper, with a constant density of  $8900 \text{ kg m}^{-3}$  and specific heat assumed constant at  $380 \text{ J kg}^{-1} \text{ K}^{-1}$ .

**Table 4.4:** Porous media characteristics for five different commercial mesh screens [200].

	Material	n	$\phi_m$	$1/\alpha$	$C_2$	Ref.
Axial	S.S	325	0.69	$9.43 \times 10^9$	76090	[204, 206]
	Copper	325	0.69	$9.43 \times 10^9$	76090	
	PhBrz	325	0.67	$1.7 \pm 0.2 \times 10^{10}$	$50,000 \pm 6000$	[120]
	S.S	635	0.63	$9.5 \pm 0.2 \times 10^{10}$	$40,000 \pm 5000$	
Radial	S.S	325	0.69	$9.43 \times 10^9$	76090	[204, 206]
	Copper	325	0.69	$9.43 \times 10^9$	76090	
	PhBrz	325	0.67	$2.9 \pm 0.2 \times 10^{10}$	$50,000 \pm 6000$	[120]
	S.S	635	0.63	$1.11 \pm 0.2 \times 10^{11}$	$120,000 \pm 20000$	

#### 4.4.2.3 Numerical scheme and nodalization

In the fluid and porous media zones, the continuity, momentum, and energy equations were numerically solved using the second-order upwind scheme. Fluent includes a dynamic mesh feature that enables users to simulate compressor motion more accurately. It enables volume contraction and expansion to be efficiently modeled. Layering is used to enable the addition or deletion of cells based on the surface's movement in the prismatic cell zones [119].

Figure 4.12 depicts the simulated system's nodalization scheme. Due to the problem's symmetry, an axisymmetric two-dimensional model, i.e., half of the domain shown in 4.11, was

used, which resulted in reduced computational effort. A fine high-density mesh nodalization was used for grid convergence in regions with expected high temperature and velocity gradients, near junction geometries, and at the cold end exchanger. In contrast, a low-density and coarser rectangular mesh were used for all other components. The total number of nodes was less than 5000, which was sufficient to yield a precise solution. For energy, momentum, and continuity, the second-order upwind scheme was used. A second-order time transient scheme was used to provide a more accurate description of the time-varying signals. 50-time steps per cycle were used to accurately predict the system's performance, with at least 28 iterations per time step; an overall convergence of  $10^{-4}$  for continuity and velocities, and  $10^{-8}$  for the energy in the iterative implicit numerical solver.

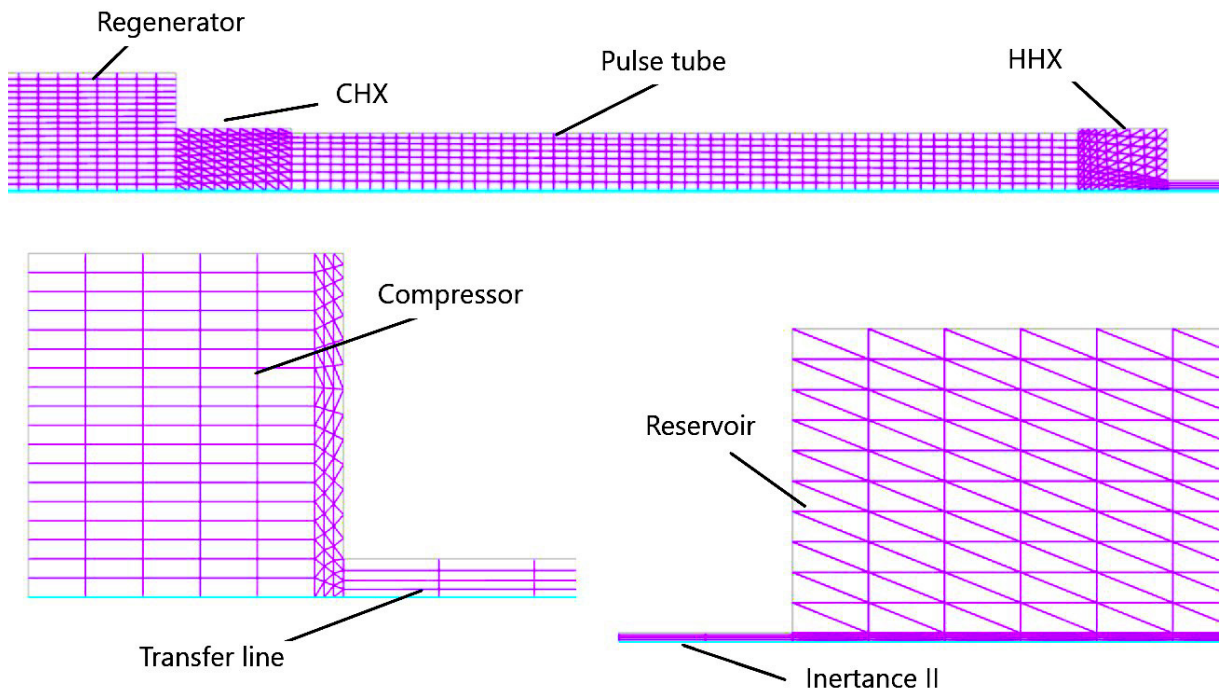


*Figure 4.12: Nodalization scheme of the system (dimensions are not to scale) [200].*

## 4.5 Common technical issues related to miniaturization

Unfortunately, reducing the size of a pulse tube cryocooler comes with a cost. It necessitates a thorough understanding of the associated issues and their effects on the system's thermodynamic properties. Although several of these issues are discussed in the literature [9, 11, 13, 14], their significance for miniaturized systems has not been adequately quantified. This section will address the most prevalent miniaturization-related matters.

### 4.5.1 Regenerator losses

Chapter 3 discussed the regenerator's losses and their relationship to other geometric and operating parameters. One of the requirements for miniature PTC is to operate at higher frequencies, i.e., higher than the conventional 50–60 Hz. Unfortunately, the high-frequency operation set constrains to the regenerator's geometry, matrix material, and average system pressure [13].

For instance, as the operating frequency increases, the regenerator's volume should decrease to ensure reasonable mass flow rates and efficient phase shift. The regenerator matrix's hydraulic diameter should also be reduced to maintain the same heat transfer surface area as the regenerator's volume decreases. Additionally, for efficient regeneration, the matrix's hydraulic diameter should be less than the thermal penetration depth. As a result, the charging pressure and operating frequency are increased, further reducing the thermal penetration depth,  $\delta_{th}$ , see equation 3.5.

Additionally, the stacking of the matrix screens inside the regenerator is usually imperfect, leaving some gaps and spaces between the matrix screen and the regenerator tube wall, resulting in a low-resistance flow path within the regenerator, thus reducing the regenerator's effectiveness. At a micron scale, it is anticipated that the effect of these gaps will be even more pronounced. Thus, due to the relatively large hydraulic diameter of conventional mesh screens, they are not a good fit for miniature PTC; in this case, novel filler materials and micro-machined regenerators should be considered. Examples of micro-fabricated regenerators include: [207, 208]; however, their operation was hampered by high conductive losses.

### 4.5.2 Thermal and viscous losses

For miniature PTCs, the small size results in significant viscous losses, particularly in smaller diameter elements. In the pulse tube element, heat transfer between the working gas and the tube's interior wall would increase, deteriorating the expected temperature gradient across the tube. These losses become apparent when the pulse tube's diameter and thickness are comparable to the thermal and viscous boundary layer thicknesses [182]. The thermal and viscous penetration depths are defined by the equations 3.5 and 3.6. By examining the preceding two equations, it is clear that thermal and viscous depths are primarily dependent on operating frequency and fluid density at a given charging pressure. The boundary layer thicknesses tend to decrease for miniature systems operating at a higher frequency and charging pressure.

### 4.5.3 Axial heat flow

The regenerator and the pulse tube are the two most critical components of a pulse tube machine. These elements' temperature profiles typically exhibit a gradient distribution between their cold and hot ends. Normally, when the axial length of these two elements is reduced, the effect of axial heat conduction in the regenerator between the solid matrix screens is increased. See section 3.6.4. Additionally, the direct heat transfer between the hot and cold gas zones in the pulse tube would increase due to the shorter length, deteriorating cooling performance.

Reduced cross-sections and tube thicknesses would aid in this endeavor. Additionally, utilizing new materials in porous media and for the tubes would be very advantageous. These novel materials should have low thermal conductivity in the axial direction. An example of this is the use of PEEK, a semi-crystalline thermoplastic polymer, in place of stainless steel in pulse tubes [98] to reduce axial heat conduction losses. However, a subsequent attempt was abandoned due to brazing and consistent tight sealing complications.

### 4.5.4 Dead volume

Reducing the size of PTC would increase the dead volume losses in the interconnects, which include junctions and capillaries. The total dead volume effect is expected to be greater in miniature-scale devices than in conventional-scale devices. Dead volumes are typically included in systems for various reasons, including the placement of sensors and instrumentation for pressure, temperature, and flow measurement. They are also included to isolate the compressor from the cold-head for heat and vibration isolation. Not to mention its detrimental effect of increasing the system's overall size. Dead volume drives up the compressor swept volume, because the extra gas requires more acoustic power to be compressed to maintain the same pressure ratio without directly adding to the cooling effect. As a result, for miniature PTCs, limiting these dead volumes is crucial.

### 4.5.5 Issues with phase shift mechanisms

The principles and explanation for the requirement for a phase shift mechanism were described in the preceding sections. As previously explained, for optimal cooling efficiency, the mass flow should be in phase with the pressure in the regenerator's center, lagging it at the cold end and leading it at the regenerator's hot end. This condition is primarily met by the use of a phase shift mechanism, and thus their use has been unavoidable up to this point.

The majority of phase shift mechanisms would contribute to the difficulties and complications when used in miniature PTCs. The precise orifice diameter construction becomes more difficult as the size of the orifice type PTCs decreases. Additionally, the possibility of clogging and irreversible flow becomes more apparent. Double-inlet PTCs have the advantage of reducing mass flow through the regenerator and thus lowering regenerator losses. However, circulating flow becomes a potential issue because it can mix the device's hot and cold zones. Proper characterization of their flow impedances may mitigate or even eliminate these effects, but still, as the system's size decreases, this task becomes more difficult. Although the inertance type PTCs are the most efficient of all, the considerably long tube form a significant obstacle to any attempt to build miniature systems. The advantage is that the inertance tube is typically integrated into the reservoir element, and as the system's size decreases, the optimal inertance tube associated with it decreases as well. Nonetheless, inertance-type phase shifters are the most promising candidates for PTC miniaturization.

### 4.5.6 Pressure wave generator

The pressure generator, or oscillator, is a critical component of the PTC system. Any successful effort at miniaturization should consider shrinking the system's compressor. Numerous efforts overlooked compressor miniaturization and relied on a large compressor operating at frequencies above its design point. As a result, they achieved only a moderate degree of success due to the large compressors with large swept volumes.

Several proposed solutions include miniaturizing conventional linear-type compressors; one such compressor operates at 150 Hz and has a swept volume of less than 1 cc [209]. Another option is to use piezoelectric oscillators [210], which have the advantage of operating at extremely high frequencies and possessing a high force-to-size ratio. However, concerns about their small displacements, which result in minimal swept volumes, must be addressed. This problem can be solved either through displacement magnifiers [99] or by coupling the piezoelectric element to a deformable membrane [201].

## 4.6 Miniature PTCs models

The miniaturization of cryocoolers has received increased attention over the last decade. For particular applications, not only the production of low temperatures is needed, but also the size of the equipment plays a significant role. It is clear now that when the size is drastically reduced, the losses, primarily in the regenerator, increase, imposing a minimum size limit below

which PTCs become practically unfeasible. On the other hand, additional factors that must be considered when discussing efficient miniature machines include, but are not limited to, high-frequency operation, small pressure wave generator, and efficient phase shift mechanisms, all of which affect the size, cost, and power density of the machine.

Recently, the literature suggests that miniaturizing PTCs compels the implementation of higher frequency systems [15, 20, 194, 211–213]. In comparison to full-scale devices, these systems are optimized for niche applications such as in-space infrared detectors, high-temperature superconducting devices, and microelectromechanical systems (MEMS) that require cooling power of  $\leq 2$  W, and rapid cool-down [8, 211].

Developing miniature cryocoolers requires using effective methods and tools, primarily for their design and performance analysis. As previously stated, the lack of software tools for optimizing cryocoolers at the miniature level may account for the current ambiguity regarding the level of miniaturization possible with a pulse tube cryocooler. As a result, analytical and numerical models of pulse tube cryocoolers are critical for optimizing their performance, predicting their operation, and engineering novel implementations. However, caution should be exercised when applying these models at the miniature scale due to the apparent discrepancy in dominant phenomena between miniature and conventional scale systems. These computational tools each have their own set of advantages and disadvantages for modeling miniature systems.

Analytic models involving control volume or phasor analysis, as described in section 4.3.2, or even models resembling cryocoolers with analogous components, as described in section 4.3.3, can generate parametric correlations. They are, however, limited at the micro-scale due to the models' numerous simplifications and assumptions, which tend to overlook critical details of the system's flow. These details are necessary for characterizing the parameters that limit the system's performance.

A more effective approach is to employ computational models that are tailored for regenerative cryocoolers. These models are generally one-dimensional, solve the system's governing heat and flow equations, and rely on a set of empirical relations and thumb rules to produce reasonably accurate results. Two well-known examples are NIST's REGEN3.3 [135], which was used to optimize the regenerator in chapter 3, and Sage<sup>®</sup> by Gedeon Associates [184], which demonstrated its reliability and presented well-validated results. Sage<sup>®</sup> is a one-dimensional tool for rapidly solving the steady-state behavior of PTCs; it also takes into account multidimensional optimization. Despite its inability to solve time-dependent behavior, Sage<sup>®</sup> has demonstrated

the ability to make reliable and reasonably accurate predictions for miniature cryocoolers [14, 98, 211, 214], particularly when correlations are deduced from corresponding experimental results.

Additionally, computational fluid dynamics (CFD) models are more accurate and relevant for modeling miniature PTCs because they avoid the simplifications and assumptions inherent in other models. Their exceptional multidimensional capabilities can incorporate intricate flow details that are overlooked in one-dimensional models. CFD models' advantages are that they can account for flow details and other system details such as turbulent models and deforming boundaries, resulting in more accurate performance predictions for pulse tube cryocoolers. Fluent is the most advanced CFD software package available. It has been extensively used to simulate both individual components and entire PTC systems. It has the advantage of incorporating user-defined functions (UDF), which are written in C and compiled into Fluent to modify boundary conditions or account for flow details, i.e., modeling the piston velocity. Due to their relatively lower computational cost, 2-D axis-symmetric CFD models are usually used for PTC systems. Enhancing the outlook and practices of PTC miniaturization can be accomplished through the use of software tools and models, such as CFD simulation, that demonstrate the possibility of PTC miniaturization far beyond what has been accomplished thus far, allowing technical challenges with the compressor, regenerator, and phase shifters to be overcome.

### 4.6.1 Sage<sup>®</sup> modelling

Sage<sup>®</sup> is a commercial graphical user interface that enables the simulation and optimization of underlying engineering model classes such as a spring-mass-damper resonant system, a Stirling-cycle machine, and a pulse tube machine. The user can create customized models by simply linking a set of component building blocks and their associated data values to form a full system representing whatever the user needs to simulate [184]. It has been shown to be an effective tool for developing and optimizing cryocoolers. Sage<sup>®</sup> uses data based on theoretical or empirical correlations to solve the nonlinear model equations via a series of linear approximations. The system is reduced to a sparse matrix containing coefficients of the linearized equations derived from numerical partial derivatives of the evaluation functions. This allows for the rapid solution of PTCs' steady-periodic behavior and delivers multi-dimensional mappings and optimizations.

The Sage<sup>®</sup> model of the inertance pulse tube cryocooler is shown in Figure 4.13. Compressor, transfer line, and cold-head are the model's primary components. These root-model components are further subdivided into several subcomponents representing the regenerator, pulse tube, inertance tubes, heat exchangers, and reservoir. Furthermore, subcomponents have child components

that include gas inlets, heat-flow ends, conductors, and interconnections, which represent mass and heat flow in the system, as shown in Figure 4.13.

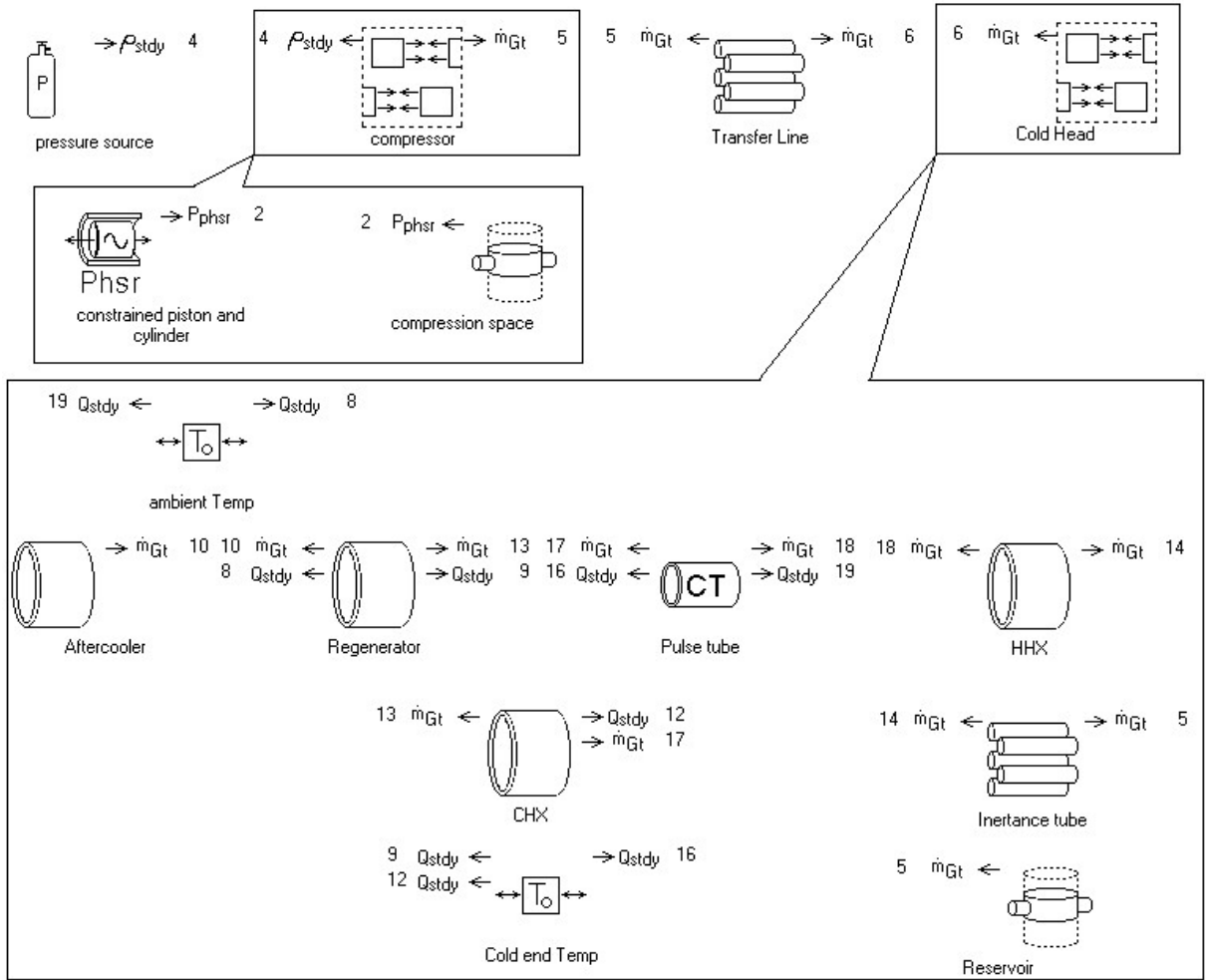


Figure 4.13: Sage<sup>®</sup> model for the simulated pulse tube cryocooler.

#### 4.6.1.1 PTC optimisation in Sage<sup>®</sup>

Initial scaling analysis for PTC is performed using Sage<sup>®</sup> to produce geometry and operating conditions different from those of conventional scale PTC. The user is given considerable flexibility in Sage<sup>®</sup> to define specific inputs and control parameters, such as material characteristics and operating boundary conditions. Numerical calculations, optimizations, and mapping can be performed on parameters such as component dimensions, compressor frequency, piston displacement, porous media characteristics, and cold-end temperature.

The optimization process begins with the assumption that the length and diameter of the regenerator are 30 and 10 mm, respectively. These initial guesses are derived from the findings in section 3.7.1, the REGEN3.3 simulation results listed in Table 3.5, and the results from the ideal regenerator's inefficiency results. The operating conditions include an average pressure of

3 MPa, a frequency of 100 Hz, and a cold end temperature of 110 K. The pressure and frequency values were chosen based on standard conditions, while the cold end temperature value was set to ensure that the device could achieve such a temperature, especially as these values will be used as a foundation for building more compact coolers.

The thermal penetration depth,  $\delta_{th}$  in equation 3.5 for the above operating conditions is approximately 140  $\mu m$ . For the pulse tube process to be adiabatic and maintain a buffer zone between the cold and hot gas zones, the radius of the pulse tube should be significantly larger than the thermal penetration depth. As a rule of thumb the radius of the pulse tube should be 20-25 times greater than the thermal penetration depth [15]. The initial guess for the tube's diameter was 8 mm, and the initial length is assumed to be the same as the regenerator. It is worth noting that the diameters must be set in order to be able to select from the standard commercially available tube catalog.

The regenerator was modeled as a porous zone with #635 stainless steel mesh, which has a wire diameter of 20  $\mu m$ , and #325 phosphor bronze wire meshes were incorporated into the heat exchanger models with a wire diameter of 35  $\mu m$ . The regenerator's filling was chosen so that the hydraulic diameter,  $D_h$ , is approximately 32  $\mu m$  as projected from section 3.7.3 and Table 3.5.

The initial guess settings resulted in tremendous input compressor power and very low COP, as listed in Table 4.5. Hence, two mapping iterations were performed. The compressor's acoustic power and axial conduction degradation factor are taken into account in the first iteration. For the second iteration, the compressor diameter and swept volume were reduced so that  $\sim 10$  W of input power was determined to keep it suitable for miniature devices and to allow for a fair comparison with the various scaled models. Meanwhile, the geometric and operating parameters were tuned to achieve a higher net cooling power and COP. To identify the optimal geometry and operating conditions of the miniature PTC system, mappings of various parameters were performed. Throughout the optimization process, the operating pressure was maintained at 3 MPa, while the frequency was tuned to maximize the value of COP. The output optimized geometry and operating parameters and the system performance results are all listed in Table 4.5.

As previously stated, cooling performance is primarily determined by the proper phasing of pressure and mass flow rates. The transmission line model was initially used to estimate the initial diameter and length of the inertance tube, as well as the reservoir volume. It was previously established that for efficient cooling, the phase shift at the inlet of the hot heat exchanger should be close to  $60^\circ$ , implying that the phase at the inertance line's entrance should be slightly higher. After some runs, the initial guess values of 1 m, 3 mm, and 10 cc of inertance tube length,

**Table 4.5:** Geometry and operating parameters of Sage<sup>®</sup> PTC optimisation model

Element	Parameter	Initial guess	1st iteration	2nd iteration
Regenerator	Length (mm)	30	30	35
	Diameter (mm)	10	10	9.5
Pulse tube	Length (mm)	30	28	33
	Diameter (mm)	8	7	6.5
Aftercooler	Length (mm)	10	2	2
	Diameter (mm)	10	10	9.5
HHX	Length (mm)	5	2	2
	Diameter (mm)	8	7	6.5
CHX	Length (mm)	5	2	2
	Diameter (mm)	10	10	9.5
Inertance tube	Length (mm)	1000	1400	1350
	Diameter (mm)	1.5	1.5	1.5
Transfer line	Length (mm)	100	20	5
	Diameter (mm)	3	3.5	3.5
Reservoir	Volume (cc)	10	8	8
Compressor	Stroke (mm)	5	3	0.5
	Diameter (mm)	23	13	25
Operating parameters	Average pressure (MPa)	3	3	3
	Cold end temperature (K)	110	110	110
	Frequency (Hz)	100	110	112
Performance	Acoustic power(W)	629	35.1	10.02
	Net cooling (W)	3.958	2.34	0.293
	COP %	0.62 %	6.67 %	2.9 %

inertance tube diameter, and reservoir volume were adopted. This resulted in a phase shift of about  $67^\circ$  according to the transmission line model. After that, the length and diameter of the inertance tube, and the reservoir volume were optimized for maximum COP and net cooling power.

Similarly, the geometry parameters for the aftercooler, hot heat exchanger, cold heat exchanger, pulse tube, and regenerator were tuned. The diameter of the aftercooler and cold heat exchanger is set to match the regenerator's length, while the diameter of the hot heat exchanger is set to match the diameter of the pulse tube. To avoid the high-pressure drop, one tapered transition junction is inserted between the cold heat exchanger and the pulse tube, and another between the hot heat exchanger and the inertance tube. Figures 4.15 to 4.14 illustrate the simulated curves of predicted net cooling power against the corresponding scaled parameter. The pressure ratios of the aftercooler and cold heat exchanger were held constant at 1.13 and 1.1, respectively.

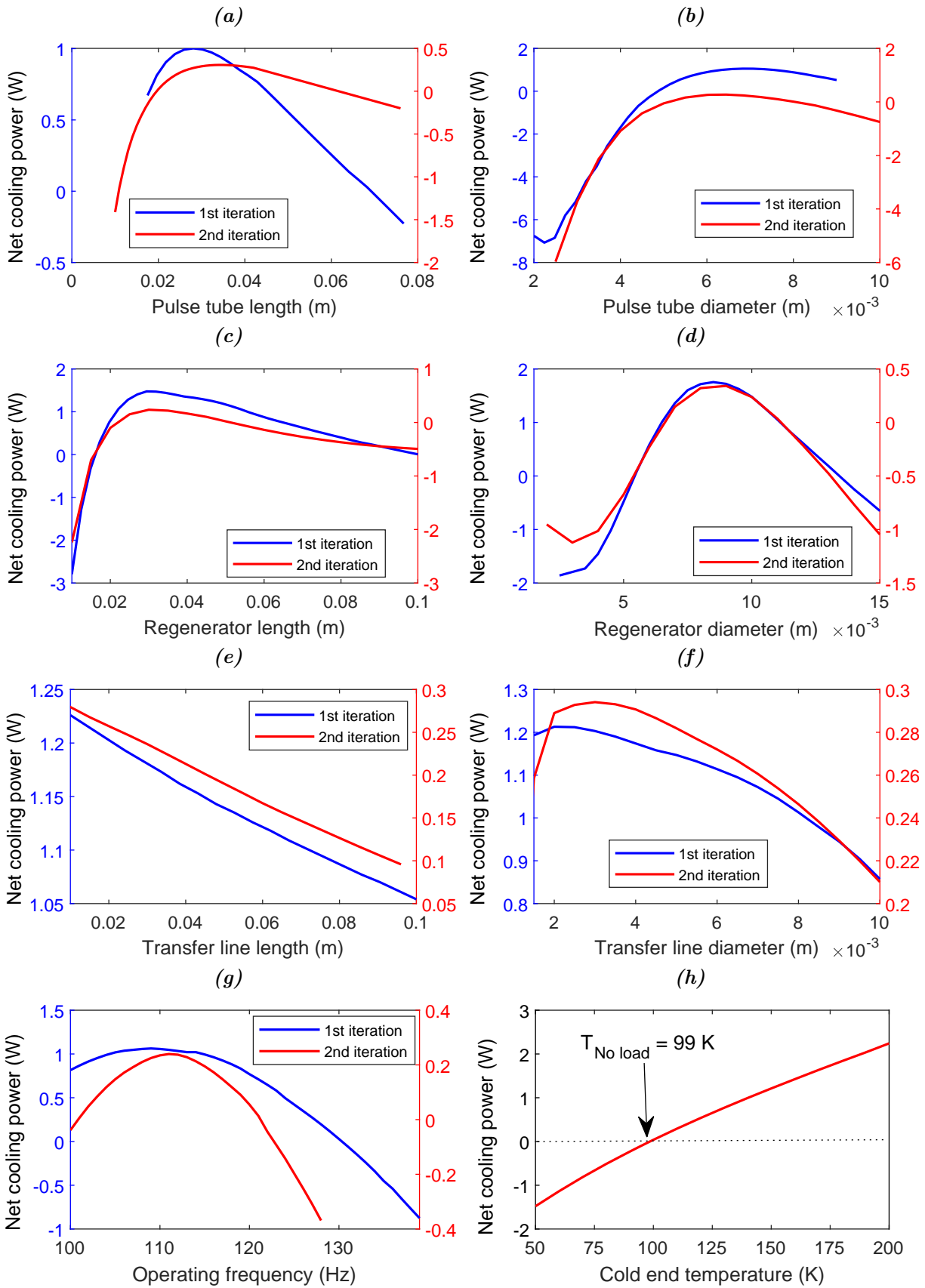


**Figure 4.14:** Sage predicted cooling power versus (a) pulse tube length. (b) pulse tube diameter. (c) regenerator length. (d) regenerator diameter. (e) transfer line length. (f) transfer line diameter. (g) operating frequency. (h) cold end temperature.

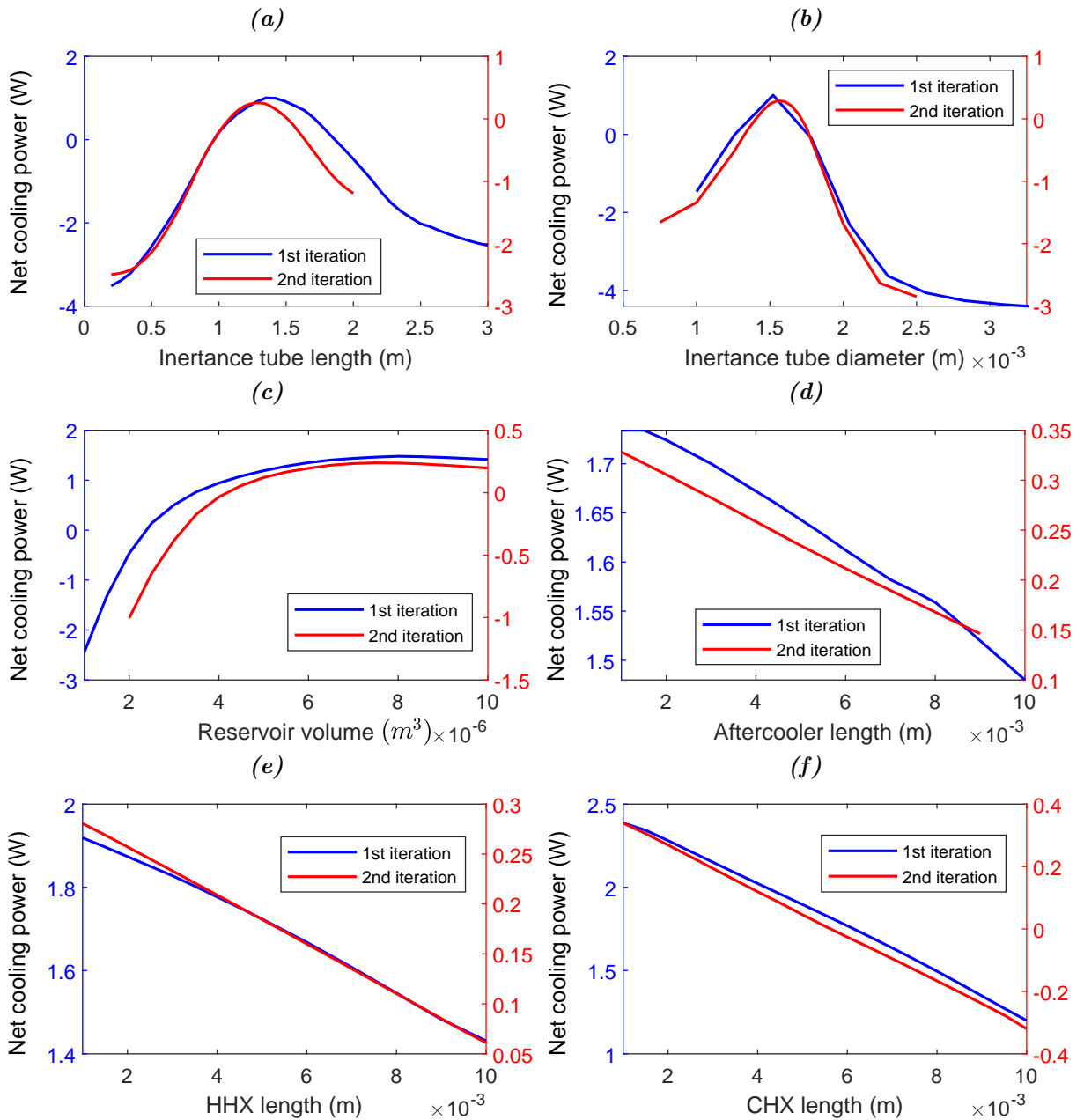


**Figure 4.15:** Sage predicted cooling power versus (a) inertance tube length. (b) inertance tube diameter. (c) Reservoir volume. (d) Aftercooler length. (e) hot heat exchanger length. (f) cold heat exchanger length.

The Sage<sup>®</sup> optimization was concluded by producing simulated load curves of heat lift from the cold end versus cold end temperature. This is shown in Figure 4.14h, where an ultimate (no-load) cold end temperature of approximately 99 K is predicted. Finally, the geometry and operating conditions obtained by the initial scaling investigation were considered suitable for the CFD modeling analysis to commence.

### 4.6.2 CFD numerical modelling

Following the preliminary optimization analysis with Sage<sup>®</sup>, a two-dimensional axis-symmetric base CFD model was created using the geometry and the operating parameters listed in Table 4.5. The base model simulation used the same porous media characteristics as in section 4.4.2. However, unlike the previous CFD model, this model incorporates isothermal wall conditions for the cold heat exchanger's outer walls at varying cold end temperatures in order to investigate net cooling power. The advantage is that the models reach periodic steady-state significantly faster and more accurately. Additionally, the hot heat exchanger and aftercooler outer walls were modeled isothermally at 300 K, and the compressor, pulse tube, and regenerator outer surfaces were modeled with adiabatic boundary conditions.

A fine mesh with approximately 8000 nodes was used, employing high-density mesh nodalization in high temperature-velocity gradients near junction geometries. This was sufficient to produce a solution that was reasonably accurate and had acceptable grid independence. A double-precision, transient pressure-based solver was used, along with enabling relative velocity flow formulation in the porous media. To account for possible oscillatory turbulent flow in the transfer and inertance tubes, a standard k-omega turbulence model was used in conjunction with a low Reynolds number correction. As a result, the model's periodic steady-state convergence was greatly improved.

Pressure discretization using "PRESTO" was used in conjunction with "PISO" pressure-velocity coupling, which is highly recommended for all transient flow calculations in Fluent [119], and all other quantities were discretized using a second-order upwind scheme. Additionally, for the time-varying signals, a second-order time transient scheme was chosen. These settings were selected to achieve the model's best and fastest convergence. The model accurately reached periodic steady-state convergence with 250-time steps per cycle and at least 230 iterations per time step. The iterative implicit numerical solver achieves an overall convergence of  $10^{-8}$  for continuity, velocities, k, omega, and  $10^{-12}$  for energy.

The computational effort was significantly reduced by first initializing the model at 300 K, and then solving the model iteratively using the steady-state solver to generate the well-known temperature gradients in the pulse tube and regenerator elements. The output temperature distribution for the steady-state initialization at 180 K is shown in Figure 4.16. Following that, the transient simulations were initiated using the unsteady solver.

Due to the fact that a pulse tube system can only achieve a periodic steady-state condition, the models were iterated until approximate periodic steady-state conditions were achieved. The

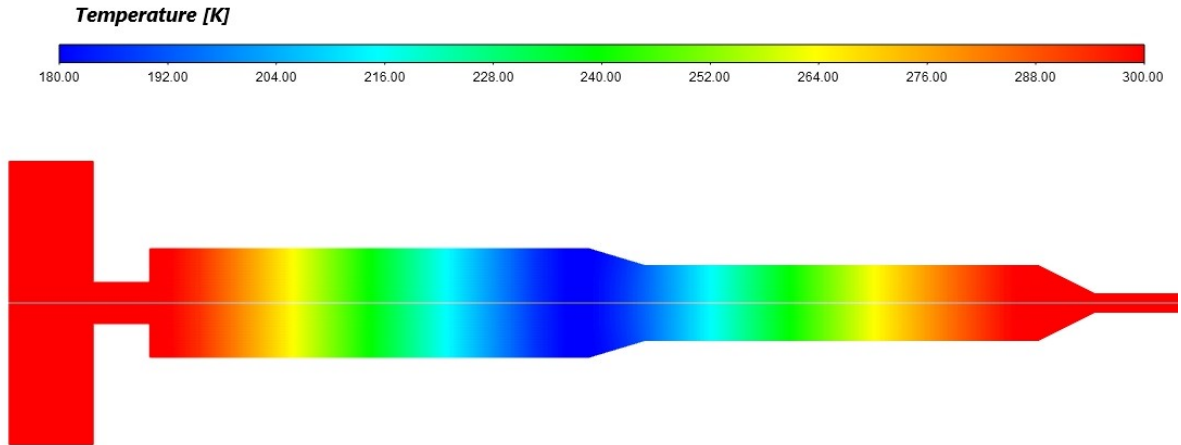


**Figure 4.16:** Initial temperature distribution for the CFD base model for 180K cold end temperature, the reservoir and inertia tube are omitted.

convergence of the models was assessed through the reporting of output variables and their cycle-average values. These include the mass flow, pressure, velocity, and enthalpy flow at each component's inlet, as well as the heat flux through the walls. Post-processing was performed using Matlab<sup>®</sup> to calculate cycle-average values, determine the enthalpy balance, and determine the phase shift between the pressure and velocity at each component's inlet. These Matlab<sup>®</sup> codes are reported in Appendix D. Figure 4.17 depicts the temporal behavior of cycle-average energy fluxes into and out of the miniature PTC model for cold end temperature of 200 K. It demonstrates unequivocally that the model is reaching a periodic steady-state. The input

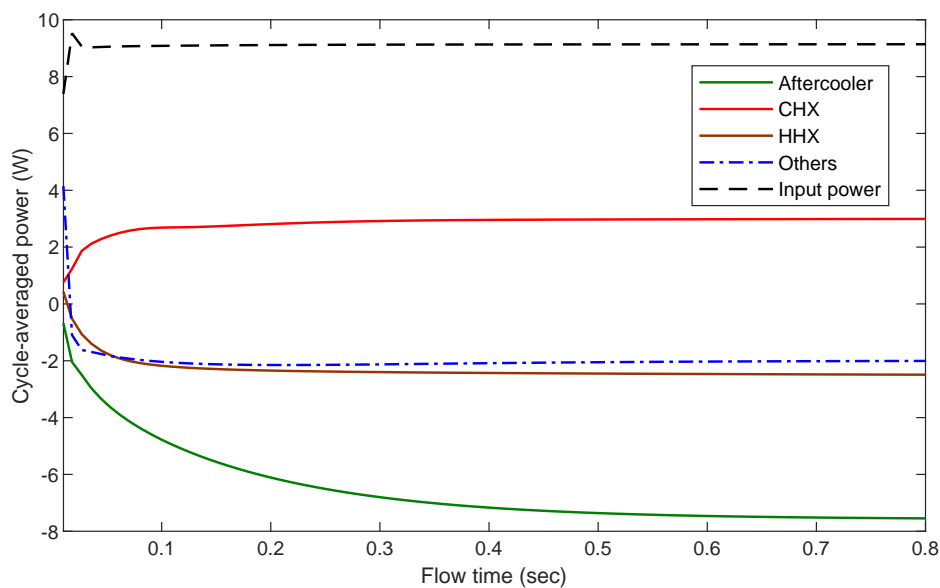


**Figure 4.17:** Time response for cycle-averaged energy flow for cold end temperature of 200 K.

power is determined by the "total heat transfer rate" at the compressor's piston. Likewise, the

aftercooler and heat exchangers' net heat fluxes are integrals of the "total surface heat flux" on these components' outer walls. In Figure 4.17, the "others" heat flux includes heat fluxes from the transfer line, inertance tube, and reservoir.

# Chapter 5

## Results and Discussion

This chapter summarizes the previous models' results. The ideal regenerator model and its simplified CFD model are discussed first in the chapter. The findings of the one-dimensional numerical model of the pulse tube element are then presented. The two-dimensional axisymmetric CFD model for the entire IPTC system is next presented. Following that, the results of the CFD optimization simulation for the base miniature model are reported. Finally, these are used to construct derived ultra-miniature PTC models that are predicted to produce cryogenic cooling.

### 5.1 Ideal regenerator<sup>5</sup>

#### 5.1.1 Ideal regenerator numerical model

This section presents the results of the ideal regenerator model. The gas and matrix temperature profiles during heating and cooling periods are depicted in Figure 5.1a. It can be demonstrated that as the temperature of the matrix material increased for all spatial elements during the heating period, the hot gas temperature gradually reduced as it crossed the regenerator, resulting in the heating of all matrix elements. The cold gas was heated as it went through the matrix,

---

<sup>5</sup> The results from section 3.5 are reported here. This section is reproduced from previous work by the author, see [117].

causing the matrix to cool down. As illustrated in Figure 5.1b, the algorithm converged and settled to a solution in which the temperature difference between the matrix and gas was minimal; this occurred after increasing the number of time and space nodes.

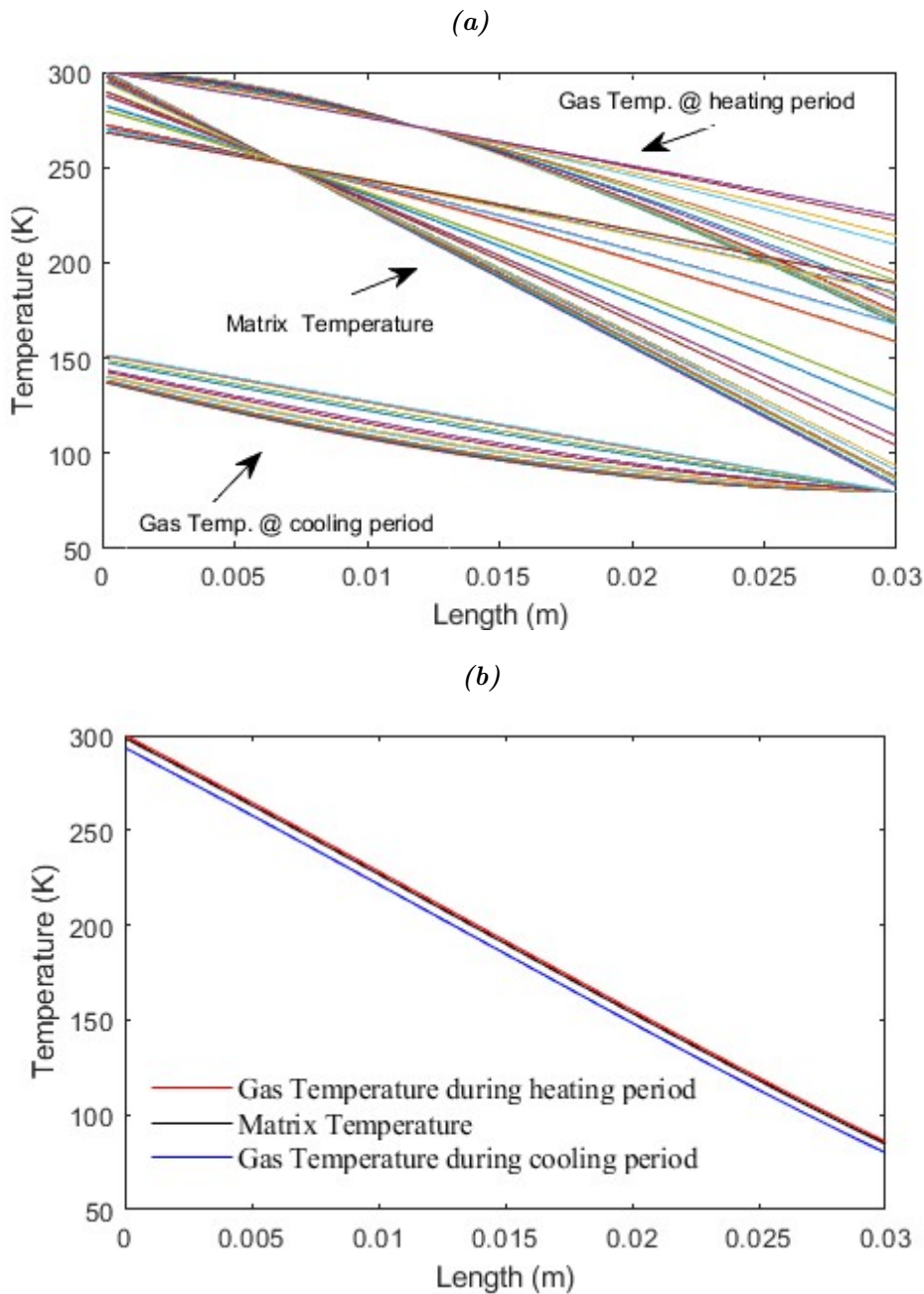


**Figure 5.1:** (a) Matrix and gas temperature variations during the heating and cooling period. (b) The final temperature profiles as they converge to a solution with increasing  $N_x$  and  $N_t$ . Reproduced from [117].

Dimensional and parametric analyses are critical for the design of an efficient regenerator. The relationship between the regenerator diameter and its efficiency (Ie) for various lengths is depicted in Figure 5.2a. Figure 5.2b illustrates the relationship between regenerator length and inefficiency (Ie) for a variety of regenerator diameters. These were based on an ideal case interpretation of the

thermal interaction between the working gas and the matrix material; consequently, conduction and viscous losses were not considered. Additionally, it was assumed that the matrix and working gas's thermal properties were constant regardless of the tube's temperature variation.

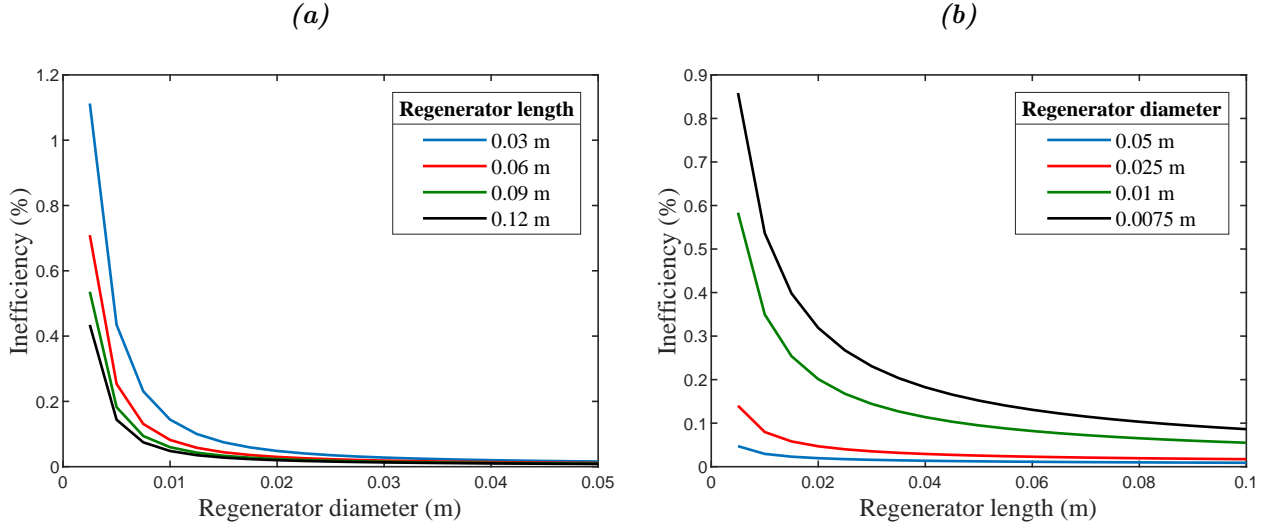


**Figure 5.2:** (a) The relation between the regenerator diameter and  $I_e$ . (b) The relation between the regenerator length and  $I_e$  (the matrix screen mesh size is  $150 \times 150$  and has a wire diameter of  $63 \mu\text{m}$ ). Reproduced from [117].

While an abrupt change in inefficiency was observed for diameters less than 0.01 m and lengths less than 0.03 m, the difference in inefficiencies was typically minimal for diameters larger than 0.025 m and lengths larger than 0.06 m. As a result, any attempt to reduce the regenerator element's size must exercise extreme caution to avoid diminishing its operation. The number of heat transfer units (NTU) is a non-dimensional parameter that indicates the heat transfer capacity of a regenerator. It is directly related to the regenerator's size, flow, and thermodynamics, where high NTU indicates high regenerator effectiveness. The inefficiency decreased as the regenerator's length and diameter increased, i.e., NTU increased as well, as the regenerator's mass and total heat transfer area increased.

Mesh screens are often used in various heat exchange configurations in many research and industry applications, including air vents, cryogenics equipment, cryocoolers, cold heads, and heat pipes. Figure 5.3a displays the relation of ( $I_e$ ) with matrix mesh size. It was evident that as the screen mesh size increased, i.e., the number of openings per inch increased, the porosity and the hydraulic diameter decreased, causing the total heat transfer area to increase, resulting in decreasing the regenerator's inefficiency ( $I_e$ ).

Figure 5.3b illustrates the relationship between inefficiency ( $I_e$ ) and the screen wire diameter for different mesh sizes. It can be asserted that increasing the wire diameter decreases the re-

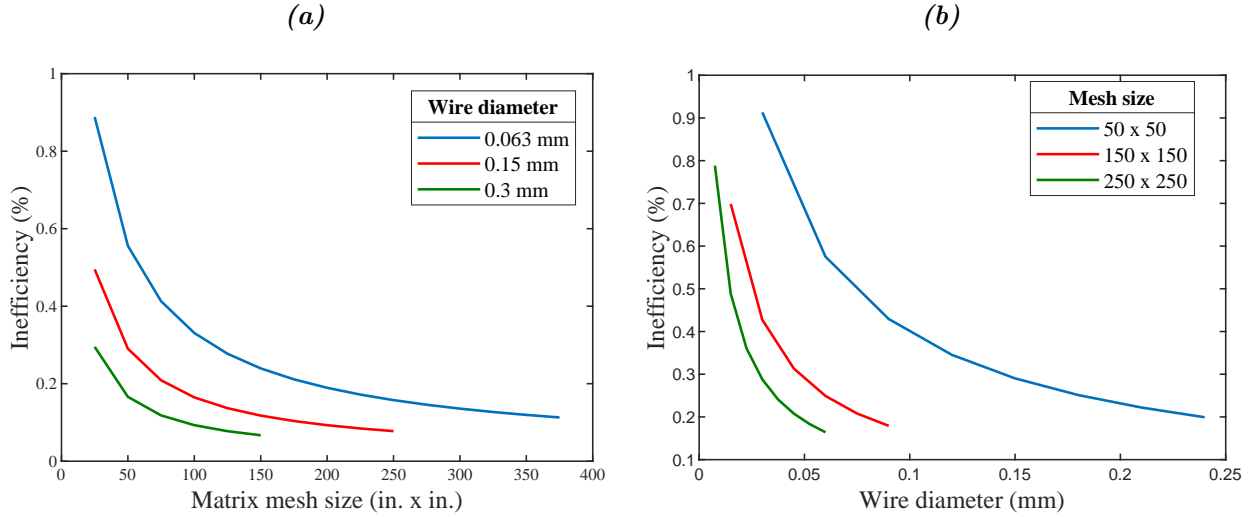


**Figure 5.3:** ( *a* ) The relation between the matrix mesh size and  $I_e$ . ( *b* ) The relation between the mesh wire diameter and  $I_e$  for several mesh sizes (for a regenerator of 7.5 mm diameter and 30 mm length). Reproduced from [117].

generator’s inefficiency because it decreases the matrix’s porosity, which is inversely proportional to the regenerator’s mass, thereby increasing the total heat transfer area. As illustrated in Figure 5.3b, the regenerator’s inefficiency decreases as the regenerator’s wire diameter increases for the same mesh screen size, which is true for all mesh screen sizes. In the non-ideal case, when the wire diameter and mesh size increase, the pressure drop increases as the gas free-flow area decreases.

The relationship between the volumetric flow rate and inefficiency is illustrated in Figure 5.4a for multiple regenerator diameter to length ratios ( $D/L$ ). As illustrated in Figure 5.4b, as the volumetric flow rate increases, the inefficiency increases due to a decrease in the total number of heat transfer units ( $NTU_{Total}$ ). Keeping the same inefficiency as flow rates increases requires increasing the matrix’s total heat transfer, which compels a larger regenerator’s diameter and length.

For the previously highlighted case,  $NTU_{Total}$  is 63, and the inefficiency ( $I_e$ ) was found to be approximately 0.21% with  $39.8 \leq Re \leq 365$ . This inefficiency level results in a thermal loss of  $\sim 0.39$  W for the regenerator, demonstrating that adequate regenerator performance can still be achieved with such small dimensions.

### 5.1.2 Ideal regenerator CFD evaluation model

This section presents the results of the regenerator’s CFD evaluation model. The model assumed that the regenerator’s initial temperature was  $T_h$ . Figure 5.5a exhibits the temperature distri-

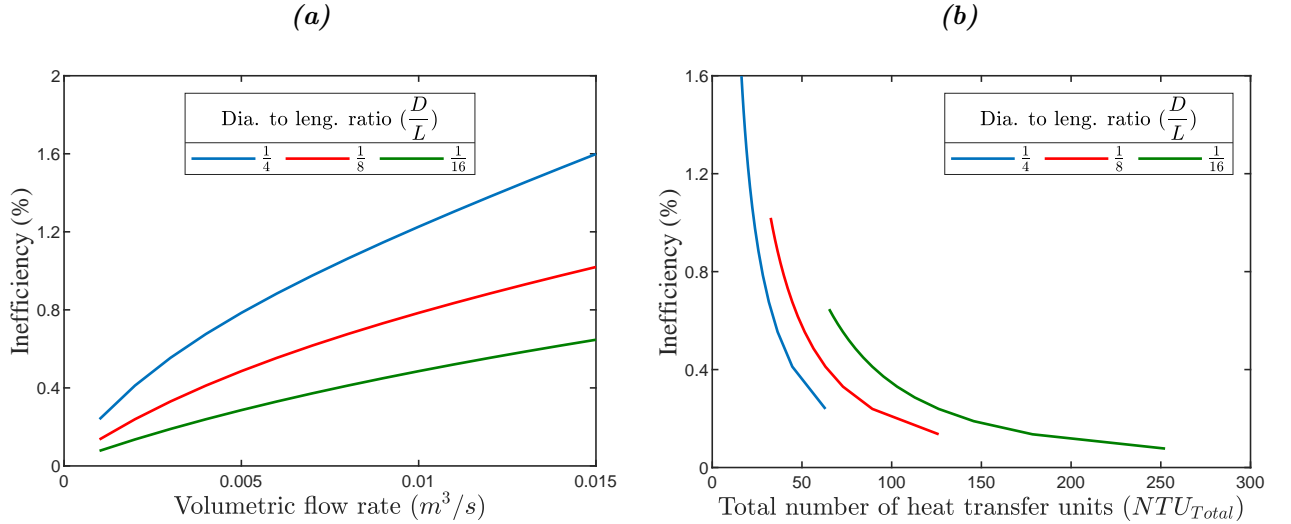


**Figure 5.4:** (a) Effect of increasing the volumetric flow rate on the regenerator's inefficiency ( $I_e$ ) for different regenerator diameter to length ratios. (b) Relation between  $NTU_{Total}$  and  $I_e$  for the same regenerator diameter to length ratios. Reproduced from [117].

butions predicted by the CFD model for the regenerator section at four different time instants. The temporal change in the regenerator's average temperature is depicted in Figure 5.5b. It illustrates the temperature dynamics during heating, and cooling cycles as the cold/hot gas flows into and out of the regenerator. Additionally, it demonstrates a stable uniform temperature distribution following approximately 80 seconds at an average temperature of 195 K. The contour plot in Figure 5.5a confirms this uniform distribution after an 80 seconds flow time.

The temperature profiles along the regenerator's center axis after several time instants are shown in Figure 5.5c. As can be seen, the temperature distribution is linear along the regenerator's length after 80 seconds. The similarity in temperature profiles between Figure 5.5c and Figure 5.1b demonstrated that the ideal regenerator model accurately described the regenerator's thermal interaction. Figure 5.6 displays the temperature changes near the hot and cold ends during the heating and cooling cycles. Assuming steady flow, the inefficiency is calculated using equations 3.14 or 3.15 and was found to be 2.5 percent for cooling and 2.3 percent for heating, respectively. The two-dimensional model demonstrated that stainless steel mesh size #635 is an excellent fit for a miniature cryogenic regenerator's filler material.

Although the model of the ideal regenerator was simplified to account for various assumptions and constraints, it moderately predicted the thermal behavior inside the regenerator and estimated the effects of the design parameter on its performance. However, for more consistent and accurate results, dimensional and non-ideal models that account for flow details are beneficial

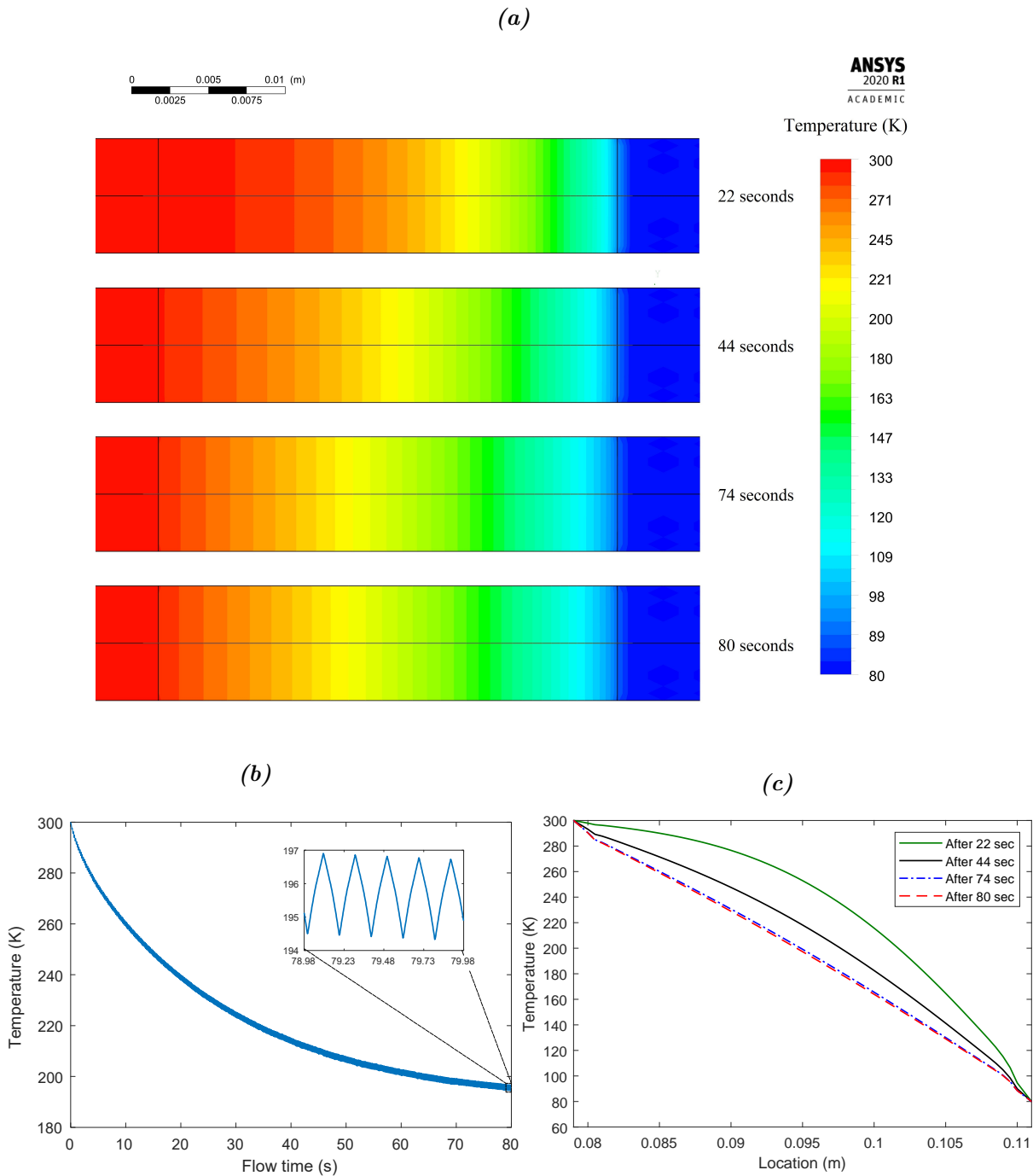


**Figure 5.5:** (a) Temperature contours after several flow times. (b) Average temperature versus flow time. (c) Temperature profiles across the regenerator’s center axis after different flow times. Reproduced from [117].

for any design or optimization efforts involving the regenerator element or the PTC system as a whole.

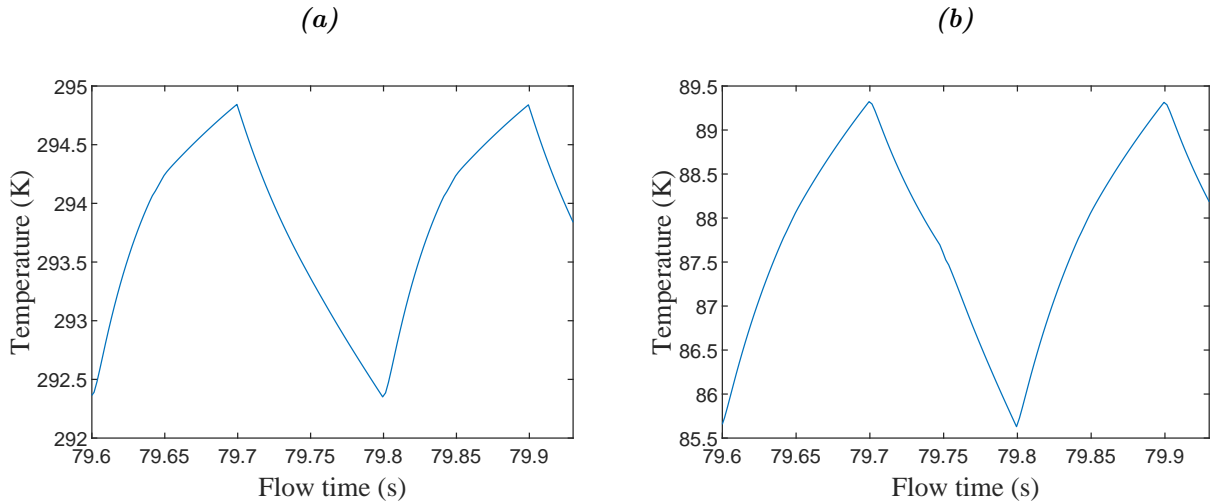


**Figure 5.6:** (a) Temperature changes during cooling and heating periods at the regenerator's hot end. (b) Temperature changes during cooling and heating periods at the regenerator's cold end. Reproduced from [117].

## 5.2 1-D numerical pulse tube element model<sup>6</sup>

### 5.2.1 Application of the model

Figure 5.7 shows the tube, orifice and the reservoir elements where the tube area, length, average pressure and charging pressure were set to  $10^{-3} \text{ m}^2$ , 0.1 m, 3 MPa and 0.3 MPa. The hot and cold end temperatures were set to 300 K and 70 K, respectively, and the orifice flow conductance  $C_{or}$  is set to  $10^{-8} \text{ m}^3 \cdot \text{Pa}^{-1} \cdot \text{s}^{-1}$ .

### 5.2.2 Temperature profiles

First, the simulation was performed at 10 Hz for a 10 cm long tube. Temperature profiles varied depending on the pressure cycle. As previously predicted, the code demonstrated that the only steady-state possible was a periodic steady-state. This state is reached after approximately ten cycles.

Figure 5.8a illustrates the steady-state temperature profiles converging toward a solution for four different corresponding pressure cycle points with 10 Hz operating frequency. It demonstrates clearly that the temperature distribution along the tube length is not uniform with respect to the pressure cycle, as indicated by the intersections and overlapping of different profiles. Figure 5.8b depicts temperature profiles for the 20 Hz case. The resulting temperature profiles are more uniform than in the previous case. The profiles are more uniform across the tube, and regardless of the pressure cycle location, the temperature settles to the desired value near the cold end for all temperature profiles.

<sup>6</sup> The results from section 4.4.1 are reported here. This section is reproduced from previous work by the author, see [165].

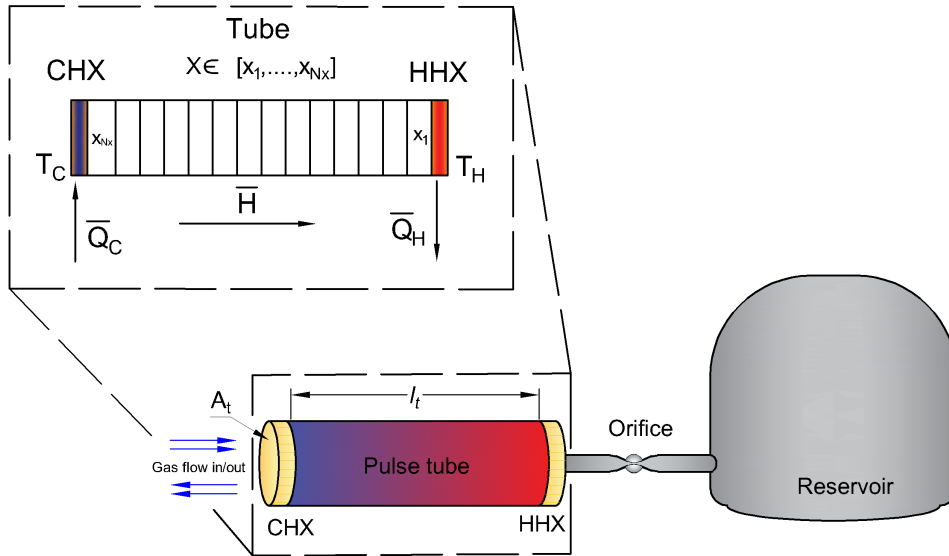


**Figure 5.7:** Schematic diagram of the tube, orifice and the reservoir elements with the tube physical and thermodynamic parameters along with the space grid shown in the zoomed-in diagram. HHX and CHX are kept at 300 K and 70 K, respectively. Reproduced from [165].

Following that, the model was then run at a higher operating frequency of 80 Hz, as illustrated in Figure 5.8c. The temperature profiles had nearly the same general shape as those obtained with a 20 Hz operating frequency. However, it was observed that the cold region was enlarged, and the temperature profiles are pushed closer to the hot region, which is not desirable in the pulse tube system. The simulation results suggest that the optimal operating frequency for this system appears to be near 20 Hz. This proves that an orifice-PTC with such settings is more efficient for frequencies near 20 Hz.

It can be noticed from Figure 5.8c that the temperature profiles are distributed uniformly across the shortened length. This suggests that the optimal tube length for the 80 Hz case is significantly less than 10 cm, where the figure suggests that it is closer to 3 cm. The findings imply that when operating at high frequencies, reducing the length of the pulse tube element is hugely important. The input acoustic power increases correspondingly as the velocity at the cold end and the mass flow rate increase with frequency. As a result, downsizing the system is crucial for reducing overall gas volume and, hence, the input power.

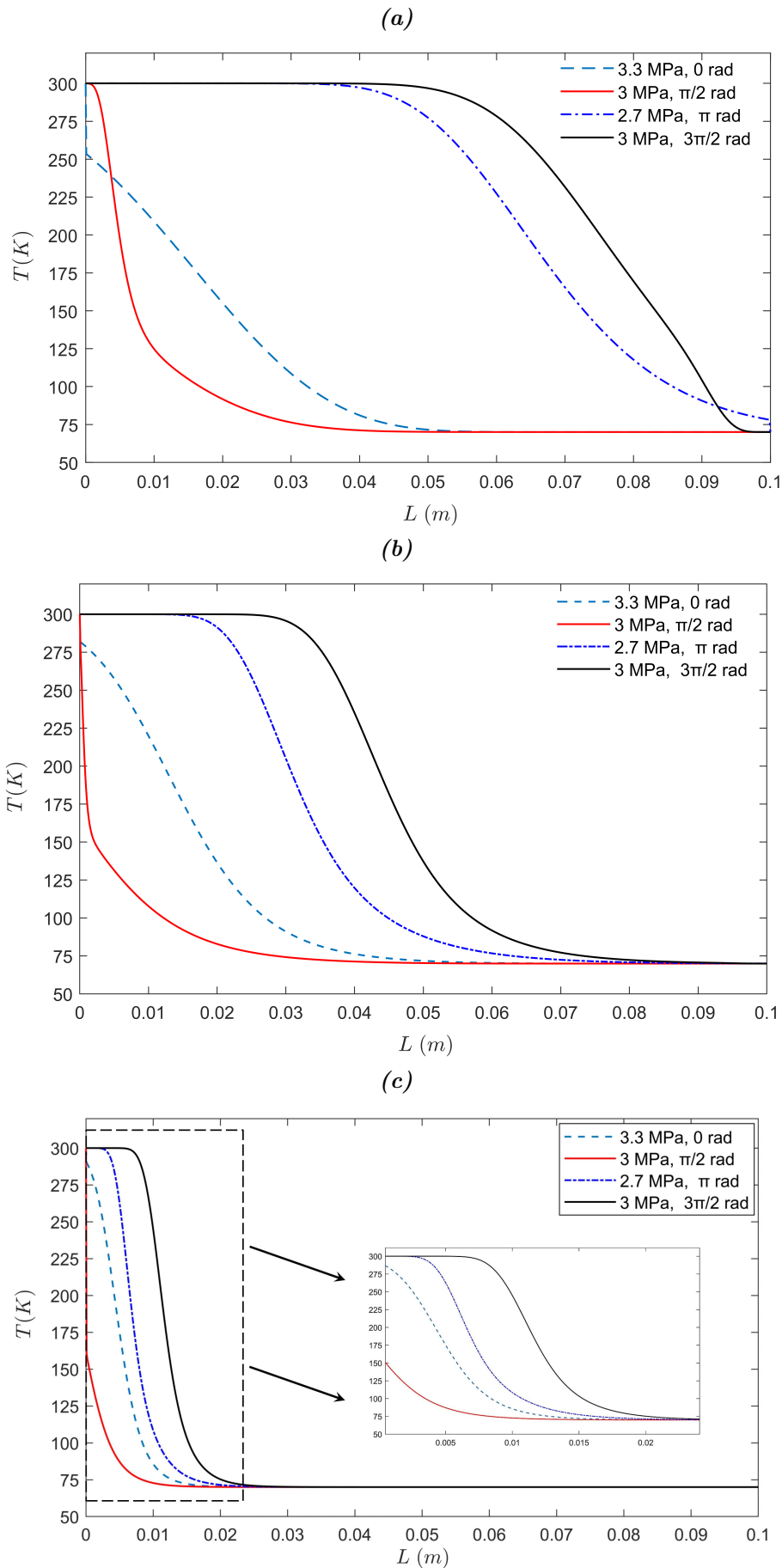


**Figure 5.8:** (a) Temperature profiles for OPTC with 10 Hz. (b) Temperature profiles for OPTC with 20 Hz. (c) Temperature profiles for OPTC with 80 Hz. Reproduced from [165].

### 5.2.3 Enthalpy and cooling power

If an ideal regenerator is assumed, the analytical values for cooling power, heat removed from the hot heat exchanger, and thus enthalpy flow through the tube, are given by [159, 176]:

$$\dot{Q}_c = \dot{Q}_h = \dot{H}_{pt} = \frac{1}{2} \cdot C_{or} \cdot p_1^2. \quad (5.1)$$

Thus, the tube's ideal enthalpy flow is determined to be 450W. For the reasons stated previously, a 20 Hz operating frequency is further investigated. Hence, the mass flow rate near both the cold and hot ends is depicted in Figure 5.9. The mass flow rate is greater at the cold end than at the hot end due to the higher density and velocity of the gas flowing near the cold end.

Equation 4.3 relates cooling power to enthalpy flow, which is dependent on the mass flow rate near the cold end. The enthalpy flows at the cold and hot ends are estimated by determining the time-average value of the mass flow-temperature product at the cold and hot ends; these are  $\sim 420$  W and 434W, respectively. The discrepancy between these values is primarily due to discretization errors, physics simplifications (e.g., the momentum equation), and imprecise characterization of the orifice flow conductance or the pressure change in the reservoir caused by the gas oscillating in the tube. Equation 4.8 suggests that the approximated cooling power is around 470 W with a phase shift angle of 0.3623 *rad*. The imbalance exists here because the model is based on several assumptions and does not account for additional losses and factors in the regenerator, reservoir, and other elements. As such, it is possible to interpret it as a best-case scenario analysis.

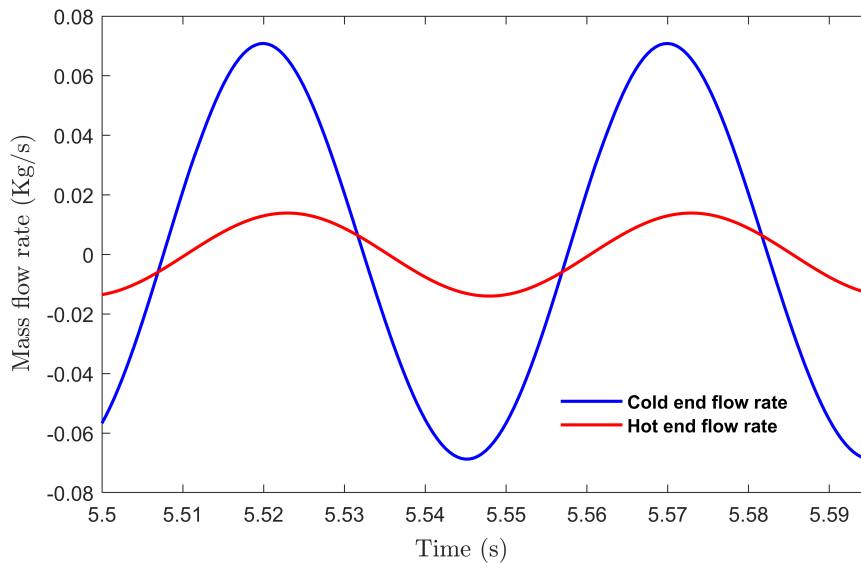


**Figure 5.9:** Mass flow rate at the hot and cold ends. Reproduced from [165].

### 5.3 2-D CFD axis-symmetric for inertance PTC<sup>7</sup>

#### 5.3.1 Temperature-time profile & validation

This section describes the temporal changes in the gas temperature for each of the three previous cases and compares the results to the experimental data. The simulated cool-down time of the cold end from room temperature for the PTC, as well as the temperature-drop history of the cold heat exchanger, are shown in Figure 5.10a for three different operating frequencies ( $f = 20, 50$  and  $120$  Hz). The thick stripes visible in the plots are caused by the cyclic pattern of the temperature profile over the simulated flow time. Among the three frequencies examined, the figure demonstrates that the best performance is obtained at  $120$  Hz. According to the simulations, when operating at  $120$  Hz, the system provides a faster cool-down time and a lower quasi-steady-state temperature. In comparison, the system performed the worst at the lowest frequency of  $20$  Hz, which is reasonable considering that the system was developed for high-frequency operation. The justification is that when the system operates at a higher frequency, it cools more rapidly due to the increased pressure ratio at the cold heat exchanger.

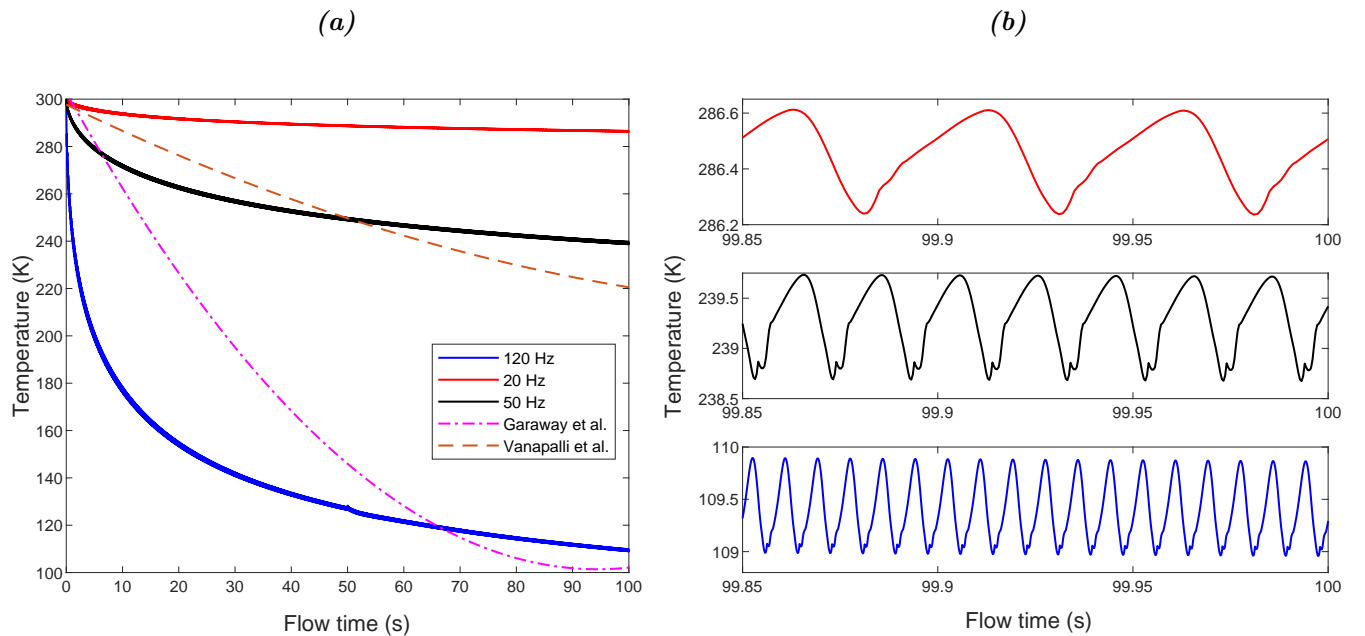


**Figure 5.10:** (a) Minimum gas temperature at the cold heat exchanger for three different frequencies, Vanapalli et al. [96], and Garaway et al. [14]. (b) Gas temperature cycles near the end of the simulations. Reproduced from [200].

Figure 5.10b shows the cyclic transient gas temperature in a zoomed-in time scale near the end of the simulations (i.e., 99.85 –100 seconds) for the three operating frequencies. The periodic variations that form the thick stripes in Figure 5.10b demonstrate that the gas temperature

<sup>7</sup> The results from section 4.4.2 are reported here. This section is reproduced from submitted work by the author, see [200].

varies with time, even over extended time periods. Thus the PTC system can achieve only a steady periodic state.

The temperature spectra for the three different frequencies are shown in Figure 5.11. As can be seen, the pressure is sinusoidal, and the signals can be expressed using fundamental and harmonic terms. The experimental system described in [15, 96, 201] reached 100 K in approximately 330 seconds using a 26 g thermal mass at the cold end with an average heat capacity of  $9.26 \text{ J.K}^{-1}$ . The relatively long cool-down time was primarily due to the large compressor used in this experiment and the difference in the solid media properties.

Garaway et al. [14] subsequent's effort modified the previously constructed miniature system, primarily by incorporating a new, smaller commercial linear compressor capable of producing a higher frequency of 150 Hz. Figure 5.10a depicts the numerical and experimental results for cool-down times plotted together. As can be seen, the speed with which the cryocooler cools down was significantly increased in the Garaway case [14]. Their modifications sped up the cooling process, with the cryocooler reaching 100 K in less than 100 seconds. Their findings support the simulation's predictions when a small compressor with reduced piston displacement is used, since operating at high frequencies causes the gas to oscillate over a much smaller swept volume. Figure 5.10a demonstrates that the CFD simulation described here is a highly predictive tool, as it can generate notably precise performance predictions for pulse tube cryocoolers. As a result, there is considerable confidence in their applicability to miniature systems, thus in their ability to optimize designs.

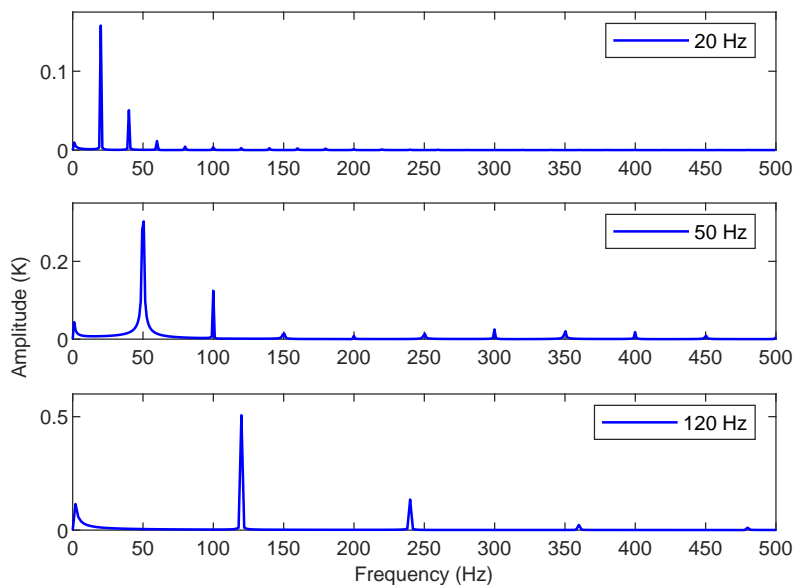


**Figure 5.11:** Frequency spectrum for the gas temperature cycles near the end of the simulations, for three pulse rates. Reproduced from [200].

### 5.3.2 Spatial temperature distribution

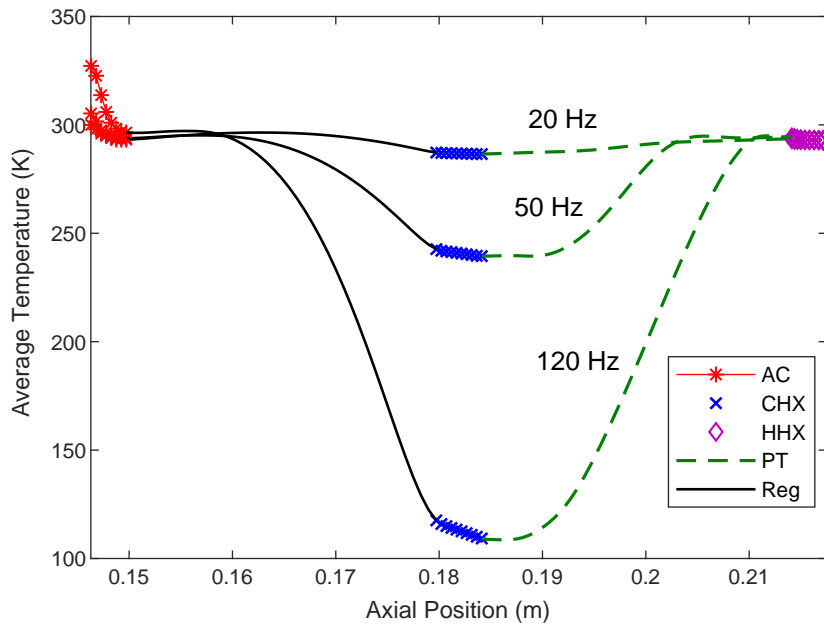
The spatial changes in the gas temperature for three different cases are presented in this section. Figure 5.12 displays the final temperature distributions along the symmetry axis, beginning at the aftercooler element's entrance and ending at the HHX's exit; for three different frequencies, the figure clearly depicts the gradient trend in the temperature of the regenerator and pulse tube elements, which corresponds to well-known data trends in similar systems.

Figure 5.13 illustrates the steady-periodic temperature contours for the three simulated cases. In contrast to the 20 Hz case, a temperature buffer zone is visible in the 120 Hz case. The buffer zone in the center of the pulse tube maintains and isolates the temperature gradient between the cold and hot ends of the tube. On the other hand, the bullet shape seen at the two lower frequencies indicates a lack of separation between cold and hot regions and a contraction of the middle buffer zone, resulting in a significant deterioration of the cooling process. This phenomenon is explained by the fact that the acoustic power density for the system is proportional to its operating frequency [211]. As system size decreases, the system's operating frequency must increase to maintain the same acoustic power density. In the studied system, the elements' dimensions are kept constant for all cases. The void volume in the pulse tube element decreases as the operating frequency decreases; thus, operating at low frequencies necessitates a larger system. Hence, operating the current system at lower frequencies reduces the cryocooler's efficiency. Another factor that could be impairing the system's performance at lower frequencies is the inertance tubes' sizing, which is optimized for operating frequencies up to 120 Hz.

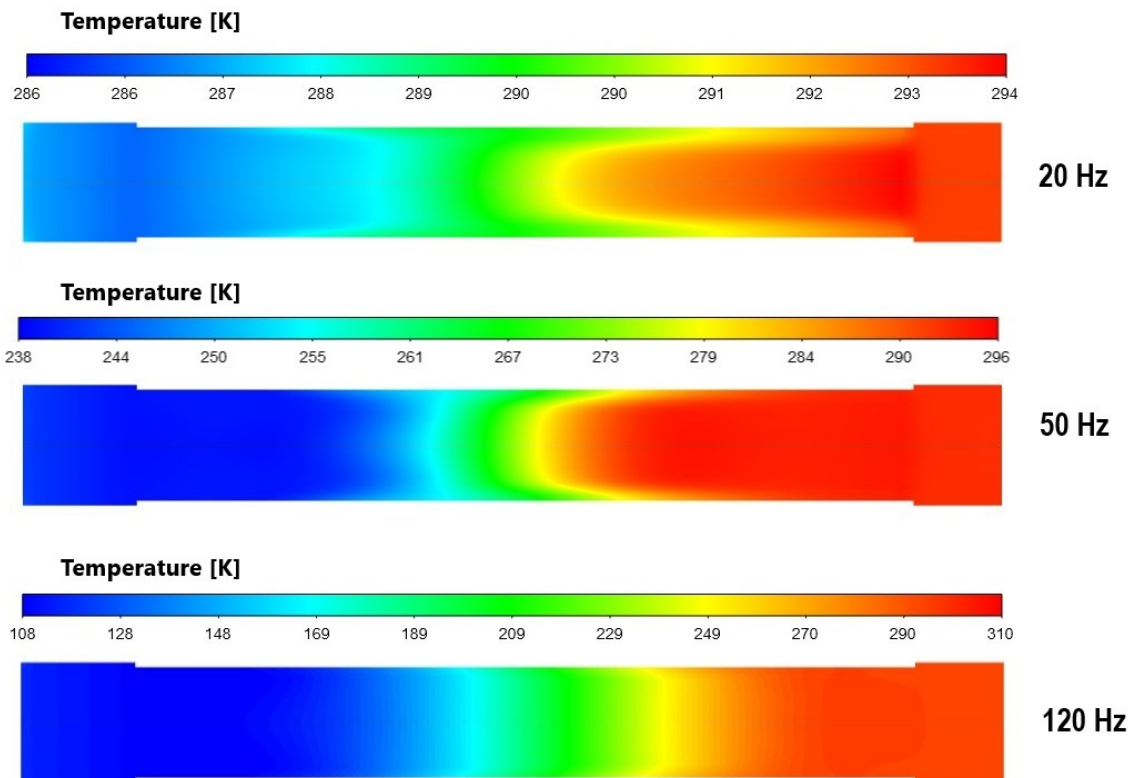
### 5.3.3 Pressure & velocity profiles

Figure 5.14 shows the axial velocity distributions along the line of symmetry for five cryocooler elements at two different frequencies. The four plots in 5.14a and 5.14b show the velocity magnitude profiles at four points during the cycle after achieving a periodic-steady state. Clearly, the variation in velocity magnitude across the regenerator and pulse tube elements is negligible due to the regenerator's short porous zone and the short length of the regenerator and the pulse tubes. Additionally, the velocity of the gas decreases as it enters the solid zone and increases as it enters the gas zone due to flow resistance. Due to the inertance tube's relatively small cross-sectional area, the velocity increases at the inlet. Additionally, the figure demonstrates that the average axial velocity increases with frequency, as expected.

Figure 5.15 displays the average pressure distributions along the symmetry axis for the same five cryocooler elements at two different frequencies. Figures 5.15a and 5.15b illustrate the



**Figure 5.12:** Distribution of the temperature after steady periodic state along the axis of symmetry. Reproduced from [200].



**Figure 5.13:** Steady-periodic average temperature contours in the CHX, pulse tube and HHX elements for three different frequencies. Reproduced from [200].

average pressure profiles at four points during the cycle following the onset of a periodic-steady state. As a result of the porous solid zone's presence, the only significant pressure variation occurs across the regenerator element.

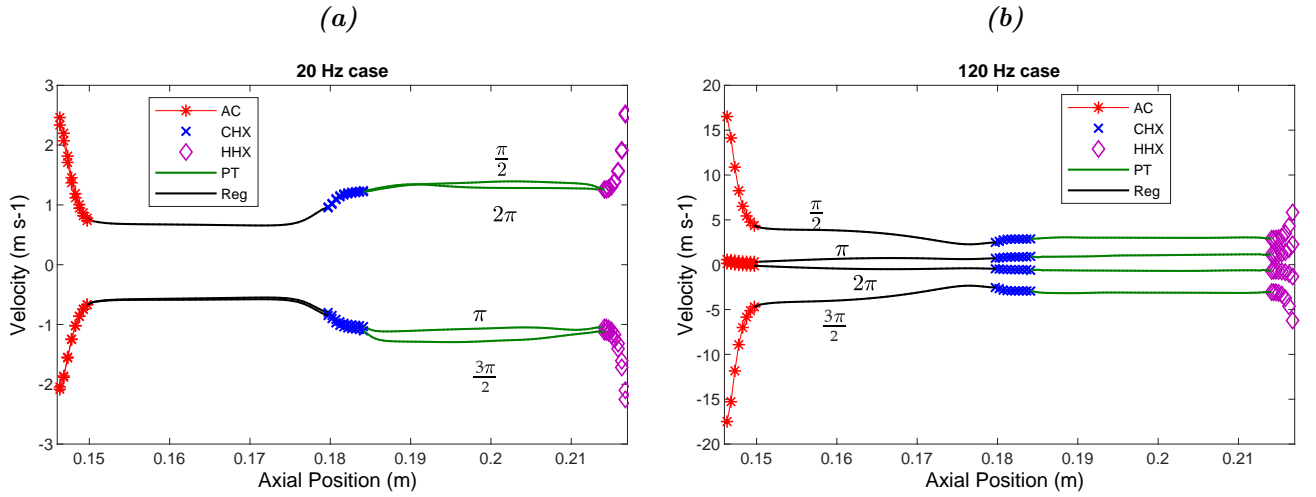


**Figure 5.14:** Distribution of the axial velocity along the axis of symmetry at four time instants (a) for 20 Hz (b) for 120 Hz. Reproduced from [200].

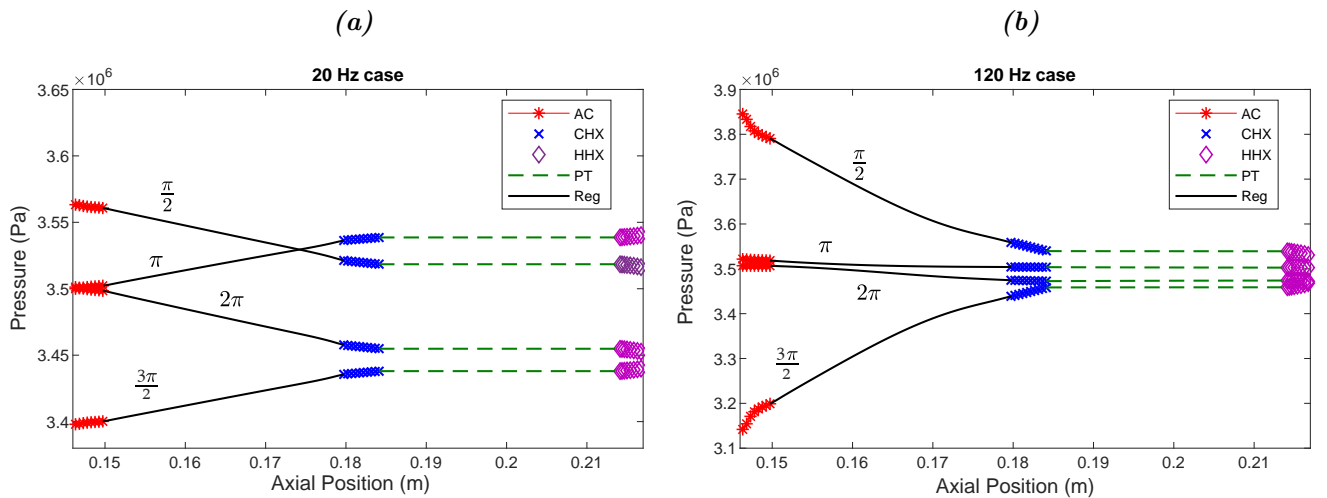


**Figure 5.15:** Distribution of the average pressure along the axis of symmetry at four time instants (a) for 20 Hz (b) for 120 Hz. Reproduced from [200].

Figure 5.16 illustrates the average pressure profiles for five distinct components. For both frequencies, the pressure follows a sinusoidal pattern, with the amplitude of the pressure wave and the pressure ratio increasing with the operating frequency. For 20 Hz and 120 Hz, the phase shifts between the pressure waves of the HHX and CHX are  $3^\circ$  and  $13^\circ$ , respectively. For 20 Hz and 120 Hz, the phase difference between the compressor's pressure wave and the reservoir are  $46^\circ$  and  $108^\circ$ , respectively. These figures demonstrate that the combination of double-inertance tubes

and reservoirs delivers good phase shift for such high-frequency operation, resulting in improved cooling performance. The phase shift between the flow and the pressure was projected to be only a few degrees for the miniature experimental setup, which was designed to operate at low power with a low mass flow in the inertance tube [122]; thus, a double inertance tube arrangement was used to provide a more proper phase shift compared to a single tube arrangement.

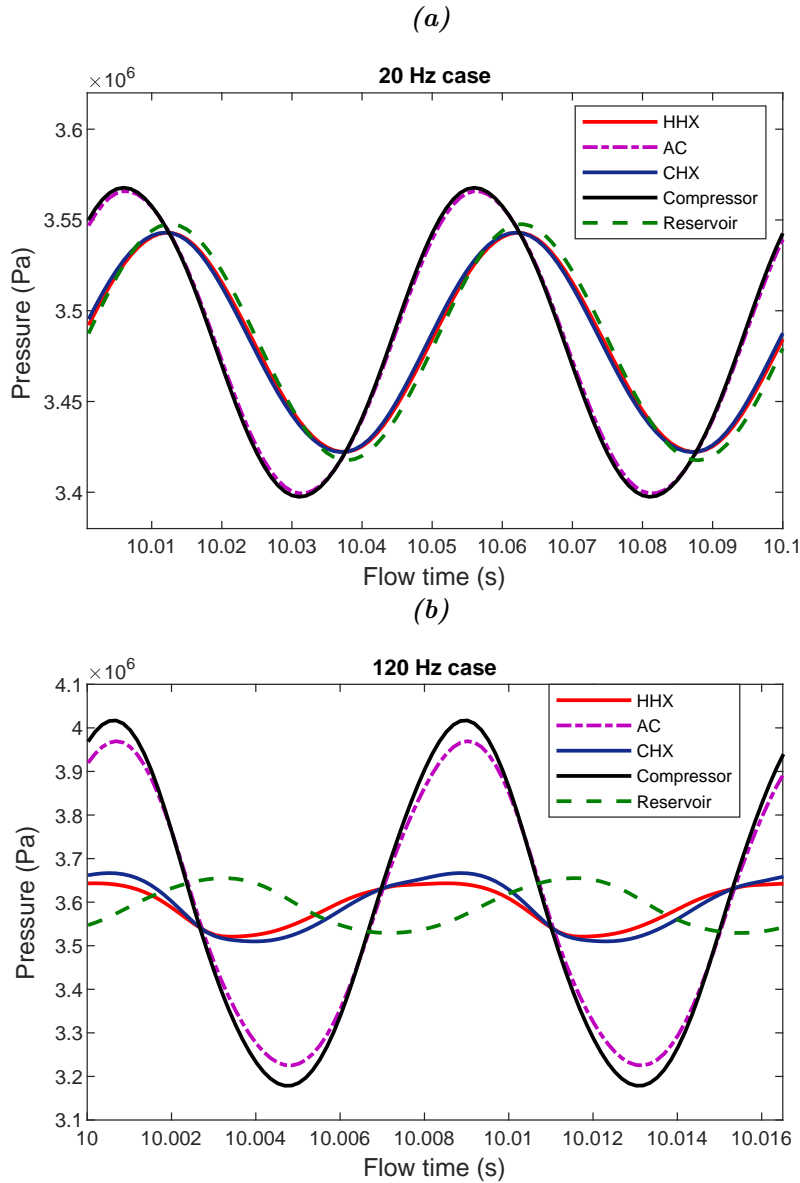


**Figure 5.16:** (a) Average pressure profile for five different elements of the PTC system for the 20 Hz case. (b) Average pressure profile for five different elements of the PTC system for the 120 Hz case. Reproduced from [200].

Figure 5.16b illustrates regions where the HHX's average pressure is greater than the CHX's. Due to the presence of these regions, the gas near the cold end undergoes periodic pressurization and depressurization, resulting in periodic cooling and heating effects. However, at low frequencies, these zones are hardly distinguishable, as illustrated in Figure 5.16a. The presence of such

regions indicates that the cooling system performs well at 120 Hz. Figure 5.17 illustrates the pressure wave spectra for three distinct components at 120 Hz. When the pressure is sinusoidal, it is obvious that the pressure signals in the CHX and HHX can be expressed using fundamental and two harmonic terms.

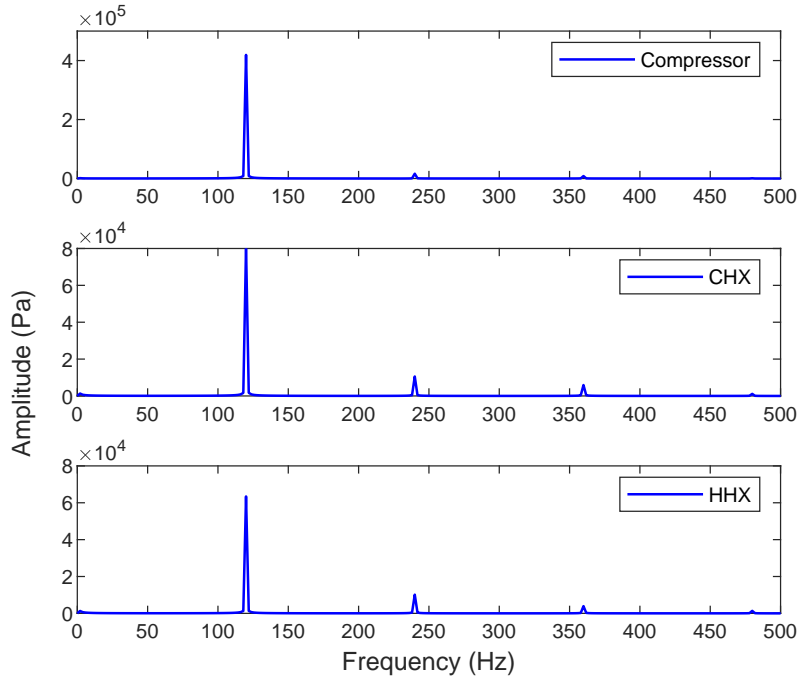


**Figure 5.17:** The pressure signals in the frequency domain for three different components in the system for a pulse rate of 120 Hz, at three locations in the PTC system. Reproduced from [200].

### 5.3.4 Enthalpy distribution and cooling power

Figure 5.18 plots the total enthalpy of selected components in the pulse tube system along the axis of symmetry, beginning with the aftercooler and ending with the HHX. The enthalpy has a negative sign because of the direction of the streaming velocities near the cold end (CHX). Additionally, it represents the cooling effect at the cold end. It is evident that a higher frequency results in not only lower temperatures but also increased cooling power. The positive enthalpy values at the aftercooler section indicate a temperature rise above 300 K, i.e., the initial temperature state, and suggesting the need for cooling to ensure optimal operation of the compressor and aftercooler sections. To estimate the cooling capacity of the system, the cold end was assumed to have an isothermal boundary condition, using the same settings described in section 4.6.2. For the 120 Hz case, the simulation predicts a cooling power of 11.25 W at 110 K cold end temperature, and reporting a coefficient of performance of 5.8%.

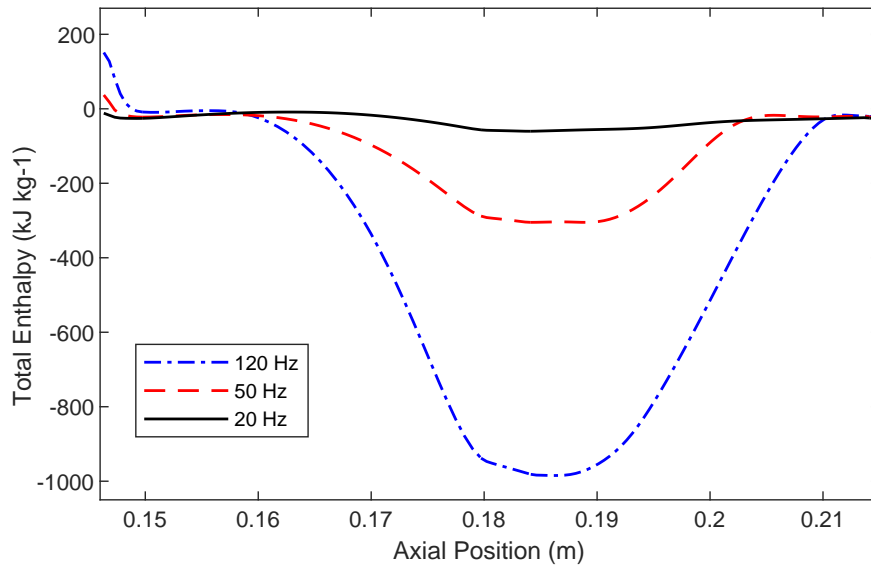


**Figure 5.18:** Averaged enthalpy profile, starting from the aftercooler to the HHX sections along the axis of symmetry for the three cases (i.e.  $f = 20$  Hz, 50 Hz and 120 Hz). Reproduced from [200].

## 5.4 Results of the miniature PTCs models<sup>8</sup>

This section compares the results from the base CFD model of the inertance tube PTC with those of Sage<sup>®</sup>. After that, the results of the base model are used to develop further miniature PTC models.

### 5.4.1 Miniature Core model

The geometry and operational parameters listed in Table 4.5 were used to construct both the Sage and Fluent models in order to compare their results. Figure 5.19a illustrates the predicted cold end cooling power curves for both the Sage and Fluent models. The input powers were nearly identical, 10.53 W for fluent and 10.52 W for Sage at  $T_c = 140$  K, and the pressure ratios were generally similar, with  $P_r = 1.11$  at the cold end. Sage predicted a lower net cooling power. The justification is that the porous media in regenerators and heat exchangers are characterized differently in the two models. While Sage models pressure drop by introducing a friction factor and employs empirical data for flow through screens, Fluent CFD designs the porous media zones by introducing a momentum loss term. Additionally, the media properties for both models are slightly different. Refer to Table 4.4. Figure 5.19b illustrates the predicted COP for both fluent and Sage models. Sage predicts that the simulated models will have lower performance with nearly the same ultimate cold tip temperature. Fluent predicts better system performance with nearly 4% COP at 100 K cold end temperature. Fluent findings are expected to be more

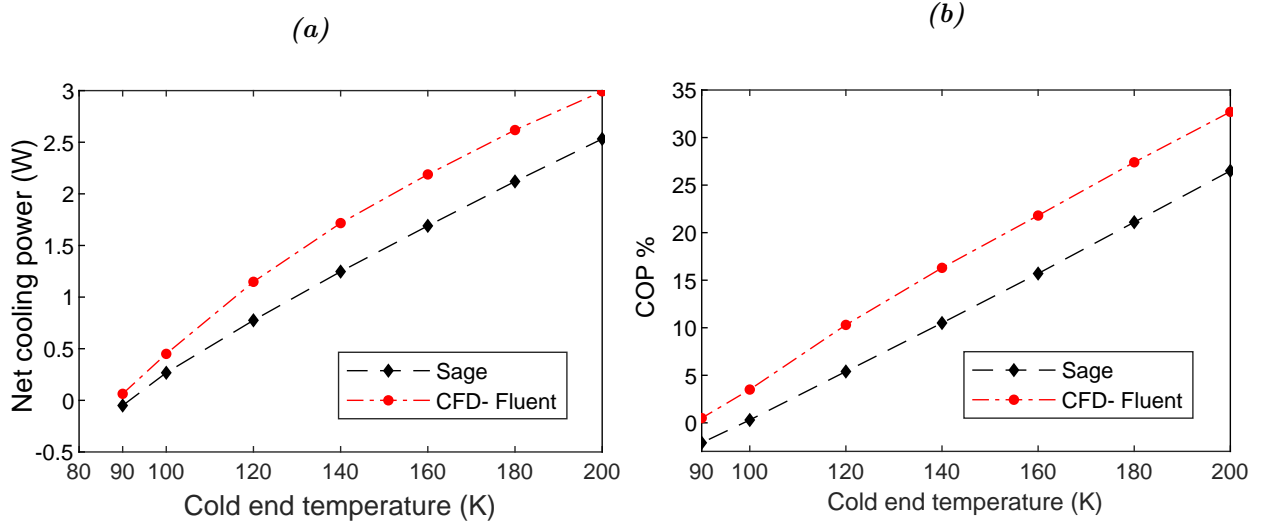


**Figure 5.19:** (a) Predicted cold end cooling power curves in Sage and Fluent. (b) Predicted COP for Sage and Fluent.

accurate since they rely on more reliable empirical data in the porous zones and the model's simplifications are limited. However, due to a lack of experimental data, the accuracy of these predictions may be tentative.

As previously stated, the phase angle between pressure and mass flow rate plays a critical role in determining the PTC's efficiency. The phase shift is primarily determined by the size of the inertance tube. As stated in section 4.6.1, the transmission line model was used to initially estimate the inertance tube size, which was then optimised using Sage software. The phase angle results for various component inlets at  $T_c = 140$  K are listed in Table 5.1.

**Table 5.1:** Phase angles at different component inlets at  $T_c = 140$  K.

No.	Component	Predicted Phase Angles, in degrees	
		Sage Model	Fluent Model
1	Transfer-line	-30.4	-31
2	Aftercooler	-28.98	-29.92
3	Regenerator	-27.86	-28.67
4	Cold heat exchanger	16.95	11.78
5	Pulse tube element	28.6	25
6	Hot heat exchanger	49	45.16
7	Inertance tube	52.43	49.07
8	Reservoir	-89.92	-89.32

An efficient PTC operation is guaranteed if the mass flow leads the pressure at the regenerator's warm end, lags the pressure at the regenerator's cold end, and is in phase with the pressure near the regenerator's midpoint. Due to the phase shift sign change in the regenerator element, which shows that flow and pressure become in phase near the regenerator center, the selected inertance tube specifications resulted in outstanding performance according to the two models' phase shift results. More miniature models will be derived in the following section using the findings of this section.

### 5.4.2 Ultra-Miniature models

This section continues the investigation by deriving miniature PTC models from the results of the previous core model. It begins with an overview of their geometry and operating parameters and concludes with a discussion of their performance. These models are being developed as proofs of concept, as several obstacles related to the practical implementation of these devices must first be overcome. The goal is to develop models capable of operating at very high frequencies with small compressor strokes and on a much smaller scale than current conventional systems.

The base model presented in the previous section was used to generate three miniature-scale models for multiples of the base operating frequency; these are 225, 450, and 900 Hz. The frequencies were kept under 1 kHz based on experimental findings for successful regenerator operation [13]. The design considers a number of the issues raised in the preceding chapter to demonstrate the feasibility of miniaturizing the PTC system, assuming higher operating frequencies and mean system pressure. The scaling procedure begins with the assumption of a cold end temperature,  $T_c = 140$  K. This design point was chosen due to the uncertainty regarding the ultimate cold end temperature that these derived systems could reach. The geometry and operating parameters for the three derived systems are listed in Table 5.2.

Although a high average system pressure could be chosen, the mean system pressure was kept at  $\leq 5$  MPa to ensure that the values remained reasonable for future practical implementation. The three frequencies chosen were nearly multiples of the frequency of the base model. The compressor sizing for the three derived systems was chosen to maintain reasonable input power values for the miniature systems. As a result, the compressor was designed to maintain an input power of  $\sim 10$  W for each of the three models. According to equation 3.17, the input acoustic compressor power is proportional to the operating frequency,  $f$ , and the system pressure. The swept volume,  $V_{swept}$ , is used to scale down the heat exchangers, reservoir, regenerator, and pulse tube.

To eliminate junctions and stepped transitions, the regenerator, after-cooler, and heat exchangers are all designed to have similar diameters to the pulse tube, resulting in decreased void volume pressure loss. According to the base model data, the regenerator diameter was about 1.5 times greater than the pulse tube diameter. Hence, the pulse tube diameter was set to almost two orders of magnitude larger than the thermal penetration depth. The component length was reduced to keep the component volume to swept volume ratio,  $V/V_{swept}$ , nearly constant. Sage was used to optimize the inertance and transfer line tubes for maximum cooling power and coefficient of performance.

Fluent was used to perform simulations of the previous three models, using the same settings described in the previous section for the base model simulation. The same porous media characteristics were employed, with #635 stainless steel and #325 bronze wire meshes for the regenerator and the heat exchangers, assuming thermal equilibrium between the fluid and solid zones. The time steps were set to 200 steps per cycle, and the simulations were executed for 6000-time steps, which was sufficient to reach a periodic steady-state and achieve accurate results.

Figure 5.20a shows the estimated heat lift versus the cold end temperature for the previously three derived models. Figure 5.20b illustrates the fluent predicted COP for the three derived models. It can be seen that the three models reached no-load temperature below 100 K. The simulation results predicted that the three derived models would perform well, almost identical to the core model's performance.

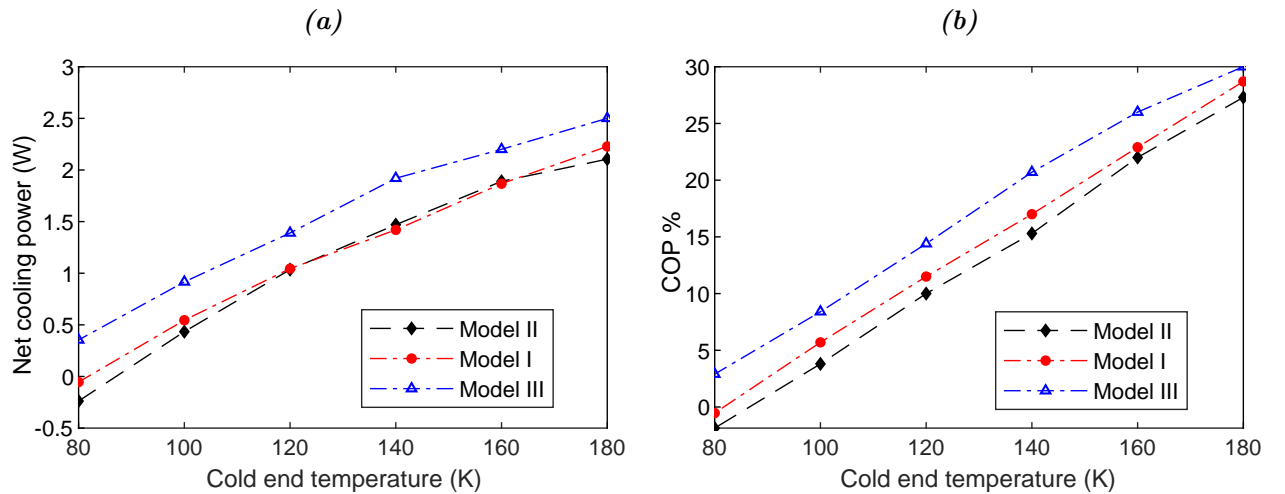


**Figure 5.20:** (a) Predicted cold end cooling power curves for the three derived models. (b) Predicted COP for Sage the three derived models.

Table 5.2: Geometry and operating conditions for the derived systems.

Component	Model I			Model II			Model III									
	$f$ (Hz)	$V_{compressor}$ (cc)	$P_{mean}$ (MPa)	$\delta_{th}$ ( $\mu m$ )	$\delta_v$ ( $\mu m$ )	$D$ (mm)	$L$ (mm)	$V/V_{swept}$	$f$ (Hz)	$V_{compressor}$ (cc)	$P_{mean}$ (MPa)	$\delta_{th}$ ( $\mu m$ )	$\delta_v$ ( $\mu m$ )	$D$ (mm)	$L$ (mm)	$V/V_{swept}$
Compressor	20	0.28 (Stroke)	1	15.8	0.22 (Stroke)	1	12	0.17 (Stroke)	1	12	0.17 (Stroke)	1	12	0.17 (Stroke)	1	1
Transfer Line	2.5	3	0.167	2	2.5	0.182	2	2.5	0.183	2	2.5	0.183	2	2	2	0.183
Aftercooler	5	2.5	0.558	4	2	0.582	4	2	0.551	3	1.5	0.551	3	1.5	3	0.551
Regenerator	5	20	4.464	4	15	4.369	4	15	4.227	3	11.5	4.227	3	11.5	3	4.227
Cold heat exchanger	5	2.5	0.558	4	2	0.582	4	2	0.551	3	1.5	0.551	3	1.5	3	0.551
Pulse tube	5	20	4.464	4	15	4.369	4	15	4.227	3	11.5	4.227	3	11.5	3	4.227
Hot heat exchanger	5	1.25	0.279	4	1	0.291	4	1	0.275	3	0.75	0.275	3	0.75	3	0.275
Inertance tube	1.5	1100	22.098	1	310	5.644	1	310	2.412	0.75	105	2.412	0.75	105	0.75	2.412
Reservoir	17	13	33.54	13	12	36.92	13	12	40.85	10	10	40.85	10	10	10	40.85
Total volume (cc)	6.9			2.8			1.26									

Table 5.3 lists the fluent simulation results for the three models, where the predicted phase shift angles for the regenerator, cold end, and reservoir are listed in the table at 140 K cold end temperature.

**Table 5.3:** Results of fluent simulations for the three models.

Component	Model I	Model II	Model III
Average pressure, (MPa)	4	4.5	5
Cold end temperature, $T_c$ , (K)	140	140	140
Hot end temperature, $T_h$ , (K)	300	300	300
Input PV power, $W_{ac}$ , (W)	9.15	9.6	9.25
Net cooling power (W)	1.42	1.47	1.92
Peak mass flow at the aftercooler (g/s)	0.39	0.335	0.301
Peak mass flow at the cold end (g/s)	0.31	0.304	0.292
Peak mass flow at the inertance tube (g/s)	0.287	0.285	0.289
Peak mass flow at the reservoir entrance (g/s)	0.296	0.241	0.213
Pressure ratio at the aftercooler	1.183	1.21	1.234
Pressure ratio at the cold end	1.124	1.153	1.164
Pressure ratio at the inertance tube	1.122	1.149	1.156
Pressure ratio at the reservoir	1.048	1.035	1.029
Phase shift at the aftercooler (deg.)	-31.56	-32.08	-32.5
Phase shift at the regenerator (deg.)	-29.96	-28.10	-28.98
Phase shift at the cold end (deg.)	9.87	16.83	24.2
Phase shift at the hot end (deg.)	44.75	61	64.5
Phase shift at the inertance tube (deg.)	50	65.5	69
Phase shift at the reservoir (deg.)	-89.59	-87.82	-87.24

As discussed in section 3.6.1, the flow should lag the pressure by almost  $30^\circ$  at the cold end and lead it by  $30^\circ$  at the regenerator's hot end, so the pressure and the flow are in-phase at the regenerator midpoint, as an indication of efficient operation. This necessitates that the pressure lead the flow at the warm end of the pulse tube by nearly  $60^\circ$ . The phase shift data for Model III indicates that the phase angle is the closest to zero near the middle point of the regenerator among the three models, meaning that the system is operating nearly at its optimal geometry and operating parameters. This explains why the model had the lower ultimate cold temperature and higher COP among all three models. The results also indicate that the flow for the three models leads the pressure at the inlet of the reservoir by almost  $90^\circ$ , this agrees with the transmission line theory prediction in equation 4.12. Based on the transmission line model,

for Model III operating conditions, the maximum predicted phase shift was found to be almost  $74^\circ$  at the inlet of the inertance tube.

The results indicate that PTC functioning at very high frequencies and with a small system size is possible, even when stainless steel wire mesh is used as a filler in the regenerator. It is projected that if even finer regenerator fill material and compact compressors were used, these ultra-miniature devices would perform even better. One of the issues is the scarcity of suitable materials with great confidence in their hydrodynamic properties when used at high frequencies. In high-frequency operation, the ratio of matrix heat capacity to working fluid heat capacity drops considerably, reducing the regenerator's efficiency [13]. Hence, high-frequency operation requires materials with very fine hydraulic diameters, much smaller than the corresponding thermal penetration depth for a given operating frequency and average pressure. As a result, proper construction would demand new, very fine filler materials with very small pore size, high thermal capacity, low axial thermal conductivity, and low-pressure loss. Figure 5.21 depicts CAD drawings of Model I and Model III. The Model III's small size suggests that micro-fabrication techniques might be used for future development, especially if a coaxial design is used and the previously noted obstacles are addressed.

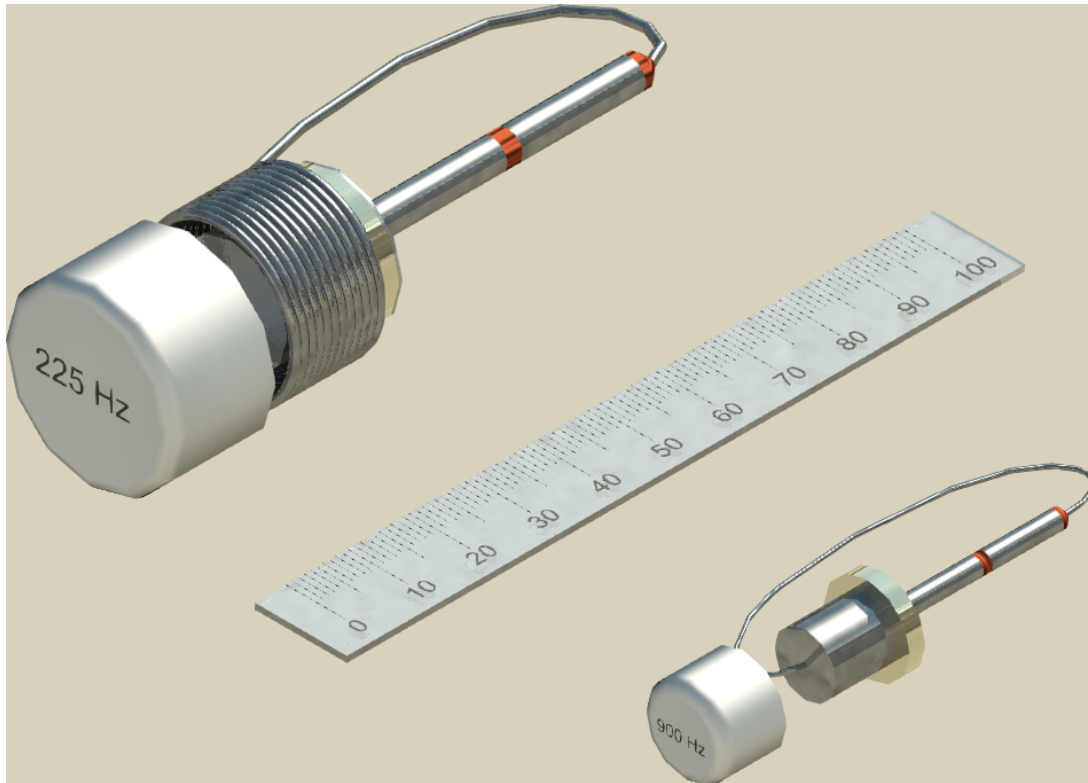


**Figure 5.21:** CAD drawings for Model I and Model III, and 100 mm ruler for size comparison.

## 5.5 Inertance PTC design and optimisation tool

A user friendly stand-alone software was developed to enable the design and optimization of the inertance pulse tube cryocooler, based on the previous results from the ideal regenerator study and the optimization approach for the regenerator described in section 3.7.1, as well as the analogous transmission line model. MATLAB App Designer<sup>®</sup> was used to construct this tool. Figure 5.22 shows the first program interface for this tool. The tool is divided into three programs: the first allows the user to map and optimize the regenerator diameter and length versus inefficiency for defined operating parameters; the results are plotted and written to a user-specified output file. The program also has the capability of animating the temperature profiles within the regenerator during heating and cooling phases while converging on a solution.

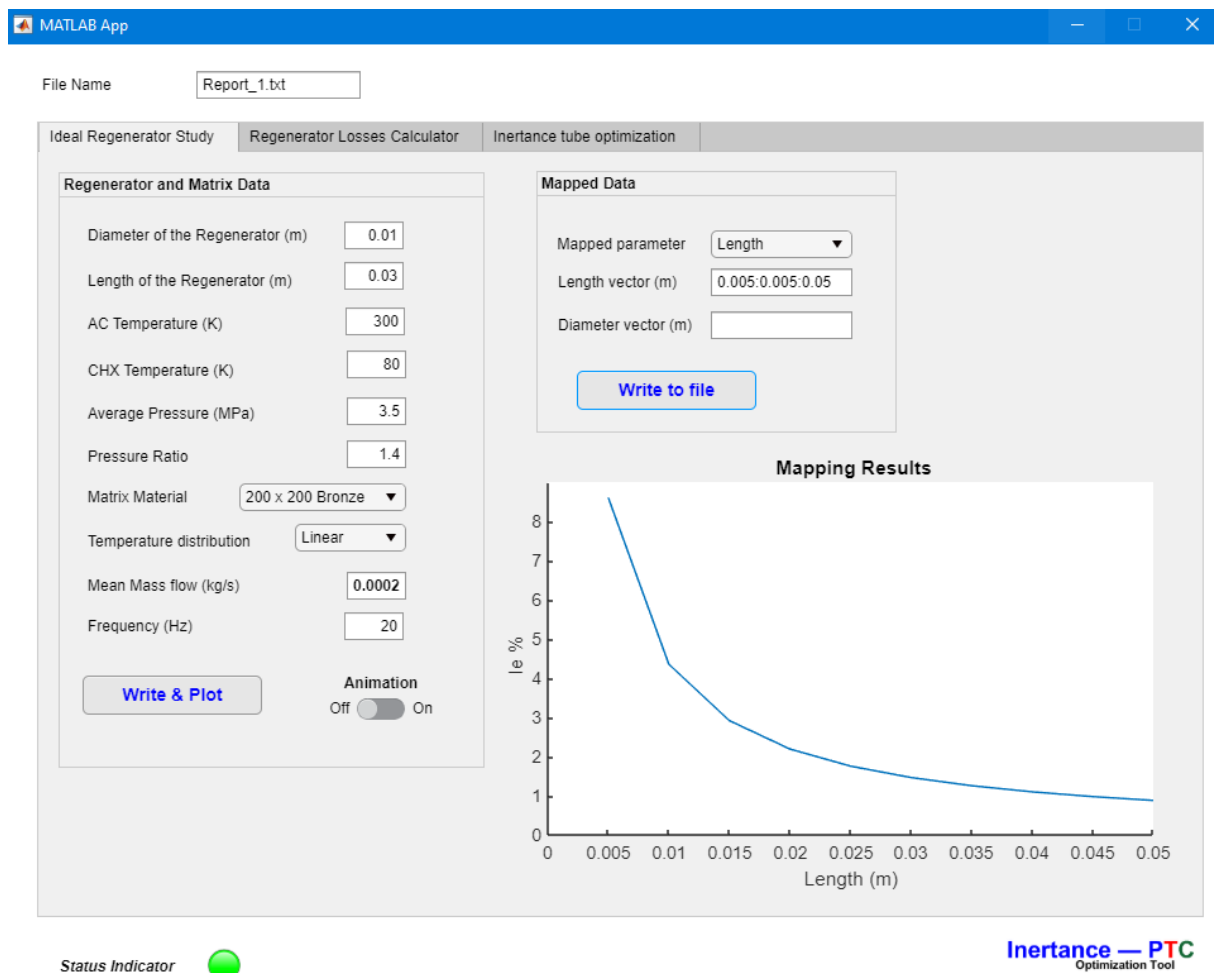


**Figure 5.22:** A MATLAB standalone software tool for Inertance PTC system optimisation: Inefficiency study.

The second program illustrated in Figure 5.23 calculates regenerator losses, which include regenerator thermal loss, void volume loss, pressure loss, and axial conduction loss. It allows users to plot the geometrical characteristics of the regenerator against the estimated net cooling

power and COP. There are several input parameters, namely the mean mass flow rate, phase angle, frequency, average pressure, pressure ratio, hot and cold end temperatures, matrix type, and conduction degradation factor. Tables, graphs, and output report files are used to display the output data.

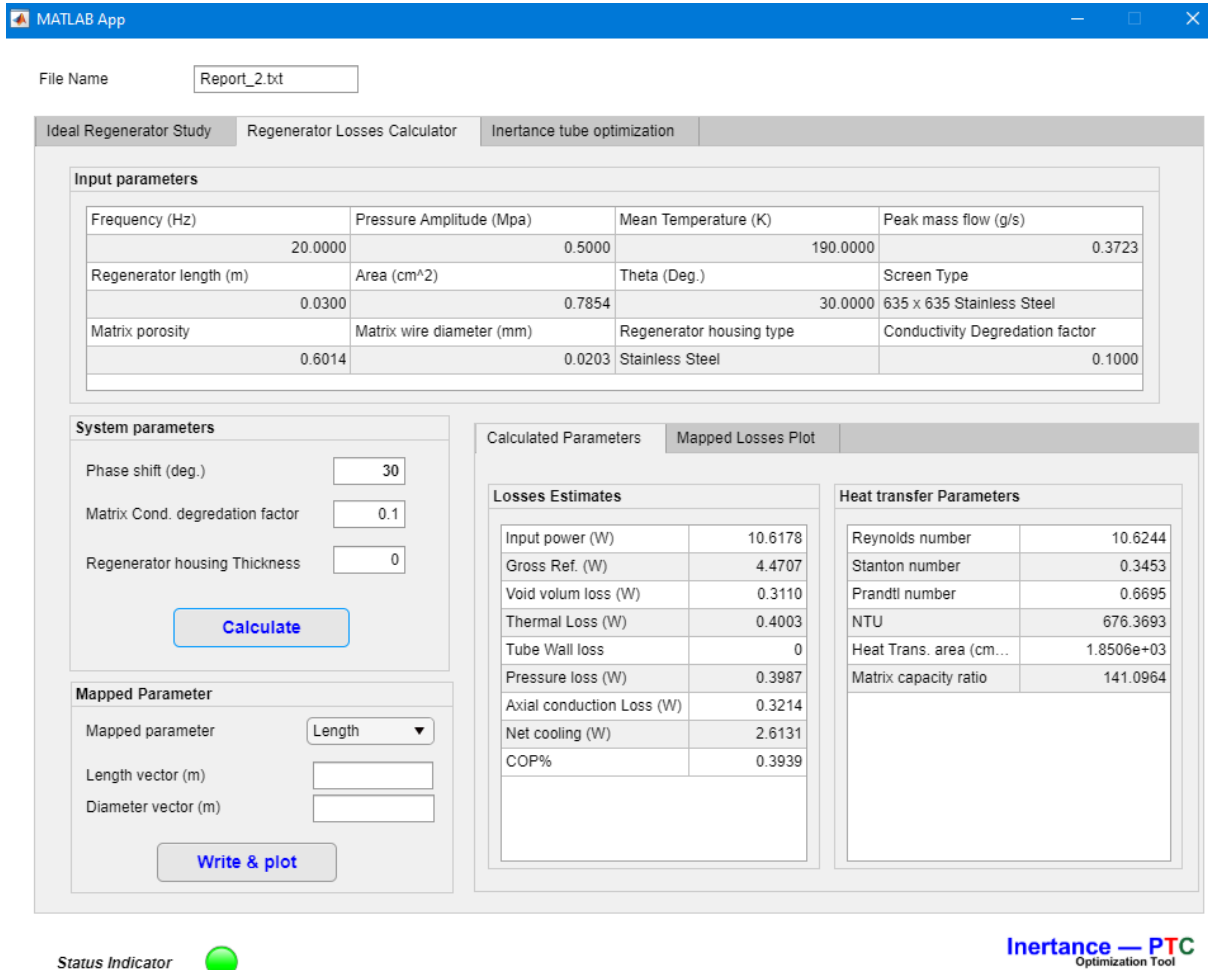


**Figure 5.23:** A MATLAB standalone software tool for Inertance PTC system optimisation: Regenerator's losses estimation.

The third program employs the analogous transmission line model to calculate the associated input power and phase shift angle for certain inertance tube lengths and diameters. Each length or diameter of an inertance tube might have various positive input powers and phase shifts. The deciding factor in this case is to choose the lowest value that meets the optimisation criterion. Generally, to accomplish optimal cooling, the inertance tube diameter and length are generally tuned for a specific input acoustic power, and the target phase shift is set to be a few degrees larger than 60°. Figure 5.24 illustrates the software predicted result for Model I presented in the previous section. This is a beta version of the inertance tube program, and further functionalities, such as numerical analyses and phasor diagrams, may be introduced in the future.

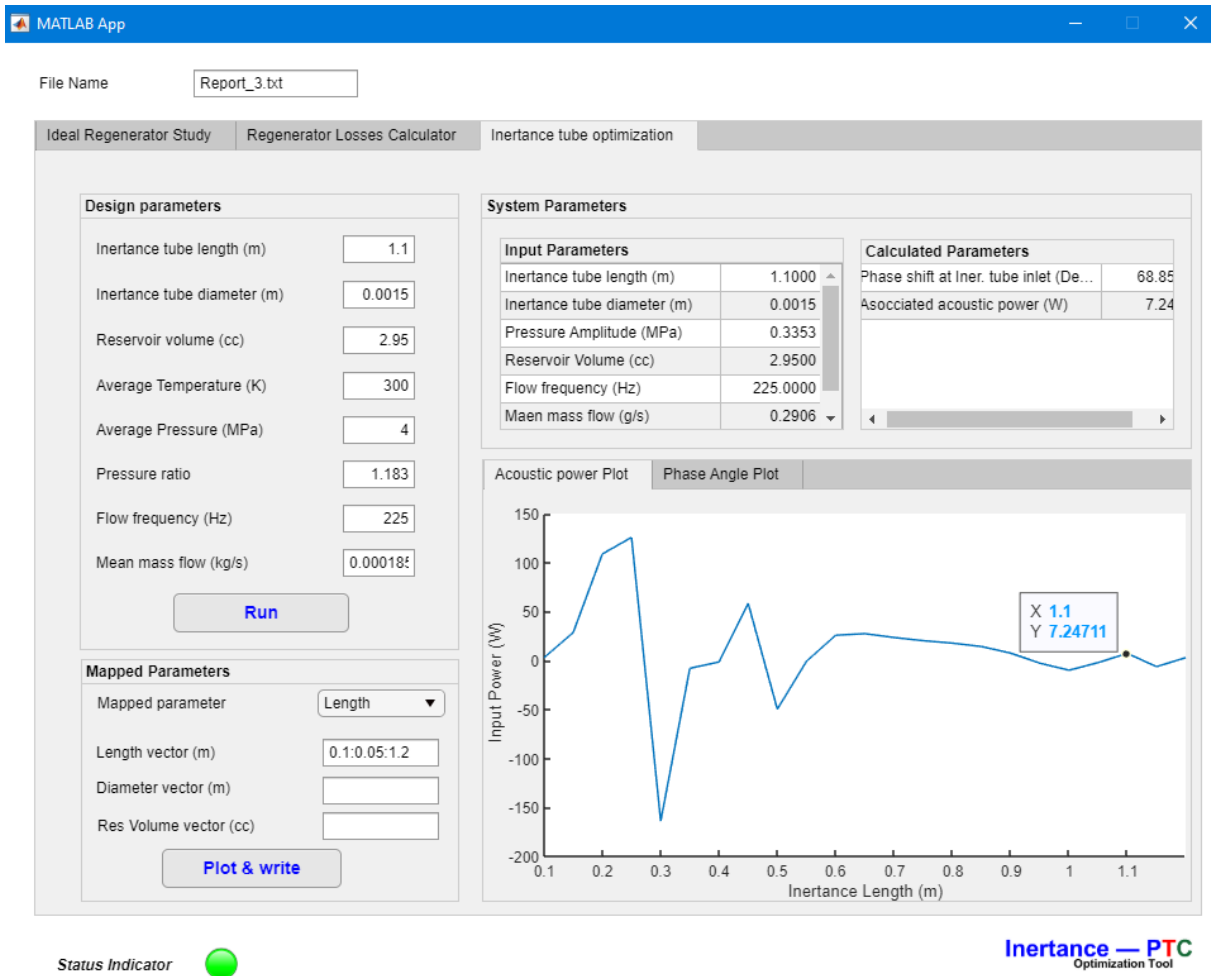


**Figure 5.24:** A MATLAB standalone software tool for Inertance PTC system optimisation: Inertance tube optimisation.

## 5.6 Experimental setup

In this section, a description of the experimental setup is presented. This experimental setup was created with the intention of providing experimental data that could be compared to the simulation model and used to confirm the model's previously predicted findings. Figure 5.25 depicts a schematic of the expected experimental setup. From previous sections, it was evident, that an ultra-miniature setup can only be developed concurrently with the development of an ultra-miniature compressor or pressure wave generator capable of operating at excessively high frequencies.

As established in prior numerical analyses such as 1-D modeling, CFD, REGEN, and Sage, the optimal geometric and operational parameters were obtained. The settings for the base model in Table 4.5 were used to establish the experimental setup as a proof of concept and to validate the simulation results. Following that, sensory equipment was ordered for future system installation. The primary goals are to detect pressure and mass flow readings at various system components'

inlets as well as to record temperature readings at the cold, hot, and aftercooler heat exchangers. Figure 5.25 depicts these sensors' locations. The following sections provide more information on the experimental setup. Full layout for the entire system is provided in Appendix E.

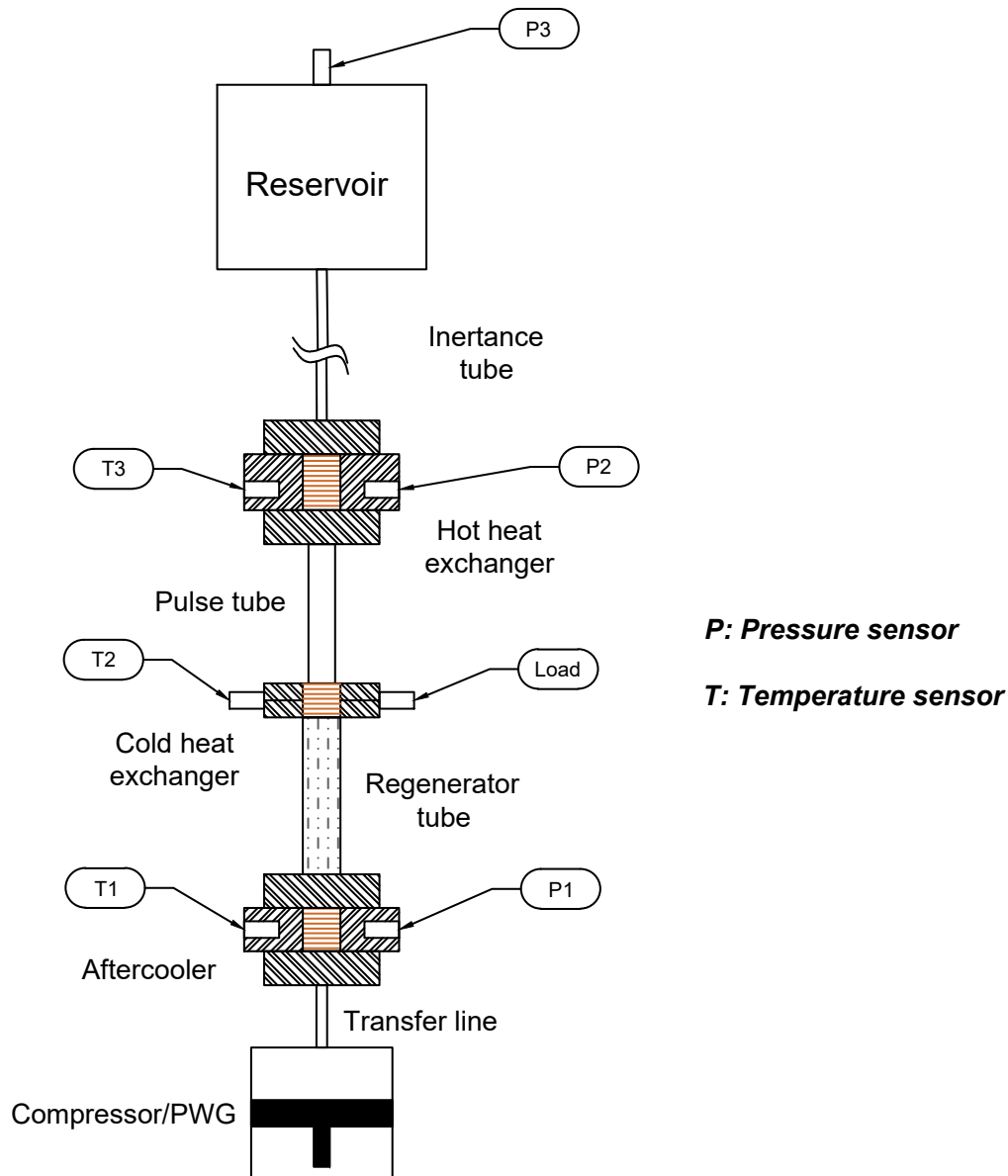


*Figure 5.25: The layout of the experimental setup for the inline inertance pulse tube cryocooler.*

## 5.6.1 Instrumentation equipment

### 5.6.1.1 Temperature measurement

The T7 labjack is a data acquisition (DAQ) card that can acquire signals from almost any type of sensor and serve out the sensor data via one of the two communication ports: Ethernet or

USB. The DT-670 silicon diode measures the cold end temperature when driven by a steady 10  $\mu\text{A}$  current source. The resultant voltage drop is then used to determine the temperature at that location. In this regard, the T7 labjack features two fixed current source terminals: 10  $\mu\text{A}$ , and 200  $\mu\text{A}$ . These can be used to power a variety of temperature sensors, such as resistance, thermistors, and RTD sensors.

Another option is the Model218E temperature monitor, which has eight sensor inputs. It is compatible with almost any diode or resistive temperature sensor. It continuously displays all eight channels at K, C°, V, or  $\Omega$ . This instrument was mainly developed for cryogenic temperature measurement due to its qualities such as low noise, excellent resolution, and a wide operating temperature range. Thermocouples would be used to measure temperatures for the other components, including the aftercooler and the HHX. The signals will be routed to the T7 labjack input ports, where the output temperature will be displayed on a PC screen. Appendix F displays images for the previously described instruments.

#### 5.6.1.2 *Pressure measurement*

Pressure measurements are performed at three different locations in the system: the inlet to the aftercooler, the inlet to the HHX, and the reservoir. A pressure transducer (END-8510B-500) is a rugged, miniature, high-sensitivity piezoresistive transducer. It comes with a three-channel amplifier capable of measuring very high pressures, up to 13 MPa. Its high sensitivity, combined with high resonance, makes it ideal for measuring dynamic pressure. See Appendix F for more information.

#### 5.6.2 **Pressure wave generator**

A compressor or a pressure wave generator is required to provide acoustic power to the cold head in order to produce cooling. It compresses and expands inert gases like helium to power acoustic loads like Stirling and pulse tube cryocoolers. A Q-drive 2S102W Pressure Wave Generator (PWG) manufactured by RIX Industries was ordered to drive the cold head in the experimental setup. It can satisfy efficient operation near the 100 Hz operating frequency. It was demonstrated to be an excellent choice for applications requiring minimum noise, no maintenance, and high reliability while supplying periodic harmonic pressure or flow. The compressor, although small, is still large compared to the experimental setup size. Thus, impedance matching by varying the transfer line length is needed to optimize the cooling power for the given acoustic power. See Appendix F for more information.

### 5.6.3 Planned experiments and test routines

Several experiments were planned to investigate various operating parameters for the experimental inline pulse tube system. Experiments on the proposed cold head with the related compressor were meant to demonstrate the relevance of high-frequency operation for the miniature pulse tube cryocooler, as demonstrated by prior simulation results. Initially, the experimental prototype apparatus will have the exact dimensions and settings as the base model described in section 4.6. The experimental recorded data was planned in order to confirm the validity of the simulated results.

The compressor, described in the previous section, was ordered to work with a variety of operating conditions such as charging pressure, pressure ratios, and operating frequency. Experiments with varying parameters were planned in order to record the lowest possible no-load temperature with the shortest cooling time and compare the results of these experiments to the predicted simulated outcomes. As suggested by the simulation, smaller compressors that can operate at a higher frequency are expected to shorten overall cooling time. Also, as demonstrated in the preceding sections, when operating at high frequencies and high charge pressure, the cryocooler size is reduced for a given input acoustic power. This is critical for many applications and can motivate the development of micro-cryocoolers for MEMS and on-chip applications. Since then, the size of a pulse-tube cryocooler is determined primarily by the size of the pressure wave generator. As a result, successful micro-cryocooler implementation would necessitate the use of a micro pressure wave generator as well.

Experiments may be carried out using the compressor to characterize the porous media hydrodynamic properties of various materials and geometries. These can be used to replace the present fillers utilized in conventional systems. The size of the pulse tube, regenerator, and inertance tube can be adjusted to optimize the cryocooler for efficient operation by adjusting the gas and porous zone characteristics as thoroughly explained in the preceding sections. Furthermore, one of the goals of the tests was to determine the cryocooler's overall COP for a given input power and to quantify the corresponding losses inside the cryocooler components. Some of the outcomes include creating load curves, cooldown curves, pressure, and mass flow signals at multiple locations. These are to be post-processed to extract phase shift data and compare them with the predicted simulation data.

One of the key goals of building and running the experimental setup was to test the theoretical prediction that a pulse-tube cryocooler operating at 100 Hz can achieve a good COP at temperatures approaching 80 K in a very short period. This is accomplished by employing higher

charging pressures and operating frequencies, a finer regenerator filler matrix, and a smaller regenerator volume.

#### **5.6.4 Difficulties and complications**

The COVID-19 pandemic has not only created a sense of threat, uncertainty, and stress that has spread at an alarming rate around the world. It also caused many delivery delays and issues related to implementing the intensive simulation and theoretical studies in this thesis into an experimental setup. Many of the components and materials faced serious issues concerning ordering and delivery. For example, the compressor was ordered nearly a year ago and has yet to be delivered as a result of the crisis. Unfortunately, owing to various distressing events during the pandemic, as well as the PhD candidate's status as an overseas researcher with visa and residency restrictions, the experimental setup could not be implemented. This unprecedented crisis not only caused problems concerning delivery and orders but also with the grant proposals that were required for purchasing vital components. It also affected the ability to access labs and arrange meetings with technicians and trained personnel due to the forced strict work environment and working-from-home regulations. Moreover, the collaborative effort was affected. Unfortunately, the experimental setup could not be established due to this global situation, and hence the simulation results could not be compared and validated with experimental data.



# Chapter 6

## Conclusions and Recommendations

**T**he thesis is summarized and concluded in this chapter. It begins by providing a statement outlining how this Ph.D. work contributes to the field. Then, an outline of the complete thesis results is presented. Following that, it explores the implications of the thesis results. The limits and complexities of the study, as well as their consequences for interpreting the findings, are then examined. Finally, suggestions and recommendations for further work are addressed.

### 6.1 Conclusions

A substantial body of theoretical and empirical literature has demonstrated the importance of cryocooler miniaturization to the prosperity of many existing and emerging applications. In this thesis, various numerical techniques have been used to investigate the miniaturization aspects of pulse tube cryocoolers (PTCs) to develop ultra-miniature cryocoolers for on-chip cryogenic cooling. A literature survey of experimental miniature PTCs was conducted, and numerical modeling techniques for assessing the performance of miniature PTCs were delivered.

### 6.1.1 Contribution statement

The objective of this thesis was to examine the viability of ultra-miniature cryocoolers by focusing on various analytical and numerical studies. The thesis proposed a 1-D model for the pulse tube element, concluding that high frequency operation is required to create a well-established hot and cool zone separation in the tube element that would result in shortening the tube length. According to the findings, a tube length of 3 cm is adequate to assure excellent functioning at frequencies greater than the standard operating frequency in a pulse tube cryocooler system.

The research next did thermal analysis on the regenerator element, which is thought to be the most important component inside the cryocooler system and where the bulk of losses and hindrances occur. Based on thermal inefficiency parametric analyses, the study established geometrical constraints. The results showed that the regenerator diameter and length could be reduced to 9 mm and 30 mm, respectively, without significantly affecting efficiency. Based on the loss analysis, an analytical approach to quantifying the various forms of losses within the regenerator was presented. The outcomes of this analytic technique were compared to those of other software tools, demonstrating that it could deliver adequate accuracy.

The study also explored the utilization of higher dimensional analysis that does not employ the simplifications and assumptions that exist in the other approaches. The objective of using CFD was to produce a miniature base system and three other derived ultra-miniature systems. The operating parameters include an average pressure ranging from 3–5 MPa, pressure ratios as low as 1.18, and a mass flow rate of  $\sim 0.3$  g/s. The results from these proposed models promise decent cooling performance even when utilizing the conventional stainless steel wire screens in the regenerator element. The operating frequencies ranged from 225 — 900 Hz, giving these models total volumes ranging from 6.9 – 1.25 cc. The investigation revealed that the three derived systems worked rather well, generating nearly 2 W of cooling power from an input power of about 9 W at a cold end temperature of 140 K. The projected phase shifts were almost  $60^\circ$  and  $90^\circ$  at the inertance tube inlet and exit, respectively. This matched well with the projections from the analogous transmission line model and proved it to be a good tool for inertance tube sizing. According to the thesis, Model III, in particular, when employed in coaxial configuration with a piezo-pressure wave generator, may be produced utilizing micro-fabrication techniques. The study predicts that the performance would be greatly enhanced if fine regenerator fillers were developed and smaller pressure wave generators were produced.

The investigation was completed by developing a user-friendly MATLAB-based stand-alone program to be used as an optimisation and design tool for the inertance pulse tube cryocooler

system. The program provides the user with numerical estimations for regenerator size, acoustic input power, major losses, and net cooling. Furthermore, based on the analogous transmission line model, it offers estimates for the size of the inertance tube as a phase shifter. Despite its beta status, the program delivers good estimations and may be used to construct and enhance pulse tube cryocooler designs.

### 6.1.2 Findings summary

Chapter 1 introduces the concept of cryogenic cooling and the major classifications of cryocooler devices. It then states the research overview, defines the study objectives, and concludes by describing the motivation of this thesis by identifying some of the potential application areas and how PTCs might be used in a variety of industrial and commercial applications.

Chapter 2 briefly describes the evolution of cryogenic cooling in the nineteenth and twentieth centuries. Following that, the chapter offers a detailed overview of closed-cycle cryocoolers before looking into particular promising application areas in MRI, NMR, and IR detectors. The chapter concludes by examining the progress achieved toward miniaturized PTCs and emphasizing that there is still substantial research work to be done before developing an efficient micro-scale PTC system.

The regenerator element is a critical component in a closed-cycle regenerative cryocooler. Chapter 3 explores the phenomena and processes that are expected to influence the performance of miniature PTCs in the regenerator element. Employing mass, energy, and momentum conservation studies, the theory of regenerative heat exchangers is discussed, as well as the physics underpinning regenerator operation. Following that, a MATLAB<sup>®</sup> code was produced to investigate the thermal interaction between the working fluid and the matrix material in a regenerator element. The algorithm was a discretization of the ideal regenerator thermal equations in time and space. In addition, a 2-D axisymmetric CFD study on a proposed simplified validation model was carried out in order to evaluate the validity of the ideal regenerator model's results. The investigation demonstrated the unsteady response of the gas and matrix within the regenerator. The study conducted several parametric investigations to determine the effect of the regenerator's length and diameter on its effectiveness and the relationship between the size of the matrix screen and the wire diameter of the screen on the regenerator's inefficiency. It also looked into the effects of the volumetric flow rate and the number of heat transfer units on the regenerator's performance. These parameters were discovered to affect regenerator inefficiency significantly and that an optimum could be sought under given constraints. Finally, the temperature profiles

from the 2-D axisymmetric model were compared to the ideal model. The study also discovered that finer mesh with a small hydraulic diameter and a regenerator length of about 30 mm and a diameter of 9 mm might be employed without considerably reducing efficiency.

Also in chapter 3, a phasor study was presented to gain a better perception of the impact of various parameters on the performance of the regenerator. The thesis revealed that the cooling process is efficient when the pressure and flow are in phase at the regenerator's center. In this manner, the pressure phasor magnitude would be reduced and the mass flow would be reduced accordingly, resulting in minimising the losses. To accomplish this criterion, normally the flow has to be  $30^\circ$  ahead of the pressure at the aftercooler element and  $30^\circ$  behind the pressure at the cold end. The losses of the regenerator, such as pressure loss, void volume loss, axial heat conduction loss, and thermal loss, are conflicting, with lowering one resulting in an increase in the other. These losses were quantified as a function of geometry and operating parameters in the regenerator. The thesis presented an analytical procedure to optimize the regenerator by minimizing these losses. This approach has been shown to provide reasonable and accurate predictions. While graphical and parameter analyses, as well as reduced models, provide valuable inputs and powerful insights, the final design of the regenerator is highly dependent on numerical tools that simultaneously solve the conservation equations for energy, momentum, and mass with as few simplifications and assumptions as possible. Hence, a special-purpose software, so-called REGEN, developed by NIST, was used to optimize the regenerator element over a set of input parameters like average pressure, pressure ratio, operating frequency, and phase angle at the cold end of the regenerator. REGEN3.3 runs were performed and produced the cooling power and losses associated with a specific set of input parameters, and the results were listed in Table 3.5. The REGEN findings backed up the earlier geometrical estimates from the preliminary suggested optimization approach and the ideal regenerator analysis.

In chapter 4, the theory and operation of pulse tube cryocooler systems were discussed, as well as their classifications. Phasor analysis was used to estimate the cooling power of an orifice-PTC system based on several inputs such as pressure ratio, average pressure, operating frequency, mass flow rate, cold end temperature, and phase angle between pressure and flow at the cold end. After that, the phasor representation for different types of PTC is derived. The study suggests that the basic-PTC system has  $90^\circ$  phase angle between the mass flow and pressure phasors at the cold end, implying zero output cooling power. The phasor study finds that phase shifters like orifice, double-inlet, and inertance tubes establish a phase angle between pressure and flow, thus maximizing the cooling power. Moreover, it suggests that the inertance tube can produce various phase shift angles and has better flexibility in designing for optimum phase

shift. An electrical circuit analogy and the transmission line model were presented to interpret the effect of different phase shifters on the phase shift angle. An inertance tube with a reservoir is analogous to electrical inductance and capacitance, according to the transmission line model in section 4.3.3. Hence, utilizing an inertance tube with the proper sizing in a PTC system can produce an optimum phase shift of approximately  $60^\circ$  at the entrance of the inertance tube element. This condition satisfies the criterion for an effective regeneration process and, thus, an efficient cooling process. Hence, the inertance tube is perfectly suited for high-frequency operation. After that, the thesis presented a one-dimensional numerical model based on mass and energy conservation equations using an unconditionally stable implicit numerical algorithm. The model was developed to estimate approximate design parameters for any similar cooling machine and estimate mass and time-averaged enthalpy flows at the cold and hot ends. In the one-dimensional simulation model, the temperature settled to the desired temperature near the cold end. It showed a condition of periodic steady-state along a 10 cm tube with a uniform distribution and a temperature gradient along the tube length for a 20 Hz operating frequency. For 80 Hz, the cold region has been enlarged, and the temperature profiles have been shifted closer to the hot region, implying that the optimal tube length is significantly less than 10 cm, and signaling that the pulse tube segment should be shorter for efficient high frequency operation.

Additionally, in chapter 4, an inertance PTC system, operating in a steady periodic state under various operating frequencies, was numerically simulated to study the fluid dynamic and heat transfer characteristics occurring within the system. The objective was to ascertain the feasibility of predictive CFD simulation for PTCs. By determining the optimum operating frequency, the CFD successfully predicted the thermodynamic trends and proved the system's merits for high-frequency operation. For given dimensions and a double inertance tube configuration, a frequency of 120 Hz provided the best cooling among the three studied scenarios. Also, it was proven that increasing average pressure in an optimized PTC system leads to shorter cool-down times.

According to the simulation, smaller compressors must be used in conjunction with high-frequency PTCs, not only for efficient operation but also for rapid cooling rate. Following that, numerical models of miniature PTCs were created using both Sage cryocooler modeling software and Fluent, a commercial computational fluid dynamics (CFD) program. A preliminary scaling analysis was performed using Sage before designing the CFD model of the base miniature PTC. The Fluent base model was created using the results of this scaling analysis, and its results were compared to those of Sage. Sage simulations predicted that the system would be less efficient than the fluent model expected, but the ultimate cold tip temperature would be about the same. Fluent predicted a coefficient of performance of 4% at an ultimate cold end temperature

of 100 K. However, comparing the accuracy of the two modeling methodologies for miniature PTCs is difficult without experimental data. Finally, these models were utilized to quantify the effects of many previously known phenomena that affected the operation of miniature PTCs. The results of these two models were used to create three smaller ultra-miniature models, operating at frequencies of 225, 450, and 900 Hz. These PTC models had total volumes ranging from 6.9 cc – 1.25 cc.

The investigation came to a close with the creation of layouts and schematics for the proposed future experimental setup, as well as a full description of the instrumentation equipment. Based on the prior analytic and numerical investigations, the study also created a stand-alone software tool that will be applied to the design and optimization of any inertance pulse tube cryocooler.

### 6.1.3 Implications of the study

The majority of the applications for miniaturized pulse tube cryocoolers require relatively small cooling power and a relatively short cool-down time. It is obvious now that not only the production of low temperatures is essential, but also the size of the equipment. Although there is a compelling need to fill the gap between the requirements of a particular application and the associated cryocooler, the findings of this thesis have broader implications for improving the relevance of miniaturization aspects in pulse tube cryocooler systems.

The findings of the thesis suggest operating close to the optimum frequency for any particular pulse tube cryocooler with specific geometry and operating parameters, so-called resonance frequency, to achieve optimum cooling performance. The gains include decreasing the cool-down time and the system's overall size and establishing a more efficient operation. Generally, when operating at high frequencies, the working gas oscillates over a much reduced swept volume due to the reduced compressor piston displacement. As a result of the decreased oscillating gas volume, it is possible to reduce the size of both the regenerator and the pulse tube components.

However, operating at higher frequencies makes viscous dissipation losses predominant. At the same time, there are safety concerns that come with miniaturization related to increasing the system charging pressure. Also, poor heat transfer characteristics in the regenerator element are anticipated and would result in considerable irreversible losses. The finding suggests that the cryocooler's cooling capacity decreases dramatically with the cryocooler's size. However, this is handled by increasing both the charging pressure and the operating frequency to compensate for the low working fluid volume.

The findings reported in this thesis demonstrate that a combination of inertance tube and

buffer volume is the most appropriate phase shifter to be used with miniature, high-frequency pulse tube cryocoolers. The function of this phase shift mechanism is to secure the required phase shift for efficient operation. The combination of an inertance tube and a reservoir, with proper sizing, would produce a phase shift of around  $60^\circ$  at the inertance tube's inlet. This means that at the midpoint of the regenerator, the flow and pressure are almost in phase, and hence, the regenerator's losses are drastically reduced.

Although the proposed derived systems performed relatively well using conventional stainless steel fillers, the thesis also reveals that novel fine regenerator fillers should be developed if more efficient high-frequency operation is sought. Because reducing the system size results in a reduction in the gas thermal penetration depth, the filler pore size should be reduced proportionately. Another area for improvement is using a mixed regenerator composed of various matrices to improve the regenerator's performance and reduce the overall flow resistance along the tube.

#### **6.1.4 Limitations and challenges**

The conclusions of this thesis should be interpreted in light of a number of constraints. The ultra-miniature models demonstrated the feasibility of pulse tube cryocoolers operating at significantly higher frequencies and on considerably smaller scales. For each operating frequency, excellent performance was predicted for the modeled cryocooler, reaching cold end temperatures of approximately 100 K. However, several challenges related to the modeling techniques and some practical construction aspects need to be addressed for the three derived ultra-miniature models.

One significant constraint is the scarcity of available hydrodynamic parameters for more appropriate materials that can be used with these ultra-miniature models. Since there is a shortfall of regenerator fillers with small enough hydrodynamic diameters to operate effectively at the required high frequencies and mean pressures. For effective regeneration, the wire diameter or hydraulic diameter of the filler material must be much less than the thermal penetration depth of the working fluid. As the system device reduces, the matrix must have a smaller pore diameter, high thermal capacity, low-pressure loss, and low axial thermal conductivity. Also, as the pulse tube component is reduced, the radius must be large compared to the thermal penetration depth of the gas. Additionally, the high average pressure and pressure ratios associated with such scales further complicate the task that rules out many of the materials used in micro-fabrication techniques.

Another limitation is that the CFD analysis was conducted under the thermal equilibrium assumption between the fluid and solid phases. While this is possible for conventional-sized

systems, additional empirical correlations for heat transfer coefficients, which are difficult to derive with high accuracy, are required to operate correctly at the miniature scale.

Finally, producing ultra-miniature PTCs requires compressors with small strokes that can operate continuously at high operating frequencies, which is another significant challenge. However, incorporating a compressor, such as a piezoelectric actuator, that is more feasible to fabricate in the near future may resolve this issue, allowing for PTC efficient miniaturization.

### 6.2 Suggestions for future work

Several avenues of future research are identified in light of the findings of this investigation. Improvements may have been made more accurately if not for equipment and time constraints, as well as a desire to keep the scope of the study manageable. This section outlines potential future work for the continuation of this study.

Experimental validation of the numerical models' results is still required before drawing solid conclusions regarding the accuracy of these derived miniature models. Additionally, extending the CFD modeling techniques used in this study to include non-equilibrium thermal between the solid and fluid phases of porous media would represent a meaningful advancement in cryocooler simulation results.

Another suggestion is to employ more effective filler materials and geometries for the regenerator and the heat exchanger components to address the regenerator's reduced size. Unless this is done, the findings of the ultra-miniature models will remain speculative. Potential regenerator fillers are small-diameter parallel microchannels and micro-pillar matrix fillers. The use of such materials and geometry will improve confidence in the results.

In addition, the ultra-miniature model could benefit from a thorough parametric study based on operating frequency, charge pressure, and piston stroke. Furthermore, proper characterization of additional losses and hydrodynamic parameters linked to the regenerator's reduced size might be conducted. Although 3D simulations require great computational effort, they are recommended for miniature or micro-scale systems due to the availability of computationally efficient modeling techniques or high-performance computers. Also, models for multi-stage or cascading PTCs can be examined. Future implementation of such miniature systems allows PTCs to reach even lower ultimate cold end temperatures. Finally, scaling down the size of a PTC includes reducing the size of the pressure wave oscillator. Hence, utilizing a small-scale piezoelectric pressure oscillator should be investigated.

# References

- [1] R. Radebaugh. “Development of the pulse tube refrigerator as an efficient and reliable cryocooler”. In: *Proc. Institute of Refrigeration (London)* 96 (2000), pp. 11–31.
- [2] G. Walker. *Cryocoolers: Part 1: Fundamentals*. New York, NY: Plenum Press, 1983.
- [3] R. K. Kirschman. “Low-temperature electronics”. In: *IEEE Circuits and Devices Magazine* 6.2 (1990), pp. 12–24.
- [4] R. Radebaugh. “Advances in cryocoolers”. In: *the proceedings of the 16th International Cryogenic Engineering Conference/International Cryogenic Materials Conference, Kitakyushu, Japan, (20-24, May 1996)*. Elsevier. 1997, pp. 33–44.
- [5] M. D. Atrey. “Cryocooler Technology: The Path to Invisible and Reliable Cryogenics”. In: *Cryocoolers: Theory and Applications*. Cham, Switzerland: Springer International Publishing, 2020, pp. 1–46.
- [6] A. R. Jha. *Cryogenic technology and applications*. Burlington, MA: Butterworth-Heinemann, 2006.
- [7] R. Mehta, S. Bapat, and M. Atrey. “Characterization of sorption compressor for mixed refrigerant JT cryocooler”. In: *AIP Conference Proceedings: Transactions of the Cryogenic Engineering Conference, Spokane, Washington (USA), (13–17 June 2011)*. Vol. 1434. 1. American Institute of Physics. 2012, pp. 1797–1804.
- [8] R. Ross. “Aerospace Coolers: A 50-Year Quest for Long-Life Cryogenic Cooling in Space”. In: *Cryogenic Engineering*. New York, NY: Springer, 2007, pp. 225–284.
- [9] R. Peterson. “Size limits for regenerative heat engines”. In: *Microscale thermophysical engineering* 2.2 (1998), pp. 121–131.
- [10] L. Bowman and J. McEntee. *Microminiature stirling cycle cryocoolers and engines*. US Patent 5,749,226. May 1998.
- [11] P. Nika et al. “Miniature pulse tube for the cooling of electronic devices: Functioning principles and practical modeling”. In: *Microscale thermophysical engineering* 8.4 (2004), pp. 301–325.
- [12] K.-i. Kanao, N. Watanabe, and Y. Kanazawa. “A miniature pulse tube refrigerator for temperatures below 100 K”. In: *Cryogenics* 34 (1994), pp. 167–170.
- [13] R. Radebaugh and A. O’Gallagher. “Regenerator operation at very high frequencies for microcryocoolers”. In: *AIP Conference Proceedings: Transactions of the Cryogenic Engineering Conference, Keystone, Colorado (USA), (29 August-2 September 2005)*. Vol. 823. 1. American Institute of Physics. 2006, pp. 1919–1928.

- [14] I. Garaway et al. “Development of a miniature 150 Hz pulse tube cryocooler”. In: *the proceedings of the 15th international cryocooler conference, Long Beach, California, USA, (9-12, June 2008)*. 2008, pp. 105–113.
- [15] S. Vanapalli et al. “120 Hz pulse tube cryocooler for fast cooldown to 50 K”. In: *Applied physics letters* 90.7 (2007), p. 072504.
- [16] T. C. Nast et al. “Miniature pulse tube cryocooler for space applications”. In: *Cryocoolers 11: A publication of the 11th international cryocooler conference held in Keystone, Colorado, on June 20-22, 2000*. Boston, MA: Springer US, 2002, pp. 145–154.
- [17] Y. Ouyang et al. “Research on 1 kg Miniature Pulse Tube Cryocooler”. In: *the proceedings of the 20th international cryocooler conference, Burlington, Vermont, USA, (18-21, June 2018)*. 2018, pp. 103–107.
- [18] M. Petach et al. “High frequency coaxial pulse tube microcooler”. In: *the proceedings of the 15th international cryocooler conference, Long Beach, California, USA, (9-12, June 2008)*. 2008, pp. 97–103.
- [19] J. Olson et al. “Coaxial pulse tube microcryocooler”. In: *the proceedings of the 18th international cryocooler conference, Syracuse, New York, USA, (9-12, June 2014)*. 2014, pp. 51–57.
- [20] H. Yu et al. “An efficient miniature 120 Hz pulse tube cryocooler using high porosity regenerator material”. In: *Cryogenics* 88 (2017), pp. 22–28.
- [21] *Defense Advanced Research Projects Agency Microsystems Technology Office*. <http://www.darpa.mil/>. 2020 (accessed December 8, 2020).
- [22] A. F. McDowell and N. L. Adolphi. “Operating nanoliter scale NMR microcoils in a 1 Tesla field”. In: *Journal of Magnetic Resonance* 188.1 (2007), pp. 74–82.
- [23] H. Ryan et al. “Contactless NMR spectroscopy on a chip”. In: *Analytical chemistry* 84.8 (2012), pp. 3696–3702.
- [24] D. J. Russell et al. “A comparison of inverse-detected heteronuclear NMR performance: conventional vs cryogenic microprobe performance”. In: *Journal of natural products* 63.8 (2000), pp. 1047–1049.
- [25] A. A. Nnanna. “Application of refrigeration system in electronics cooling”. In: *Applied Thermal Engineering* 26.1 (2006), pp. 18–27.
- [26] R. Mongia et al. “Small scale refrigeration system for electronics cooling within a notebook computer”. In: *Thermal and Thermomechanical Proceedings 10th Inter-society Conference on Phenomena in Electronics Systems, 2006. IThERM 2006, San Diego, CA, USA, (30 May-2 June 2006)*. IEEE. 2006, pp. 751–758.

- 
- [27] P. E. Phelan, V. A. Chiriac, and T.-Y. Lee. “Current and future miniature refrigeration cooling technologies for high power microelectronics”. In: *IEEE Transactions on Components and Packaging Technologies* 25.3 (2002), pp. 356–365.
- [28] X. C. Tong. “Liquid Cooling Devices and Their Materials Selection”. In: *Advanced Materials for Thermal Management of Electronic Packaging*. New York, NY: Springer, 2011, pp. 421–475.
- [29] C. Kirkconnell. *A cryocooler in your laptop computer? Maybe*. [www.electronics-cooling.com/2008/11/a-cryocooler-in-your-laptop-computer-maybe](http://www.electronics-cooling.com/2008/11/a-cryocooler-in-your-laptop-computer-maybe). (Online: accessed on 1-10 March 2020).
- [30] A. C. Kirk. “On the mechanical production of cold (includes plates and appendix)”. In: *Minutes of the Proceedings of the Institution of Civil Engineers (London)*. Vol. 37(1874). Thomas Telford-ICE Virtual Library. 1874, pp. 244–282.
- [31] S. Collins and R. Cannaday. “Expansion Machines for Low Temperature Processes”. In: *American Journal of Physics* 27.7 (1959), pp. 530–530.
- [32] E. Solvay. (1887), *Deutsches Reichspatent*. No. 39280.
- [33] G. Walker. *Stirling engines*. Oxford: Clarendon Pr., 1980.
- [34] J. Kohler and C. Jonkers. “Construction of a gas refrigerating machine”. In: *Philips Tech. Rev* 16.5 (1954), pp. 105–115.
- [35] S. C. Russo. *Study of a Vuilleumier cycle cryogenic refrigerator for detector cooling on the limb scanning infrared radiometer*. Tech. rep. (Contract report No. CR-145078). Culver City, California: by Hughes Aircraft Company Presented to NASA, July, 1976, p. 11211.
- [36] W. H. Higa and E. Wiebe. “One Million Hours at 4.5 Kelvin”. In: *Applications of Closed-cycle Cryocoolers to Small Superconducting Devices: Proceedings of a Conference Held at the National Bureau of Standards, Boulder, Colorado, October 3-4, 1977*. Vol. 13. 1977, pp. 99–108.
- [37] W. H. Higa. “A practical Philips cycle for low-temperature refrigeration.” In: *Cryogenic Technology* 8 (1965), pp. 203–209.
- [38] W. E. Gifford and R. C. Longworth. “Pulse-Tube Refrigeration”. In: *Journal of Engineering for Industry* 86.3 (1964), pp. 264–268.
- [39] R. C. Longworth. “An Experimental Investigation of Pulse Tube Refrigeration Heat Pumping Rates”. In: *Advances in Cryogenic Engineering*. Ed. by K. D. Timmerhaus. Boston, MA: Springer US, 1967, pp. 608–618.
- [40] E. I. Mikulin, A. A. Tarasov, and M. P. Shkrebyonock. “Low-Temperature Expansion Pulse Tubes”. In: *Advances in Cryogenic Engineering: Volume 29*. Boston, MA: Springer US, 1984, pp. 629–637.
-

- [41] R. Radebaugh et al. “A comparison of three types of pulse tube refrigerators: new methods for reaching 60 K”. In: *Advances in cryogenic engineering*. Boston, MA: Springer, 1986, pp. 779–789.
- [42] S. W. Zhu et al. “Phase Shift Effect of the Long Neck Tube for the Pulse Tube Refrigerator”. In: *Cryocoolers 9: A publication of the 9th International Cryocooler Conference held in Waterville Valley, New Hampshire, on June 25-27, 1996*. Boston, MA: Springer US, 1997, pp. 269–278.
- [43] R. Mahajan, C.-p. Chiu, and G. Chrysler. “Cooling a microprocessor chip”. In: *Proceedings of the IEEE* 94.8 (2006), pp. 1476–1486.
- [44] G. S. Nolas, J. Sharp, and J. Goldsmid. *Thermoelectrics: basic principles and new materials developments*. Vol. 45. Springer Series in Materials Science. Springer Berlin Heidelberg, 2013.
- [45] S. B. Riffat and X. Ma. “Thermoelectrics: a review of present and potential applications”. In: *Applied thermal engineering* 23.8 (2003), pp. 913–935.
- [46] D. Enescu and E. O. Virjoghe. “A review on thermoelectric cooling parameters and performance”. In: *Renewable and Sustainable Energy Reviews* 38 (2014), pp. 903–916.
- [47] R. Buist et al. “Low Temperature Thermoelectric Cooler for 145 K Detector Array Package”. In: *US Army Night Vision Laboratories, Fort Belvoir, Virginia, Technical Report ADB008934 (Borg-Warner Thermoelectrics)* (1976).
- [48] J. S. Brown and P. A. Domanski. “Review of alternative cooling technologies”. In: *Applied Thermal Engineering* 64.1-2 (2014), pp. 252–262.
- [49] V. Franco et al. “Magnetocaloric effect: From materials research to refrigeration devices”. In: *Progress in Materials Science* 93 (2018), pp. 112–232.
- [50] V. K. Pecharsky and K. A. Gschneidner Jr. “Giant magnetocaloric effect in Gd<sub>5</sub>(Si<sub>2</sub>Ge<sub>2</sub>)”. In: *Physical review letters* 78.23 (1997), p. 4494.
- [51] A. Kitanovski and P. W. Egolf. “Innovative ideas for future research on magnetocaloric technologies”. In: *International journal of refrigeration* 33.3 (2010), pp. 449–464.
- [52] T. W. Hänsch and A. L. Schawlow. “Cooling of gases by laser radiation”. In: *Optics Communications* 13.1 (1975), pp. 68–69.
- [53] J. Dalibard and C. Cohen-Tannoudji. “Dressed-atom approach to atomic motion in laser light: the dipole force revisited”. In: *Journal of the Optical Society of America B* 2.11 (1985), pp. 1707–1720.
- [54] P. Pringsheim. “Zwei bemerkungen über den unterschied von lumineszenz-und temperaturstrahlung”. In: *Zeitschrift für Physik* 57.11-12 (1929), pp. 739–746.

- 
- [55] G. Nemova and R. Kashyap. “Twenty Years of Laser Cooling of Solids”. In: *Journal of Physics: Conference Series*. Vol. 619. 1. IOP Publishing, 2015, p. 012037.
- [56] B. Heeg et al. “Comparative intra-versus extra-cavity laser cooling efficiencies”. In: *Journal of applied physics* 91.5 (2002), pp. 3356–3362.
- [57] T. Gosnell. “Laser cooling of a solid by 65 K starting from room temperature”. In: *Optics Letters* 24.15 (1999), pp. 1041–1043.
- [58] M. P. Hehlen et al. “First demonstration of an all-solid-state optical cryocooler”. In: *Light: Science & Applications* 7.1 (2018), pp. 1–10.
- [59] D. R. Brown et al. “The prospects of alternatives to vapor compression technology for space cooling and food refrigeration applications”. In: *Energy Engineering* 109.6 (2012), pp. 7–20.
- [60] F. Zink, J. S. Vipperman, and L. A. Schaefer. “Environmental motivation to switch to thermoacoustic refrigeration”. In: *Applied Thermal Engineering* 30.2-3 (2010), pp. 119–126.
- [61] G. Walker and E. R. Bingham. *Low-capacity cryogenic refrigeration*. Oxford: Clarendon Press, 1994.
- [62] R. A. Ackermann. *Cryogenic regenerative heat exchangers*. New York, NY: Plenum Press, 1997.
- [63] H. O. McMahon and W. E. Gifford. “A new low-temperature gas expansion cycle”. In: *Advances in cryogenic engineering*. Boston, MA: Springer US, 1960, pp. 354–367.
- [64] W. Swift, F. Dolan, and M. Zagarola. “The NICMOS cooling system—5 years of successful on-orbit operation”. In: *AIP Conference Proceedings: Transactions of the Cryogenic Engineering Conference, Chattanooga (Tennessee), (16–20 July 2007)*. Vol. 985. 1. American Institute of Physics. 2008, pp. 799–806.
- [65] R. W. Hill et al. “A recuperative heat exchanger for space-borne turbo-Brayton cryocoolers”. In: *the proceedings of the 14th International Cryocooler Conference, Annapolis (Maryland), (14-16, June 2006)*. 2006, pp. 525–533.
- [66] R. Radebaugh. “Cryocoolers: the state of the art and recent developments”. In: *Journal of Physics: Condensed Matter* 21.16 (2009), p. 164219.
- [67] R. Radebaugh. “Refrigeration for superconductors”. In: *Proceedings of the IEEE* 92.10 (2004), pp. 1719–1734.
- [68] F. Steinmeyer et al. “Towards the invisible cryogenic system for magnetic resonance imaging”. In: *AIP Conference Proceedings: Proceedings of the Cryogenic Engineering Conference, Madison, Wisconsin (USA), (16-20 July 2001)*. Vol. 613. 1. American Institute of Physics. 2002, pp. 1659–1666.
-

- [69] S. Yoon et al. “The performance of the conduction cooled 2G HTS magnet wound without turn to turn insulation generating 4.1 T in 102 mm bore”. In: *Physica C: Superconductivity* 494 (2013), pp. 242–245.
- [70] J. H. Bae et al. “Design, fabrication and evaluation of a conduction cooled HTS magnet for SMES”. In: *Physica C: Superconductivity* 469.15-20 (2009), pp. 1794–1798.
- [71] H. Tanaka et al. “Development of cryogenic cooling system using a double G-M cryocooler for NMR spectrometer”. In: *Journal of Physics: Conference Series* 97 (2008), p. 012232.
- [72] O. Kirichek et al. “Nuclear magnetic resonance magnet actively cooled by pulse tube refrigerator”. In: *Review of scientific instruments* 76.5 (2005), p. 055104.
- [73] H. Kovacs, D. Moskau, and M. Spraul. “Cryogenically cooled probes—a leap in NMR technology”. In: *Progress in Nuclear Magnetic Resonance Spectroscopy* 2.46 (2005), pp. 131–155.
- [74] V. Kotsubo and R. Nast. “Cryogenic System for a High Temperature Superconductor NMR Probe”. In: *Advances in Cryogenic Engineering: Part A*. Boston, MA: Springer US, 1996, pp. 1857–1864.
- [75] K. Saitoh et al. “Development of cryogenic probe system for high-sensitive NMR spectroscopy”. In: *Journal of Physics: Conference Series* 97 (2008), p. 012141.
- [76] M. D. Atrey et al. “Pulse tube refrigerator based cryogenic cooling circuit for NMR cold probes”. In: *AIP Conference Proceedings: Transactions of the Cryogenic Engineering Conference, Keystone, Colorado (USA), (29 August-2 September 2005)*. Vol. 823. 1. American Institute of Physics. 2006, pp. 41–48.
- [77] H. Dunmire. “U.S. Army Cryocooler Status Update”. In: *Military and Commercial Applications for Low Cost Cryocoolers* (1998). San Diego, Jan. 1998, Electronic Industries Association (ETA), Arlington, VA.
- [78] C. Keung et al. “Design and fabrication of a long-life stirling cycle cooler for space application”. In: *Philips Final Report, NASA Contract No NAS5-26688, NASA-Goddard Space Flight Center* (Nov, 1990).
- [79] A. Daniels, M. Gasser, and A. Sherman. “Magnetically suspended Stirling cryogenic space refrigerator status report”. In: *Advances in Cryogenic Engineering* 27 (1982), pp. 711–719.
- [80] B. Wang and Z. Gan. “A critical review of liquid helium temperature high frequency pulse tube cryocoolers for space applications”. In: *Progress in Aerospace Sciences* 61 (2013), pp. 43–70.

- 
- [81] M. Mai et al. “AIM space cryocooler programs”. In: *the proceedings of the 16th International Cryocooler Conference, Atlanta, Georgia (USA), (17-20, May 2010)*. 2010, pp. 133–141.
- [82] R. G. Ross Jr and R. F. Boyle. “An Overview of NASA Space Cryocooler Programs”. In: *the proceedings of the 14th International Cryocooler Conference, Annapolis, Maryland (USA), (14-16, June 2006)*. 2006, pp. 1–10.
- [83] J. D. Dobak, E. Ryba, and S. Kovalcheck. “A new closed-loop cryosurgical device for endometrial ablation”. In: *The Journal of the American Association of Gynecologic Laparoscopists* 7.2 (2000), pp. 245–249.
- [84] E. D. Marquardt, R. Radebaugh, and J. Dobak. “A Cryogenic Catheter for Treating Heart Arrhythmia”. In: *Advances in Cryogenic Engineering*. Boston, MA: Springer US, 1998, pp. 903–910.
- [85] D. Theodorescu. “Cancer cryotherapy: evolution and biology”. In: *Reviews in urology* 6.Suppl 4 (2004), S9–S19.
- [86] M. Xu et al. “Experimental research of a miniature coaxial pulse tube refrigerator using nylon tube”. In: *Cryogenics* 36.2 (1996), pp. 131–133.
- [87] P. Curlier. “Ultrareliable miniature pulse tube cryocooler for non-commercial space application”. In: *Sixth European Symposium on Space Environmental Control Systems, Noordwijk, the Netherlands, (20-22, May 1997)*. Vol. 400. 1997, p. 471.
- [88] P. Curlier. “Ultrareliable pulse tube cryocooler with a flexure-bearing linear-drive compressor”. In: *Infrared Technology and Applications XXII*. Vol. 2744. International Society for Optics and Photonics. Bellingham, WA: SPIE, 1996, pp. 302–307.
- [89] P. Curlier. “Progress on miniature pulse tube cryocoolers for the commercial and military market”. In: *Infrared Technology and Applications XXIII*. Vol. 3061. International Society for Optics and Photonics. Bellingham, WA: SPIE, 1997, pp. 84–92.
- [90] J. Liang et al. “Study on miniature pulse tube cryocooler for space application”. In: *Cryogenics* 40.3 (2000), pp. 229–233.
- [91] C. K. Chan et al. “IMAS Pulse Tube Cooler Development and Testing”. In: *Cryocoolers 10: A publication of the 10th International Cryocooler Conference held in Monterey, California, on May 26-28, 1998*. Boston, MA: Springer US, 2002, pp. 139–147.
-

- [92] H. L. Chen et al. “An Integrated Miniature Pulse Tube Cryocooler at 80K”. In: *AIP Conference Proceedings: Transactions of the Cryogenic Engineering Conference, Chattanooga (Tennessee), (16–20 July 2007)*. Vol. 985. 1. American Institute of Physics. 2008, pp. 673–677.
- [93] T. Trollier et al. “Design of a Miniature Pulse Tube Cryocooler for space applications”. In: *AIP Conference Proceedings: Transactions of the Cryogenic Engineering Conference, Anchorage, Alaska (USA), (22–26 September 2003)*. Vol. 710. 1. American Institute of Physics. 2004, pp. 1318–1325.
- [94] E. Tward et al. “Miniature pulse tube cooler”. In: *AIP Conference Proceedings: Transactions of the Cryogenic Engineering Conference, Anchorage, Alaska (USA), (22–26 September 2003)*. Vol. 710. 1. American Institute of Physics. 2004, pp. 1326–1329.
- [95] N. Matsumoto et al. “Development of the miniature pulse tube cryocooler”. In: *AIP Conference Proceedings: Transactions of the Cryogenic Engineering Conference, Anchorage, Alaska (USA), (22–26 September 2003)*. Vol. 710. 1. American Institute of Physics. 2004, pp. 1339–1346.
- [96] S. Vanapalli et al. “Modeling and experiments on fast cooldown of a 120 Hz pulse tube cryocooler”. In: *AIP Conference Proceedings: Transactions of the Cryogenic Engineering Conference, Chattanooga (Tennessee), (16–20 July 2007)*. Vol. 985. 1. American Institute of Physics. 2008, pp. 1429–1436.
- [97] I. Garaway and G. Grossman. “Studies in high frequency oscillating compressible flow for application in a micro regenerative cryocooler”. In: *AIP Conference Proceedings: Transactions of the Cryogenic Engineering Conference, Keystone, Colorado (USA), (29 August–2 September 2005)*. Vol. 823. 1. American Institute of Physics. 2006, pp. 1588–1595.
- [98] I. Garaway and G. Grossman. “A study of a high frequency miniature reservoir-less pulse tube”. In: *AIP Conference Proceedings: Transactions of the Cryogenic Engineering Conference, Chattanooga (Tennessee), (16–20 July 2007)*. Vol. 985. 1. American Institute of Physics. 2008, pp. 1547–1554.
- [99] I. Garaway and G. Grossman. “Piezo-hydraulic actuation for driving high frequency miniature split-stirling pulse tube cryocoolers”. In: *AIP Conference Proceedings: Transactions of the Cryogenic Engineering Conference, Chattanooga (Tennessee), (16–20 July 2007)*. Vol. 985. 1. American Institute of Physics. 2008, pp. 622–629.
- [100] I. Garaway et al. “Diagnostics and optimization of a miniature high frequency pulse tube cryocooler”. In: *AIP Conference Proceedings: Transactions of the Cryogenic Engineering Conference, Tucson, (28 June–2 July 2009)*. Vol. 1218. 1. American Institute of Physics. 2010, pp. 167–174.

- 
- [101] S. Sobol, Y. Katz, and G. Grossman. “A study of a miniature in-line pulse tube cryocooler”. In: *the proceedings of the 16th International Cryocooler Conference, Atlanta, Georgia (USA), (17-20, May 2010)*. 2010, pp. 87–95.
- [102] A. Zhang et al. “Study on a 10 W/90 K in-line pulse tube cryocooler”. In: *Cryogenics* 52.12 (2012), pp. 800–804.
- [103] T. Trollier et al. “150K Pulse Tube Cooler for Micro-Satellites”. In: *the proceedings of the 17th International Cryocooler Conference, Los Angeles, California, (9-12, July 2012)*. 2012, pp. 53–60.
- [104] T. Conrad et al. “Raytheon advanced pulse-tube cryocoolers”. In: *Tri-Technology Device Refrigeration (TTDR)*. Vol. 9821. International Society for Optics and Photonics. Bellingham, WA: SPIE, 2016, pp. 23–27.
- [105] H. Dang et al. “Advances in single-and multi-stage Stirling-type pulse tube cryocoolers for space applications in NLIP/SITP/CAS”. In: *IOP Conference Series: Materials Science and Engineering*. Vol. 278. 1. IOP Publishing. 2017, p. 012008.
- [106] Z. Jiang and Y. Wu. “A miniature pulse tube cryocooler used in a superspectral imager”. In: *Tri-Technology Device Refrigeration (TTDR) II*. Vol. 10180. International Society for Optics and Photonics. Bellingham, WA: SPIE, 2017, pp. 14–18.
- [107] H. Dang et al. “Review of recent advances in Stirling-type pulse tube cryocoolers”. In: *IOP Conference Series: Materials Science and Engineering*. Vol. 502. 1. IOP Publishing. 2019, p. 012034.
- [108] R. Stirling. “Stirling air engine and the heat regenerator”. In: *US Patent* 4081 (1816), p. 16.
- [109] W. Nusselt. “Die Theorie des Winderhitzers”. In: *Zeitschrift des Vereines deutscher Ingenieure* 71.3 (1927), p. 85.
- [110] C. E. Iliffe. “Thermal analysis of the contra-flow regenerative heat exchanger”. In: *Proceedings of the Institution of Mechanical Engineers* 159.1 (1948), pp. 363–372.
- [111] T. Kuriyama et al. “High Efficient two-Stage GM Refrigerator with Magnetic Material in the Liquid Helium Temperature Region”. In: *Advances in Cryogenic Engineering: Part A & B*. Boston, MA: Springer US, 1990, pp. 1261–1269.
- [112] G. Walker. *Cryocoolers: part 2: applications*. International Cryogenics Monograph Series. Boston, MA: Springer US, 2012.
- [113] W. M. Kays and A. L. London. *Compact heat exchangers*. McGraw-Hill, New York, NY, 1984.
-

- [114] S. Kakaç, M. R. Avelino, and H. F. Smirnov. *Low Temperature and Cryogenic Refrigeration*. Nato Science Series II: Dordrecht, the Netherlands: Springer, 2003. ISBN: 9781402012730.
- [115] H. J. M. ter Brake and G. F. M. Wiegerinck. “Low-power cryocooler survey”. In: *Cryogenics* 42.11 (2002), pp. 705–718.
- [116] R. Gupta. *Selected Cryogenic Data Handbook*. Brookhaven National Laboratory, US Department of Energy. 2017.
- [117] N. Almtireen, J. J. Brandner, and J. G. Korvink. “Numerical Thermal Analysis and 2-D CFD Evaluation Model for An Ideal Cryogenic Regenerator”. In: *Micro-machines* 11.4 (2020), p. 361.
- [118] H. Schlichting and K. Gersten. *Boundary-Layer Theory*. Springer Berlin Heidelberg, 2016.
- [119] A. Fluent. *ANSYS R1 user’s guide*. Canonsburg, Pennsylvania, USA: ANSYS Inc. 2019.
- [120] E. C. Landrum et al. “Hydrodynamic parameters of mesh fillers relevant to miniature regenerative cryocoolers”. In: *Cryogenics* 50.6-7 (2010), pp. 373–380.
- [121] R. Radebaugh. “A Review of Pulse Tube Refrigeration”. In: *Advances in Cryogenic Engineering: Part A & B*. Boston, MA: Springer US, 1990, pp. 1191–1205.
- [122] R. Radebaugh et al. “Inertance tube optimization for pulse tube refrigerators”. In: *AIP Conference Proceedings: Transactions of the Cryogenic Engineering Conference, Keystone, Colorado (USA), (29 August-2 September 2005)*. Vol. 823. 1. American Institute of Physics. 2006, pp. 59–67.
- [123] F. Kuriyama and R. Radebaugh. “Analysis of mass and energy flow rates in an orifice pulse-tube refrigerator”. In: *Cryogenics* 39.1 (1999), pp. 85–92.
- [124] R. Radebaugh. “Pulse Tube Cryocoolers”. In: *Low Temperature and Cryogenic Refrigeration*. Dordrecht: Springer Netherlands, 2003, pp. 415–434.
- [125] R. Radebaugh and B. Louie. “A simple, first step to the optimization of regenerator geometry”. In: *the proceedings of the 3rd Cryocooler Conference, Boulder, Colorado (USA), (17-18, September 1984)*. 1985, pp. 177–198.
- [126] I. Rühlich and H. Quack. “Investigations on Regenerative Heat Exchangers”. In: *Cryocoolers 10: A publication of the 10th International Cryocooler Conference held in Monterey, California, on May 26-28, 1998*. Boston, MA: Springer US, 2002, pp. 265–274.

- 
- [127] M. A. Lewis and R. Radebaugh. “Measurement of Heat Conduction through Bonded Regenerator Matrix Materials”. In: *Cryocoolers 12: A publication of the 12th International Cryocooler Conference held in Cambridge, Massachusetts, on June 18-20, 2002*. Boston, MA: Springer US, 2003, pp. 517–522.
- [128] R. A. Ackermann. “The Influence of the Wall and Longitudinal Conduction Effects on the Performance of a Periodic-Flow Regenerator”. PhD thesis. Syracuse University, 1967.
- [129] T. J. Lambertson. “Performance factors of a periodic-flow heat exchanger.” PhD thesis. Monterey, California: Naval Postgraduate School, 1957.
- [130] G. D. Bahnke and C. P. Howard. “The Effect of Longitudinal Heat Conduction on Periodic-Flow Heat Exchanger Performance”. In: *Journal of Engineering for Power* 86.2 (1964), pp. 105–117.
- [131] J. Gary, D. E. Daney, and R. Radebaugh. “A computational model for a regenerator”. In: *the proceedings of the 3rd Cryocooler Conference, Boulder, Colorado (USA), (17-18, September 1984)*. 1985, pp. 199–211.
- [132] M. A. Lewis et al. “Pulse tube cryocooler for rapid cooldown of a superconducting magnet”. In: *the proceedings of the 15th International Cryocooler Conference, Long Beach, California (USA), (9-12, June 2008)*. 2008, pp. 167–176.
- [133] Q. Cao et al. “Theoretical and experimental study on a pulse tube cryocooler driven with a linear compressor”. In: *the proceedings of the 15th International Cryocooler Conference, Long Beach, California (USA), (9-12, June 2008)*. 2008, pp. 149–156.
- [134] Z. H. Gan et al. “A two-stage Stirling-type pulse tube cryocooler with a cold inertance tube”. In: *Cryogenics* 50.6-7 (2010), pp. 426–431.
- [135] J. Gary et al. “REGEN 3.3: User Manual”. In: *National Institute of Standards and Technology* 4 (2008).
- [136] C. Li and G. Peterson. “The effective thermal conductivity of wire screen”. In: *International Journal of Heat and Mass Transfer* 49.21-22 (2006), pp. 4095–4105.
- [137] J. Shi, J. M. Pfothauer, and G. F. Nellis. “Dimensionless Analysis for Regenerator Design”. In: *the proceedings of the 14th International Cryocooler Conference, Annapolis, Maryland, (14-16, June 2006)*. 2006, pp. 419–427.
- [138] J. Pfothauer, R. Wang, and F. Miller. “Regenerator design optimization: Results from REGEN 3.3”. In: *Cryogenics* 97 (2019), pp. 77–84.
- [139] L. Y. Wang et al. “Optimization design on single stage regenerators for various working conditions”. In: *Journal of Engineering Thermophysics* 35.11 (2014), pp. 2134–2139.
-

- [140] T. Ki and S. Jeong. “Stirling-type pulse tube refrigerator with slit-type heat exchangers for HTS superconducting motor”. In: *Cryogenics* 51.6 (2011), pp. 341–346.
- [141] J. Y. Hu et al. “A double-acting thermoacoustic cryocooler for high temperature superconducting electric power grids”. In: *Applied Energy* 112 (2013), pp. 1166–1170.
- [142] A. Rogalski. “Recent progress in infrared detector technologies”. In: *Infrared Physics & Technology* 54.3 (2011), pp. 136–154.
- [143] R. Radebaugh. “Pulse tube cryocoolers for cooling infrared sensors”. In: *Infrared Technology and Applications XXVI*. Vol. 4130. International Society for Optics and Photonics. Bellingham, WA: SPIE, 2000, pp. 363–379.
- [144] R. Lewis et al. “Micro cryogenic coolers for IR imaging”. In: *Infrared Technology and Applications XXXVII*. Vol. 8012. International Society for Optics and Photonics. Bellingham, WA: SPIE, 2011, pp. 797–805.
- [145] N. Rando et al. “Space science applications of cryogenic detectors”. In: *Nuclear Instruments and Methods in Physics Research Section A: Accelerators, Spectrometers, Detectors and Associated Equipment* 522.1-2 (2004), pp. 62–68.
- [146] R. F. Boyle and R. G. Ross Jr. “Overview of NASA space cryocooler programs”. In: *AIP Conference Proceedings: Proceedings of the Cryogenic Engineering Conference, Madison, Wisconsin (USA), (16-20 July 2001)*. Vol. 613. 1. 2002, pp. 1037–1044.
- [147] R. Radebaugh. “Pulse Tube Refrigeration—A New Type of Cryocooler”. In: *Japanese Journal of Applied Physics* 26.S3-3 (1987), p. 2076.
- [148] Y. Zhao et al. “CFD modeling and experimental verification of oscillating flow and heat transfer processes in the micro coaxial Stirling-type pulse tube cryocooler operating at 90–170 Hz”. In: *Cryogenics* 90 (2018), pp. 30–40.
- [149] A. Hofmann and H. Pan. “Phase shifting in pulse tube refrigerators”. In: *Cryogenics* 39.6 (1999), pp. 529–537.
- [150] E. D. Marquardt and R. Radebaugh. “A pulse tube oxygen liquefier”. In: *Advances in cryogenic engineering* 45.A (2000), pp. 457–464.
- [151] W. E. Salazar. “Status of Programs for the DoD Family of Linear Drive Cryogenic Coolers for Weapon Systems”. In: *Cryocoolers 11: A publication of the 11th international cryocooler conference held in Keystone, Colorado, on June 20-22, 2000*. Boston, MA: Springer US, 2002, pp. 11–16.
- [152] Y. Matsubara. “Classification of pulse tube cryocoolers”. In: *ICEC 17: international cryogenic engineering conference (Bournemouth, 14-17 July 1998)*. 1998, pp. 11–16.

- 
- [153] Z. Shaowei, W. Peiyi, and C. Zhongqi. “Double inlet pulse tube refrigerators: an important improvement”. In: *cryogenics* 30.6 (1990), pp. 514–520.
- [154] S. Backhaus and G. Swift. “A thermoacoustic Stirling heat engine”. In: *Nature* 399.6734 (1999), pp. 335–338.
- [155] K. M. Godshalk et al. “Characterization of 350 Hz Thermoacoustic Driven Orifice Pulse Tube Refrigerator with Measurements of the Phase of the Mass Flow and Pressure”. In: *Advances in Cryogenic Engineering: Part A*. Boston, MA: Springer US, 1996, pp. 1411–1418.
- [156] D. L. Gardner and G. W. Swift. “Use of inertance in orifice pulse tube refrigerators”. In: *Cryogenics* 37.2 (1997), pp. 117–121.
- [157] K. G. Narayankhedkar and V. D. Mane. “Investigation of pulse tube refrigerator”. In: *Journal of Manufacturing Science and Engineering, Transactions of the ASME* 95.1 (1973), pp. 373–378.
- [158] A. De Waele, P. Steijaert, and J. Gijzen. “Thermodynamical aspects of pulse tubes”. In: *Cryogenics* 37.6 (1997), pp. 313–324.
- [159] A. De Waele, P. P. Steijaert, and J. Koning. “Thermodynamical aspects of pulse tubes II”. In: *Cryogenics* 38.3 (1998), pp. 329–335.
- [160] P. Kittel et al. “General pulse tube theory”. In: *Cryogenics* 36.10 (1996), pp. 849–857.
- [161] R. Richardson and B. Evans. “A review of pulse tube refrigeration”. In: *International journal of refrigeration* 20.5 (1997), pp. 367–373.
- [162] G. Chen et al. “Thermodynamic performance prediction of pulse tube refrigeration with mixture fluids”. In: *Cryogenics* 40.4-5 (2000), pp. 261–267.
- [163] P. Nika and Y. Bailly. “Comparison of two models of a double inlet miniature pulse tube refrigerator: Part A thermodynamics”. In: *Cryogenics* 42.10 (2002), pp. 593–603.
- [164] L. Mohanta and M. Atrey. “Phasor analysis of pulse tube refrigerator”. In: *the proceedings of the 16th International Cryocooler Conference, Atlanta, Georgia (USA), (17-20, May 2010)*. May, 2010, pp. 299–308.
- [165] N. Almtireen, J. J. Brandner, and J. G. Korvink. “Pulse Tube Cryocooler: Phasor Analysis and One-Dimensional Numerical Simulation”. In: *Journal of Low Temperature Physics* 199 (5 2020), pp. 1179–1197.
- [166] N. Chen, C. Yang, and L. Xu. “Optimal vector analysis of the phase shifter in the pulse tube refrigerator”. In: *the proceedings of the 20th international cryogenic engineering conference (ICEC20), Beijing, China, (11-14, May 2004)*. Elsevier, 2005, pp. 261–264.
-

- [167] M. D. Chokhawala et al. “Phasor analysis for double inlet pulse tube cryocooler”. In: *Advances in cryogenic engineering* 45 (2000), pp. 159–166.
- [168] D. Abraham, C. Damu, and B. T. Kuzhiveli. “Numerical analysis of inertance pulse tube cryocooler with a modified reservoir”. In: *IOP Conference Series: Materials Science and Engineering* 278(1) (2017), p. 012154.
- [169] A. Scheidegger. “The Physics of Flow Through Porous Media”. In: *Soil Science* 86.6 (1958), p. 355.
- [170] P. C. Magnusson et al. *Transmission lines and wave propagation*. CRC press, Boca Raton, Florida, 2017.
- [171] S. Zhu and Y. Matsubara. “Numerical method of inertance tube pulse tube refrigerator”. In: *Cryogenics* 44.9 (2004), pp. 649–660.
- [172] C. Wang, P. Y. Wu, and Z. Q. Chen. “Numerical analysis of double-inlet pulse tube refrigerator”. In: *Cryogenics* 33.5 (1993), pp. 526–530.
- [173] N. Almtireen, J. J. Brandner, and J. G. Korvink. “One-dimensional numerical analysis for Gifford-McMahon pulse tube cryocooler”. In: *15th International Institute of Refrigeration Conference on Cryogenics, CRYOGENICS 2019; Prague; Czech Republic; 8 April 2019 through 11 April 2019*. Vol. Part F147717. Refrigeration Science and Technology. 43.22.01; LK 01. International Institute of Refrigeration, Paris, 2019, pp. 209–214.
- [174] S. W. Zhu and Z. Q. Chen. “Isothermal model of pulse tube refrigerator”. In: *Cryogenics* 34.7 (1994), pp. 591–595.
- [175] M. D. Atrey and K. G. Narayankhedkar. “Development of second order isothermal model of orifice type pulse tube refrigerator (OPTR) with linear compressor”. In: *18th International Cryogenic Engineering Conference (ICEC-18), Mumbai, India, (21-25, Feb 2000)*. 2000, pp. 519–522.
- [176] D. W. J. Willems and J. A. M. Dam. “Three-dimensional pulse tube simulations”. In: *AIP Conference Proceedings: Proceedings of the Cryogenic Engineering Conference, Madison, Wisconsin (USA), (16-20 July 2001)*. Vol. 613. 1. 2002, pp. 934–941.
- [177] I. A. Lyulina et al. “Numerical simulation of pulse-tube refrigerators”. In: *International Journal of Nonlinear Sciences and Numerical Simulation* 5.1 (2004), pp. 79–88.
- [178] Y. L. Ju, C. Wang, and Y. Zhou. “Numerical simulation and experimental verification of the oscillating flow in pulse tube refrigerator”. In: *Cryogenics* 38.2 (1998), pp. 169–176.

- 
- [179] H. Yaling et al. “Numerical simulation of convergent and divergent tapered pulse tube cryocoolers and experimental verification”. In: *Cryogenics* 41.10 (2001), pp. 699–704.
- [180] C. Wang, P. Wu, and Z. Chen. “Numerical modelling of an orifice pulse tube refrigerator”. In: *Cryogenics* 32.9 (1992), pp. 785–790.
- [181] B. Flake and A. Razani. “Modeling pulse tube cryocoolers with CFD”. In: *AIP Conference Proceedings: Transactions of the Cryogenic Engineering Conference, Anchorage, Alaska (USA), (22-26 September 2003)*. Vol. 710. 1. American Institute of Physics. 2004, pp. 1493–1499.
- [182] G. W. Swift and S. L. Garrett. “Thermoacoustics: A Unifying Perspective for Some Engines and Refrigerators”. In: *Acoustical Society of America Journal* 113.5 (2003), pp. 2379–2381.
- [183] B. Ward, J. Clark, and G. Swift. “Design environment for low-amplitude thermoacoustic energy conversion, DeltaEC Version 6.4 b2 Users Guide”. In: *Los Alamos National Laboratory Network* (2016).
- [184] D. Gedeon. *Sage User’s Guide*. Version 11. Gedeon Associates. Athens, Ohio, 2016.
- [185] J. M. Lee et al. “Steady Secondary Momentum and Enthalpy Streaming in the Pulse Tube Refrigerator”. In: *Cryocoolers 8: A publication of the 8th International Cryocooler Conference held in Vail, Colorado, on June 28-30, 1994*. Boston, MA: Springer US, 1995, pp. 359–369.
- [186] J. M. Lee. “Steady secondary flows generated by periodic compression and expansion of an ideal gas in a pulse tube”. PhD thesis. University of Colorado at Boulder, 1997.
- [187] J. S. Cha et al. “Multi-dimensional flow effects in pulse tube refrigerators”. In: *Cryogenics* 46.9 (2006), pp. 658–665.
- [188] Y. P. Banjare, R. K. Sahoo, and S. K. Sarangi. “CFD simulation of a Gifford–McMahon type pulse tube refrigerator”. In: *International Journal of Thermal Sciences* 48.12 (2009), pp. 2280–2287.
- [189] I. Nachman, N. Pundak, and G. Grossman. “CFD modeling of reciprocating flow around a bend in pulse tube cryocoolers”. In: *the proceedings of the 15th International Cryocooler Conference*. Long Beach, California, (9-12, June 2008), 2008, pp. 251–259.
- [190] T. Kamoshita, Y. Yasukawa, and K. Ohshima. “Miniature pulse tube cooler”. In: *Fuji Electric Journal* 75.5 (2002). Fuji Electric Co., Ltd., Tokyo, Japan.
-

- [191] Y. L. He, Y. B. Tao, and F. Gao. “A new computational model for entire pulse tube refrigerators: Model description and numerical validation”. In: *Cryogenics* 49.2 (2009), pp. 84–93.
- [192] X. B. Zhang et al. “CFD study of a simple orifice pulse tube cooler”. In: *Cryogenics* 47.5-6 (2007), pp. 315–321.
- [193] Y. Hozumi, M. Shiraishi, and M. Murakami. “Simulation of thermodynamics aspects about pulse tube refrigerator”. In: *AIP Conference Proceedings: Transactions of the Cryogenic Engineering Conference, Anchorage, Alaska (USA), (22-26 September 2003)*. Vol. 710. 1. American Institute of Physics. 2004, pp. 1500–1507.
- [194] T. R. Ashwin, G. S. V. L. Narasimham, and S. Jacob. “CFD analysis of high frequency miniature pulse tube refrigerators for space applications with thermal non-equilibrium model”. In: *Applied Thermal Engineering* 30.2-3 (2010), pp. 152–166.
- [195] D. S. Antao and B. Farouk. “Computational fluid dynamics simulations of an orifice type pulse tube refrigerator: Effects of operating frequency”. In: *Cryogenics* 51.4 (2011), pp. 192–201.
- [196] G. K. Batchelor. *An Introduction to Fluid Dynamics*. Cambridge Mathematical Library. Cambridge, UK: Cambridge University Press, 2000.
- [197] A. H. Shapiro. *The dynamics and thermodynamics of compressible fluid flow, Vol. 1*. Vol. 454. Ronald Press, New York, 1953.
- [198] W. R. Smith. “One-dimensional models for heat and mass transfer in pulse-tube refrigerators”. In: *Cryogenics* 41.8 (2001), pp. 573–582.
- [199] W. Y. Yang et al. *Applied numerical methods using MATLAB*. Hoboken, New Jersey: John Wiley & Sons, 2005, pp. 401–411.
- [200] N. Almtireen, J. J. Brandner, and J. G. Korvink. “Axisymmetrical CFD and heat transfer in a high frequency pulse tube cryocooler”. (Manuscript submitted for publication).
- [201] S. Vanapalli et al. “High frequency pressure oscillator for microcryocoolers”. In: *Review of scientific instruments* 79.4 (2008), p. 045103.
- [202] K. Nam and S. Jeong. “Novel flow analysis of regenerator under oscillating flow with pulsating pressure”. In: *Cryogenics* 45.5 (2005), pp. 368–379.
- [203] J. S. Cha, S. M. Ghiaasiaan, and C. S. Kirkconnell. “Longitudinal hydraulic resistance Parameters of cryocooler and stirling Regenerators in periodic flow”. In: *AIP Conference Proceedings: Transactions of the Cryogenic Engineering Conference, Chattanooga (Tennessee), (16–20 July 2007)*. Vol. 985. 1. American Institute of Physics. 2008, pp. 259–266.

- 
- [204] J. J. Cha. “Hydrodynamic parameters of micro porous media for steady and oscillatory flow: Application to cryocooler regenerators”. PhD thesis. Georgia Institute of Technology, 2007.
- [205] J. S. Cha, S. M. Ghiaasiaan, and C. S. Kirkconnell. “Oscillatory flow in microporous media applied in pulse-tube and Stirling-cycle cryocooler regenerators”. In: *Experimental thermal and fluid science* 32.6 (2008), pp. 1264–1278.
- [206] J. P. Harvey. “Parametric study of cryocooler regenerator performance”. PhD thesis. Georgia Institute of Technology, 1999.
- [207] D. J. Guidry, J. J. McLean, and W. P. Avants. “Microfabricated Microchannel Regenerators for Cryocoolers”. In: *AIP Conference Proceedings: Transactions of the Cryogenic Engineering Conference, Keystone, Colorado (USA), (29 August-2 September 2005)*. Vol. 823. 1. American Institute of Physics. 2006, pp. 1895–1903.
- [208] P. Nika et al. “An integrated pulse tube refrigeration device with micro exchangers: design and experiments”. In: *International journal of thermal sciences* 42.11 (2003), pp. 1029–1045.
- [209] A. Veprik et al. “Micro-miniature split stirling linear cryocooler”. In: *AIP Conference Proceedings: Transactions of the Cryogenic Engineering Conference, Tucson, Arizona, (28 June-2 July 2009)*. Vol. 1218. 1. American Institute of Physics. 2010, pp. 363–370.
- [210] S. Sobol and G. Grossman. “Linear resonance compressor for Stirling-type cryocoolers activated by piezoelectric stack-type elements”. In: *IOP Conference Series: Materials Science and Engineering*. Vol. 101. 1. IOP Publishing. 2015, p. 012093.
- [211] R. Radebaugh, I. Garaway, and A. M. Veprik. “Development of miniature, high frequency pulse tube cryocoolers”. In: *Infrared Technology and Applications XXXVI*. Vol. 7660. International Society for Optics and Photonics. Bellingham, WA: SPIE, 2010, 76602J.
- [212] H. Z. Dang et al. “Development of a miniature coaxial pulse tube cryocooler for a space-borne infrared detector system”. In: *Infrared Technology and Applications XXXVI*. Vol. 7660. International Society for Optics and Photonics. Bellingham, WA: SPIE, 2010, 76602Q.
- [213] J. Li et al. “Modelling and experimental study of a 700 g micro coaxial Stirling-type pulse tube cryocooler operating at 100-190 Hz”. In: *IOP Conference Series: Materials Science and Engineering*. Vol. 502. 1. IOP Publishing. 2019, p. 012031.
- [214] C. S. Kirkconnell et al. “Development of a miniature Stirling cryocooler for LWIR small satellite applications”. In: *Tri-Technology Device Refrigeration (TTDR) II*. Vol. 10180. International Society for Optics and Photonics. Bellingham, WA: SPIE, 2017, pp. 1–13.
-



# Publications

## Journal Articles

### Published

- **Almtireen, N.**, Brandner, J.J. and Korvink, J.G., 2020. Pulse Tube Cryocooler: Phasor Analysis and One-Dimensional Numerical Simulation. *Journal of Low Temperature Physics*, pp.1-19.
- **Almtireen, N.**, Brandner, J.J. and Korvink, J.G., 2020. Numerical Thermal Analysis and 2-D CFD Evaluation model for an ideal cryogenic regenerator. *Micromachines*, 11(4), p.361.

### Submitted

- **N. Almtireen**, J. J. Brandner, and J. G. Korvink. Axisymmetrical CFD and heat transfer in a high frequency pulse tube cryocooler. Submitted for publication.

## Conference Proceeding

- **N. Almtireen**, J. J. Brandner, and J. G. Korvink. 2019, One-dimensional numerical analysis for Gifford-Mcmahon pulse tube cryocooler. Paper presented at the Refrigeration Science and Technology CRYOGENICS 2019 , Part F147717, 209-214.
- **N. Almtireen**, J. J. Brandner, and J. G. Korvink. Proceedings of the International Symposium on Thermal Effects in Gas flows in Microscale ISTE GIM 2019, Ettlingen, Germany.



# Appendix

## Appendix A: Ideal regenerator model MATLAB code

*Listing 1: Ideal regenerator model algorithm*

```
1 %*****
2 % MATLAB code for ideal regenerator model and its parametric study
3 %*****
4 Input_parameters=[ Case, dwire, Poro, L_reg, d_reg, freq,
5                   Theta_c, P_1, P_0, rho_mean, m_dot, W_prssDrop,
6                   Mu_mean, kg_mean, Mu_Cooling, kg_Cooling,
7                   rho_heating, Mu_Heating, kg_Heating, R, N_meshSize
8                   rhoBronze, rhoCopper, cp_m, cp_f, K_steel
9                   ]
10
11 %***** The regenerator and matrix parameters *****
12 Areg=pi*((d_reg)/2)^2;
13 V_reg=Areg*L;
14 Dh= (dwire*Poro)/(1-Poro);
15 N_meshes=L/(2*dwire);
16 As=Poro*Areg*(4*L_reg/Dh);
17 M=rhoBronze*(1-Poro)*(pi*(d/2)^2)*L;
18 Vdot= m_dot_mean/rho_mean;
19 m_dotHeating=rho_heating*Vdot;
20 Pr_heating=(cp_f*Mu_Heating)/(kg_Heating);
21 m_dotCooling=rho_cooling*Vdot;
22 Pr_cooling=(cp_f*Mu_Cooling)/(kg_Cooling);
23
24 V_1=1*W_net/(0.15*pi*f*P_1*cos(theta));
25 Volume_ratio1=V_reg*Poro/V_1;
26 V_mat= (1-Poro)*V_reg;
27
28 Mmat=rhoBronze*V_mat;
29 G=(m_dot_mean/(Poro*Areg));
30 G_h=(m_dotHeating/(Poro*Areg));
31 G_c=(m_dotCooling/(Poro*Areg));
32 %***** Dimensionless parameters for the heating and cooling period
33 %*****
34 Pr_mean=(cp_f*Mu_mean)/(kg_mean);
35 Re_mean=(Dh*(m_dot_mean))/(Poro*Areg*Mu_mean);
36 St_mean= 0.68*(Re_mean^(-0.4))/(Pr_mean^(0.667));
37 NTU_mean=0.5*St_mean*(L/(Dh/4));
38
39 ReHeating=(Dh*(m_dotHeating))/(Poro*Areg*Mu_Heating);
40 ReCooling=(Dh*(m_dotCooling))/(Poro*Areg*Mu_Cooling);
41 St_cold= 0.68*(ReCooling^(-0.4))/(Pr_cooling^(0.667));
```

```

1 St_hot= 0.68*(ReHeating^(-0.4))/(Pr_heating^(0.667));
2 NTU_h=0.5*St_hot*(L/(Dh/4));
3 NTU_c=0.5*St_cold*(L/(Dh/4));
4 C_r = (M*300)/(m_dot_mean*5193*(1/(2*f)));
5 NuHeating=0.68*(ReHeating^(0.6))*(Pr_heating^(0.333));
6 NuCooling=0.68*(ReCooling^(0.6))*(Pr_cooling^(0.333));
7 Nu_mean=0.68*(Re_mean^(0.6))*(Pr_mean^(0.333));
8 C_min=m_dotHeating/m_dotCooling;
9 C_max=m_dotCooling/m_dotHeating;
10 if C_min<C_max
11     C_min=C_min;
12 else
13     C_min=C_max;
14 end
15 Ratio_c=C_r/C_min;
16
17 LL= L_friction(Re_mean);           % Friction factor determination
18
19 %***** initial conditions for the Numerical Model *****
20 Nt=200;           % spatial and temporal grid size
21 Nx=500;
22 Dx=L/Nx;
23 Dt=1/Nt;
24 Tf(1:Nx,1:Nt)= 0;
25 Tm(1:Nx,1:Nt)= 0;
26 Tf_Heating(1,1:Nt+1)= 300;
27 Tf_cooling(1,1:Nt+1)= 80;
28 for i=1:Nx
29     Tm_INITIAL(i,1)= 300-((i-1)/(Nx))*220;
30 end
31
32 %***** Main code *****
33 for k=1:50
34     if k >= 2
35     end
36     for j=1:Nt
37         Tm_Heating(1:Nx,1)= Tm_INITIAL(1:Nx,1);
38         for i=1:Nx
39             h_Heating=1*(NuHeating*kg_Heating)/(Dh);
40             K1(i)= (2*NTU_h*(Dx/L))/(1+ (Dt*(2*NTU_h*(Dx/L))/(Ratio_c*(1/(2*f))))
                    +(0.5*((2*NTU_h*(Dx/L))));
41             K2(i)= ((Dt*(2*NTU_h*(Dx/L))/(Ratio_c*(1/(2*f))))/(1+ (Dt*(2*NTU_h*(Dx/
                    L))/(Ratio_c*(1/(2*f))))+(0.5*((2*NTU_h*(Dx/L))));
42
43             Tf_Heating(i+1,j)= Tf_Heating(i,j)-K1(i)*(Tf_Heating(i,j)-Tm_Heating(i,j
                    ));
44

```

```

1 Tm_Heating(i,j+1)= Tm_Heating(i,j)+K2(i)*(Tf_Heating(i,j)-Tm_Heating(i,j
   ));
2 end
3 end
4 Tm_cooling(1:Nx,1)= fliplr((Tm_Heating((1:Nx),Nt))')';
5 for j=1:Nt
6 for i=1:Nx
7 h_Cooling=(1)*(NuCooling*kg_Cooling)/(Dh);
8 K1(i)= (2*NTU_c*(Dx/L))/(1+ (Dt*(2*NTU_c*(Dx/L))/(Ratio_c*(1/(2*f))))
   +(0.5*((2*NTU_c*(Dx/L))));
9 K2(i)= ((Dt*(2*NTU_c*(Dx/L))/(Ratio_c*(1/(2*f))))/(1+ (Dt*(2*NTU_c*(Dx/
   L))/(Ratio_c*(1/(2*f)))) +(0.5*((2*NTU_c*(Dx/L))));
10 Tf_cooling(i+1,j)= Tf_cooling(i,j)-K1(i)*(Tf_cooling(i,j)-Tm_cooling(i,j
   ));
11 Tm_cooling(i,j+1)= Tm_cooling(i,j)+K2(i)*(Tf_cooling(i,j)-Tm_cooling
   (i,j));
12 Sign1(i,j)=Tf_cooling(i+1,j)- Tm_cooling(i,j+1);
13 end
14 end
15 NTU_Total2= 2*(NTU_Heating*NTU_Cooling)/(NTU_Heating+NTU_Cooling);
16 Ie=(1-(Thot-mean(Tf_Heating(Nx+1,Nt)))/(Thot-Tcold));
17 Thermal_loss= (Thot-Tcold)*cp_f*m_dot_mean*Ie
18 Thermal_loss_ratio=Thermal_loss/((W_net/0.15));
19 Axial_conduction_loss=K_m*(Thot-Tcold)*(1-Poro)*Areg/L_reg;
20 Axial_conduction_loss_ratio=Axial_conduction_loss/((W_net/0.15));
21
22 if case1 == 1
23 V_1=2*W_net/(0.15*pi*f*P_1*sin(theta));
24 Pressure_ratio=Poros*((pi*(d/2)^2)*L)/V_1;
25 elseif case1 == 2
26 V_1=1*W_net/(0.15*pi*f*P_1*cos(theta));
27 Pressure_Void_drop_loss2= (1-sqrt(1-(80*(Volume_ratio1*log((P_0+P_1)/(
   P_0-P_1)))/(190))^2))*1*(W_net/0.15);
28 end
29 Pressure_Void_drop_ratio2= (1-sqrt(1-((Poros*(V_reg)*Tcold*log((P_0+P_1)
   /(P_0-P_1)))/(V_1*Tmean))^2));
30 Pressure_drop_loss=(NTU_mean/(LL*rho_mean))*(Pr_mean^(0.667))*(G^2)*(1/
   P_1)*1*(W_net/0.15);
31 thickness_reg= 1*(3)*(P_0+P_1)*(d/(2*250e6));
32 Wall_losses= (300-80)*(pi*d*thickness_reg*K_s)/(L);
33 %*****

```

## Appendix B: One-dimensional model for the pulse tube element

*Listing 2: 1-D numerical model for the pulse tube*

```
1 %*****
2 % MATLAB code for the pulse tube 1-D model
3 %*****
4 Input_parameters=[ Cp,Cv,kg,Cor,P_0,P_1
5                   dtube, u_bar, freq, L_tube
6                   Dx,Dt,Vbuffer,Tcold,Thot
7                   ]
8
9 Range= (L)/(Dx);
10 Time= Span/Dt;
11 time1(1:Time)=0;
12 Displacment=0:Dx:L;
13 M=Range;
14 N=Time;
15 %***** Parameters and Temperature initial conditions *****
16 u(1:Range+1, 1:Time)=1;
17 u= single(u);
18 Pb(1:Time+1)=0;
19 Pb= single(Pb);
20 T(1:Range, 1:Time)=Thot;
21 b(1:Range, 1:Time)=0;
22 b= single(b);
23 T= single(T);
24 T(1, :)=Thot;
25 T(Range+1,:)=Tcold;
26 P(1:Time+1)=0;
27 P= single(P);
28 Pt(1:Time+1)=0;
29 Pt= single(Pt);
30 f1( 1:Time+1)=0;
31 f2( 1:Time+1)=0;
32 f1= single(f1);
33 f2= single(f2);
34 DPDt( 1:Time+1)=0;
35 DPDt= single(DPDt);
36 Phi( 1:Time+1)=0;
37 Phi= single(Phi);
38 %***** Pressure for the reservoir and source *****
39 t=0:Dt:Span;
40 t= single(t);
41 Pt= (cos(2*pi*f*t));
42 P= (P1*Pt)+P0;
43 Pb(1)=P0;
```

```

1 %***** Velocity matrix *****
2 for k = 1:Time
3 Pb(k+1)=Pb(k)+ ((Dt*((Cor*Cp)/(Vb*Cv)))*Pb(k)*(P(k)-Pb(k)));
4 DPDt(k)= (1/(2*pi*f))*((1)/Dt)*(Pt(k+1)-Pt(k));
5 f1(k)= (((A1/Cp) -A1)*(1/(Ao+A1*Pt(k)))*DPDt(k));
6 f2(k)=((1/Cp)*(1/(Ao+A1*Pt(k)))*DPDt(k));
7 Phi(k)=((kg/Cp)*(1/(Ao+A1*Pt(k))));
8 time1(k+1)= time1(k)+Dt;
9 u(1,k)= -1*((Cor)/(At))*(P(k)-Pb(k));
10 for i = 2:Range+1
11 if i < Range+1
12     u(i,k)= u(i-1,k)+(Phi(k)/Dx)*( T(i-1,k)-2*T(i,k)+T(i+1,k))+ Dx*f1(k);
13     elseif i==Range+1
14     u(i,k)= u(i-1,k)+(Phi(k)/Dx)*( T(i,k)-2*T(i-1,k)+T(i-2,k))+ Dx*f1(k);
15 end
16 rmp(1,k)= 1+(2*(Phi(k)*Dt*T(1,k)/(Dx^2)))-(Dt*f2(k))-((Dt/Dx)*u(1,k));
17 rmn(1,k)= 1+(2*(Phi(k)*Dt*T(1,k)/(Dx^2)))-(Dt*f2(k))+((Dt/Dx)*u(1,k));
18 rn1(1,k)= ((Phi(k)*Dt*T(1,k)/(Dx^2)))+((Dt/Dx)*u(1,k));
19 rn2(1,k)= ((Phi(k)*Dt*T(1,k)/(Dx^2)))-((Dt/Dx)*u(1,k));
20 r1(1,k)=((Phi(k)*Dt*T(1,k)/(Dx^2)));
21
22 rmp(i,k)= 1+(2*(Phi(k)*Dt*T(i,k)/(Dx^2)))-(Dt*f2(k))-((Dt/Dx)*u(i,k));
23 rmn(i,k)= 1+(2*(Phi(k)*Dt*T(i,k)/(Dx^2)))-(Dt*f2(k))+((Dt/Dx)*u(i,k));
24 r1(i,k)= ((Phi(k)*Dt*T(i,k)/(Dx^2)));
25 rn1(i,k)= ((Phi(k)*Dt*T(i,k)/(Dx^2)))+((Dt/Dx)*u(i,k));
26 rn2(i,k)= ((Phi(k)*Dt*T(i,k)/(Dx^2)))-((Dt/Dx)*u(i,k));
27
28 if u(i-1,k)>0
29     A(i-1,i-1) = rmn(i-1,k);
30 elseif u(i-1,k)<0
31     A(i-1,i-1) = rmp(i-1,k);
32 end
33 if i > 1 && u(i-1,k)>0
34     A(i-1,i) = -r1(i-1,k);
35 elseif i > 1 && u(i-1,k)<0
36     A(i-1,i) = -rn2(i-1,k);
37     end
38 if i > 1 && u(i,k)< 0
39     A(i,i-1) = -r1(i,k);
40 elseif i > 1 && u(i,k)>0
41     A(i,i-1) = -rn1(i,k);
42 end
43 end
44 A=A(1:Range,1:Range);
45 if A(1,2)== -rn2(1,k)

```

```

1 b(1,k)=(r1(1,k)*(300))+T(2,k);
2 elseif A(1,2)== -r1(1,k)
3     b(1,k)=(rn1(1,k)*(300))+T(2,k);
4     end
5
6 if A(Range,Range-1)== -rn1(Range,k)
7 b(Range,k)= (r1(Range,k)*(70))+T(Range-1,k);
8
9 elseif A(Range,Range-1)== -r1(Range,k)
10    b(Range,k)= (rn2(Range,k)*(70))+T(Range-1,k);
11
12 end
13 b(2:Range-1,k)=T(2:Range-1,k);
14 TT(1:Range,k)= trid(A,b(:,k));
15 T(2:M,k+1)=TT(2:Range,k);
16 end

```

## Appendix C: Used-defined function for the CFD modeling

*Listing 3: UDF for defining the piston velocity*

```
1 /*****  
2 UDF for specifying compressor wall motion profile boundary  
3 profile for inertance PTC system  
4 *****/  
5 #include "udf.h"  
6 static real vel_xx = 0.0;  
7 DEFINE_CG_MOTION(Piston_Motion_X,dt,vel,omega,time,dttime)  
8 {  
9   NV_S(vel, =, 0.0);  
10  NV_S(omega, =, 0.0);  
11  real t = time;  
12  real P_disp = 0.003;  
13  real f = 120;  
14    vel_xx = P_disp *2*pi*f*cos(2*pi*f*t);  
15    vel[0] = vel_xx;  
16  Message("time=%f, vel[0]=%f\n",t,vel[0]);  
17 }  
18 /*****/
```

## Appendix D: Post-processing MATLAB codes for the CFD models

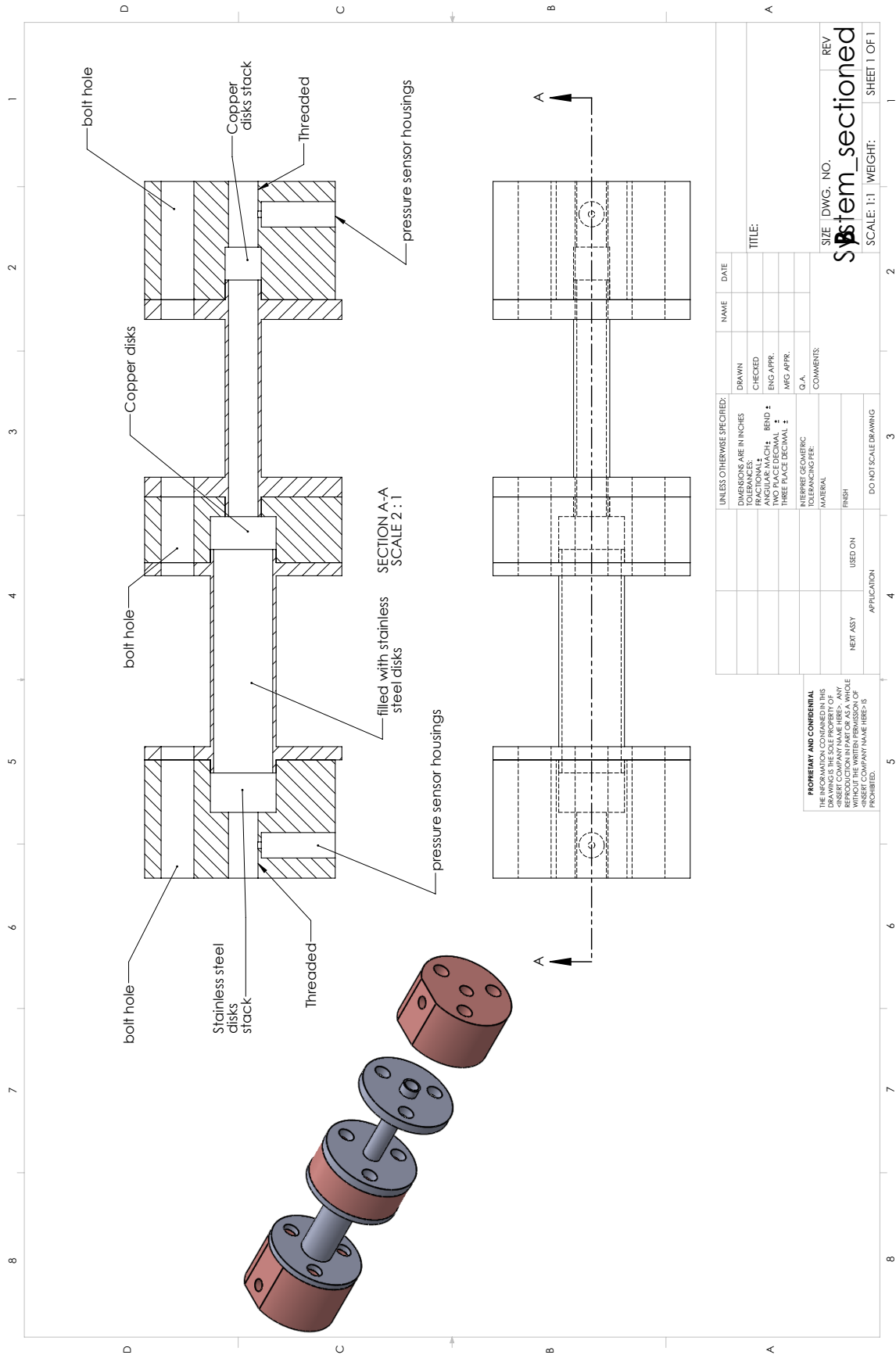
*Listing 4: MATLAB function to calculate signal cycle-averaged values*

```
1 %*****
2 % MATLAB function to calculate cycle-averaged values
3 %*****
4 function average_value = average_cyc(x,f,Ns)
5 power_mat=x;
6 N=Ns*floor(size(power_mat,1)/Ns);
7 count=(N)/Ns;
8 Avg= zeros(count,size(power_mat,2)-2);
9 Dt=1/(f);
10 for i=1:Ns:N
11     j=floor(i/Ns)+1;
12
13     Avg(j,1:size(power_mat,2)-3)=mean(power_mat(i:(i+Ns-1),2:size(
14     power_mat,2)-2));
15     Avg(j,size(power_mat,2)-2)=Dt*j;
16 end
17 average_value=Avg;
18 end
19 %*****
```

*Listing 5: MATLAB function to calculate phase shift between velocity and pressure*

```
1 %*****
2 % MATLAB function to calculate phase shift
3 %*****
4 function Phase=plot_phase(V,I,f)
5
6 t=0:(1/(f*length(V))):(1/f)-(1/(f*length(V)));
7 V=V/max(V);
8 DC_v=(abs(max(V))-abs(min(V)))*0.5;
9 VV=V-DC_v;
10 DC_I1=(abs(max(I))+abs(min(I)))*0.5;
11 II=I-DC_I1;
12 II=II/max(II);
13 DC_I2=(abs(max(II))-abs(min(II)))*0.5;
14 III=II-DC_I2;
15 y_rad=acos(dot(VV,III)/(norm(VV)*norm(III)));
16 y_deg=y_rad*360/(2*pi);
17 Phase=[y_deg,y_rad];
18 plot(t,VV)
19 hold on
20 plot(t,III)
21 end
22 %*****
```

# Appendix E: Experimental setup sectioned layout



# Appendix F: Hardware and transducers equipment

T7 labjack



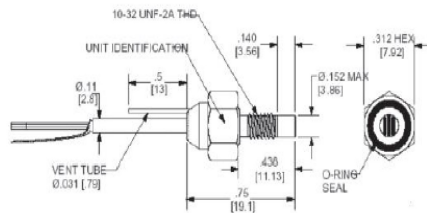
DT-670 silicon diode



Model 218E temperature monitor



2S102W Pressure Wave Generator



Piezoresistive pressure transducer and amplifier

